IPAC20

10 > 15
MAY 2020

11th INTERNATIONAL PARTICLE ACCELERATOR CONFERENCE

– PROCEEDINGS VOLUME

> Organizing Committee Chair
Mike SEIDEL, PSI, Switzerland

> Scientific Programme Committee Chair
Ralph ASSMANN, DESY, Germany

> Local Organizing Committee Chair
Frédéric CHAUTARD, GANIL, France

CAEN | FRANCE

www.ipac20.org

IPAC2020 – Organising Committee (IOC)

Philip Bambade		LAL	Brazil
Mark J. Boland		CLS	Canada
Paul Collier		CERN	Switzerland
Wolfram Fischer		BNL	USA
Ubaldo Iriso		CELLS	Spain
Prapong Klysubun		SLRI	Thailand
Shane Koscielniak		TRIUMF	Canada
Evgeny Levichev		BINP SB RAS	Russia
Liu Lin		LNLS	Brazil
Fernando Sannibale		LBNL	USA
Mike Seidel	**OC Chair**	PSI	Switzerland
Purushottam Shrivastava		RRCAT	India
Hitoshi Tanaka		SPRING-8	Japan

IPAC2020 – Organising Committee (IOC)

Ralph Assmann	**SPC Chair**	DESY	Germany
Mei Bai		GSI	Germany
Giovanni Bisoffi		INFN/LNL	Italy
John Byrd		ANL	USA
Sara Casalbuoni		EuXFEL	Germany
James Clarke		STFC/DL/ASTeC	UK
Marie-Emmanuelle Couprie		SOLEIL	France
Kuo-Tung Hsu		NSRRC	Taiwan
Andreas Jansson		ESS	Sweden
Heung-Sik Kang		PAL	Korea
Tadashi Koseki		KEK	Japan
Peter McIntosh		STFC/DL/ASTeC	UK
Fulvia Pilat		ORNL	USA
Qin Qing		ESRF & PKU	China
Tor Raubenheimer		SLAC	USA
Sven Reiche		PSI	Switzerland
Todd Satogata		JLAB	USA
Cristina Vaccarezza		INFN	Italy
Maurizio Vretenar		CERN	Switzerland
Zimmermann Frank		CERN	Switzerland

IPAC2020 – Scientific Advisory Board (Europe, Middle East and Africa)

Avni Aksoy	Ankara University	Turkey
Deepa Angal-Kalinin	STFC/DL/ASTeC	UK
Gianluigi Arduini	CERN	Switzerland
Riccardo Bartolini	DLS	UK
Simona Bettoni	PSI	Switzerland
Jacobus Conradie	iThemba LABS	South Africa
Arnaud Devred	CERN	Switzerland
Di Mitri Simone	Elettra	Italy
Dan Faircloth	STFC/RAL/ISIS	UK
Angeles Faus-Golfe	LAL	France
Robin Ferdinand	GANIL	France
Massimo Ferrario	INFN/LNF	Italy
Giuliano Franchetti	GSI	Germany
Gianluca Geloni	EuXFEL	Germany
Luca Giannessi	ENEA	Italy
Bernhard Hidding	USTRAT/SUPA	UK
Shaukat Khan	DELTA	Germany
Jens Knobloch	University of Siegen	Germany
Mike Lamont	CERN	Switzerland
Andreas Lehrach	FZJ	Germany
Mats Lindroos	ESS	Sweden
Andreas Maier	University of Hamburg	Germany
Barbara Marchetti	DESY	Germany
Ryutaro Nagaoka	SOLEIL	France
Andrea Pisent	INFN/LNL	Italy
Holger Podlech	IAP	Germany
Guenther Rehm	DLS	UK
Angela Salom	ALBA-CELLS	Spain
Ulrich Schramm	HZDR	Germany
Marcel Schuh	KIT	Germany
Daniele Sertore	INFN/LASA	Italy
Evgeny Syresin	JINR	Russia
Hamed Tarawneh	MAX IV	Sweden
Peter Urschütz	EBG MedAustron	Austria
Nikolay Vinokurov	NSU	Russia
Hans Weise	DESY	Germany
Carsten Peter Welsch	University of Liverpool	UK
Adriana Wawrzyniak	Solaris	Poland

IPAC2020 – Scientific Advisory Board (Americas)

Felicie Albert	LLNL	USA
Alexander V. Aleksandrov	ORNL	USA
Richard Baartman	TRIUMF	Canada
Ivan Vasilyevich Bazarov	Cornell University	USA
David Leslie Bruhwiler	RadiaSoft LLC	USA
Alexey Burov	Fermilab	USA
Bruce Carlsten	LANL	USA
Gianluigi Ciovati	Jlab	USA
Manoel Conde	ANL	USA
Alexei V. Fedotov	BNL	USA
Cameron Guy Robinson Geddes	LBNL	USA
Eliana Gianfelice-Wendt	Fermilab	USA
Anna Grassellino	Fermilab	USA
Robert W. Hamm	R&M Technical Enterprises	USA
Xiaobiao Huang	SLAC	USA
Zhirong Huang	SLAC	USA
Sang-Ho Kim	ORNL	USA
Ryan Roger Lindberg	ANL	USA
Michiko Minty	BNL	USA
Pietro Musumeci	UCLA	USA
Regis Neuenschwander	LNLS	Brazil
GianLuca Sabbi	LBNL	USA
Andrei Seryi	JLab	USA
Christoph Steier	LBNL	USA

IPAC2020 – Scientific Advisory Board (Asia)

Pei-Chen Chiu	NSRRC	Taiwan
Sundeep Chopra	IUAC	India
Caozheng Diao	SSLS	Singapore
Ryoichi Hajima	QST	Japan
Ji-Hong Hong	Chang Gung Mem. Hospital	Taiwan
Wenhui Huang	TUB	China
Yen-Chieh Huang	NTHU	Taiwan
Dong-O Jeon	IBS	South Korea
Bocheng Jiang	Advanced Research Inst.	China
Changbum Kim	PAL	South Korea
Willem Kleeven	IBA	China
Srinivas Krishnagopal	BARC	India
Hyeok-Jung Kwon	KAERI	South Korea
Victor Malka	LOA	Israel
Mika Masuzawa	KEK	Japan
Hiroki Okuno	RIKEN Nishina Center	Japan
Thapakron Pulampong	SLRI	Thailand
Sakhorn Rimjaem	Chiang Mai University	Thailand
Toshiyuki Shirai	QST-NIRS	Japan
Hyyong Suk	GIST	South Korea
Liangting Sun	IMP/CAS	China
Shiro Takano	JASRI	Japan
Yaw-Ren Eugene Tan	AS-ANSTO	Australia
Sheng Wang	IHEP	China
Seiya Yamaguchi	KEK	Japan
Xueqing Yan	PKU	China

IPAC2020 – Local Organising Committee (LOC)

Frederic Chautard	**LOC Chair**	GANIL	France
Laurent Serani	**LOC Co-Chair**	CNRS CENBG	France
Eric Lecorche	**LOC Deputy Chair**	GANIL	France
Maud Baylac		CNRS LPSC	France
David Boilley		GANIL	France
Elian Bouquerel		CNRS IPHC	France
Brigitte Cros		CNRS LPGP	France
Antoine Dael		MESRI	France
Nicolas Delerue		CNRS LAL	France
Angeles Faus-Golfe		CNRS LAL	France
Laurent Fortin		GANIL	France
Adeline Jeanne	**Event Manager**	GANIL	France
Charles Kitegi		SOLEIL	France
Guillaume Lalaire		GANIL	France
Samuel Meyroneinc		Institut Curie	France
Marie-Hélène Moscatello		GANIL	France
Laurent Nadolski		SOLEIL	France
Luc Perrot		CNRS IPNO	France
Freddy Poirier		ARRONAX	France
Jean-Luc Revol		ESRF	France
Yannick Saintigny		CIMAP	France

IPAC2020 – JACoW Editorial & Support Team (JEST)

Laurent Serani	**Editor-in-Chief**	GANIL	France
Volker RW Schaa	**Technical Editor**	GSI	Germany
Ivan Andrian		Elettra	Italy
Gustavo Bruno		LNLS	Brazil
Jan Chrin		PSI	Switzerland
Maxim Kuzin		BINP	Russia

Contents

ISBN: 978-3-95450-213-4 ISSN: 2673-5490 doi:10.18429/JACoW-IPAC2020-MOVIRO05

PERMANENT MAGNETS FOR ACCELERATORS

B. J. A. Shepherd†,1, STFC Daresbury Laboratory, Warrington WA4 4AD, UK
[1]also at Cockcroft Institute, Warrington WA4 4AD, UK

Abstract

Several groups internationally have been designing and building adjustable permanent magnet based quadrupoles for light sources, colliders, and plasma accelerators because of their very high gradients and zero power consumption. There are now examples of widely adjustable PM dipoles too. The ZEPTO project, based at STFC Daresbury Laboratory, developed several highly adjustable PM-based dipole and quadrupole prototypes for CLIC, and is now building a quadrupole to be installed in Diamond to gain experience ahead of the Diamond-2 upgrade. This is a review and comparison of the recent designs globally with comments on the future prospects.

INTRODUCTION

Permanent magnets (PMs), are materials that retain a strong remanent magnetisation after the applied magnetising field is removed. Energy is stored in the material, and a PM can produce a strong field especially when combined with other ferromagnetic elements to form a flux circuit.

Development of PMs is arguably one of the technological success stories of the 20th century [1], with the energy product BH_{max} doubling on average every twelve years thanks to the discovery of ferrites and later SmCo and NdFeB (Fig. 1), the latter being an 'almost ideal' PM material with a high proportion of iron and a relatively abundant rare-earth element. Both Sm_2Co_{17} and $Nd_2Fe_{14}B$ are near their theoretical maxima of 294 kJ/m³ and 512 kJ/m³ respectively. The discovery of new PMs led to technological developments in many other fields, including information storage, transport and energy generation.

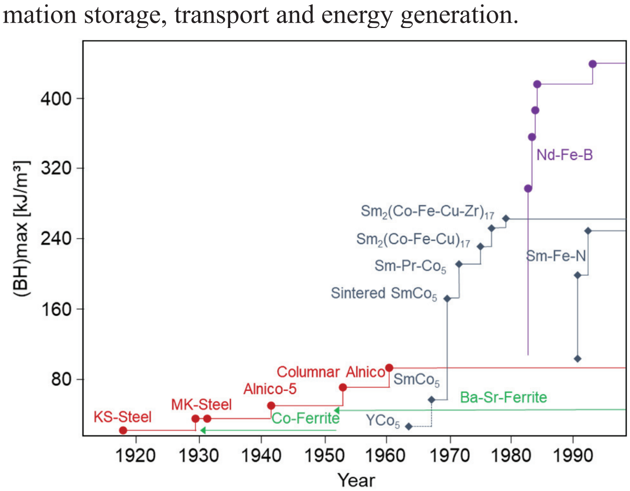

Figure 1: Development of PMs in the 20th century.

In accelerators, a major use of PMs over the years has been undulators and wigglers (insertion devices or IDs) in light sources [2], first proposed by Ginzburg in 1947 and used in storage rings from the 1970s onwards. When short periods and small gaps are required, PMs are usually a better choice for IDs. The Halbach array with four magnets per period gives an enhanced field on one side of each array which combines to give a strong field in the beam tube. These IDs have been extensively written about elsewhere [3] and are not the focus of this paper.

BEAMLINE PM DEVICES

The Halbach array can also be 'wrapped' around a cylinder to create a multipole magnet [4, 5]. Fields from an array of wedge-shaped PMs combine to give a strong field in the magnet centre (Fig. 2). These magnets typically have small apertures, and high gradients can be achieved. The gradient in a Halbach quadrupole is given by:

$$G = 2B_r K \left(\frac{1}{r_i} - \frac{1}{r_e}\right)$$

Here, B_r is the remanent field in the PM, r_i and r_e are the inner and outer radii, and K is an efficiency factor which approaches 1 as the number of segments increases.

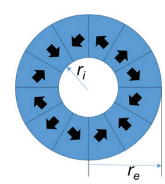

Figure 2: Schematic of a Halbach PM quadrupole, showing the inner and outer radii of the PMs.

Other multipole magnets (e.g. dipoles, sextupoles and combined function magnets) can be produced in this way.

Light source upgrades in recent years have focused on increasing the brightness, which often means a push to smaller apertures. When an electromagnet is scaled down by a factor k, if the current density is kept equal, the field will be reduced by k. In order to restore the field, either the current density or cross-section of the coils must be increased. PM-based magnets do not have this limitation, and this seems to favour the use of PM magnets for lower-aperture devices [6].

Advantages of Permanent Magnets

PM-based magnets require no current to provide a constant field. No large power supplies are required, and no current-carrying cables. No heat is dissipated, and so no water cooling is required (which also eliminates a potential source of vibration). So overall the infrastructure and running costs can be lower than electromagnets, and of course the CO_2 emissions during operation are greatly reduced.

† ben.shepherd@stfc.ac.uk

ISBN: 978-3-95450-213-4   ISSN: 2673-5490   doi:10.18429/JACoW-IPAC2020-MOVIRO05

Disadvantages and Mitigation

Temperature Stability Remanent field B_r changes as a function of temperature. This is a larger effect for NdFeB than for SmCo, with temperature coefficients in the vicinity of -1x10^{-3}/°C and -3x10^{-4}/°C respectively. This effect can be mitigated in a magnet by adding a shunt material with the opposite sign coefficient [6-9]. As the temperature increases, less flux is produced by the PM, but less is shunted away (Fig. 3). A typical shunt material is FeNi, traded as "Thermoflux".

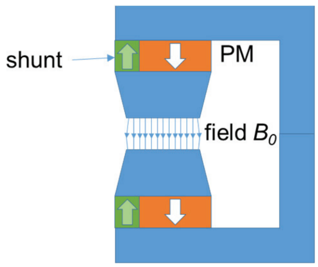

Figure 3: Schematic of a temperature compensation shunt in a PM dipole.

Radiation Impact of a high-energy particle in a PM material can cause a release of energy, leading to nucleation of inverse domains in a PM. Another mechanism is wide-area energy release from a large number of low-energy particles, and this effectively heats up the material.

Radiation damage can be mitigated in a number of ways, and research over several decades has identified many different variables that can have an impact [10-11].

- A higher-coercivity material performs better in a radiation environment, so for instance SmCo would be better than NdFeB.
- Operating at a lower temperature also increases the coercivity; experiments have shown that demagnetisation from 2.5 GeV electrons is reduced by 99% when the temperature is reduced to 140 K compared to room temperature.
- Baking PMs before use gives a small controlled demagnetisation, but can significantly reduce the radiation-induced demagnetisation.
- Altering the magnetic circuit or the shape of the PMs to change the operating point or permeance coefficient $Pc = B/H$. This reduces the demagnetising field seen by the PMs.
- Moving PMs away from the beam can reduce the amount of radiation that the PMs experience. This is potentially much easier to do for beamline magnets than for insertion devices, where the PMs are positioned as close to the beam as possible.

Tolerances A batch of PM blocks will have tolerances on dimensions and magnetisation strength and direction. For Halbach magnets and insertion devices, the field quality is directly influenced by differences between individual PMs. However for beamline magnets, blocks are often made up of individual smaller PMs, and the field quality is set by the shape of steel poles. Tolerances on individual PM blocks may be "smeared out" in this case.

Tuning This is perhaps the most obvious problem in designing PM-based magnets. Coils can be added to a PM-based magnet; however the operating point is in the flat part of the *B-H* curve, so the permeability is the same as free space. Large coils are needed for a relatively small change in field; so if a large adjustment range is needed, it becomes simpler to just replace the PMs with coils. A typical example of a PM dipole with adjustment provided by coils is shown in Fig. 4.

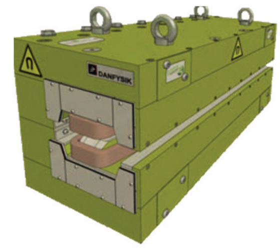

Figure 4: A 1 T dipole manufactured by Danfysik for the ASTRID-2 facility. The coils provide around ±3% of adjustment of the central field.

PMS AT ACCELERATOR FACILITIES

Synchrotron light sources around the world are upgrading to low-emittance lattices to increase their output brightness. In many cases these upgrades involve new PM devices as part of their magnetic lattice.

Sirius

At Brazil's LNLS facility, the Sirius facility requires 20 so-called 'Superbend' magnets (Fig. 5) with a maximum field of 3.2 T at a point in the magnet centre, and long combined function sections either side providing 0.5 T field and 9.5 T/m gradient. Adjustment via 'floating poles' and a control gap in the return yoke provides ±4% of tuning range in both field and gradient.

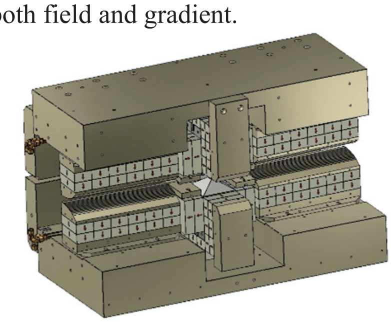

Figure 5: The Sirius facility's 'Superbend' magnet [12].

All the Superbend magnets have now been measured and installed, and at least 10 mA of beam has been circulated in the machine [13].

The ESRF

The "Extremely Brilliant Source" upgrade at the ESRF [6, 14] requires a total of 128 longitudinal gradient (LG) dipoles (Fig. 6), which have all been built using PMs. The dipoles are composed of five modules each with a constant field. The field steps up from 0.17 T to 0.53 T (or 0.64 T); this contributes to a reduced emittance by matching the field to the varying horizontal dispersion.

ISBN: 978-3-95450-213-4 ISSN: 2673-5490 doi:10.18429/JACoW-IPAC2020-MOVIR005

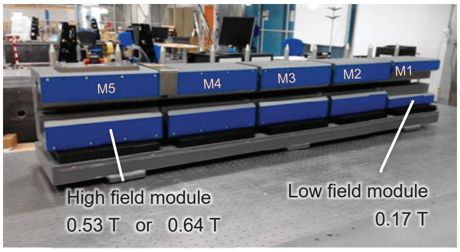

Figure 6: A PM LG dipole for the ESRF EBS upgrade.

Sm_2Co_{17} blocks are used to build the dipoles; all the modules (except the lowest field M1) are constructed identically except with a different number of PM blocks to alter the field. There is no capacity for tuning the dipoles. FeNi “Thermoflux” shunts are used, with a thickness between 0.8-4.5 mm, to bring the residual temperature coefficient down to 10 ppm/°C around room temperature (23°C).

The magnets are installed at the ESRF and commissioning is under way. Stored beam was achieved in December 2019, and first X-rays were produced in January 2020 [15].

Diamond Light Source

Like the ESRF-EBS, the planned upgrade for Diamond has fixed-field LG dipoles; the Diamond-II design [16] requires 96 of these, each with fields ranging from 0.29 T to 0.76 T (Fig. 7). Sm_2Co_{17} blocks are used, with FeNi shunts to compensate temperature variation.

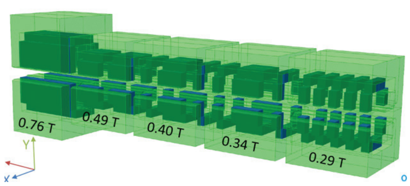

Figure 7. The LG dipole design for Diamond-II [17].

The current design for the combined-function DQ magnets for the storage ring is based on electromagnets; using PM magnets for these is also a possibility.

SPring-8

The SPring-8-II upgrade [18] is again based around PM-based LG dipoles, with a field range of 0.25-0.79 T in each magnet [19]. Tuning of the field is achieved by including a movable outer plate in the design (Fig. 8). A 400 mm long prototype has been built using NdFeB blocks, with three modules producing a 0.2-0.55 T field. FeNi magnetic shunts with thicknesses between 5-18 mm reduce the field variation with temperature down to 5-10 ppm/°C. A ‘window’ in the magnet backleg provides space for an NMR probe for long-term field observation.

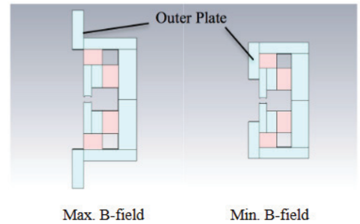

Figure 8: Cross-section of the SPring-8-II LG dipole prototype, showing outer plates used to provide field tuning.

R&D into a PM-based septum magnet (Fig. 9) has also taken place at SPring-8 [20]. This could potentially replace a single multi-kilowatt pulsed septum magnet. The baseline field is 1.2 T, and movable steel shunt plates provide a 2% adjustment range. The 5.5 mm thick FeNi magnetic shunt reduces the temperature variation down to around 1 ppm/°C. The 7 mm thick septum plate and counter-field PMs reduce the field seen by the stored beam down to almost zero.

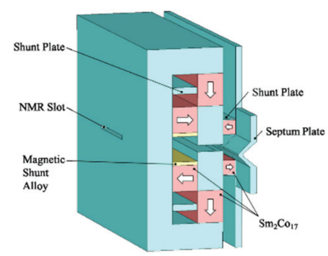

Figure 9: Schematic of a PM-based septum magnet for SPring-8-II.

Prototypes of the LG dipole and the septum magnet have been built and tested; they all meet the specifications.

Table 1 shows a summary of the PM dipoles used in the light source upgrade projects mentioned in this paper.

CBETA

CBETA is a 4-pass energy recovery linac (ERL) machine with a compact non-scaling FFAG lattice. This design is based entirely on PM-based magnets, with 216 fixed-field quadrupole and combined-function Halbach magnets [21]. Each magnet is composed of 16 PM wedges, with larger wedges being used for the DQ magnets (Fig. 10).

Table 1: Summary of PM Dipoles Used in Light Source Upgrade Projects

Parameter	Sirius	ESRF-EBS	Diamond-II	SPring-8-II
Energy	3 GeV	6 GeV	3.5 GeV	6 GeV
Lattice	5BA	7BA	6BA	5BA
Emittance	250 pm	135 pm	160 pm	149 pm
Number of dipoles	20	128	96	168
Dipole strength	0.5 T, 3.2 T	0.17-0.64 T	0.29-0.76 T	0.25-0.79 T
Gap	11 mm	25 mm	25 mm	25 mm
Adjustment range	±4%	None	None	Few %
Temperature stability	Not specified	10 ppm/°C	TBD	5-10 ppm/°C

11th Int. Particle Acc. Conf. IPAC2020, Caen, France JACoW Publishing
ISBN: 978-3-95450-213-4 ISSN: 2673-5490 doi:10.18429/JACoW-IPAC2020-MOVIR005

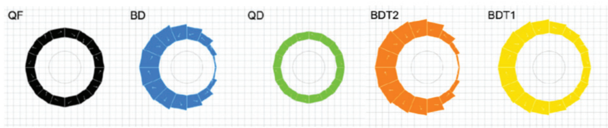

Figure 10: 2D outlines of the five CBETA magnet types.

The CBETA magnets have lengths between 122-133 mm, with gradients of ±11 T/m and bend fields of 0.3 T. Apertures are 80-98 mm.

To correct field errors arising from PM block tolerances, steel rods of varying lengths were inserted into a 3D printed insert just inside the magnet aperture (Fig. 11). This novel field correction method reduced the overall field errors down to an RMS value of 2.6×10^{-4}.

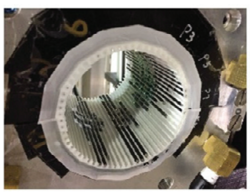

Figure 11: Field error tuning rods used in CBETA magnets.

QUAPEVA

At the COXINEL laser-plasma experiment [22], strong small-aperture quadrupoles are needed to focus a highly-divergent plasma-accelerated electron beam. SOLEIL have developed a highly-tunable PM quadrupole [23]. A central hybrid Halbach array is combined with rotating PM cylinders in the outer part of the magnet (Fig. 12), controlled by four independent motors. The magnet aperture is 12 mm and the adjustment range is 100-200 T/m. The early prototype had some issues with magnetic centre movement during adjustment, but this is reduced to around ±10 µm in the later models. A triplet of QUAPEVA magnets has been installed on the COXINEL beamline [24].

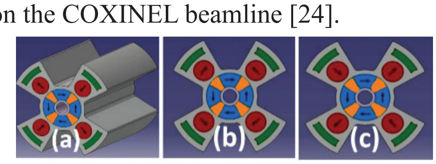

Figure 12: Adjustment principle of the QUAPEVA magnets; (a) maximum, (b) middle, and (c) minimum gradient.

THE ZEPTO PROJECT

In recent years, ASTeC and CERN have been collaborating on a project to develop highly tunable PM-based quadrupoles, aimed at the specifications for CLIC's drive beam decelerator (DBD). The motivation was to find an alternative to the 13.5 MW of electrical power required for 41,848 quadrupoles in the DBD line.

The ZEPTO (ZEro-Power Tunable Optics) concept is based around fixed steel poles and large PMs which are moved vertically, altering the magnetic circuit and provide a wide adjustment range. Two prototypes were designed, built and tested at DL and CERN – the first [25, 26] was designed to reach a large maximum gradient (60 T/m), sufficient for the high-energy end of the DBD, and the second [27, 28] to give a wide tuning range. In the first, tuning is achieved by introducing a gap between the PMs and the poles; the second moves the PMs perpendicular to the magnetisation axis and shifts the flux to a secondary outer circuit. In each case, the PMs are controlled by a single motor through a set of gearboxes and dual-threaded ballscrews.

Measurements of the ZEPTO quadrupoles indicated that they performed well against the CLIC specifications. One issue that arose was a small shift in the magnetic centre as the magnets were tuned from low to high strength; this was attributed to weakly ferromagnetic rails used in the motion system, which were not vertically symmetric.

A PM dipole magnet was also built as a prototype for the dipoles in the drive beam turnaround loops [29, 30]. This operates on similar lines, with a very large PM block sliding horizontally out in the dipole backleg to give a tuning range from 0.46-1.1 T. This very large block proved to be quite difficult to handle since the magnetic forces were so large; however the magnet performed very well and meets the specifications in terms of field quality and strength.

A third ZEPTO quadrupole magnet is currently under construction at Daresbury Laboratory. This one will be installed on Diamond's BTS transfer line, as a drop-in replacement for an electromagnetic quadrupole, with the aim of demonstrating that this PM technology can be used on an operating user facility. This is a further step towards commercialisation of our innovative PM technology. The concept is similar to ZEPTO-Q2, with two PMs moving vertically between a primary and secondary circuit for a large adjustment range. Two motors are used to ensure the magnet centre stays fixed during adjustment. SmCo blocks are used for improved temperature stability and radiation resistance. The magnet is splittable horizontally to enable installation around an existing vacuum chamber.

Table 2: Comparison of ZEPTO Magnet Parameters

Parameter	ZEPTO-Q1	ZEPTO-Q2	ZEPTO-D1	ZEPTO-Q3
Aperture	27.2 mm	27.6 mm	42 mm	32 mm
Magnet length	230 mm	190 mm	500 mm	300 mm
Field / gradient range	15-60 T/m	4-35 T/m	0.46-1.1 T	0.5-19 T/m
PM block size	18x100x230 mm	37.2x70x190 mm	500x400x200 mm	68x35.5x300mm
Number of blocks	4	2	1	2
Movement range	64 mm	75 mm	355 mm	90 mm
Good field region	±0.1%, 23 mm	±0.1%, 23 mm	±0.1%, 40 mm (H)	±0.1%, 20 mm
Measured centre shift	100 µm	80 µm	Zero	N/A

ISBN: 978-3-95450-213-4 ISSN: 2673-5490 doi:10.18429/JACoW-IPAC2020-MOVIRO05

Design of ZEPTO-Q3 is complete, and construction and installation will take place in late 2020. Table 2 shows a summary of the parameters of all four ZEPTO magnets.

CONCLUSIONS

PM-based magnets are finding increasingly widespread use as beamline magnets in accelerator facilities worldwide, particularly where compact magnets and high fields are required. They have many advantages over traditional electromagnets in terms of resource use and infrastructure and operating costs. There are several well-documented issues in using PMs, for instance radiation hardness, temperature stability, tuning, and block-to-block variations. However, these can be mitigated using several innovative techniques. Coils can be combined with PM magnetic circuits for a few per cent adjustment, or larger tuning ranges can be achieved using mechanical movement. Increasing use of this technology will no doubt lead to further innovations, as we have seen in the field of insertion devices – where recent innovation such as cryogenic PM undulators have led to further increases in performance. As we transition to a greener economy in the next decade, low-emission technologies like PMs will become increasingly important.

REFERENCES

[1] J. M. D. Coey, "Hard magnetic materials: a perspective", *IEEE Trans. Mag.*, vol. 47, no. 12, pp. 4671-4681, Dec. 2011. doi:10.1109/TMAG.2011.2166975

[2] A. L. Robinson, "X-Ray data booklet", https://xdb.lbl.gov

[3] J. A. Clarke, "The science and technology of undulators and wigglers", Oxford, UK: Oxford University Press, 2004.

[4] K. Halbach, "Design of permanent multipole magnets with oriented rare earth cobalt material", *Nucl. Instrum. Methods*, vol. 169, pp. 1-10, 1980. doi:10.1016/0029-554X(80)90094-4

[5] C. Benabderrahmane and J. Chavanne, "Review of permanent magnet technology for accelerators", presented at IPAC'17, Copenhagen, Denmark, May 2017, paper THYB1, unpublished.

[6] J. Chavanne, "Permanent accelerator magnets for light sources", presented at the 5th ESSRI Workshop, PSI, Nov. 2019, unpublished.

[7] Vacuumschmelze material data, https://vacuumschmelze.com/Products/Permanent-Magnets

[8] F. Bødker *et al.,* "Permanent magnets in accelerators can save energy, space and cost", presented at IPAC'13, Shanghai, China, May 2013, paper THPME001, pp. 3511-3513.

[9] S. H. Kim and C. Doose, "Temperature compensation of NdFeB permanent magnets", presented at PAC'97, Vancouver, Canada, May 1997, paper 2P001, pp. 3227-3229.

[10] A. J. Samin, "A review of radiation-induced demagnetization of permanent magnets", *J. Nucl. Mat.*, vol. 503, pp. 42-55, May 2018. doi:10.1016/j.jnucmat.2018.02.029

[11] B. J. A. Shepherd, "Radiation damage to permanent magnet materials: a survey of experimental results", CLIC Note 1079, May 2018.

[12] J. Citadini, L. N. P. Vilela, R. Basílio and M. Potye, "Sirius – details of the new 3.2T permanent magnet superbend", presented at MT-25, Amsterdam, The Netherlands, Aug 2017, paper Tue-Af-Po2.02-07.

[13] L. Liu, "Sirius commissioning results", presented virtually at IPAC'20, May 2020, paper MOVIR06, this conference.

[14] G. Le Bec *et al.*, "Magnets for the ESRF diffraction-limited light source project", *IEEE Trans. Appl. Supercond.*, vol. 26, no. 4, pp. 1-8, June 2016. doi:10.1109/TASC.2015.2510402

[15] ESRF EBS blog, https://ebs.esrf.fr

[16] Diamond-II upgrade CDR and science case, https://www.diamond.ac.uk/Home/About/Vision/Diamond-II.html

[17] A. Shahveh, presented at Diamond-II MAC, Feb. 2020, private communication.

[18] H. Tanaka, "Upgrade strategy and development status of accelerator system at SPring-8/SACLA", PSI seminar, Dec. 2019, https://indico.psi.ch/event/8362

[19] T. Taniuchi *et al.*, "R&D of permanent dipole magnet for SPring-8-II", in *PASJ'16*, Chiba, Japan, Aug. 2016, paper MOP109 (in Japanese).

[20] T. Taniuchi *et al.*, "DC septum magnet based on permanent magnet for next-generation light sources", *Phys. Rev. Accel. Beams*, vol. 23, p. 012401, Jan. 2020. doi: 10.1103/PhysRevAccelBeams.23.012401

[21] S. Brooks *et al.*, "CBETA permanent magnet production run", in *Proc. IPAC'19*, Melbourne, Australia, May 2019, pp. 4318-4321. doi:10.18429/JACoW-IPAC2019-THPTS088

[22] D. Oumbarek Espinos *et al.*, "Skew quadrupole effect of laser plasma electron beam transport", *Appl. Sci.* vol. 9, no. 12, p. 2447, Jun. 2019. doi:10.3390/app9122447

[23] F. Marteau *et al.*, "Variable high gradient permanent magnet quadrupole (QUAPEVA)", *Appl. Phys. Lett.*, vol. 111, no. 25, p. 253503, Nov. 2017. doi:10.1063/1.4986856

[24] A. Ghaith *et al.*, "Tunable high gradient quadrupoles for a laser plasma acceleration based FEL", *Nucl. Instrum. Methods*, vol. 909, pp. 290-293, Nov. 2018. doi:10.1016/j.nima.2018.02.098

[25] B. J. A. Shepherd *et al.*, "Tunable high-gradient permanent magnet quadrupoles", *J. Inst.*, vol. 9, T11006, Nov. 2014. doi:10.1088/1748-0221/9/11/T11006

[26] B. J. A. Shepherd *et al.*, "Prototype adjustable permanent magnet quadrupoles for CLIC", in *Proc. IPAC'13*, Shanghai, China, May 2013, paper THPME043, pp. 3606-3608.

[27] B. J. A. Shepherd *et al.*, "Novel adjustable permanent magnet quadrupoles for the CLIC drive beam decelerator", *IEEE Trans. Appl. Supercond.*, vol. 22, no. 3, p. 4004204, Mar. 2012. doi:10.1109/TASC.2012.2191632

[28] B. J. A. Shepherd *et al.*, "Design and measurement of a low-energy tunable permanent magnet quadrupole prototype", in *Proc. IPAC'14*, Dresden, Germany, June 2014, pp. 1316-1318. doi:10.18429/JACoW-IPAC2014-TUPRO113

[29] A. R. Bainbridge *et al.*, "The ZEPTO dipole: zero power tuneable optics for CLIC", in *Proc. IPAC'17*, Copenhagen, Denmark, May 2017, pp. 4338-4340. doi:10.18429/JACoW-IPAC2017-THPIK105

[30] A. R. Bainbridge *et al.*, "Measurement report on the prototype ZEPTO dipole magnet for CLIC", presented at IMMW21, Grenoble, France, June 2019, unpublished.

ISBN: 978-3-95450-213-4 ISSN: 2673-5490 doi:10.18429/JACoW-IPAC2020-MOVIR01

THE FUTURE CIRCULAR COLLIDER STUDY*

A.-S. Müller, Karlsruhe Institute of Technology (KIT), 76131 Karlsruhe, Germany
M. Benedikt, F. Zimmermann†, CERN, 1211 Geneva 23, Switzerland

Abstract

At the end of 2018, a large worldwide collaboration, with contributors from more than 350 institutes completed the conceptual design of the Future Circular Collider (FCC), a ~100 km accelerator infrastructure linked to the existing CERN complex, that would open up the way to the post-LHC era in particle physics. We present an overview of the two main accelerator options considered in the design study, namely the lepton collider (FCC-ee), serving as highest-luminosity Higgs and electroweak factory, and the 100-TeV energy-frontier hadron collider (FCC-hh), along with the ongoing technological R&D efforts and the planned next steps. A recently approved EU co-funded project, the FCC Innovation Study (FCCIS), will refine the design of the lepton collider and prepare the actual implementation of the FCC, in collaboration with European and global partners, and with the local authorities.

INTRODUCTION

The FCC Conceptual Design Report (CDR) [1–4] was released at the end of 2018. The results of the conceptional design study naturally gave rise to an integrated FCC programme [5–7], which was proposed as input to the European Strategy Process: Inspired by the successful past LEP-LHC sequence at CERN, this integrated programme features in its first stage the lepton collider FCC-ee — namely a Higgs and electroweak factory, which will produce Z, W and H bosons, and top quarks at considerable rates: At its design luminosity, FCC-ee will repeat the the entire LEP Z physics programme in about 1 minute. The second stage will be the FCC-hh proton collider (~100 TeV c.m. energy) as the natural continuation of the LHC at the energy frontier, with additional ion and lepton-hadron collision options. The integrated FCC programme represents a comprehensive cost-effective approach, aimed at maximizing the physics opportunities. FCC-ee and hh will offer complementary physics, while profiting from common civil engineering and technical infrastructures. They will both build on, and reuse, CERN's existing infrastructure. In addition, the FCC integrated project, with its technical schedule, allows for a seamless continuation of High Energy Physics (HEP) after the High Luminosity LHC (HL-LHC) programme, expected to end in the second half of the 2030's.

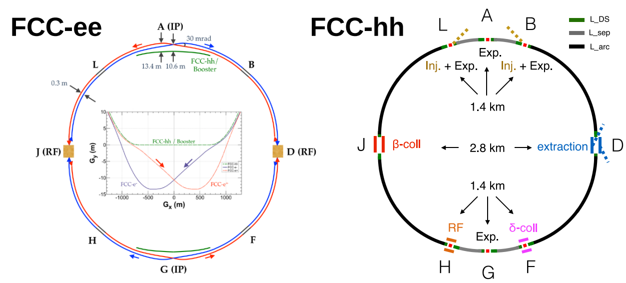

Figure 1: Layouts of FCC-ee and FCC-hh successively housed in the same tunnel [2, 3, 6].

FCC-ee

FCC-ee is conceived as a double-ring e^+e^- collider whose 97.75 km baseline circumference follows the footprint of FCC-hh, except around the Interaction Points (IPs) at locations A and G — see Fig. 1. The FCC Interaction Region (IR) features an asymmetric layout and optics in order to limit synchrotron radiation (SR) emitted towards the detector [8]. The critical photon energy is kept below 100 keV over the last 450 m from the IP, which is one of the lessons learnt from the LEP collider [9]. The present baseline envisions 2 IPs. Alternative layouts with 3 or 4 IPs are under study. The electron and positron bunches are collided under a large horizontal crossing angle of 30 mrad with a so-called crab-waist optics [10, 11]. The IR optics accommodates only one sextupole pair per final focus side, used for a local correction of the vertical chromaticity, with a cancellation of geometric aberrations. Reducing the strength of the outer sextupoles creates the crab waist [8]. This low number of strong sextupoles ensures a minimum amount of nonlinearity and a correspondingly large dynamic aperture. The FCC-ee synchrotron radiation power is limited to 50 MW per beam at all beam energies. The magnet strengths in the arcs are tapered so as to match the local beam energy. A common radiofrequency (RF) system is used for the $t\bar{t}$ running, where the maximum RF gradient is required, but the number of bunches is quite low, so that parasitic collisions in the RF straights can be avoided.

Key parameters of FCC-ee are compiled in Table 1. Figure 2 illustrates that the FCC-ee offers an attractive luminosity level over its entire centre-of-mass energy range from 90 to 365 GeV. From about 2 TeV onward a hypothetical muon collider (MAP-MC) is expected to yield the best performance. Between about 400 GeV and 1 or 2 TeV the linear colliders ILC and CLIC, respectively, appear optimally suited.

The FCC-ee design is based on proven techniques from past and present colliders, not pushing any key parameter (beam lifetime, β_y^*, e^+ production rate, SR photon energy)

* This work was supported, in part, by the European Commission under the HORIZON2020 Research and Innovation Programme, grant agreement 951754 (FCCIS).
† frank.zimmermann@cern.ch

ISBN: 978-3-95450-213-4 ISSN: 2673-5490 doi:10.18429/JACoW-IPAC2020-MOVIR01

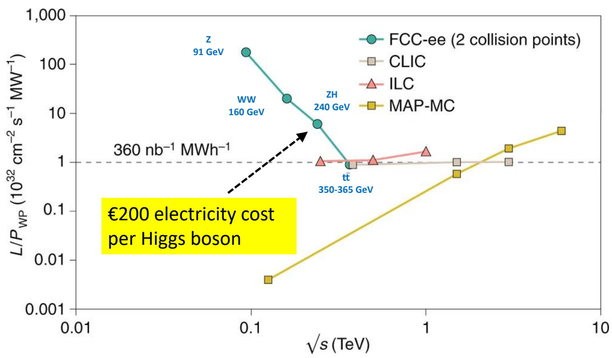

Figure 2: Luminosity L per supplied electrical wall-plug power P_{WP} is shown as a function of centre-of-mass energy for several proposed future lepton colliders [7, 12]. Also indicated is the FCC-ee electricity cost per Higgs boson, assuming a price of 50 Euro MWh^{-1} [2, 7].

Table 1: Key Parameters of FCC-ee

parameter		Z	WW	ZH	$t\bar{t}$
c.m. energy	[GeV]	91	160	240	365
beam current	[mA]	1390	147	29	5.4
no. bunches/beam		16640	2000	393	48
bunch intensity	[10^{11}]	1.7	1.5	1.5	2.3
longit. damping	[turns]	1281	235	70	20
hor. IP beta	[m]	0.15	0.2	0.3	1
vert. IP beta	[mm]	0.8	1	1	1.6
hor. emittance	[nm]	0.3	0.8	0.6	1.5
vert. emittance	[pm]	1.0	1.7	1.3	2.9
lum./IP	[10^{34} cm^{-2}s^{-1}]	230	28	8.5	1.55
beam lifetime	[min.]	68	49	12	12

beyond what has already been achieved. The B-factories KEKB and PEP-II, along with DAΦNE, have demonstrated the merit of double-ring lepton colliders, and the possibility of operating with high beam currents, of up to a few Ampere. KEKB, PEP-II, BEPC-II and SuperKEKB have successfully used top-up injection, greatly increasing the daily integrated luminosity. SuperKEKB has already achieved the low β_y^* of 1 mm [13], as required for FCC-ee; it is ultimately aiming for values of about 0.3 mm. Both DAΦNE and SuperKEKB have improved their specific luminosity and beam-beam performance by operating with the crab-waist collision scheme. LEP has explored operation at high beam energy, with about the same SR power per unit length and very similar critical photon energies as planned for FCC-ee. LEP and VEPP-4M have pioneered precision energy calibration based on resonant depolarisation [14, 15]. The KEKB and SuperKEKB e^+ sources provide a positron production rate similar to the one needed for FCC-ee top up injection, which is less than the world record achieved at the SLC. HERA, LEP, and RHIC have established various techniques of spin gymnastics and for optimising the degree of self-polarisation, which are relevant for the FCC-ee energy calibration at the Z and WW energies. In particular, SuperKEKB, presently under commissioning, is demonstrating FCC-ee key concepts. Its design beam lifetime is 3–6 times shorter than the smallest lifetime expected at FCC-ee.

Nevertheless, the FCC-ee design must also address a few new challenges. The FCC-ee IR will potentially experience significant heat loads from radiative Bhabha scattering (kW level), beamstrahlung (possibly MW level, intercepted about 50 m downstream of the IP), resistive wall heating (kW), higher order mode (HOM) excitation — which is addressed by an optimised chamber design and a dedicated HOM absorber close to the crotch [16] — and SR from the final quadrupoles. The IR magnet system is quite complex. In addition to the 2 T detector solenoid and final focusing quadrupole Q1, it features a compensation solenoid in front of Q1, and a shielding solenoid surrounding Q1 [17]. To maximise the detector acceptance a novel thin-wall cryostat has been proposed [18].

For a ~100 km long collider the resistive wall becomes a dominant source of impedance. If the vacuum chamber is coated with a standard 1 μm thick NEG film, this impedance can drive the longitudinal microwave instability [19]. Therefore, for the FCC-ee, a novel ultrathin NEG coating, of about 100 nm thickness, has been developed and qualified with respect to pumping properties, secondary emission yield, activation behaviour, and impedance [20].

In collision, the FCC-ee bunch profiles are strongly affected by beamstrahlung. Suitable high-throughput single-shot diagnostics is being developed at KIT's KARA facility, where longitudinal bunch profiles are already recorded with an electro-optical spectral decoding setup [21–23].

LEP saw no polarisation for beam energies above 65 GeV. The much larger bending radius of FCC-ee reduces the beam energy spread, and, thereby, the spin tune spread. This should allow for reaching several tens of per cent polarisation, not only on the Z pole, but also at the WW threshold [24], enabling a precise energy calibration at the 10^{-6} level in both these modes of operation [25]. The precise knowledge of the collision energy is an important component of the physics program for the electroweak factory.

While R&D efforts also pursue cost-effective, low-power, low-field magnets for the FCC-ee collider arcs [26], the thrust of FCC-ee technology R&D is on the superconducting RF (SRF) system, especially advanced cavities, RF power sources, and cryomodules. Here the R&D aims at improving performance and efficiency, and at reducing cost. Example FCC-ee SRF developments include improved Nb/Cu coating/sputtering (e.g. electron cyclotron resonance fibre growth, high-power impulse magnetron sputtering) new cavity fabrication techniques (e.g. electro-hydraulic forming [27], improved polishing, seamless production, ...), coating of A15 superconductors (e.g. Nb_3Sn), cryo-module design optimisation, bulk Nb cavity R&D in collaboration with FNAL, JLAB, and Cornell (also KEK and IHEP are active in this domain), MW-class fundamental power couplers for 400 MHz, and novel high-efficiency klystrons exploiting new bunching methods.

ISBN: 978-3-95450-213-4 ISSN: 2673-5490 doi:10.18429/JACoW-IPAC2020-MOVIR01

FCC-hh

The FCC-hh seeks an order of magnitude performance increase in both energy and luminosity, with 100 TeV c.m. collision energy (versus 14 TeV for LHC), and 20 ab^{-1} accumulated per experiment collected over 25 years of operation, to be compared with 3 ab^{-1} for the (HL-)LHC. The transition from LHC to FCC-hh amounts to a similar performance increase as the step from the Tevatron to LHC. Table 2 compares the main parameters for two phases of FCC-hh with those of HL-LHC and LHC. Beam and optics parameters of FCC-hh appear to be less demanding than those for the HL-LHC. The key technology to realize the FCC-hh is high-field magnets, that is developing and fabricating a few thousand dipole magnets with a field of 16 T in a reliable and economical way. Recently substantial progress has been made in Nb_3Sn magnet development at both FNAL (demonstrator magnet MDPCT1 reached 14.1 T at 4.5 K [28]) and CERN (eRMC achieved a field of 16.5 T at the conductor [29]). Alternative options under study include magnets based on high-temperature superconductor.

Table 2: Parameters of FCC-hh Compared with (HL-)LHC

parameter		FCC-hh	HL-LHC	LHC
c.m. energy	[TeV]	100	14	14
dipole field	[T]	16	8.33	8.33
beam current	[A]	0.5	1.1	0.58
no. bunches/beam		10400	2760	2808
bunch intensity	[10^{11}]	1.0	2.2	1.15
SR power/ring	[kW]	2400	7.3	4.6
longit. damping	[hr]	0.54	12.9	12.9
IP beta	[m]	1.1 0.3	0.15	0.55
norm. emittance	[μm]	2.2	2.5	3.75
lum./IP	[10^{34} cm^{-2}s^{-1}]	5 30	5 (lev.)	1
events/crossing	[100]	1.7 10	1.3	0.3
energy/beam	[GJ]	8.4	0.7	0.38

Other challenging FCC-hh parameters pertain to the synchrotron radiation (SR) power, the number of physics events per bunch crossing, and the energy stored in the beam. At FCC-hh, almost 5 MW of SR power is emitted inside the cold arc magnets. To efficiently remove this heat it is intercepted by a beam screen (BS) at an elevated temperature of about 50 K (to be compared with 4.5–20 K for the LHC). This beam screen is mounted inside the 1.9 K cold bore of the magnets. The beam screen should also provide sufficient pumping capacity, present a low impedance to the beam, suppress photo-electrons and prevent electron cloud. An optimized "double" beamscreen design for FCC-hh was developed in the framework of the EuroCirCol project [30], and illuminated with synchrotron radiation at the KIT KARA facility, whose electron-beam SR power spectrum closely resembles the one of the FCC-hh proton beam [31]. Results in a warm setup have confirme the chosen approach [32]. Recently installed liquid nitrogen lines also allow experiments at cryogenic temperature. The tests at KARA demonstrate a drastic reduction of molecular photo-desorption yield for the FCC-hh BS geometry as compared with flat Cu chamber (factor 15), and when irradiating at cold (factor 100 except H_2) [33].

FCC IMPLEMENTATION

The present baseline position for the 97.75 km long tunnel was established by choosing the least risky, fastest and cheapest construction, and feasible positions for large span caverns (which are the most challenging structures). More than 75% of this tunnel lies in France, including 8 or 9 out of a total of 12 access points; the other 3 or 4 access points are located in Switzerland. The next step of the site investigation entails a review of these site locations and of the machine layout. Figure 3 illustrates the tunnel integration for FCC-ee and FCC-hh in the arcs, where the inner tunnel diameter is 5.5 m, to be compared with 3.8 m for the LEP/LHC tunnel.

The technical schedule of the FCC integrated project is shown in Fig. 4. At present, the R&D for the FCC-ee (in yellow) focuses on an optimized engineering design, energy efficiency, and maintainability. The R&D for FCC-hh (in green) concentrates on conductor development and high-field magnet technology. With a start in 2020 the entire programme would conclude by 2090, after another ~20 years of LHC, 15 years of FCC-ee and 25 years of FCC-hh operation. The only period without physics is the ten years, ~2055–64, needed to dismantle the FCC-ee and install the FCC-hh.

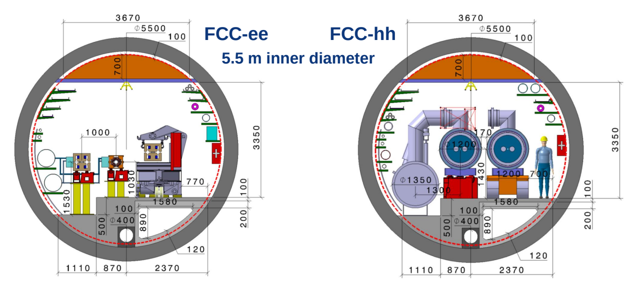

Figure 3: FCC tunnel integration in the arcs [2, 3, 6].

FCC COLLABORATION

The FCC study proceeds as a collaborative, world-wide effort. One example is the participation of the Karlsruhe Institute of Technology (KIT), which is contributing to both FCC-ee and FCC-hh.

At present, the FCC collaboration includes 139 institutes and 30 companies hailing from 34 countries, plus support from the European Commission through various projects like EuroCirCol, EasiTrain and the FCCIS. Further increasing the international collaboration is a prerequisite for success: Links with science, research & development and high-tech industry are essential for preparing the FCC implementation.

EuroCirCol was a European Union Horizon 2020 program with 3 MEuro co-funding, that was completed in December 2019. It included 15 European beneficiaries and KEK plus, as associated partners, the US laboratories FNAL, BNL,

ISBN: 978-3-95450-213-4
ISSN: 2673-5490
doi:10.18429/JACoW-IPAC2020-MOVIR01

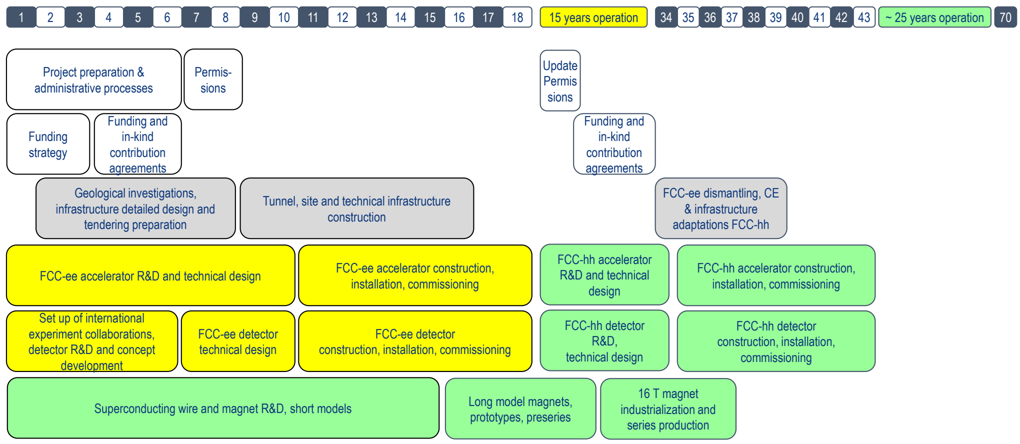

Figure 4: Technical schedule of FCC integrated project [7,12]. Top row shows the years from start of project implementation.

LBNL, and NHFML. The EuroCirCol scope covered the key work packages for the FCC-hh collider: Optics design for arcs and IR; design of the cryogenic beam vacuum system including beam tests at KARA; the 16 T dipole design with a construction folder for demonstrator magnets. The FCCIS was recently accepted for funding by the European Commission with the highest achievable score. Its beneficiaries are displayed in Fig. 5. Also included as important partners are the local authorities in Switzerland (État de Genève) and France (D.R.R.T.), the US D.O.E., BINP in Russia and Oxford University in the UK. FCCIS covers the FCC-ee design optimisation, preparation of construction planning and environmental evaluation, management of excavation materials, user community building, public engagement, and socio-economic impact studies.

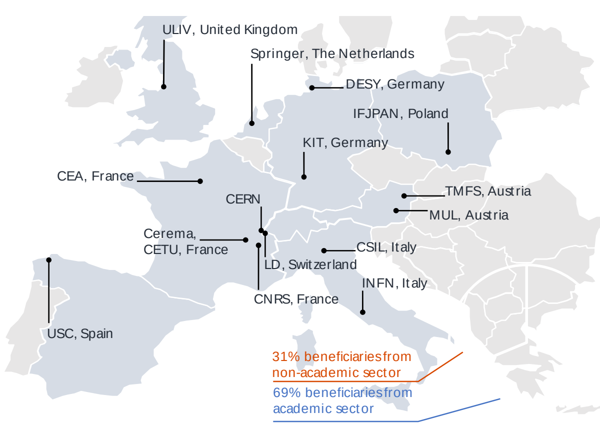

Figure 5: Beneficiaries of the FCCIS (J. Gutleber).

Preparatory work with the host states is progressing. Administrative processes for the project preparatory phase were developed; a first review of the tunnel placement was performed. Requirements for urban, environmental, and economic impact, land acquisition and construction-permit processes are being defined. A common optimisation of the collider tunnel and surface site infrastructure is underway.

SUMMARY AND OUTLOOK

FCC-ee is a compelling Higgs and electro-weak factory at c.m. energies from 90 to 365 GeV. The FCC-ee key concepts, ingredients, and parameters were already demonstrated, or exceeded, at various past and present machines. The main technologies for FCC-ee exist today; a strong R&D program with industry is being set up for optimising energy efficiency maintainability, machine availability, and construction cost.

FCC-hh is the highest-energy collider conceivable in the 21st century. Its design is based on lessons from the LHC. The required high-field 16 T magnets are not yet at hand. A rigorous conductor and magnet R&D program aims at rendering these magnets available around 2050/55.

The FCC-ee/FCC-hh integrated programme represents a coherent long-term strategy, with a sharing of tunnel, technical infrastructure (electricity, cooling and ventilation, etc.), perhaps reuse of detector modules, along with complementary physics, and exploitation of existing CERN facilities.

The first phase of the FCC study delivered baseline machine designs with a performance matching the physics requirements. The integrated FCC programme was submitted to the European Strategy Update 2019/20. The next step will develop a concrete implementation scenario in collaboration with the host-state authorities, accompanied by machine optimisation, physics studies and technology R&D. This step is supported by the EC H2020 Design Study FCCIS.

The long-term goal is to provide a world-leading HEP infrastructure for the 21st century, which will push the particle-physics precision and energy frontiers far beyond the present state-of-the-art.

REFERENCES

[1] M. Mangano *et al.*, "FCC Physics Opportunities," *Eur. Phys. J. C*, vol. 79, p. 474, 2019. doi:10.1140/epjc/s10052-019-6904-3

[2] M. Benedikt *et al.*, "FCC-ee: The Lepton Collider," *Eur. Phys. J. ST*, vol. 228, pp. 261–623, 2019. doi:10.1140/epjst/e2019-900045-4

ISBN: 978-3-95450-213-4 ISSN: 2673-5490 doi:10.18429/JACoW-IPAC2020-MOVIR01

[3] M. Benedikt *et al.*, "FCC-hh: The Hadron Collider," *Eur. Phys. J. ST*, vol. 228, pp. 755–1107, 2019. doi:10.1140/epjst/e2019-900087-0

[4] F. Zimmermann *et al.*, "HE-LHC: The High-Energy Large Hadron Collider," *Eur. Phys. J. ST*, vol. 228, pp. 1109–1382, 2019. doi:10.1140/epjst/e2019-900088-6

[5] M. Benedikt *et al.*, "Future Circular Collider – The Integrated Programme (FCC-int)," input document to the 2019/20 European Strategy Update no. 135, CERN-ACC-2019-0007 (2019). https://cds.cern.ch/record/2653673

[6] M. Benedikt *et al.*, "Future Circular Colliders," *Ann. Rev. Nucl. Part. Science*, vol. 69, pp. pp 389-415, 2019. doi:10.1146/annurev-nucl-101918-023748

[7] M. Benedikt, A. Blondel, P. Janot, *et al.*, "Future Circular Colliders succeeding the LHC, " *Nat. Phys.*, vol. 16, pp. 402–407, 2020. doi:10.1038/s41567-020-0856-2

[8] K. Oide *et al.*, "Design of beam optics for the future circular collider e^+e^- collider rings, " *Phys. Rev. Accel. Beams*, vol. 19, p. 111005, 2016. doi:10.1103/PhysRevAccelBeams.19.111005

[9] M. Boscolo, H. Burkhardt, and M. Sullivan, "Machine detector interface studies: Layout and synchrotron radiation estimate in the future circular collider interaction region," *Phys. Rev. Accel. Beams*, vol. 20, pp. 011008, 2017. doi:10.1103/PhysRevAccelBeams.20.011008

[10] M. Zobov *et al.*, "Test of 'Crab-Waist' Collisions at the DAΦNE Φ Factory, " *Phys. Rev. Lett.*, vol. 104, p. 174801, 2010. doi:10.1103/PhysRevLett.104.174801

[11] A. Bogomyagkov, E. Levichev, and D. Shatilov, "Beam-beam effects investigation and parameters optimization for a circular e^+e^- collider at very high energies," *Phys. Rev. ST Accel. Beams*, vol. 17, p. 041004, 2014. doi:10.1103/PhysRevSTAB.17.041004

[12] R.K. Ellis *et al.*, "Physics Briefing Book: Input for the European Strategy for Particle Physics Update 2020," CERN-ESU-004, arXiv:1910.11775, 2019.

[13] K. Shibata, "Highlights from SuperKEKB Beam Commissioning, " virt. presented at IPAC'20, Caen, France, Jun. 2020, paper MOVIR03, this conference.

[14] L. Arnaudon *et al.*, "Energy calibration with a polarized beam at LEP," *Int. J. Mod. Phys. A, Proc. Suppl.*, vol. 2B, pp. 994–996, 1993. https://cds.cern.ch/record/239599

[15] A.S. Müller, "Precision measurements of the LEP beam energy for the determination of the W boson mass, " PhD Thesis U. Mainz, Shaker Verlag, Aachen, 2000. https://cds.cern.ch/record/492582

[16] A. Novokhatski *et al.*, "Unavoidable trapped mode in the interaction region of colliding beams," *Phys. Rev. Accel. Beams*, vol. 20, p. 111005, 2017. doi:10.1103/PhysRevAccelBeams.20.111005

[17] M. Koratzinos, "The FCC-ee Interaction Region Magnet Design, " in *Proc. eeFACT2016*, Daresbury, UK, Oct. 2016, pp. 57–60. doi:10.18429/JACoW-eeFACT2016-TUT1AH3

[18] M. Koratzinos, private communication, 2019.

[19] M. Migliorati *et al.*, "Impact of the resistive wall impedance on beam dynamics in the Future Circular e^+e^- Collider," *Phys. Rev. Accel. Beams*, vol. 21, p. 041001, 2018. doi:10.1103/PhysRevAccelBeams.21.041001

[20] E. Belli *et al.*, "Electron cloud buildup and impedance effects on beam dynamics in the Future Circular e^+e^- Collider and experimental characterization of thin TiZrV vacuum chamber coatings," *Phys. Rev. Accel. Beams*, vol. 21, p. 111002, 2018. doi:10.1103/PhysRevAccelBeams.21.111002

[21] S. Funkner *et al.*, "High throughput data streaming of individual longitudinal electron bunch profiles," *Phys. Rev. Accel. Beams*, vol. 22, p. 022801, 2019. doi:10.1103/PhysRevAccelBeams.22.022801

[22] B. Kehrer *et al.*, "Synchronous detection of longitudinal and transverse bunch signals at a storage ring," *Phys. Rev. Accel. Beams*, vol. 21, p. 102803, 2018. doi:10.1103/PhysRevAccelBeams.21.102803

[23] S. Funkner *et al.*, "Revealing the dynamics of ultrarelativistic non-equilibrium many-electron systems with phase space tomography," arXiv:1912.01323, 2019.

[24] E. Gianfelice-Wendt, "Investigation of beam self-polarization in the future e^+e^- circular collider," *Phys. Rev. Accel. Beams*, vol. 19, p. 101005, 2016. doi:10.1103/PhysRevAccelBeams.19.101005

[25] A. Blondel *et al.*, "Polarization and Centre-of-mass Energy Calibration at FCC-ee," arXiv:1909.12245, 2019.

[26] A. Milanese, "Efficient twin aperture magnets for the future circular e^+e^- collider," Phys. Rev. Accel. Beams 19, 112401 (2016). doi:10.1103/PhysRevAccelBeams.19.112401

[27] E. Cantergiani *et al.*, "Niobium superconducting rf cavity fabrication by electrohydraulic forming," *Phys. Rev. Accel. Beams*, vol. 19, p. 114703, 2016. doi:10.1103/PhysRevAccelBeams.19.114703

[28] A. V. Zlobin *et al.*, "Development and First Test of the 15 T Nb_3Sn Dipole Demonstrator MDPCT1," *IEEE Trans. Appl. Supercond.*, vol. 30, no. 4, pp. 1–5, no. 4000805, 2020. doi:10.1109/TASC.2020.2967686

[29] C. Pralavorio, "A demonstrator magnet produces a record magnet field," CERN News, 25 March 2020. https://home.cern/news/news/accelerators/demonstrator-magnet-produces-record-magnet-field

[30] I. Bellafont *et al.*, "Design of the future circular hadron collider beam vacuum chamber," *Phys. Rev. Accel. Beams*, vol. 23, p. 033201, 2020. doi:10.1103/PhysRevAccelBeams.23.033201

[31] L.A. Gonzalez *et al.*, "Commissioning of a beam screen test bench experiment with a future circular hadron collider type synchrotron radiation beam," *Phys. Rev. Accel. Beams*, vol. 22, p. 083201, 2019. doi:10.1103/PhysRevAccelBeams.22.083201

[32] I. Bellafont *et al.*, "Beam induced vacuum effects in the future circular hadron collider beam vacuum chamber," *Phys. Rev. Accel. Beams*, vol. 23, p. 043201, 2020. doi:10.1103/PhysRevAccelBeams.23.043201

[33] L.A. Gonzalez, private communication, 2020.

ISBN: 978-3-95450-213-4 ISSN: 2673-5490 doi:10.18429/JACoW-IPAC2020-MOVIR06

PRELIMINARY SIRIUS COMMISSIONING RESULTS

L. Liu†, M. B. Alves, F. C. Arroyo, J. F. Citadini, F. H. de Sá, R. H. A. Farias, J. G. R. S. Franco, R. J. Leão, S. R. Marques, R. T. Neuenschwander, A. C. S. Oliveira, X. R. Resende, A. R. D. Rodrigues, C. Rodrigues, F. Rodrigues, R. M. Seraphim, Brazilian Centre for Research in Energy and Materials (CNPEM)/Brazilian Synchrotron Light Laboratory (LNLS), Campinas, Brazil

Abstract

Sirius is a 4th generation 3 GeV low emittance electron storage ring that is in final commissioning phase at the Brazilian Centre for Research in Energy and Materials (CNPEM) campus in Campinas, Brazil. Presently (April 2020) we have accumulated 15 mA of current, limited by vacuum, using a nonlinear kicker for injection. In this paper we report on the Sirius main commissioning results and main subsystems issues during installation and commissioning.

INTRODUCTION

Sirius is a new light source in Brazil based on a low emittance 3 GeV electron storage ring with 518 m circumference. The storage ring natural emittance of 0.25 nm.rad is reached with twenty 5BA lattice cells and it can be further reduced to 0.15 nm.rad as insertion devices are added. Sirius will be an international multiuser research facility with up to 37 beamlines: 20 from permanent magnet superbends reaching peak magnetic field of 3.2 T (and therefore 19 keV critical photon energy); 4 from insertion devices at high beta sections and 13 at low beta sections. The low beta sections are optimized to maximize brightness from insertion devices by matching the electron beam and undulator radiation phase spaces. In these low beta sections, where the horizontal and vertical beta functions are simultaneously reduced to 1.5 m in the centre, small horizontal gap devices such as Delta undulators can be installed. Sirius main parameters are shown in Table 1 and the optical functions in Figure 1.

Table 1: Main Sirius Storage Ring Parameters

Parameter	Value	Unit
e-beam energy	3.0	GeV
Circumference	518.4	m
Lattice	20 x 5BA	
Hor. emittance (bare lattice)	0.25	nm.rad
Betatron tunes (H/V)	49.11 / 14.17	
Natural chrom. (H/V)	-119.0 / -81.2	
Energy spread	0.85e-3	
Energy loss/turn (dipoles)	473	keV
Damping times (H/V/L)	16.9/22.0/12.9	ms
Nominal current	350	mA

The injection into the storage ring will be based on conventional off-axis accumulation in the horizontal plane using a non-linear kicker (NLK). The injection system is composed of a 150 MeV Linac and a full-energy synchrotron booster with 497m circumference, built in the same tunnel and concentric with the storage ring. The booster has a very small emittance of 3.5 nm.rad at 3 GeV that is essential for a high injection efficiency using the NLK.

Commissioning activities were interrupted on last March 23rd due to the Covid-19 pandemic, when most of the staff switched to teleworking. We have reached 15 mA of accumulated current with off-axis injection in the horizontal plane using the NLK. This current is presently limited by vacuum. We are now slowly returning to work to continue with beam commissioning and proceed with installation of the first undulator for the protein crystallography beamline MANACÁ.

The Sirius project has effectively started in July 2012 when the decision to change to a low emittance 5BA lattice was taken, implying completely new components design. Installation of the accelerator subsystems in the machine tunnel started on May 2018 and the first turn in the storage ring with on-axis injection was achieved on Nov. 22nd, 2019. The first stored beam was obtained 3 weeks later, on Dec. 14th. Two days later, first light from a superbend was observed at the MOGNO beamline and first X-ray microtomography results were taken (see Figure 2). First beam accumulation with the NLK was obtained on Feb. 20th, 2020. Figure 3 shows a picture of the main accelerator tunnel.

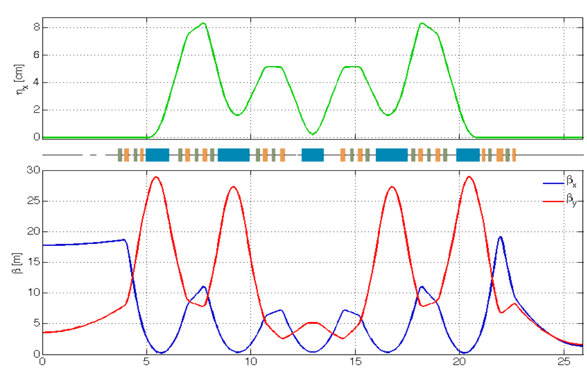

Figure 1: Sirius optical functions with a high-beta section on the left and a low-beta section on the right. The optics is 5-fold symmetric with 5 high-beta and 15 low-beta sectors. The centre dipole is a permanent magnet superbend.

† liu@lnls.br

ISBN: 978-3-95450-213-4 ISSN: 2673-5490 doi:10.18429/JACoW-IPAC2020-MOVIR06

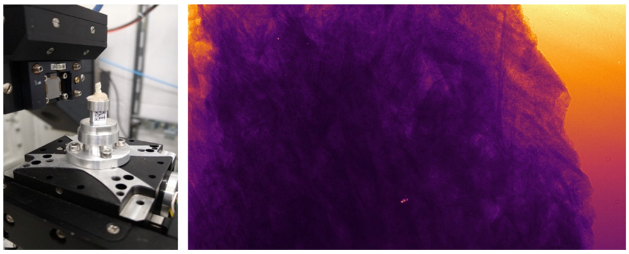

Figure 2: First X-ray microtomography of a carbonate rock sample obtained on Dec.16th 2019 at beamline MOGNO, using white X-ray beam from 8 keV to 200 keV from the 3.2 T superbend permanent magnet dipole source. The image was obtained two days after storing the first beam with on-axis injection.

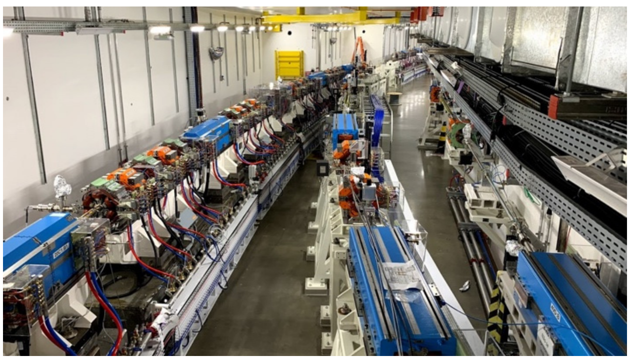

Figure 3: View of Sirius accelerators tunnel with storage ring on the left, booster on the right and BTS transfer line.

ACCELERATOR PHYSICS ISSUES

The main issues related to accelerator physics during booster commissioning were: (i) an unexpected gradient field in the booster pulsed injection septum had to be introduced in the LTB model to improve optics matching and thus injection efficiency at 150 MeV. This is a very strong septum, with a deflection of ~22 deg. (ii) the very small booster momentum compaction factor α_c causes a non-negligible effect of beam velocity variation on orbit period during the ramp (as compared to the energy contribution) that was not anticipated. As the revolution time is fixed by the RF frequency, this causes a variation of beam energy deviation δ during the ramp, requiring extra horizontal aperture (~2 mm in our case). The main accelerator physics issues related to the storage ring commissioning were: (i) a systematic error from building shrinking resulted in different RF frequencies for the booster and SR. The measured difference between the rings (~800 Hz) is larger than expected. This caused some difficulty in searching for the correct SR frequency in the beginning because a change in RF frequency requires a re-optimization of the injector. (ii) a large calibration error of electromagnet dipoles B1 and B2 with respect to permanent magnet dipole BC (2.5%) was noticed during initial optics measurements with the on-axis injected beam. After correction, measured optics functions are closer to the model and accumulation with the NLK was successful. Figure 4 shows the measured dispersion function as compared to the nominal. Further optimization work is on-going to improve the optics and injection efficiency, presently at about 60%.

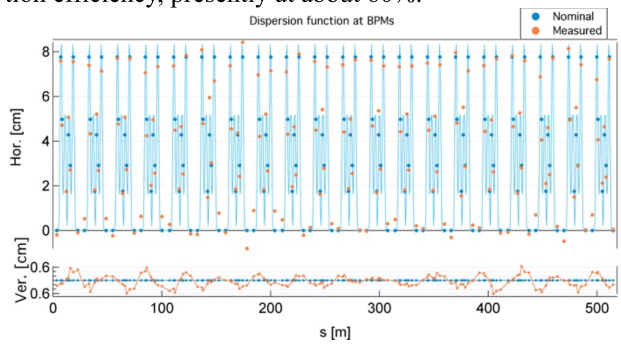

Figure 4: Measured dispersion function along the storage ring as compared to the nominal after correction of dipole calibration error.

DC AND PULSED MAGNETS

All Sirius DC electromagnets were fabricated using stacked laminations by a Brazilian company, and are aligned by mechanical design on the girders, using reference surfaces, with no adjustment flexibility, to improved stiffness and stability. The 20 permanent magnet superbends BC (reaching 3.2 T peak field) in the centre of the achromatic arc have been produced in-house. Figure 5 shows a picture of storage ring magnets in one 5BA arc.

The main issue related to DC magnets was the magnetic field calibration of electromagnet dipoles with respect to the permanent magnet dipole. The cause of the problem is being investigated but is probably related to the large range of measured field intensities. Another issue is the storage ring pulsed injection septa leakage field. Additional shielding is being planned to mitigate this effect.

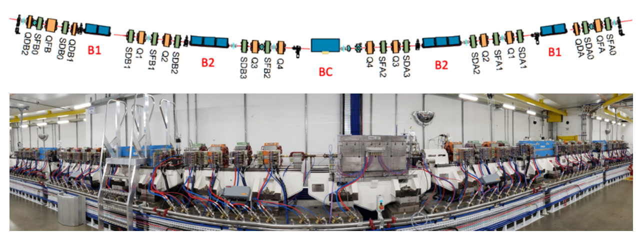

Figure 5: View of Sirius magnets in one 5BA arc.

VACUUM SYSTEM

The Sirius vacuum system for the storage ring is based on fully in-house NEG-coated copper chambers. The NEG activation process was carried out by in-situ bake-out with the magnets in place, and by using a custom developed heating system [1]. During installation, a few issues occurred and were all easily solved: one sector vented after NEG activation, few RF shielded bellows stuck during bake-out and a few components presented leak. During operation, the main issues were a leak in a septum chamber due to arcing that required substituting the chamber, two ion-pumps short-circuited, and a photon beam induced hot-spot that was mitigated by realignment of the chamber. Figure 6 shows some of the described problems.

ISBN: 978-3-95450-213-4 ISSN: 2673-5490 doi:10.18429/JACoW-IPAC2020-MOVIR06

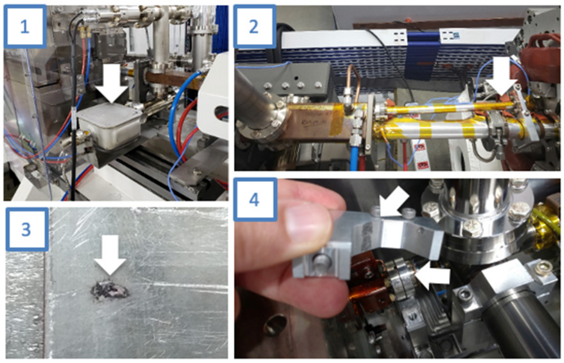

Figure 6: Some problems related to vacuum system during operation: (1) storage ring ion pump short-circuit; (2) photon beam induced hot-spot; (3) septum chamber leak; (4) booster extraction septum arc on the chamber.

The pressure in the storage ring is evolving smoothly, as can be seen in Figure 7.

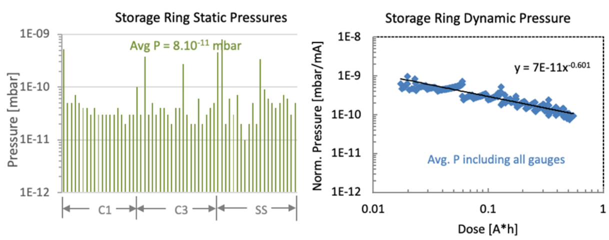

Figure 7: Storage ring static pressure and evolution of dynamic pressure as a function of accumulated dose.

BEAM DIAGNOSTICS

Here we present two beam diagnostic systems that have most interesting results up to now.

Beam Position Monitors

The storage ring 160 BPMs had all parts contracted to Brazilian industry. The buttons were assembled and brazed in-house and welded to the BPM body in-house as well. All BPMs have bellows on both sides and are referenced to the girders by design. BPM electronics were developed in-house and produced by a local Brazilian company.

Figure 8 shows the results of measured BPM electrical offset calibration and Beam Based Alignment (BBA) offset calibration using normal and skew quadrupole trim coils.

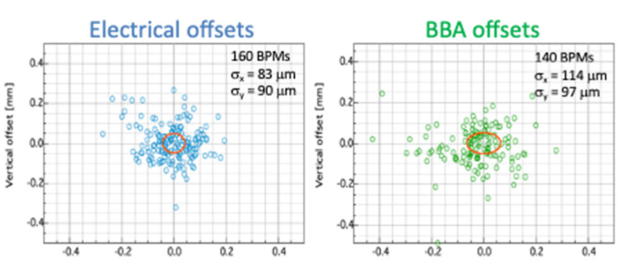

Figure 8: Measured BPM electrical and BBA offsets.

The main issue related to BPMs was a strong electromagnetic interference induced by the injection kicker on the BPM next to it. The problem has been mitigated by the implementation of a digital filter, as can be seen in Figure 9.

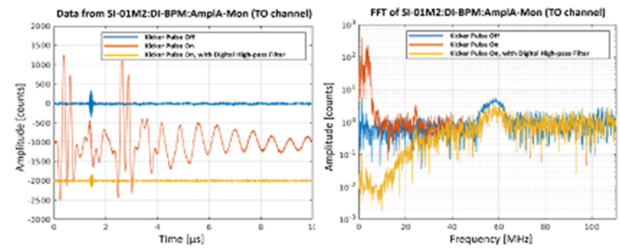

Figure 9: Effect of injection kicker electromagnetic interference on the closest BPM signal was mitigated by means of a digital filter.

Beam Scrapers

Special scrapers have been designed for Sirius to minimize beam coupling impedance effects. The design uses a special round blade geometry with angular motion, driven by a linear-to-angular motion transmission. See picture in Figure 10. The main difficulties in this design were the indirect blade position feedback, that required 3D measurements. After installation and baking, the linear stages of the horizontal scraper were found to be offset, not allowing one blade to fully open, and the opposite blade stuck after first 2 days of testing. The horizontal scraper has been removed for inspection and will be reinstalled in the next opportunity. The vertical scraper had no problems up to now.

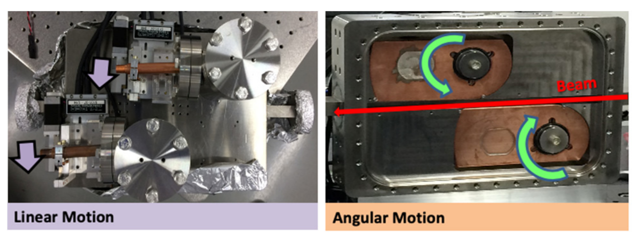

Figure 10: Sirius scraper design minimizes beam coupling impedance. It is based on a special round blade geometry with angular motion driven by a linear-to-angular transmission.

RF SYSTEM

Sirius is being commissioned with a reduced RF system. A single RF plant delivering up to 120 kW of power at 500 MHz drives one 7-cell Petra cavity. The final system consists of 2 superconducting cavities and is expected to be installed within 2 years. The 50 kW, one 5-cell cavity booster RF system is fully operational. The conditioning of the 7-cell cavity for high power is still under way, progressing at a much slower pace than expected. Planned operation voltage is 1.8 MV (70 kW in the cavity). A new version of ALBA LLRF was developed for Sirius and is fully operational for commissioning. The amplifiers have been tested during cavity conditioning up to 100 kW in pulsed mode, 80 kW in CW mode. The main storage ring RF parameters during commissioning and final design are shown in Table 2.

11th Int. Particle Acc. Conf. IPAC2020, Caen, France JACoW Publishing
ISBN: 978-3-95450-213-4 ISSN: 2673-5490 doi:10.18429/JACoW-IPAC2020-MOVIR06

Table 2: Main Storage Ring RF Parameters

	Commissioning	Design
RF Cavities	1 x 7-cell	2 x SC CESR
Power/cavity	120 kW	240 kW
Acc Voltage	1.6-1.8 MV	3 MV
Max beam current	50 mA	350 mA

NON-LINEAR KICKER

The Sirius NLK is based on the Bessy design [2] using 8 wires. Figure 11 shows the position of the wires and the NLK being assembled. The resulting magnetic field shape is close to zero at the center and has maximum intensity at -8 mm from the beam axis, were the injected beam from the booster is deflected into the storage ring acceptance. A vertical full gap of 9 mm at the ceramic chamber center is set to allow positioning of the wires. The single piece NLK ceramic chamber was produced by a Brazilian company and precise channels were machined to position the wires. The coating with titanium was performed in-house. The main challenges during chamber manufacturing were achieving the internal profile tolerances and producing a homogeneous Ti coating. A new split ceramic design is expected to reduce the profile tolerance from present 0.4 mm to 0.05 mm. The Ti coating was successful after replacing DC by RF magnetron sputtering as can be seen in Figure 12.

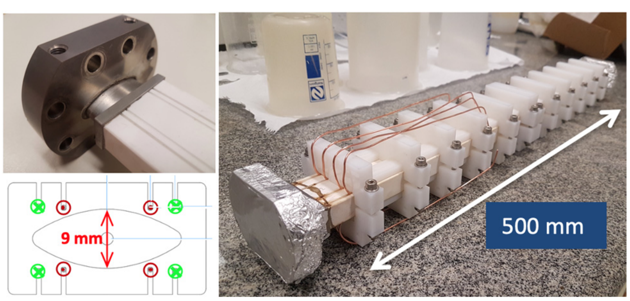

Figure 11: Sirius non-linear kicker being assembled.

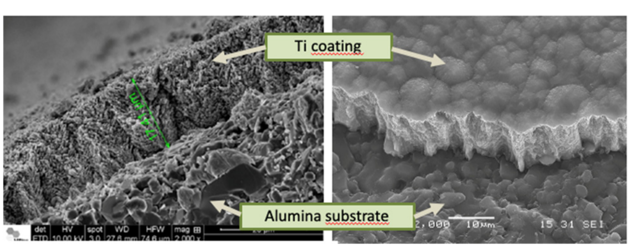

Figure 12: Ti coating on NLK ceramic chamber with DC (left) and RF (right) magnetron sputtering. The Ti layer thickness is 17.4 µm and 8 µm respectively.

CONTROL SYSTEM

The Sirius control system is based on EPICS framework and the main applications and IOCs are running on Control Servers. The nodes are based on open source and low-cost Single Board Computers (BeagleBone Black). Hardware and software are developed in-house. Presently there are approximately 110 k connected EPICS PVs, 60 GB of data per day with 2.5 Gbps of data traffic on core switch.

For the High-Level system, the main development language is Python and Soft IOC servers are based on PCASpy and PyEpics. Currently there are 222 Soft IOCs running with 2 to 10 Hz update rates. HLAs are mainly based on PyQt and PyDM.

POWER SUPPLIES

The Sirius power supplies (PS) were designed in-house and contracted to a Brazilian company for fabrication. Regarding the injection system PS, the measured tracking error for booster magnets were initially above specification when tested in the real machine and required more time than expected to be adjusted. The main issues related to the storage ring PS are: (i) overheating of dipole power supplies that caused capacitor explosion in 3 units, as can be seen in Figure 13. The manufacturer sent new capacitors and the problem did not happen again after all capacitors were substituted. This problem caused a big inconvenience in commissioning because it required turning the storage ring off for one hour after one-hour operation, until all capacitors were substituted. (ii) a cross-talk between quadrupole trim coils appeared in the final installation and took longer than expected to be solved.

Figure 13: Damaged capacitors of storage ring dipole power supply.

FINAL COMMENTS

Many problems only appear during real operating conditions. A well prepared team capable of investigating the problems is fundamental. Beam commissioning could have been briefer if the subsystems were thoroughly tested beforehand. Precise and accurate beam diagnostics tools (hardware and software) are fundamental for commissioning. In particular, precise BPM turn-by-turn capabilities and flexible analysis and simulation software tools are very helpful. The booster commissioning while the storage ring was being installed in the same tunnel led to an intermittent booster commissioning schedule that was not very effective. The booster might have been commissioned close to the end of storage ring installation. Provision for on-axis injection in the storage ring was essential for initial optics adjustments based on beam measurements. The control system with remote control capability proved to be very useful, especially in the present Covid-19 pandemic case.

ACKNOWLEDGEMENTS

The work presented here is the result of a collective effort from all Sirius team.

ISBN: 978-3-95450-213-4 ISSN: 2673-5490 doi:10.18429/JACoW-IPAC2020-MOVIR06

REFERENCES

[1] P. H. Nallin *et al.*, "The Sirius heating system for the in-situ NEG activation", in *Proc. 10th Int. Particle Accelerator Conf. (IPAC'19)*, Melbourne, Australia, May 2019, pp. 4109-4111. doi:10.18429/JACoW-IPAC2019-THPTS004

[2] T. Atkinson, M. Dirsat, O. Dressler, P. Kuske, and H. Rast, "Development of a non-linear kicker system to facilitate a new injection scheme for the Bessy II storage ring", in *Proc. 2nd Int. Particle Accelerator Conf. (IPAC'11),* San Sebastián, Spain, Jun. 2011, paper THPO024, pp. 3394-3396.

11th Int. Particle Acc. Conf. IPAC2020, Caen, France JACoW Publishing
ISBN: 978-3-95450-213-4 ISSN: 2673-5490 doi:10.18429/JACoW-IPAC2020-TUVIR06

REVIEW OF REQUIRED PROOF-OF-PRINCIPLE EXPERIMENTS TOWARDS A MUON COLLIDER

Alessandro Variola, INFN – Sezione di Roma, P.le Aldo Moro 2, I-00185 Rome, Italy

Abstract

The HEP scientific community is, at present, exploring different scenario concerning the post LHC era. In fact, after the Higgs boson discovery, the future facility will require not only to improve the LHC and HL-LHC physics programs but also to continue the search for phenomena beyond the Standard Model into an extended energy domain. In this framework ideas and proposals, together with the results obtained in accelerator research, introduce a scenario where the feasibility of a multi-TeV muon collider should be explored.

This article will describe the advantages provided by the muon collider scheme. The proposed schemes will be shortly illustrated. The very important recent results obtained in proof-of-principle experiments will be subsequently described. Finally, for each scheme, the future possible directions for proof-of-principle experiments to demonstrate the muon collider feasibility will be presented.

INTRODUCTION

The future challenges in the high energy colliders frontier, cannot be decoupled from the luminosity requirements keeping as fundamental constraint the necessity to build and operate the facility with a reasonable construction and operation budget. In this context a high energy muon collider should represent a true opportunity. In this framework a still-in-progress physics case has been elaborated [1] and this has been recently taken into account in the input for the European Strategy for Particle Physics Update 2020 in the Physics Briefing Book [2].

Different considerations make the muon collider option very attractive. First of all, the center of mass energy can be considerably reduced in respect to the p-p configuration where a significant fraction of the proton-beams energy in the interaction point is carried away by the partons contribution. Furthermore, the leptonic nature of the muons also assure a direct exploitation with a significant noise reduction, resulting in foster the muon potential not only as high energy but also as a precision collider. On the other side this solution presents definite advantages with respect to the e^+e^- configuration, mainly due to the about 200 mass scaling factor. This strongly relaxes the constraints in synchrotron radiation power emission and in the beamstrahlung effect that represent one of the main performance limitations respectively for the circular and linear lepton collider options. Finally, the luminosity parameter for the high energy configuration is linearly dependent from the energy at constant beam power, when compared to the constant behaviour of the linear collider option.

A final definitive assessment of the luminosity requirement should be delivered in a CDR phase where an extensive investigation of the physics channels should be carried out. Nevertheless, basic considerations allow to fix a luminosity target of 2 10^{34}cm^{-2}s^{-1} at 3 TeV [3].

The undeniable advantages represented by the muon collider option are nevertheless challenged by the main limitation given by the muon 2.2 μs at rest lifetime, rather short in a collider perspective. This is an important limiting factor namely at the muon production. In fact, muons bunches are produced with a very large 6D emittance and a limited number of particles per bunch limited by the primary beam power and the target technology. To provide a collider design matching the luminosity requirements, any applicable cooling technique needs, thereby, to show unprecedented efficiency to guarantee the emittance shrinking with a very fast process immediately after the production. This will permit the subsequent beam shaping, transport and post acceleration phases. Different techniques should also be envisaged to recombine muon bunches before a final cooling stage, to benefit of the luminosity quadratic dependence on the single bunch intensity. All these considerations underline the crucial aspect of the source design for the muon collider option. To provide a reliable design of a muon source integrating all the production, shaping, cooling and recombination phases represented for years the true challenge and it resulted in an important and long R&D effort sustained by the community. In this framework it is important to underline the muon collider R&D strong synergies with the neutrino physics programs.

MUON COLLIDER SCHEMES

At present there are two main proposed scenarios for a muon collider facility the difference being essentially in the muon source design. The first has been elaborated in the framework of the US Muon Accelerator program (MAP) and it consider the muons as tertiary particles in the decays of the pions created by an intense proton beam interacting a heavy material target. The second, the LEMMA scheme, takes into account the process $e^+e^-\rightarrow\mu^+\mu^-$ just above threshold for the muon generation considering a high energy positron beam impinging on a target. After the peculiar phases of bunch generation and emittance shaping associated to the specific production process, similar technical and design issues for the two schemes are found in the post acceleration stage. At the end, depending on the beam emittances, different collider ring design requirements are also considered.

MAP: THE PROTON DRIVEN SCHEME

The Muon Accelerator Program [4] started in 2011 to develop the conceptual designs and to face all the technological R&D challenges associated to the Muon Colliders and Neutrino Factories. To establish the program priorities a baseline scheme was proposed [5]. The collider layout takes into account five different stages. The first includes

ISBN: 978-3-95450-213-4 ISSN: 2673-5490 doi:10.18429/JACoW-IPAC2020-TUVIR06

the production and shaping of the high intensity primary proton beam. The second stage takes into account the generation of the muon bunches by means of the pion production in a MW class target and the front end section consiting in a decay channel for the muon production and a first longitudinal capture section. The third stage envisages the muon beam 6D emittance decrease by ionization cooling and the bunches recombination. A post cooling channel is foreseen after the recombination due to the subsequent Liouville emittance enhancement of this phase. The fourth and the fifth stages take into consideration, respectively, different design proposals for the post acceleration process and the injection and the beam storage in the collider ring. The MAP program has reached a high maturity level by systematically determining and carrying out different proof-of-principle experiments and techonological programs. Among them it is important to highlight the important progresses obtained thanks to the MICE, EMMA and CBETA facilities.

MICE: The Ionization Cooling Demonstrator

One of the most important part of the MAP proposed layout is given by the ionization cooling section, that has to assure the availability of high brightness muon bunches. This is a classical cooling mechanism where the particles lose energy in many degrees of freedom through ionization, in an appropriate material absorber, and restore it in one degree of freedom thanks to a RF post-acceleration. The final emittance budget is the result of the equilibrium between the ionization energy losses cooling mechanism and the heating process given by the multiple scattering in the absorber medium. To assure also the longitudinal muon beam cooling, different solutions are proposed to implement an emittance exchange mechanism by correlating the transverse to the longitudinal dimensions and inserting wedge shaped absorbers. In this framework it was essential, as first proof-of-principle experiment to validate the efficiency of the ionization cooling mechanism in a real 4D cooling channel with a muon beam. At this scope the MICE international collaboration [6] implemented a muon transverse cooling demonstrator at RAL. The apparatus consists in an absorber section inserted in a tight focusing twelve superconductive solenoids lattice, where the 4T spectrometer and the 3.5T on-axis field magnet allow for, respectively, the momentum measurements and the achievement of a small β function (430 mm) at the absorber location to increase the cooling efficiency. As far as the absorbers cooling performance is concerned, low atomic number materials with a large radiation length / rate of energy loss ratio, like liquid-hydrogen (LH) and lithium hydride (LiH), were chosen. The muons phase space was reconstructed before and after the cooling section by TOF and Cerenkov counters measuring the particles' velocities and by five planar scintillating-fibre stations trackers determining the muon positions and momentum. A 140 MeV/c muon beam with a normalised emittance varying from 4 to 10 mm was delivered extracting the ISIS synchrotron beam on a target.

To evaluate the effective cooling efficiency of the channel different analysis were performed comparing the upstream and downstream phase space in presence or absence of the absorbers effect. A recent outstanding publication [7] provided the first transverse ionization cooling demonstration observing the increasing of the downstream small amplitude particles and the beam phase density increase.

EMMA and CBETA: Post Acceleration Schemes.

The short muons lifetime demands another innovation effort in the muon collider post acceleration system design. Indeed, this phase duration has to be minimized to avoid relevant muon decay losses. Due to the difficulty to provide very fast high field ramping magnets one of the most promising solutions was to explore non-scaling FFGA systems whose characteristics allows fast acceleration.

A first proof-of principle experiment, the EMMA electron ring, was studied and built in Daresbury. It aimed to demonstrate, in the 10-20 MeV range, the possibility to obtain a reduced momentum compaction and hence a smaller orbit excursion, in respect to the scaling systems, with a non-scaling design and by operating fixed frequency accelerating cavities (asynchronous or serpentine acceleration), [8]. This allows reducing the elements complexity since linear magnetic fields can be associated to small orbit oscillations so increasing the dynamic aperture. Furthermore, it shows that CW operation is possible in the context of the future application to the muon acceleration. Forty-two identical cells containing offset quadrupole doublets provide the EMMA ring beam optics and the bending force [9]. To take into account the fast ramping needed for the muon bunches a RF system consisting of nineteen single-cell normal-conducting cavities, and resulting in an energy increase of more than 1 MeV per turn, was integrated [10].

Finally, it was demonstrated a stable acceleration in a serpentine channel from 12 to 18 MeV in six turns with a reduced orbit shift and where different integer H&V tunes were crossed throughout the acceleration without increasing the beam oscillations amplitude [11].

Another important proof-of-principle concept was recently demonstrated with the results obtained in the CBETA facility in Cornell, a SC Linac ERL with four accelerating passes at 42, 78, 114 and 150 MeV but integrated in a single Fixed Field Alternating Linear Gradient (FFA-LG) return beam line [12]. The different energy beams are merged by a 4 arms beam spreader. The single pass acceleration is assured by six SRF1.3 GHz 7-cell cavities cryomodules, with a 12,5 MeV/cryomodule energy gain, around the double of what is necessary for the 42 MeV pass. The ERL efficiency is estimated at 99.9%. The return loop is based on 214 permanent magnets divided in quadrupoles and combined-function gradient magnets using a variant of the circular Halbach design. The line is based on doublet cells with a focusing quadrupole and one defocusing-bending quadrupole allowing for a maximum transverse displacement of less than 46.6 mm. Recently CBETA announced the first successful eight pass (4 accelerating

ISBN: 978-3-95450-213-4 ISSN: 2673-5490 doi:10.18429/JACoW-IPAC2020-TUVIR06

and 4 decelerating to demonstrate energy recovery) operation becoming, therefore, the first 4 pass ERL based on the innovative single permanent magnet return line [13].

Outstanding R&D Programs

The MAP's technological challenges related to the muon collider project require different R&D programs that, for their innovation content, can be considered as veritable proof-of principle experiments. Among others it is important to stress the test of high gradient cavities under strong magnetic fields, representing the technology core of the ionization cooling cells. Different 800 MHz class cavities (Q_0 value ranging from 1.5 ÷ 3 10^4) were tested in 5T solenoidal field [14], achieving peak surface fields of the order of 20MV/m corresponding to accelerating gradients of more than 50 MV/m. In parallel the realization and commissioning of the MICE 201 MHz cavity was carried out. For the so-call Helical Cooling Channel, it was also important to demonstrate the feasibility of pressurized high gradient cavities. Measurements were performed under 30-100 Atm pressure of pure hydrogen, nitrogen and helium, or with a SF6 doping, demonstrating gradient up to 60 MV/m in the hydrogen case. In the same pressure range a proton beam test was also successful achieving 50MV/m in a 3T field for a RF pulse length of 40μs [15]. The reach of very high magnetic fields, providing a small beta function in the cooling channel, was explored by the NHMFL R&D program on high field HTS magnets with YBCO-coated tape conductors and Bi-2212 round wires that succeeded in demonstrating a field on-axis higher than 30T [16]. As far as the Bi 2212 cables are concerned it must be highlighted that, a recent publication, illustrates the stable operation at wire current density of 1000 A/mm^2 [17]. The requirements for very high power targets, namely in the framework of the neutrino program, were addressed in the CERN MERIT proof-of-principle experiments where an 8 MW at 70Hz Hg jet target was successfully tested [18].

Future Perspectives

The undeniable success of the different over mentioned experimental programs results in a strong maturity of the MAP proposed scheme that could move into a CDR phase. Therefore, following the 4D cooling demonstration accomplishment, the future step forward should be represented by the full test of a 6D cooling cell. The cell will have to be redesign taking into account the achieved results on the different components technology, starting from the high magnet field to the cavities accelerating gradients. An emittance exchange configuration should be integrated to assure the test of the longitudinal cooling. A subsequent engineering phase should allow the realization of a cell prototype to be commissioned and finally tested on a muon (or proton) beam line as a true proof-of-principle experiment. The extension of the results of this experiment to a full 6D cooling line should confirm the theoretical possibility to attain the final required emittance before the post acceleration phase in a linear cooling channel, as a first fundamental step. The subsequent step should be represented by the measurement of the cooling efficiency of the full 6D cooling line. Even if the final baseline design takes into account a linear channel, it would be extremely interesting to set up a test facility based on one of the proposed circular systems, like the RFOFO [19] or the Dipole-Solenoid rings [20] that can represent a true validation at a reasonable cost and effort. The first system is based on a focusing-drift-focusing lattice with axial field polarity inversion in the middle of the cell. In this configuration the dispersion, the acceleration and the energy loss in a single hydrogen wedge are taken into account in each cell. The second one is composed of modules consisting of a straight section and an arc. The former is dispersion-free and takes into account the injection, the extraction and RF cavities drifts. The latter introduce the 6D cooling necessary dispersion for the energy-loss wedge absorbers.

A proof of principle experiment, in this context, should ambitiously consider the realization of a full facility based on these designs where, also in this case, all the recent technology results should be integrated in the rings lattice.

A separate context is represented by the possibility to have a proof-of-principle facility to demonstrate the Parametric-resonance Ionization Cooling concept [21]. This is supposed to be effective for the final 6D cooling stage of a high-luminosity muon collider allowing a cooling efficiency increase of one order of magnitude in respect to the conventional ionization cooling alone. The PIC technique scheme takes into account a ring with a cooling channel where a half-integer parametric resonance is induced. This converts the usual periodical elliptical phase-space trajectories into a hyperbolic shape, therefore, reducing the geometrical oscillations amplitudes and increasing the angular ones. The damping mechanism, introduced by the absorbers at the focal points, avoid the resonant instability growth reaching an equilibrium. The consequent beam size reduction in the absorbers location results in an effective cooling efficiency gain. Due to this very particular beam dynamics the PIC scheme proof-of-principle validation should be carried out in a dedicated facility.

Finally, it is important to point out that there are still some fundamental R&D programs, working on the performance of a component, to be carried out in the MAP framework. Among others a very important role is played by the development of the 400Hz - 2T fast ramping cycling magnets for the post acceleration phase [22]

LEMMA: THE POSITRON DRIVEN SCHEME

In the past years another muon collider basic scheme, LEMMA, has been proposed [23]. In this context the primary beam is made of 45 GeV positrons impinging on a target, interacting with the material electrons and consequently creating a secondary beam of muons pairs at threshold. The attractive characteristics of the γ-boosted muon bunches are a reduced emittance and a longer lifetime at creation. The drawback of this design is the very low production cross section in a collider framework. To profit of the luminosity quadratic dependence on the bunch

ISBN: 978-3-95450-213-4 ISSN: 2673-5490 doi:10.18429/JACoW-IPAC2020-TUVIR06

population it is therefore necessary to introduce a bunch recombination scheme not increasing the bunch emittance. This is taken into account by recirculating in two separate rings the μ^+–μ^- beams. After one turn they are focalized with a new positron bunch on the production target so overlapping the generated pairs with the recirculated particles. This allows to bypass the Liouville theorem constraint by stacking the new generated muons in the existing bunches phase space, but taking into account the heating given by the multiple scattering in the target. After N cycles the bunches are extracted for the post acceleration process. The reduced emittance of the LEMMA design allows to integrate very small β^* IP regions in the collider, so drastically reducing the bunch intensity at constant luminosity and consequently the radiation and the background problems associated with the muons decay.

To face all the technological and design challenges of the LEMMA proposal a global design process has started recently [24] where different schemes have been proposed. The more robust considers a complex cycles succession involving a Positron Source (PS) with a Damping Ring (DR), a Positron Accumulator ring (PR), two Muons Accumulator rings (MA) and different linear accelerating systems. After a first injection of 1000 positrons bunches in the PR and their subsequent cooling the positron bunches are extracted for the first muon recirculated production cycle. All the production phase has to last less than 300μs to take into account the muon population exponential decay and, at the end, the muon bunches are extracted and send to the post acceleration complex. Following the muon production, the spent positron bunches are re-injected, with a certain efficiency, in the PR to cool down the large energy spread acquired in the target by Bremsstrahlung emission. In 10 ms the positrons are subsequently spilled out and sent, depending on the final design, either into the DR where the lost positrons population is recovered by stacking from the PS or towards an embedded positron source to generate positrons bunches with an efficiency greater than unity. This slow spill process allows also to envisage reasonable average and peak positron currents in the accelerating or decelerating linear systems. After that the positron bunch intensity and emittances have been recovered it is possible to start a new muon generation phase.

Future Perspectives

Being relatively recent the LEMMA scheme has not reached the same design maturity of MAP. A first proof-of-principle experiment has been realised in a CERN test beam, to assess the produced emittance by positrons annihilations [25]. The results showed a 20% dissymmetry in the μ^+– μ^- phase space distributions but a good agreement with the simulated values. Another proposal, in the framework of the CERN UA9 program, aims at exploring the recombination of bunches in a curved crystal and measuring its efficiency. Other experimental tests or R&D are not precisely identified by the determination of their final outcomes, but on the other side, the possibility to work with an established feasibility scheme allows to individuate the different programs topics. A first proposal should concern the possibility to measure the beam dynamics, and so the beam lifetime, in a lepton storage ring under an energy spread dominated regime given by the insertion of a target. Also if performed at a lower energy this test should confirm the reliability of the simulations results.

As far as the R&D programs are concerned one of the most important field to explore is the availability of high power targets capable to minimize the thermo-mechanical stress effects. Both the muon and the positron sources should benefit from extensive R&D programs exploring also innovative ideas as the utilization of liquid Hydrogen pellet targets, the evaluation of rotating or pendulum targets, both in amorphous or in granular configuration, and the design of shockwave impedance matching systems. On the other side the requirements of manipulating in the linear systems very intense positron beams in short periods would require a dedicated project on high gradient - hundreds mA class SC cavities. Finally, a more ambitious program should be imagined with the realization and the test of the muon recombination ring, one of the most critical systems of the whole scheme.

GAMMA FACTORY: AN ALTERNATIVE PROPOSAL

In the framework of the gamma factory activity at CERN [26] the proposal to utilize the high energy photons to produce muons pairs in a target was made. In this proposal the high energy gammas are created by Compton backscattering when very high energy ions beams collide with a laser pulse. This muon source should provide also relatively low emittances beams but requiring a very high gamma flux. At present the gamma based muon collider has not been integrated in a scheme, so it is in a very preliminary conceptual phase. Nevertheless, an important proof-of-principle experiment will be represented by the measurements planned at CERN [27] that will characterize the flux and the spectrum of the backscattered photons.

CONCLUSION

For many years the muon collider community has demonstrated creativity in proposing innovative solutions and in defining advanced R&D programs to explore its feasibility. These programs successes, in some case, represented a true breakthrough in the accelerator physics fields. The MAP program achieved a strong maturity to move to the CDR phase and its possible proof-of-principle experiments should be dedicated to the 6D cooling cell and its efficiency definition. Further ambitious program can be envisaged to test a cooling line by realising a dedicated facility that should consider also innovative proposal like the PIC resonance cooling. The LEMMA scheme has to go through a phase of definition of possible proof-of-principle experiments, especially in the domain of the targets for the high intensity positrons sources and of the energy spread dominated beam dynamics. The gamma factory proposal has already an established program to demonstrate the source performance.

ISBN: 978-3-95450-213-4 ISSN: 2673-5490 doi:10.18429/JACoW-IPAC2020-TUVIR06

ACKNOWLEDGEMENTS

The author wants to acknowledge all the different colleagues that provide useful information. A special thanks to Mark Palmer for his priceless help on all the MAP related topics.

REFERENCES

[1] E. Eichten, "The Basics of Muon Collider Physics", Fermilab, Batavia, IL, USA, Rep. FERMILAB-PUB-09-225-T, 2009.

[2] European Strategy for Particle Physics Preparatory Group, "Physics Briefing Book", arXiv:1910.11775v2 [hep-ex], 2020.

[3] The Muon Collider Working Group, Input to the European Particle Physics Strategy Update, "Muon Colliders", arXiv:1901.06150v1 [physics.acc-ph], 2019.

[4] https://map.fnal.gov/

[5] J.-P. Delahaye *et al.*, "Enabling Intensity and Energy Frontier Science.: A White Paper Submitted to the 2013 U.S. Community Summer Study of the Division of Particles and Fields of the American Physical Society", Fermilab, Batavia, IL, USA, Rep. FERMILAB-CONF-13-307-APC, Aug. 2013.

[6] http://mice.iit.edu

[7] M. Bogomilov, R. Tsenov, G. Vankova-Kirilova, *et al.*, "Demonstration of cooling by the Muon Ionization Cooling Experiment", *Nature* vol. 578, pp. 53–59, 2020. doi:10.1038/s41586-020-1958-9

[8] R. Edgecock *et al.*, "EMMA: The World's First Non-scaling FFAG", *in Proc. 11th European Particle Accelerator Conf. (EPAC'08)*, Genova, Italy, Jun. 2008, paper THPP004, pp. 3380-3382.

[9] J. S. Berg, "The EMMA main ring lattice", *Nucl. Instrum. Methods A,* vol. 596, pp.276-284, 2008. doi:10.1016/j.nima.2008.08.068.

[10] A. Wheelhouse *et al.*, "Progress of the RF System for EMMA at Daresbury Laboratory", *in Proc. 1st Int. Particle Accelerator Conf. (IPAC10)*, Tokyo, Japan, May 2010, paper THPEB05, pp. 3999-4001.

[11] S. Machida, R. Barlow, J. Berg, *et al.* "Acceleration in the linear non-scaling fixed-field alternating-gradient accelerator EMMA", *Nature Phys.*, vol. 8, pp. 243–247, 2012.

[12] R. J. Michnoff *et al.*, "Acceleration in the linear non-scaling fixed-field alternating-gradient accelerator EMMA." CBETA – novel superconducting ERL", *in Proc. 10th Int. Particle Accelerator Conf. (IPAC19)*, Melbourne, Australia, May 2019, paper TUPGW102, pp. 1651-1653. doi:10.18429/JACoW-IPAC2019-TUPGW102

[13] https://www.eurekalert.org/pub_releases/2020-01/dnl-ta012120.php

[14] D. Bowring *et al.*, "RF breakdown of 805 MHz cavities in strong magnetic fields", *in Proc. 6th Int. Particle Accelerator Conf. (IPAC'15)*, Richmond, VA, USA, May 2015, pp. 53-56. doi:10.18429/JACoW-IPAC2015-MOAD2

[15] B. Freemire *et al.*, "The experimental program for high pressure gas filled radio frequency cavities for muon cooling channels", *JINST* , vol. 13, p. 01029, 2018. doi:10.1088/1748-0221/13/01/P01029

[16] https://nationalmaglab.org/news-events/news/new-world-record-magnet-fulfills-superconducting-promise

[17] T. Shen, E. Bosque, D. Davis, *et al.*, "Stable, predictable and training-free operation of superconducting Bi-2212 Rutherford cable racetrack coils at the wire current density of 1000 A/mm2", *Sci. Rep.* vol. 9, p. 10170, 2019. https://doi.org/10.1038/s41598-019-46629-3

[18] K. T. McDonald *et al.*, "The MERIT high-power target experiment at the CERN PS", *in Proc.23rd Particle Accelerator Conf. (PAC'09)*, Vancouver, Canada, May 2009, paper TU4GRI03, pp. 1-5.

[19] R. B. Palmer *et al.*, "Ionization cooling ring for muons", *Phys. Rev. ST. Accel. Beams*, vol. 8, p. 061003, 2005. doi:10.1103/PhysRevSTAB.8.06100

[20] X. P .Ding *et al.,* "Racetrack Muon Ring Cooler Using Dipoles and Solenoids for a Muon Collider", *in Proc. 24th Particle Accelerator Conf. (PAC'11)*, New York, NY, USA, Mar.-Apr. 2015, paper MOP054, pp. 202-204.

[21] V. S. Morozov *et al.,* "Parametric-resonance Ionization Cooling of Muon Beams", *in AIP Conference Proceedings* vol. 1507, p. 843, 2012. doi:10.1063/1.4773808

[22] H. Witte, J. S. Berg and M. L. Lopes, "Progress on the Dipole Magnet for a Rapid Cycling Synchrotron", in *Proc. 5th Int. Particle Accelerator Conf. (IPAC'14)*, Dresden, Germany, Jun. 2014, pp. 1322-1324. doi:10.18429/JACoW-IPAC2014-TUPRO115

[23] M. Antonelli *et al.*, "Novel proposal for a low emittance muon beam using positron beam on target", *Nucl. Instrum. Meth. A,* vol. 807, pp.101-107, 2016. doi:10.1016/j.nima.2015.10.097

[24] D. Alesini *et al.*, "Positron driven muon source for a muon collider", 2019. arXiv:1905.05747 [physics.acc-ph]

[25] N. Amapane, "LEMMA approach for the production of low-emittance muon beams", *Il Nuovo Cimento C*, vol. 42, no. 6, article 259, 2019. doi:10.1393/ncc/i2019-19259-6

[26] M. W. Krasny, "The Gamma Factory proposal for CERN", 2015, arXiv:1511.07794 [hep-ex]

[27] M.W. Krasny, "Gamma Factory Proof-of-Principle Experiment", CERN, Geneva, Switzerland, Rep. CERN-SPSC-2019-031/SPSC-I-253, Mar. 2019.

ISBN: 978-3-95450-213-4 ISSN: 2673-5490 doi:10.18429/JACoW-IPAC2020-TUVIR11

IFMIF/EVEDA RFQ BEAM COMMISSIONING AT NOMINAL 125 mA DEUTERON BEAM IN PULSED MODE

F. Grespan, L. Bellan, M. Comunian, E. Fagotti, A. Palmieri, A. Pisent, F. Scantamburlo
INFN-LNL, Legnaro, Italy
T. Akagi, Y. Hirata, K. Kondo, Y. Shimosaki, T. Shinya, M. Sugimoto, QST, Aomori, Japan
P. Cara, IFMIF/EVEDA Project Team, Aomori, Japan
H. Dzitko, A. Jokinen, A. Marqueta, I Moya, F4E, Garching, Germany
B. Bolzon, N. Chauvin, J. Marroncle, CEA-IRFU, Gif-sur-Yvette, France
A. Rodriguez Paramo, ESS Bilbao, Zamudio, Spain
D. Jimenez-Rey, I. Podadera, CIEMAT, Madrid, Spain

Abstract

In summer 2019 the IFMIF/EVEDA Radio Frequency Quadrupole (RFQ) accelerated its nominal 125 mA deuteron (D+) beam current up to 5 MeV, with 90% transmission for pulses of 1 ms at 1Hz. The Linear IFMIF Prototype Accelerator (LIPAc) is a high intensity D+ linear accelerator; it is the demonstrator of the International Fusion Material Irradiation Facility (IFMIF). In particular the RFQ is the longest and most powerful ever operated. An intense campaign of measurements has been performed in Rokkasho to characterize several performances of this complex machine: transmission, emittances, energy spectrum and beam loading. The history and the results of the commissioning until this important project milestone are here described. An overview of the foreseen activities to be carried out to reach the CW operation is also presented.

INTRODUCTION

The LIPAc RFQ is a CW linac, capable of delivering 125 mA of D+ beam at 5 MeV. The 10-m long, 175 MHz cavity is designed to accelerate a DC 100 keV, 130 mA D+ beam from the injector with transmission > 90% [1].

RFQ is installed in Rokkasho (Fig. 1) since April 2016. The low power RF characterization was concluded in September 2016. We installed the 8 power couplers in December 2016, checking the field by pick-up reading. After baking and connection to cooling system and to the 8 RF systems, RF conditioning started in July 2017 (Fig. 2). After a first period where some hardware and integration problems have been faced, in Spring 2018 the RF operation concentrated to stabilize the conditions for the proton beam injection [2]. In June 2018 first proton (H+) beam was successfully accelerated through the RFQ [3]. After maintenance, conditioning restarted in February 2019 (Fig. 2) with the goal of reaching the conditions to accelerate D+ [4]. First D+ injection was possible in March 2019, then we reached in July 132 kV-2.5 ms-20 Hz and in July 24th we achieved a 125 mA D+ current at 1 ms/1 Hz out the RFQ, with transmission>90% (Fig. 3).

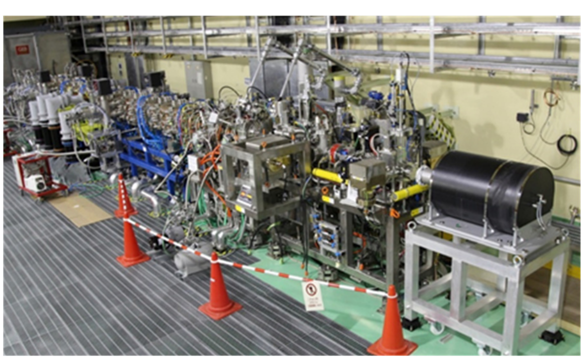

Figure 1: IFMIF/EVEDA LIPAc in Rokkasho.

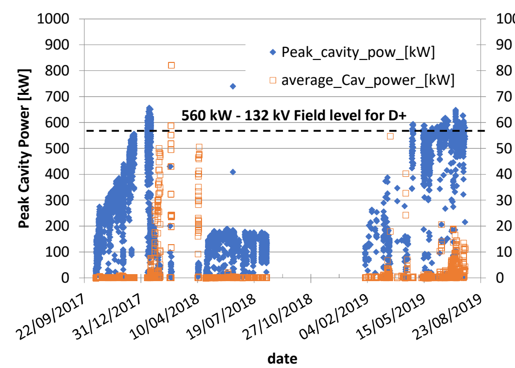

Figure 2: RF history of the RFQ (Sep. 2017 – Aug. 2019).

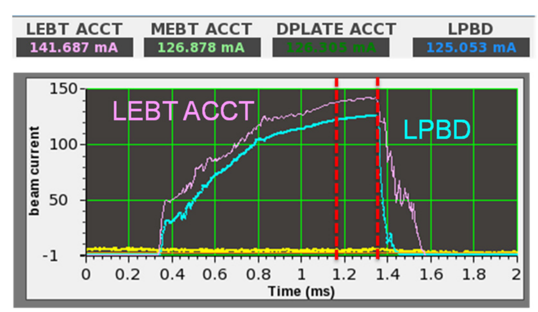

Figure 3: Image of the 125 mA D+ beam transmitted to the Low Power Beam Dump (LPBD).

LIPAC CONFIGURATION

The configuration for beam commissioning of LIPAc RFQ is shown in Fig. 4. LEBT optics includes two solenoids (Sol#) with integrated steering magnet pairs (ST#). Diagnostics include Doppler-Shift Spectroscopy, a 4-grid analyser, an Allison-Scanner, a beam stop, two CCD beam profile monitors. Three cm from RFQ matching point, there is LEBT-ACCT. RFQ input plate includes an electron repeller (-3 kV). Cavity is maintained at 10^{-8} mbar vacuum

ISBN: 978-3-95450-213-4 ISSN: 2673-5490 doi:10.18429/JACoW-IPAC2020-TUVIR11

level by 10 cryo-pumps. For RFQ beam characterization, MEBT is equipped with an ACCT just after the gate valve separating it from the RFQ, a Fast Current Transformer (FCT) and 4 BPMs. Diagnostic-Plate (D-Plate) next to MEBT includes 3 BPMs, 2 Slits combined with SEM-Grids for profile and emittance measurement, an ACCT-DCCT, a Residual Gas Bunch Length Monitor (RGBLM), a Fluorescence Profile Monitor (FPM) and an Ionization Profile Monitor (IPM). Low Power Beam Dump (LPBD) is used as Faraday Cup.

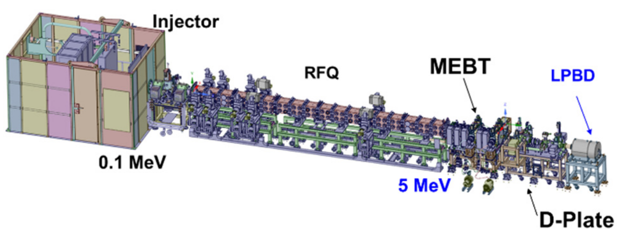

Figure 4: LIPAc configuration showing main systems.

CRITERIA AND PROCEDURE FOR RFQ INPUT BEAM

The beam injection into the RF has been prepared in the previous years by a detailed characterization of the Ion Source (IS) and LEBT beam [5]. The Twiss parameters were measured moving the Allison Scanner at the IS exit, between the 2 Sol# and after the RFQ injection cone. The large number of measurements have been used to benchmark a model of the line, based on WARP for space charge compensation patterns and LEBT transport, IBISIMU for the IS extraction, Tracewin for matching routines and outputs and Toutatis for the RFQ model "as built", i.e. containing mechanical and voltage errors measured on the real cavity.

Since during RFQ operation the Allison Scanner would be located in the box between the two LEBT Sol#, we wanted to determine a fast experimental criteria to define if a certain IS beam is acceptable for the RFQ injection, looking to the emittance just after Sol1.

The practical result is that, in order to limit the emittance growth in the second half of the LEBT for any couple of Sol#, the emittance after Sol1 must be $\varepsilon < 0.2\ \pi$ mm mrad normalized rms (Fig. 5). This should ensure a transmission of at least 90% accelerated particles through the RFQ at full current. It should be noticed here that in 2018 [6] we reported 0.15 π mm mrad as limit for RFQ input match; a successive analysis showed that this number was affected by an error on the Allison Scanner gap that caused underestimation of the emittance [5].

After the first H+ beam injection, the procedure applied to each RFQ injection point has been:

1. Study of the point at the injector level, in particular check if the emittance between the two Sol# is compliant with the criteria
2. Solenoid set to theoretical value.
3. Rough ST# optimization, to maximize LPBD current.
4. Sol# scan and ST# refinement with a dedicated routine.
5. Slight MEBT quadrupoles tuning.

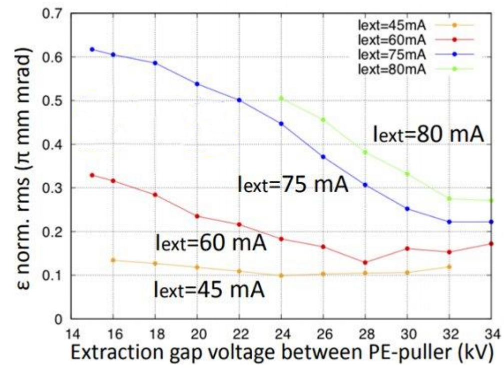

Figure 5: Limit for the emittance between two Sol#, here for H+ as function of the voltage between plasma electrode (PE) and puller electrode.

BEAM COMMISSIONING RESULTS

We report now some significant results of the H+ and D+ beam campaigns.

A technical problem limited the use of the chopper for the high current D+ experiments (Summer 2019). Therefore, we injected the full un-chopped IS pulse into the RFQ. Because of the LPBD power limit, the IS beam pulse was kept around 1.3 ms. Normally, high perveance operation from the IS requires pulse of at least 3 ms, in order to have a stable plasma at the end of the pulse. Two main effects follow such short, un-chopped pulse:

- The IS pulse was unstable. Therefore, the current was oscillating with a $\sigma = 2$ mA, increasing the error on the current measurements.
- The D+ fraction was around 80%, lower than the nominal IS tuning, where D+ ≈ 90 % for IS pulses > 3 ms. This caused an overestimation of the current at the RFQ input, given by the presence of other molecular species extracted from the IS.

These two experimental uncertainties are taken into account on the transmission calculation and they are as well applied to the assumptions withstanding the simulations.

Moreover, because of the chopper unavailability with high D+ currents in this campaign, the D-Plate emittance measurement unit was not usable with such a long pulse. For the RFQ emittance analysis we report the results for H+ at 1/3 perveance of the beam (23 mA, 2.5 MeV) [6].

Transmission vs. Voltage Curve

The Transmission-Voltage curve is a key characteristic to validate the RFQ design. The current transmission is given between RFQ Input (I_{LEBT}) and the LPBD (I_{LPBD}), in order to use the MEBT quadrupoles as filters for off-momentum particles. Such measurement scans the longitudinal and transverse dynamics of the RFQ, supplying a good insight of the machine performances.

Before scanning the RFQ voltage, input conditions are optimized looking for the values of LEBT Sol# and ST# that maximize I_{LPBD} (Fig. 6). Three points of the Sol# scan at I_{LPBD} = 125 mA have been simulated, showing a good agreement with measurement (Table 1). The higher error

11th Int. Particle Acc. Conf. IPAC2020, Caen, France JACoW Publishing
ISBN: 978-3-95450-213-4 ISSN: 2673-5490 doi:10.18429/JACoW-IPAC2020-TUVIR11

of point 1 of Table 1 (10%) is due to the larger approximation of the LEBT model, when describing beams with important losses on the metallic walls of the line.

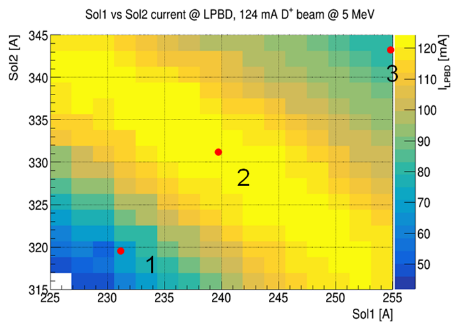

Figure 6: I_{LPBD} as function of Sol1/Sol2 currents, for I_{LEBT}=137 mA D+.

Table 1: Sim./Meas. Comparison of the Sol Scan in Fig. 6

Sol1-Sol2 point	ILPBD meas. ILEBT = 137±2 mA	ILPBD sim. ILEBT = 135 mA
1	82 mA	86±8 mA
2	124 mA	122.5±0.5 mA
3	64 mA	70.5±0.5 mA

Figure 7 shows the RFQ transmission-voltage scan for three different H+ currents compared with simulation of 24 mA H+ beam current, recorded in Summer 2018 and described in [7]. We only observe here that:

- small discrepancies at I_{LEBT}=21.7 mA and 27 mA are due to contaminant species at RFQ input;
- The larger discrepancy for I_{LEBT} = 29.3 mA is due to the non-compliancy of the input conditions with the criteria of 0.2 π mm mrad.

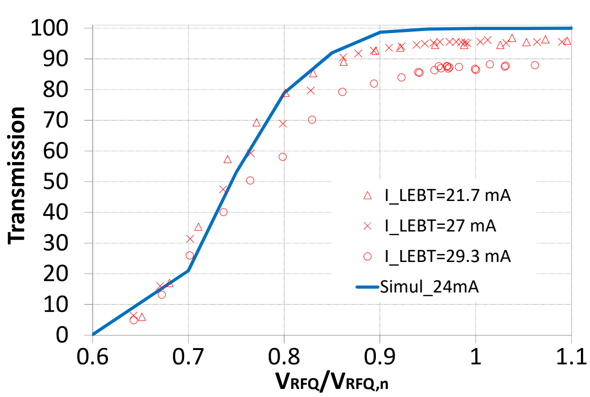

Figure 7: Transm.-Voltage curve for some H+ beams.

Figure 8 shows transmission-voltage scan for D+ beam at I_{LEBT} = 137 mA, performed with input conditions reported at point 2 of Table1. Simulation error are calculated by uncertainties of the input values used, for example slightly variations on the beam input current and Twiss parameters that can in any case fit the experimental data. The experimental results are compatible with the model.

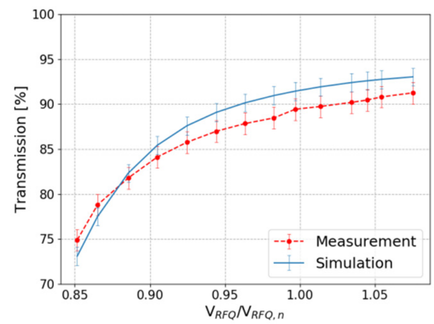

Figure 8: Transm.-Voltage curve for 125 mA D+ beam.

Beam Time of Flight (TOF)

Energy of first H+ beam campaign was measured with bunchers off and detuned. The TOF between the three D-Plate BPMs was performed with oscilloscope. In absence of re-bunching, the bunches spread in phase at D-Plate position, but a structure was still present and the BPM signals were three shifted sine-like waves at 175 MHz. From phase differences we obtained an energy of 2.5 MeV within 1% error [7]. For the D+ campaign we calibrated and processed the BPM's acquired data, and the measurements were done with bunchers operative [8]. The data in Fig. 9, plotted as function of the RFQ voltage, give an output energy of 5.0 MeV within 1% error.

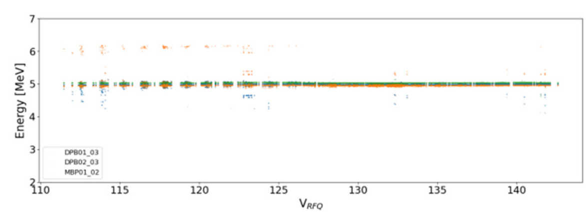

Figure 9: D+ TOF energy from different pairs of BPMs of the D-Plate and MEBT as function of the RFQ voltage.

The TOF measurements gave also an interesting result observed during the voltage scan of the RFQ (Fig. 10): the beam energy oscillates in a range of 20 keV as function of the cavity voltage. This effect can be linked to a slight RFQ input beam energy offset, that causes a synchrotron oscillation of the bunch inside the separatrix and around the nominal energy point. The amplitude of the oscillation is compatible with an injection energy 0.7 keV – 1 keV higher than nominal input energy. The effect shall be furtherly explored after the activity restarts.

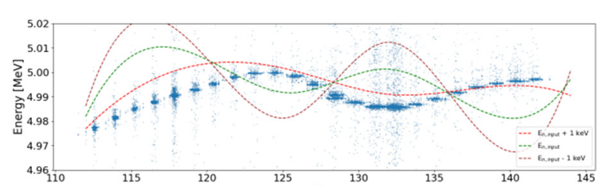

Figure 10: ToF for D+s as a function of RFQ voltage.

RFQ Beam Loading

The beam loading calculation, applied to the RFQ as a multicell cavity for 125 mA D+ (or 62.5 mA H+), gives

ISBN: 978-3-95450-213-4 ISSN: 2673-5490 doi:10.18429/JACoW-IPAC2020-TUVIR11

+8.1 kHz detuning to be at resonance with beam. The calculations are based on the following definitions (where i is the cell index):

- Effective synch. phase $\phi = atan\frac{\sum_i V_i T_i sin\phi_i}{\sum_i V_i T_i cos\phi_i}$
- Effective acc. voltage $\left|\widetilde{V_c}\right| = \frac{\sum_i V_i T_i cos\phi_i}{cos\phi}$
- Effective shunt impedance $r_s = \left|\widetilde{V_c}\right|^2 / P_{Cu}$

Beam operation is only possible at f_{RF} = 175 MHz, thus we measured the beam loading through two indirect effects on the forward (FWD) phase and cavity phase, compared with calculations. The experimental steps were (Fig. 11):

1. Tuning of the cavity ($f_{RF} = f_{CAV}$ = 175 MHz), adjusting the cooling water temperature to maximize the cavity voltage at 175 MHz;
2. In close loop ($f_{RF} = f_{CAV}$ = 175 MHz), measurement of FWD phase correction required at beam entrance, to be compared with $\Delta\varphi = atan\left(\frac{V_c \sin(\varphi)}{V_c \cos(\varphi) + V_b}\right) - \varphi$;
3. In amplitude and phase open loop ($f_{RF} = f_{CAV}$ = 175 MHz), measurement of the beam induced phase in cavity voltage, compared with $\Delta\psi = atan\left(-\frac{I_{beam} r_s \sin(\varphi)}{V_c(1+\beta)}\right)$.

These measurements of beam detuning include more sources of errors, with respect to the direct frequency measurement, for example a slight drop of the cavity voltage can occur in the open loop measurement. The results are satisfactory in a large range of currents (Fig. 11).

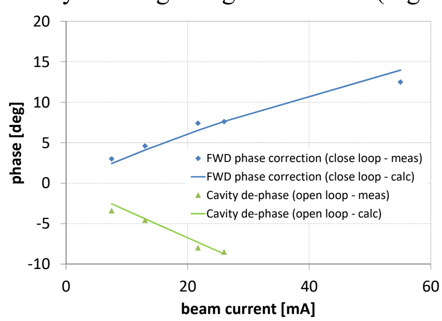

Figure 11: Beam loading induced de-phase for different H+ currents (Sim/Meas). In open loop it was impossible to measure the 55 mA H+ current because of the significant RFQ voltage drop induced by the beam.

Transverse Emittances Downstream of the RFQ

For the nominal D+ beam currents, the un-chopped IS pulse length (1.3 ms/1 Hz) overcomes the power limitation of the D-Plate slits, used for the transverse emittance measurements after the RFQ (limit = 100 µs/1 Hz at 125 mA). Then, it was impossible to measure the transverse emittance for such current. However, a benchmark measurement was performed for 22 mA of 2.5 MeV H+ beam (1/3 of the nominal perveance, equivalent to 41.6 mA of D+). Figure 12 shows an example of the reconstructed phase spaces after RFQ, simulated and measured. Table 2 shows some values of benchmarked emittances with respect to RFQ voltage and LEBT Sol#. An overall good agreement is achieved, showing that the emittance and the Twiss parameters are reproducible by the integrated simulation model (LEBT, RFQ, MEBT).

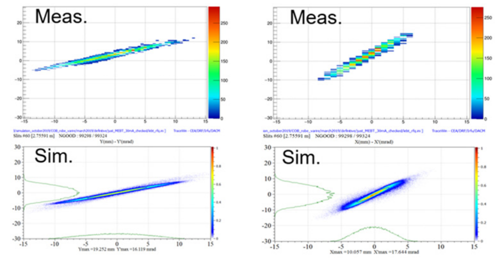

Figure 12: H+ simulated and measured emittance for xx' and yy' plane after RFQ (point 3 of Table 2).

Table 2: Sim./Meas. Comparison of RFQ H+ Emittances

Point	1	2	3	4	5	6
Sol1 [A]	131	135	135	135	135	135
Sol2 [A]	162	162	160	160	160	160
VRFQ [kV]	70	70	70	66	66	62
ILPBD [mA]	22.1	22.0	22.8	21.8	22.4	21.8
εexp/εsim [π mm mrad]	0.24 /0.28	0.22 /0.23	0.23 /0.23	0.24 /0.24	0.24 /0.24	0.24 /0.24
βexp/βsim [mm/π mrad]	6.5 /6.0	6.6 /6.3	6.9 /6.1	7.1 /7.5	7.0 /7.0	8.0 /8.1
αexp/αsim	-4.4 /-4.5	-4.3 /-4.3	-4.6 /-4.6	-4.8 /-5.5	-4.7 /-5.0	-5.4 /-6.0

CONCLUSIONS AND PERSPECTIVES

The results obtained up to now show that the RFQ works as designed, with good agreement between simulations and measurements: transmission-voltage curve, beam loading calculation, LEBT Sol# scan and RFQ transverse emittances are reproducible and benchmarked.

In future pulsed mode operations, we need to measure:

- the transverse emittance for the nominal beam intensity, with chopper now repaired;
- the longitudinal emittance;
- the x/y profiles at the nominal beam intensity.

After these last pulsed beam tests, it is essential to run the RFQ in CW mode in order to fully demonstrate its performances in terms of RF and thermal stability and verify the effects on the cavity when subjected to long run CW beam operation.

The maintenance from September 2019 to February 2020 has been dedicated to an important upgrade of the RF system in order to improve the conditioning of the cavity to CW RF operation. Moreover a dedicated beam transport extension has been installed after the MEBT (Fig. 13). The purpose of this line is to fully characterize the RFQ before installing the Superconducting Linac. The D-Plate has been shifted ahead, the HEBT is now installed and the LPBD is now replaced by the High-Power Beam Dump, able to receive up to 1.12 MW beam power.

ISBN: 978-3-95450-213-4 ISSN: 2673-5490 doi:10.18429/JACoW-IPAC2020-TUVIR11

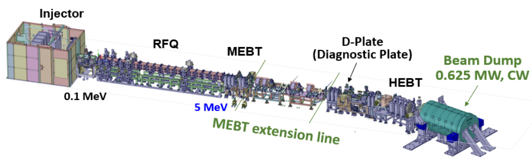

Figure 13: the present configuration (April 2020) of the IFMIF/EVEDA installation in Rokkasho.

REFERENCES

[1] M. Comunian and A. Pisent, "Beam dynamics redesign of IFMIF/EVEDA RFQ for larger input beam acceptance", in *Proc. IPAC'11*, San Sebastian, Spain, Sep. 2011, pp. 670-672.

[2] E. Fagotti *et al.*, "Beam commissioning of the IFMIF/EVEDA very high power RFQ", in *Proc. IPAC'18*, Vancouver, BC, Canada, Apr.-May 2018, pp. 2902-2907. doi:10.18429/JACoW-IPAC2018-THXGBF2

[3] M. Sugimoto *et al*., "Progress report on Lipac", in *Proc. of LINAC'18*, Beijing, China, Sep. 2018, pp. 308-313. doi:10.18429/JACoW-LINAC2018-TU2A04

[4] K. Kondo *et al*., "Validation of the Linear IFMIF Prototype Accelerator (LIPAc) in Rokkasho", *Fusion Engineering and Design*, vol. 153, 2020.

[5] L. Bellan, "Beam Dynamics analysis/interpretation of the results obtained during phase B", in *Proc. CBO2019 Workshop*, Rokkasho, Japan, Nov. 2019.

[6] J. Marroncle *et al.*, "Transverse emittance in 2.5 MeV Proton Beam on LIPAc, IFMIF's Prototype", in *Proc. IBIC'19*, Malmö, Sweden, Sep. 2019, pp. 288-292. doi:10.18429/JACoW-IBIC2019-TUPP006

[7] E. Fagotti *et al.*, "IFMIF/EVEDA RFQ Preliminary Beam Characterization", in *Proc. of LINAC'18*, Beijing, China, Sep. 2018, pp. 834-837. doi:10.18429/JACoW-LINAC2018-THP062

[8] I. Podadera *et al.*, "Beam commissioning of beam position and phase monitors for LIPAc", in *Proc. IBIC'19*, Malmö, Sweden, Sep. 2019, pp. 534-538.doi:10.18429/JACoW-IBIC2019-WEPP013

ISBN: 978-3-95450-213-4 ISSN: 2673-5490 doi:10.18429/JACoW-IPAC2020-TUVIR14

THE SIS100 RF SYSTEMS – UPDATES AND RECENT PROGRESS

J. S. Schmidt, R. Balß, M. Frey, P. Hülsmann, H. Klingbeil[1], H. G. König,
U. Laier, D. E. M. Lens, A. Stuhl, GSI, Darmstadt, Germany
[1]also at Technische Universität Darmstadt, Darmstadt, Germany

Abstract

Within the FAIR (Facility for Antiproton and Ion Research) accelerator complex, the SIS100 synchrotron will provide high intensity proton to heavy ion beams to the various beam lines and storage rings. This paper presents the recent progress of the SIS100 overall RF system in its preparation towards installation. The RF system is split into four separate sub-systems with a significant number of RF stations. Each RF station consists of a ferrite or MA loaded cavity, a tetrode-based power amplifier, a switching mode power supply unit and various analogue or digital LLRF components for feedback and feedforward control. Fourteen ferrite cavities will generate the accelerating field, while nine cavities loaded with magnetic alloy ring cores are used for bunch compression. The barrier bucket system, which is used to apply a pre-compression of the beam, as well as the longitudinal feedback system for stabilization of beam oscillations will be realized by in total four cavities of the same type.

INTRODUCTION

The Facility for Antiproton and Ion Research is an accelerator facility, which will provide high intensity beams for experimental programs with a wide range of particles including protons, all kinds of heavy ions as well as antiprotons. The existing accelerators of the GSI Helmholtzcentre for Heavy Ion Research will be used as injectors for the FAIR chain of accelerators, beam lines, storage rings and experimental stations. A major upgrade program is ongoing for the GSI machines as well.

The synchrotron SIS100 is the main accelerator of the FAIR complex. With a circumference of ~1.1 km the machine is designed to accelerate high intensity proton and heavy ion beams. Its name reflects the Bρ value of the ring, which will consist of a mixture of superconducting and normal conducting components [1]. The lattice is optimized for the broad ion spectrum between protons and uranium. Special care has been taken to control particle losses due to residual gas effects. The construction of the SIS100 complex is ongoing and advancing well [2].

Four different RF systems are being prepared for SIS100, namely: the acceleration system, the bunch compression system and the broadband systems: barrier bucket and longitudinal feedback with a total number of 27(+13) RF stations [3, 4]. The "(+13)" stations will be added only in a later stage of a SIS100 upgrade.

- 14 (+6) Acceleration System (AC)
- 9 (+7) Bunch Compression System (BC)
- 2 Barrier Bucket (BB)
- 2 Longitudinal Feedback (LF)

In a simplified view each RF station is a compound of one cavity, with its amplifier, power supply unit and LLRF system. Still, the system with all its details will be much more complex, including the gap periphery, water cooling, controls integration and much more. Figure 1 visualizes the distribution of the RF stations along the SIS100 ring. The RF stations are located in all sectors (except sector 5, where the extraction system is located). For all of those systems the goal is to provide robust components for reliable operation of the RF stations.

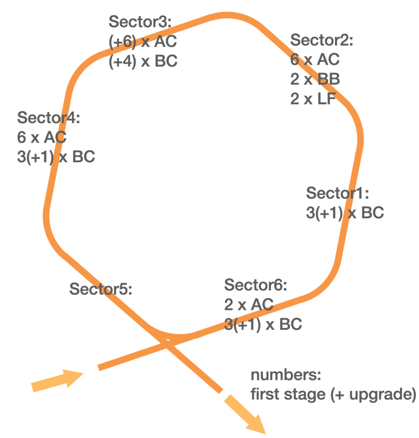

Figure 1: The distribution of the RF stations along the SIS100 ring. The numbers in brackets represent a later stage of a SIS100 upgrade

THE ACCELERATION SYSTEM

The 14(+6) RF stations of the AC system will accelerate ions in fast ramping cycles. The cavities are designed to provide high acceleration gradients of 20 kVp per cavity in cw operation. The design is based on the SIS18 design with two ferrite core stacks operating against one ceramic gap to provide the acceleration voltage. One of the challenges is to control degrading effects like dynamic and quality loss effects (ferrite characteristics) [5]. The tuning rates of ≥10 MHz/s lead to the need of a dedicated frequency tuning system.

The main parameters of the AC RF stations are:

- Continuous wave operation (cw)
- Frequency range from 1.1 MHz to 3.2 MHz
- Nominal voltage of 20 kVp
- Impedance seen by the beam <2 kOhm
- Cavity length of 3 m
- Tuning rate ≥ 10 MHz/s

The acceleration system is being realized by RI Research Instruments GmbH in collaboration with Ampegon Power Electronics AG for the power supply units. The first-of-series RF station has been successfully tested in a test stand

ISBN: 978-3-95450-213-4 ISSN: 2673-5490 doi:10.18429/JACoW-IPAC2020-TUVIR14

at GSI [6] and currently, the production of the series is ongoing with a rate of about two cavity and amplifier systems per month. By end of May, 4 cavity and amplifier systems together with two power supply units are expected to be delivered to GSI. Two more systems are undergoing the factory acceptance tests at the moment. The photo in Fig. 2 shows one of the test stands at Research Instruments, where the cavity is tested in the system with a power supply unit and LLRF.

All systems are planned to be completed by autumn this year.

Figure 2: Test stand for factory acceptance tests of the cavity and amplifiers at RI (courtesy of RI Research Instruments GmbH).

THE BUNCH COMPRESSION SYSTEM

The bunch compression system will allow to create bunches of less than 50 ns bunch length due to a bunch rotation in longitudinal phase space by means of intentionally mismatched buckets. Therefore a 3 ms RF burst with a rise time of <30 µs and an overall gap voltage of 360 kV(+280 kV) is planned. The design of the 9(+7) RF stations is (like for the acceleration system) based on the RF stations operating in SIS18 [7,8]. To be able to generate the peak voltages of 40 kV on a cavity length of just a bit more than 1 m, magnetic alloy ring cores are used instead of ferrites.

The main parameters of the BC RF stations are:

- Burst mode or pulsed wave operation 3 ms/s
- Frequency range from 310 kHz to 560 kHz
- Nominal voltage of 40 kVp
- Impedance seen by the beam <1 kOhm
- Cavity length of 1.2 m
- Amplitude rise time <30 µs (fall time uncritical)

The cavities and amplifiers for the bunch compression system are manufactured by Aurion Anlagentechnik GmbH, while the power supply units are realized by OCEM Power Electronics. All cavity and amplifier systems have been built already, you can see some of them as they are in storage at GSI currently together with a test stand at the manufacturing company Aurion with a power supply unit, cavity and amplifier in Fig. 3. Also all power supply units are in preparation for their factory acceptance tests at OCEM.

The first-of-series of the cavity-and-amplifier-systems as well as the power supply unit have been tested by the GSI

Figure 3: Photo of the test stand at the manufacturing company Aurion (left) and components in storage at GSI (right).

team under high power operating conditions. Those tests have shown that the system reaches the required parameters.

Still some topics were found, which led to adaptions of the series components. During high power tests sparking on the ceramic gap on the bunch compressor beam pipe had been observed. Also the power supply unit showed some issues with overheating on the anode modules, which prevented long term operation.

Both of these topics are currently being addressed. A new gap design has been defined, which is optimized to improve the shielding of ceramic to metal contacts from the high electric fields on the beam axis. New beam pipes with this gap geometry are in manufacturing right now and are planned to be verified before the end of this year. Also the first of series power supply unit has been upgraded and a 16 h duration test (on the cavity) has been carried out successfully (see Fig. 4). The implementation in the series is ongoing and first modules of the „new“ series are expected for testing on site soon.

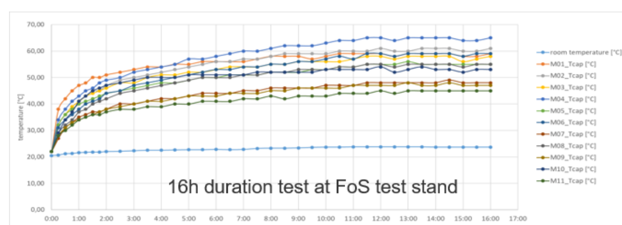

Figure 4: Temperature on the power supply unit anode modules stabilize at ~65°C during a 16 h duration test on the cavity.

LLRF FOR THE ACCELERATION AND BUNCH COMPRESSION SYSTEMS

The LLRF concept [9] for the AC and BC systems is very similar. Each of the cavities will be controlled in amplitude and phase. In addition, the AC system will be equipped with a frequency tuning loop to be able to follow the required tuning rates instantaneously.

One of the challenges for the LLRF systems in SIS100 is the distribution of the supply rooms around the ring. Solutions had to be found to ensure the synchronization of the systems at different locations. Central clock signals on a fixed frequency are distributed with the Bunch Phase Timing System (BuTiS) and processed in the common system to distribute the reference signals to the local cavity systems.

ISBN: 978-3-95450-213-4 ISSN: 2673-5490 doi:10.18429/JACoW-IPAC2020-TUVIR14

The generic layout is presented in Fig. 5.

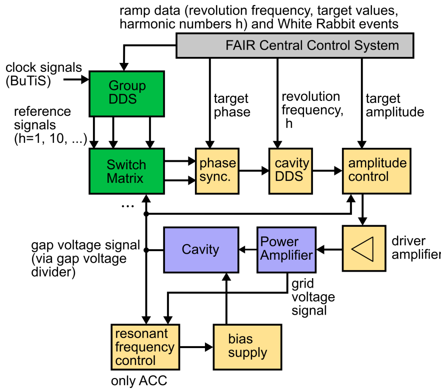

Figure 5: Schematic of the LLRF control loops for the SIS100 AC and BC systems.

Most LLRF modules are dedicated developments (in-house and in cooperation with external partners), e.g.

- rf distribution amplifier
- direct digital synthesis (DDS) module
- analog pre-processing phase detection modules
- DSP system (Sundance Multiprocessor Technology Ltd.)
- FPGA interface board FIB3 (KTS GmbH)

In the past years major developments for those LLRF modules have taken place. The high level of standardization of the LLRF modules for different systems allows to keep a common stock of spare modules for fast exchange in case of failures of modules in operation. Figure 6 shows a test installation of the LLRF racks.

About 50% of the series components have been delivered already and pre-assembly of the racks has started. This will allow us to minimize the installation time for the LLRF racks in the supply tunnel, once the tunnel is ready for installation.

Figure 6: Installation of the LLRF racks in the test stand of the AC first of series RF station at GSI.

THE BROADBAND SYSTEMS

Barrier Bucket System

A barrier bucket system with two RF stations is being designed for SIS100, which will be able to create potential barriers formed by two single sine pulses, whose amplitude and phase difference can be quickly modified within one cycle. This will allow to introduce longitudinal manipulations like for example pre-compression of a coasting beam.

It is planned to build two RF stations with magnetic alloy cavities. This is needed, since 15 kV have to be provided on a short length of 1.2 m.

The main requirements of the BB RF stations are:

- 15 kV pulse amplitude at cavity length ~1.2 m
- broadband pulses of duration 666 ns at repetition periods between 3.7 µs and 9.1 µs

Another major point of the design is the desired signal quality of the single sine pulse. A broad frequency range of 110 kHz up to 15 MHz and a pre-distortion of the input-signal are needed to match this requirement.

To generate the input signal, the transfer function $\underline{H}(\omega)$ is measured for each system and its inverse is calculated. With this information the Fourier-coefficients of the pre-distorted signal $\underline{\tilde{c}}_n = \underline{H}^{-1}\underline{\tilde{c}}_n$ can be defined, which compensates the set up characteristics individually.

Longitudinal Feedback System

The longitudinal feedback system is a preventive system to flexibly cope with different bunch oscillations [10]. For example, it will be used to damp longitudinal oscillations, acting individually on single bunches complementary to the beam-phase control. It consists of two RF stations with Fast Current Transformer (FCT) as beam pick-up and 2 broadband kicker cavities with tetrode amplifiers. The kicker acts on dedicated bunches in addition to the acceleration cavities, which can be used to damp cohered modes. The beam signal for each bunch is extracted to calculate the proper signal for the kicker cavity to correct its phase or shape. The correction signals for all bunches are combined afterwards in the overall kicker signal to generate the correct signal for the full bunch chain.

The main requirements of the LF RF stations are:

- signal processing individually for each bunch
- bunch gap >50 ns results in bandwidth (3 dB) requirement 20 MHz for overall system
- 12 kV required, cw operation

Status of the Broadband Systems

Following a staged approach in the project, the focus had been set on the AC and BC systems first. Meanwhile, machine experiments have been performed in the GSI Experimental Storage Ring and SIS18 to test the concepts of the BB and LF systems with quite good results. To give an example: the plot in Fig. 7 shows the measurement of a single-sine barrier pulse with very high quality that was taken on the BB system in the experimental storage ring. Also the signal processing for the LF system has been demonstrated at the SIS18 acceleration cavities.

Since the requirements in terms of frequency range and gap voltage are very similar, a common design for the cavity and amplifier systems of the LF an BB systems is preferred.

11th Int. Particle Acc. Conf. IPAC2020, Caen, France JACoW Publishing
ISBN: 978-3-95450-213-4 ISSN: 2673-5490 doi:10.18429/JACoW-IPAC2020-TUVIR14

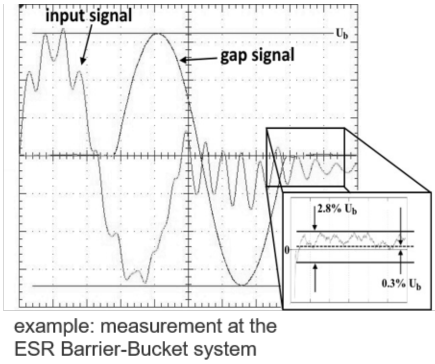

Figure 7: Measurement of a single-sine barrier pulse in comparison to the pre-distorted input signal in the BB system of the experimental storage ring.

A design study for broadband systems has shown that parameters like they are expected for the BB and LF operation in SIS100 are feasible. A visualization from this study is shown in Fig. 8.

Currently, detailed specifications for the SIS100 Barrier-Bucket system are in preparation.

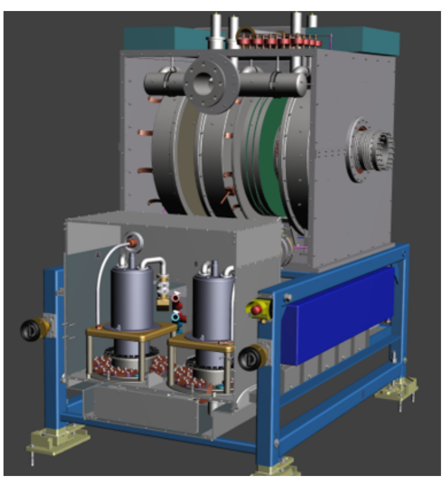

Figure 8: Visualization of a possible broadband cavity and amplifier system from the „Research and Development-study for magnetic alloy broadband cavities“ (Aurion Anlagentechnik GmbH)

LLRF for the Broadband Systems

The general concept of the LLRF systems for the broadband RF stations follows the one as presented for the AC and BC systems. Separate LLRF systems will be prepared for BB and LF in the first stage of operation, a later flexible usage of the LLRF for all four cavities will be studied. While the BB LLRF system is optimized for the generation of the single-sine RF barrier signals, in the LF system, signal processing for the individual bunches is needed as described before [11].

The LLRF systems are realized with many standard modules that are also used for SIS100 AC and BC (e.g. DSP, DDS). Dedicated modules for LF system include:

- Demultiplexer (DEMUX) and Multiplexer (MUX) developed by Novotronik GmbH
- broadband amplitude modulator

Dedicated modules for BB system include:

- waveform generator (Tabor)
- RF disabling unit
- trigger generation unit

Prototype LLRF architecture and machine development experiments have been realized for both systems.

An example of the demultiplexed bunch signals of an emulated chain of 4 bunches is shown in Fig. 9. Experiments like this one have shown the functionality of the systems.

Figure 9: Measurement of demultiplexed bunch signals of an emulated chain of 4 bunches.

CONCLUSION

The current status for the SIS100 RF systems can be summarized like this: The acceleration and bunch compression systems and the LLRF systems are in the phase of FATs and deliveries, while the broadband systems are in the phase of specification and design.

The placement of contract for First-of-Series (FoS) of the broadband cavities is planned for 2020. Other ongoing topics are the development of semi-conductor gap switches, which are needed to cope with the very high expected numbers of switching cycles in the gap periphery, or the integration of the LLRF system into the common control system.

Preparations for the installation and commissioning phase are ongoing. It is planned to start the installation of the SIS100 systems in 2021.

ACKNOWLEDGEMENTS

We would like to thank all our partners in industry and all GSI colleagues for the good collaboration and productive work on these projects.

ISBN: 978-3-95450-213-4 ISSN: 2673-5490 doi:10.18429/JACoW-IPAC2020-TUVIR14

REFERENCES

[1] P. Spiller *et al.*, "FAIR Technical Design Report SIS100", 2008.

[2] P. J. Spiller *et al.*, "FAIR SIS100 - Features and Status of Realisation", in *Proc. 8th Int. Particle Accelerator Conf. (IPAC'17)*, Copenhagen, Denmark, May 2017, pp. 3320–3322. doi:10.18429/JACoW-IPAC2017-WEPVA030

[3] H. Klingbeil *et al.*, "Status of the SIS100 RF Systems", in *Proc. 8th Int. Particle Accelerator Conf. (IPAC'17)*, Copenhagen, Denmark, May 2017, pp. 4136–4138. doi:10.18429/JACoW-IPAC2017-THPIK016

[4] M. Frey *et al.*, "Status of the Ring RF Systems for FAIR", in *Proc. 6th Int. Particle Accelerator Conf. (IPAC'15)*, Richmond, VA, USA, May 2015, pp. 2789–2791. doi:10.18429/JACoW-IPAC2015-WEPMA018

[5] H. G. Koenig and S. Schaefer, "Reduction of Q-loss-effects in Ferrite-loaded Cavities", in *Proc. 11th European Particle Accelerator Conf. (EPAC'08)*, Genoa, Italy, Jun. 2008, paper MOPP094, pp. 772–774.

[6] H. G. Koenig *et al.*, "The FAIR-SIS100 Accelerating RF Station", in *Proc. 9th Int. Particle Accelerator Conf. (IPAC'18)*, Vancouver, Canada, Apr.-May 2018, pp. 2762–2764. doi:10.18429/JACoW-IPAC2018-WEPML033

[7] P. Hülsmann, R. Balss, H. Klingbeil, and U. Laier, "Bunch Compression for FAIR", in *Proc. 23rd Particle Accelerator Conf. (PAC'09)*, Vancouver, Canada, May 2009, paper TU5PFP023, pp. 864–866.

[8] H. G. Koenig *et al.*, "The FAIR-SIS100 Bunch Compressor RF Station", in *Proc. 9th Int. Particle Accelerator Conf. (IPAC'18)*, Vancouver, Canada, Apr.-May 2018, pp. 2759–2761. doi:10.18429/JACoW-IPAC2018-WEPML032

[9] H. Klingbeil *et al.*, "New digital low-level rf system for heavy-ion synchrotrons", *Phys. Rev. Accel. Beams*, vol. 14, p. 10280, 2011. doi:10.1103/PhysRevSTAB.14.102802

[10] H. Klingbeil, "SIS100 Longitudinal Feedback Cavity System", 21st Fair Machine Advisory Committee Meeting 2019.

[11] D. Lens and H. Klingbeil, "Detailed Specification of the SIS100 Longitudinal Feedback System", F-DS-RRF-en-RF 0032, V004, 10.04.2019.

ISBN: 978-3-95450-213-4 ISSN: 2673-5490 doi:10.18429/JACoW-IPAC2020-TUVIR15

LONG-TERM BEAM POSITION AND ANGLE STABILITIES FOR THE J-PARC MAIN RING SLOW EXTRACTION

M. Tomizawa*, Y. Arakaki, T. Kimura, S. Murasugi,
R. Muto, K. Okamura, E. Yanaoka, ACCL, KEK, Tsukuba, Japan
Y. Komatsu, Y. Shirakabe, IPNS, KEK, Tsukuba, Japan

Abstract

A 30 GeV proton beam accelerated in the J-PARC Main Ring (MR) is slowly extracted by the third integer resonant extraction and delivered to the hadron experimental hall. A unique dynamic bump scheme for the slow extraction has been applied to reduce the beam loss. The current extraction efficiency is very high, 99.5%. However, the dynamic bump scheme is sensitive to the beam orbit angle at the first electrostatic septum (ESS1). The orbit angle of the dynamic bump must be sometimes readjusted to keep such a high efficiency. A long term stability of the orbit depending to momentum has been investigated.

INTRODUCTION

A high-intensity proton beam accelerated in the J-PARC main ring (MR) is slowly extracted by the third integer resonant extraction and delivered to the hadron experimental hall to drive various nuclear and particle physics experiments [1]. Most of the proposed experiments are best performed using a coasting beam without an RF structure and a uniform beam intensity during the extraction time. One of the critical issues in slow extraction (SX) of a high intensity proton beam is an inevitable beam loss caused by the extraction process at septum devices. A unique dynamic bump scheme for the slow extraction has been applied to reduce the beam loss [2]. The layout of J-PARC MR Slow extraction devices is shown in Fig. 1.

The beam power of 30 GeV slow extraction has achieved to 51 kW at 5.2s cycle in current physics runs. The extraction efficiency is very high, typically 99.5%. However, the dynamic bump scheme is sensitive to the beam orbit angle at the first electrostatic septum (ESS1). The orbit angle of the dynamic bump must be sometimes readjusted to keep such a high efficiency. A long-term stabilities of the orbit and the relative momentum have been investigated in this paper. The work in this paper is useful for a diffuser [3] and/or a silicon bend crystal [4] to achieve further high slow extraction efficiency introduced in future. They could be more sensitive to the orbit and momentum shifts.

CURRENT SLOW EXTRACTION PERFORMANCES

The momentum pattern of the current slow extraction is shown in Fig. 2. The repetition cycle is 5.2 s, in which the flat top length is 2.61 s. The proton number per cycle is 5.6×10^{13} ppp corresponding to 51 kW. The extraction

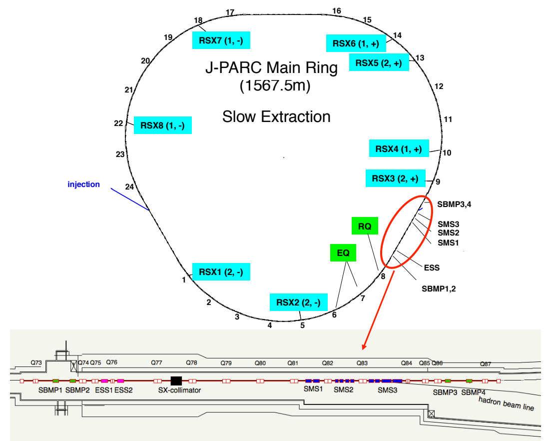

Figure 1: Layout of J-PARC slow extraction devices.

efficiency is very high, 99.5% [5,6]. The typical spill length and spill duty factor is 2 s and 50%, respectively [6]. In the current beam power, the transverse instability during the debunch process to obtain an uniform time structure is serious. To solve this problem, the beam is injected to the RF buckets with phase offset of 50−60 degree [5]. The resultant momentum width is spread to ~0.5% in full width at the flat top.

The dynamic bump orbit tuning associated with the position and angle of the electrostatic septa (ESS1 and ESS2) and the magnetic septa (SMS1 and SMS2) is the most important to obtain a high extraction efficiency. Figure 4 shows extraction efficiency as a function of the bump orbit angle at the entrance of the ESS1. The bump orbit angle is for the end of extraction and the actual bump orbit angle is shifted so as to superimpose the extraction arms from the separatrices

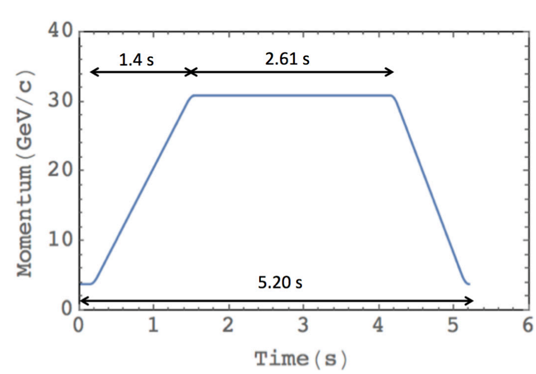

Figure 2: Momentum pattern of MR slow extraction operation.

* masahito.tomizawa@kek.jp

ISBN: 978-3-95450-213-4 ISSN: 2673-5490 doi:10.18429/JACoW-IPAC2020-TUVIR15

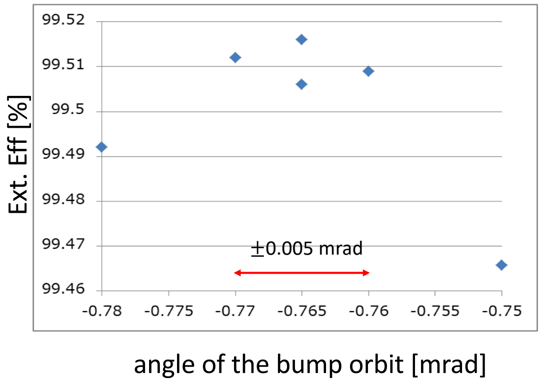

Figure 3: Measured extraction efficiency and the bump orbit angle at the ESS1 entrance.

during the extraction. The extraction efficiency is sensitive to the bump orbit angle, and must be tuned with an accuracy of 5 μrad to optimize the extraction efficiency (Fig. 3).

ORBIT ANGLE AND MOMENTUM SHIFTS

The orbit angle x' and the position x at the ESS1 entrance are derived from the beam positions measured by beam position monitors (BPMs) located just upstream and downstream of the ESS1 and so-called Twiss parameter β_x, α_x and phase advance at the three locations. The straight section where the ESSs is located is dispersion free. The 24 BPMs with large dispersions in the arc sections are chosen to derive the shift $\Delta p/p$ for the reference momentum defined by the bending field and the RF frequency. The COD in MR is corrected by the steering magnets at any acceleration timing in typical rms COD of ~0.5 mm. The beam position x_i of the i-th BPM is written as

$$x_i = \eta_i \cdot \frac{\Delta p}{p} + \delta x_i, \tag{1}$$

where η_i and δx_i are dispersion and COD, respectively. Then the momentum shift $\Delta p/p$ can be expressed as

$$\frac{\Delta p}{p} \sim \frac{1}{24} \sum_{i=1}^{24} \frac{x_i}{\eta_i}. \tag{2}$$

The COD term δx_i in Eq. (2) can be approximately canceled in the summation. The observing timing for plots shown in next section is at the flat top start just before debunch and exciting the bump orbit. The bump orbit is actually incorporated in the actual orbit angle during slow extraction.

LONG TERM STABILITIES OF EFFICIENCY, ORBIT ANGLE AND MOMENTUM SHIFT

Figure 4 shows trends of slow extraction efficiency, orbit position x and angle x' at the ESS1 entrance and momentum shift. The extraction efficiency can be derived from the

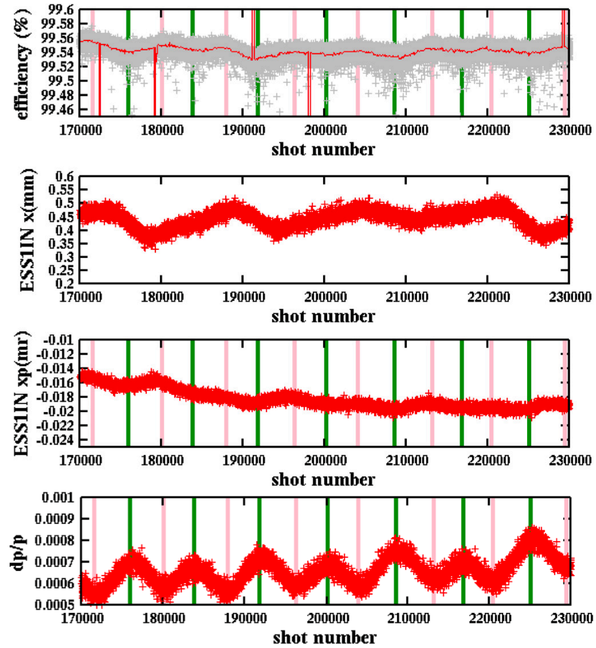

Figure 4: Trends of extraction efficiency, horizontal position x, angle x' and $\Delta p/p$.

beam loss monitors (BLMs) around the ESSs and SMSs area (see Fig. 1). The horizontal axis shows accumulated shot numbers (one shot is 5.2 s MR cycle). In this figure, the data derived from the BPMs are plotted every 10 shots. The interesting oscillation pattern can be seen in the $\Delta p/p$ trend. The oscillation pattern has a half-day cycle. The orbit angle at the ESS1 entrance also has a pattern synchronized with the $\Delta p/p$ oscillation pattern. The extraction efficiency seems to have a similar oscillation, though it is not so clear.

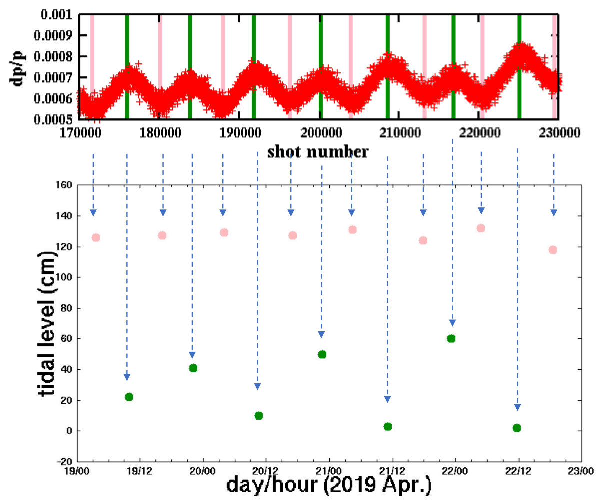

Figure 5: Relation between $\Delta p/p$ trend and tidal level in Oarai coast.

Figure 5 shows the relation between the $\Delta p/p$ pattern and tidal level in Oarai coast [7]. Oarai coast is located at 20 km far from J-PARC cite as shown in Fig. 6. Low and high tides are shown in green and pink in Figure 5, respectively. The $\Delta p/p$ peaks coincide with the low tides, on the other hand, the $\Delta p/p$ valleys coincide with the high tides. The

ISBN: 978-3-95450-213-4 ISSN: 2673-5490 doi:10.18429/JACoW-IPAC2020-TUVIR15

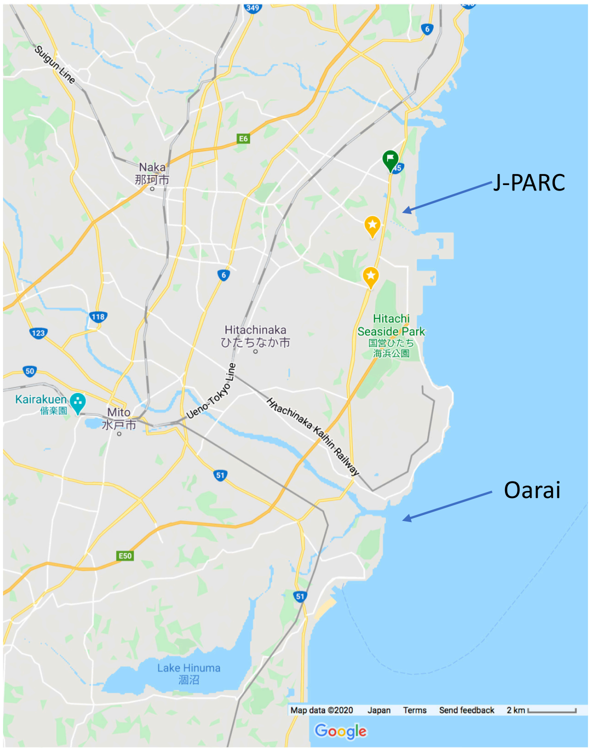

Figure 6: Location of J-PARC and Oarai coast.

peaks have large and small amplitudes alternately, which corresponds to the strong and week low tides. The valleys are also similar. The $\Delta p/p$ oscillation pattern is estimated to be generated by the circumference change of the ring due to the tidal force. If RF frequency and bending field are constant, $\Delta p/p$ can be written as

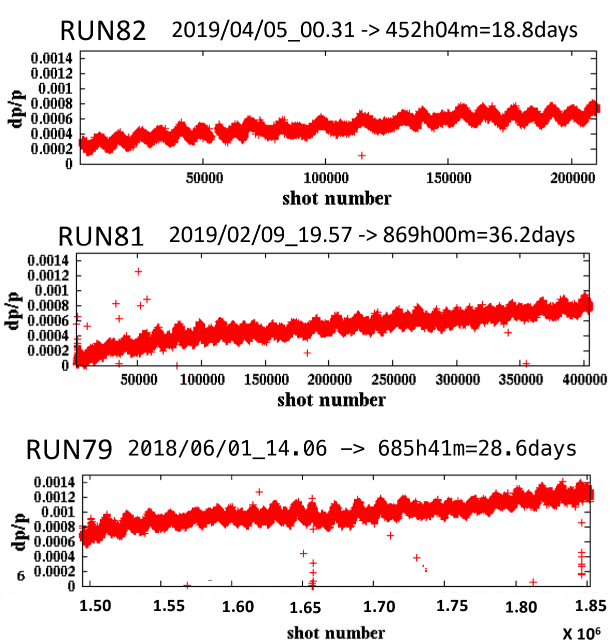

Figure 7: Long term $\Delta p/p$ shifts for three runs.

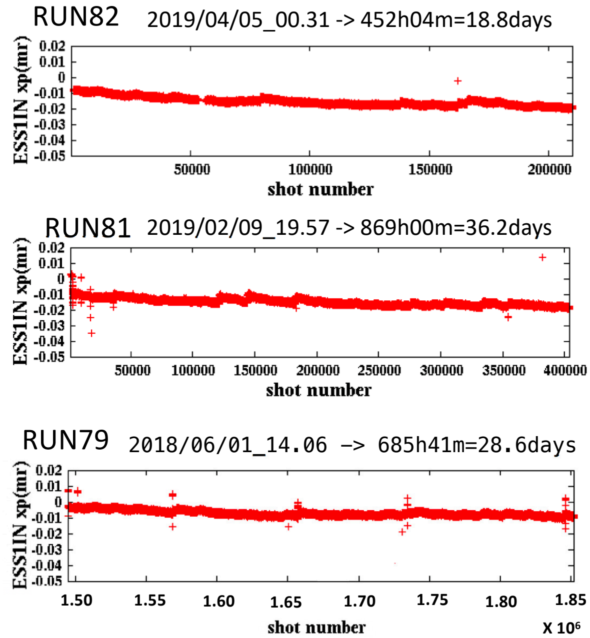

Figure 8: Long term shifts of x' at ESS1 entrance corresponding to Fig. 7.

$$\frac{\Delta p}{p} = \gamma^2 \cdot \frac{\Delta C}{C}, \tag{3}$$

where, γ and C are Lorentz factor and the ring circumference, respectively [8]. From Eq. (3), when $\Delta p/p$ increases by 0.0001 at 30 GeV, the corresponds C expansion becomes 0.144 mm (= ΔC).

Figure 7 shows a longer term stability of orbit angle at the ESS1 entrance and $\Delta p/p$, three different run cases are plotted. The $\Delta p/p$ increases monotonically in the long period at any run (0.002~0.003/100days). The long term $\Delta p/p$ shifts is rather larger than the oscillation amplitude by the tide. On the other hands, the orbit angle at the ESS1 entrance shifts monotonically in the long period at any run (-0.05~-0.03 mrad/100 days). Temperature in the MR tunnel has been controlled by air conditioners in three machine buildings connected to the MR tunnel. The air temperature in the SX operation is roughly 4 degree higher than the air temperature in the machine maintenance period. The tunnel concrete may expand gradually by the air temperature increase of 4 degree during the slow extraction operation.

CONCLUSION

A 30 GeV proton beam accelerated in the J-PARC Main Ring (MR) is slowly extracted by the third integer resonant extraction and delivered to the hadron experimental hall. A unique dynamic bump scheme for the slow extraction has been applied to reduce the beam loss. We have achieved 51 kW stable operation at 5.2s cycle in the recent physics run. The extraction efficiency is very high, typically 99.5%. However, the dynamic bump scheme is sensitive to the beam orbit angle at the first electrostatic septum (ESS1). The orbit

ISBN: 978-3-95450-213-4 ISSN: 2673-5490 doi:10.18429/JACoW-IPAC2020-TUVIR15

angle of the dynamic bump must be sometimes readjusted to keep such a high efficiency. A long-term stabilities of the beam position and angle at the ESS1 and $\Delta p/p$ have been investigated. We observed an oscillation synchronized with tides in Oarai coast. We also observed a monotonical $\Delta p/p$ increase in the long period at any run. They are estimated to be caused by the tunnel expansion.

ACKNOWLEDGMENT

We are grateful to Prof. K. Niki for providing the air temperature information in the MR tunnel.

REFERENCES

[1] Accelerator Group, JAERI/KEK Join Project Team, "Accelerator Technical Design Report for J-PARC", KEK Report 2002–13, 2002, p.204.

[2] M. Tomizawa *et al.*, "Slow extraction from J-PARC main ring using a dynamic bump", *Nucl. Instr. and Methods*, A902, 2018, pp.51–61, doi:10.1016/j.nima.2018.06.004

[3] B. Goddard *et al.*, "Reduction of 400GeV/c slow extraction beam loss with a wire diffuser at the CERN Super Proton Synchrotron", *Phys.Rev.Accel.Beams*, 23, 2020, 2, 023501, doi:10.1103/PhysRevAccelBeams.23.023501

[4] F.M. Velotti, *et al.*, "Septum shadowing by means of a bent crystal to reduce slow extraction beam loss", *Phys.Rev.Accel.Beams*, 22, 2019, 093502, doi:10.1103/PhysRevAccelBeams.22.093502

[5] M. Tomizawa *et al.*, "Status and Beam Power Ramp-Up Plans of the Slow Extraction Operation at J-Parc Main Ring", in *Proc. 61st ICFA Advanced Beam Dynamics Workshop on High-Intensity and High-Brightness Hadron Beams (HB'18)*, Daejeon, Korea, Jun. 2018, pp. 347–351. doi:10.18429/JACoW-HB2018-THA1WD03

[6] R. Muto *et al.*, "Current Status of Slow Extraction from J-PARC Main Ring", *IOP Journal of Physics Conference Series*,1350, 012105, doi:10.1088/1742-6596/1350/1/012105

[7] Oarai Tide Table, Japan Meteorological Agency, https://www.jma.go.jp/jma/index.html

[8] C. Bovet *et al.*, "A selection of formula and data useful for the design of A.G. synchrotrons", CERN/MPS-SI/Int. DL/70/4, 23 April, 1970.

ISBN: 978-3-95450-213-4 ISSN: 2673-5490 doi:10.18429/JACoW-IPAC2020-WEVIR03

MICROBUNCH ROTATION AS AN OUTCOUPLING MECHANISM FOR CAVITY-BASED X-RAY FREE ELECTRON LASERS*

R. A. Margraf†1, Z. Huang[1], J. P. MacArthur, G. Marcus
SLAC National Laboratory, Menlo Park, USA
[1]also at Stanford University, Stanford, USA

Abstract

Electron bunches in an undulator develop periodic density fluctuations, or microbunches, which enable the exponential gain of power in an X-ray free-electron laser (XFEL). For certain applications, one would like to preserve this microbunching structure of the electron bunch as it experiences a dipole kick which bends its trajectory. This process, called microbunch rotation, rotates the microbunches and aligns them perpendicular to the new direction of electron travel. Microbunch rotation was demonstrated experimentally by MacArthur et al. with soft x-rays [1] and additional unpublished data demonstrated microbunch rotation with hard x-rays. Further investigations into the magnetic lattice used to rotate these microbunches showed that microbunches can be rotated using an achromatic lattice with a small R56, connecting this technique to earlier studies of achromatic bends. Here, we propose and study a practical way to rotate Angstrom-level microbunching as an out-coupling mechanism for the Optical Cavity-Based X-ray FEL (CBXFEL) project at SLAC.

CAVITY-BASED XFELS AND THE CBXFEL PROJECT

Current state-of-the-art XFELs, including the LCLS at SLAC, are SASE (Self-Amplified Spontaneous Emission) XFELs, as depicted in Fig. 1A. A several GeV electron beam passes through an undulator, a series of alternating north-south magnets which rapidly bend the e-beam trajectory back and forth. An e-beam/radiation collective instability occurs when this oscillating electron beam interacts with light at a resonant wavelength, developing periodic density modulations, "microbunches," which increase the coherence of resonant X-ray synchrotron radiation emitted by the electrons. In a SASE XFEL, the light which seeds the XFEL arises from noise. This light is incoherent and low intensity, thus many undulators are required to microbunch the electron beam and produce bright X-rays. The resultant X-ray pulse is transversely coherent, but longitudinally chaotic, with a longitudinal coherence length inversely proportional to the spectral bandwidth of the XFEL amplifier, $l_{coh} \sim \frac{1}{\sigma_\omega}$ [2]. This longitudinal coherence can be increased by seeding with X-rays of a narrower bandwidth than the XFEL amplifier. Lacking compact coherent X-ray sources, one solution is to use monochromatized X-rays generated from SASE to seed the XFEL process, as is done in a cavity-based XFEL.

The CBXFEL Project will demonstrate two-pass gain in the LCLS-II hard X-ray undulator line using the LCLS copper linac in two-bunch mode. Four diamond (400) mirrors will wrap seven undulators (~ 35 m) to form a rectangular optical cavity as depicted in Fig. 1B. Hard X-rays at 9.83 keV from the first bunch will Bragg reflect and return to seed a trailing fresh electron bunch on the subsequent pass.

CBXFEL will develop technologies to enable future production-level cavity-based XFELs which leverage the high repetition rate (1 MHz) and electron energy (8 GeV) of the LCLS-II High Energy (HE) upgrade [3]. These cavities may wrap the entire 130 m undulator line at SLAC such that the photon cavity round trip time matches the arrival of MHz electron bunches.

Table 1 summarizes the projected outputs of such production-level facilities in two modes, X-ray Regenerative Amplifier FEL (XRAFEL) and X-ray FEL Oscillator (XFELO). XRAFEL is a high gain system, regenerating a large percentage of the X-ray power on each pass through the cavity. XRAFEL can produce >5 times the peak power and 100 times the energy resolution of a SASE FEL, while maintaining short pulse lengths. XFELO is a low-gain system which builds up X-ray power over many passes. XFELO produces X-ray pulses with 10,000 times narrower energy resolution, and 1000 times higher average spectral brightness, with the trade-off of longer X-ray pulses. Both have high longitudinal coherence and stability, replacing chaotic arrival times of SASE spikes.

Table 1: Projected Cavity-based XFEL Properties [4, 5]

	SASE	XRAFEL	XFELO
Gain	High	High	Low
Passes to Saturation	1	10's	100's
Peak Power	10 GW	>50 GW	10 MW
Average Power	100 W (1 MHz)	10 W (10 kHz)	20 W (1 MHz)
Bandwidth	10 eV	0.1 eV	20 meV
Average Spectral Brightness $\left(\frac{\text{photons}}{\text{s mm}^2\,\text{mrad}^2.1\,\%\text{BW}}\right)$	10^{25}	10^{26}	10^{28}
Pulse Length	1-100 fs	20 fs	1 ps
Temporal Stability and Coherence	Poor	Excellent	Excellent

* This work was supported by the Department of Energy, Laboratory Directed Research and Development program at SLAC National Accelerator Laboratory, under contract DE-AC02-76SF00515.
† rmargraf@stanford.edu

ISBN: 978-3-95450-213-4 ISSN: 2673-5490 doi:10.18429/JACoW-IPAC2020-WEVIR03

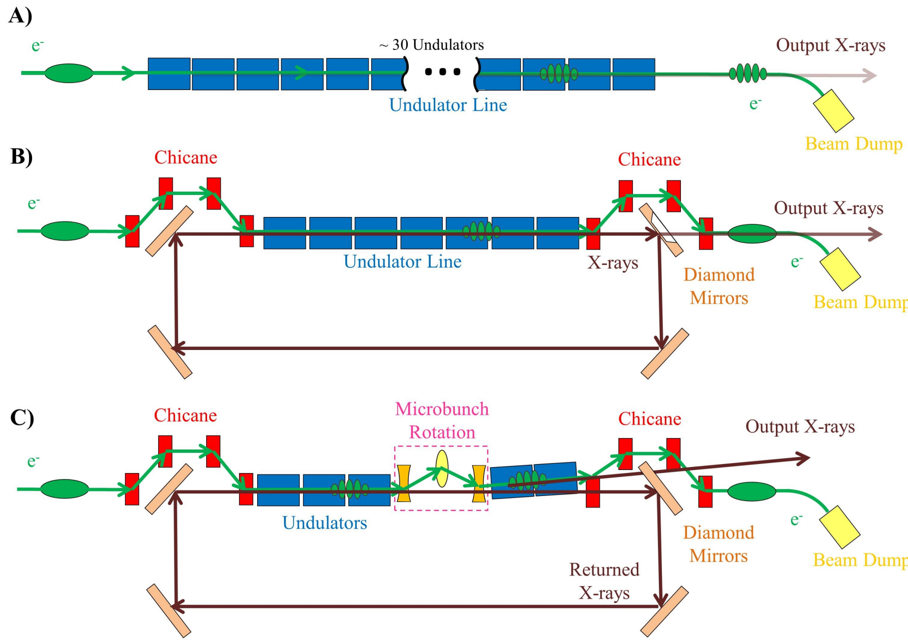

Figure 1: XFEL Schemes: A) a single-pass conventional SASE XFEL, B) a cavity-based XFEL with drumhead crystal outcoupling, C) a cavity-based XFEL with microbunch rotation outcoupling.

The projections shown in Table 1 represent recent studies on XRAFEL and XFELO, and incorporate two different methods of out-coupling X-rays from the optical cavity. CBXFEL is investigating several possible outcoupling methods. The baseline for CBXFEL will be outcoupling through a drumhead diamond crystal which has been thinned to ~ 20 µm, as depicted in Fig. 1B [6], but other methods include drilling a ~ 100 µm hole in the mirror [7], inserting a grating beamsplitter to separate the X-ray beam into multiple diffraction orders [8], or utilizing an active Q-switching method [9]. The former three of these are passive methods, which outcouple a portion of the X-ray pulse on each pass through the cavity, while the last is an active method, where an optical pulse actively controls the reflectivity of the outcoupling mirror to outcouple a larger portion of the X-ray beam after a certain number of passes. The passive methods retain a high repetition rate, and thus a high average power, but only couple out a small percentage of the X-ray power on each pass, reducing their peak power. Active outcoupling methods outcouple a large percentage of the X-ray power, and thus have large peak power, but lower repetition rate and thus lower average power as they outcouple less frequently.

These properties are reflected in Table 1, where the XRAFEL scheme shown utilized an active q-switching method, and the XFELO scheme utilized a drumhead crystal outcoupling. A passive outcoupling scheme which can outcouple a large percentage of the X-ray power could dramatically increase the average power of XRAFEL and the peak power of XFELO above the values given in Table 1.

Microbunch rotation is a passive outcoupling method CBXFEL is investigating to outcouple X-ray power comparable to the cavity power by exploiting the electron beam.

MICROBUNCH ROTATION OUTCOUPLING

A cavity-based X-ray FEL with microbunch rotation outcoupling is depicted in Fig. 1C. Electron microbunches generated in the XFEL process are preserved as the electron bunch experiences a dipole kick. These microbunches can then be lased in a downstream undulator to produce X-rays at an angle to the original beam axis. X-rays rotated outside the diamond rocking curve (~ 8 µrad), will not be reflected by the cavity mirrors and will exit the cavity.

Microbunch rotation through an achromatic bend was previously demonstrated for outcoupling infrared FEL oscillators [10], and has also been demonstrated experimentally with X-ray microbunches. MacArthur et al. demonstrated a 5 µrad rotation with soft x-ray microbunches [1] and additional unpublished data demonstrated 5 µrad rotation with hard x-ray microbunches. Shorter radiation wavelengths are more challenging for microbunch rotation, as microbunches are separated at the radiation wavelength, λ_r, and the bunching factor for a given microbunch, $b = \langle e^{i\theta} \rangle$, $\theta \approx (\frac{2\pi}{\lambda_r} + \frac{2\pi}{\lambda_u})z$, is more sensitive to changes in the z position of the particles relative to the center of the microbunch. CBXFEL must use hard, 9.83 keV, X-rays to Bragg-reflect at 45° from diamond 400, and we must achieve a ~ 10 µrad rotation to miss the diamond 400 rocking curve. Thus, we must extend previous work on hard X-ray microbunch rotation to higher angles.

Recent work has demonstrated microbunch rotation by employing three offset quadrupole magnets of the strong focusing (FODO) lattice in the undulator line. This enables existing magnets to provide the dipole kicks, and reduces the need to rematch the beta function following rotation.

ISBN: 978-3-95450-213-4 ISSN: 2673-5490 doi:10.18429/JACoW-IPAC2020-WEVIR03

Analytical Matrix Method

We model propagation of a single electron microbunch through an offset quadrupole triplet using a beam transport matrix. In the first order beam transport matrix in $x, x', z, \frac{\Delta\gamma}{\gamma}$ phase space,

$$R = \begin{bmatrix} R11 & R12 & R15 & \mathbf{R16} \\ R21 & R22 & R25 & \mathbf{R26} \\ R51 & R52 & R55 & \mathbf{R56} \\ R61 & R62 & R65 & R66 \end{bmatrix}, \tag{1}$$

there are three matrix elements (in bold) which couple energy spread, $\frac{\Delta\gamma}{\gamma}$, to the transverse and longitudinal dimensions of the bunch. Setting all three of these matrix elements to zero (an isochronous lattice) would eliminate all first order microbunching degradation. Here, to simplify the implementation, we only require the lattice to be achromatic ($R16 = 0$ and $R26 = 0$), and R56 to be small.

We construct a beam transport matrix of three offset quadrupoles with focal lengths f_1, f_2, and f_3 and drifts L_1 and L_2 between them, and require the transport matrix to be achromatic as described in detail in [11] (The authors note a typo in the offsets found in that document; the correct offsets in the thin quadrupole approximation are given here). Doing this, we find the optimal offsets for each quadrupole o_1, o_2, and o_3 at final beam trajectory angle α:

$$\begin{aligned} o_1 &= \frac{-\alpha f_1 f_2}{L_1} \\ o_2 &= \frac{\alpha f_2 (f_2 L_1 + f_2 L_2 - 2 L_1 L_2)}{L_1 L_2} \\ o_3 &= \frac{-\alpha (L_2^2 + f_2 f_3)}{L_2}. \end{aligned} \tag{2}$$

If we implement microbunch rotation in a FODO lattice where $f_1 = f_3 = -f_2$, and $L_1 = L_2 = L$, these simplify to:

$$\begin{aligned} o_1 &= \frac{\alpha f_1^2}{L} \\ o_2 &= 2\alpha f_1 \left(1 + \frac{f_1}{L}\right) \\ o_3 &= \frac{\alpha (f_1^2 - L^2)}{L}. \end{aligned} \tag{3}$$

We also choose our lattice such that the R56 is small. For an offset quadrupole triplet in a FODO lattice, R56 is:

$$R_{56} = \alpha^2 f_1 \left(1 + \frac{2 f_1}{L}\right) + \frac{2L}{\gamma^2}. \tag{4}$$

Examining this, the $\frac{2L}{\gamma^2}$ factor is the drift R56, and the $\alpha^2 f_1 \left(1 + \frac{2f_1}{L}\right)$ factor is due to the dipole kick in the center quadrupole. These two contributions can be seen clearly in Fig. 2. In the convention used here, the drift R56 will always be positive. Considering a stable FODO lattice will always have $L \leq 2|f_1|$, we find the dipole kick R56 will also always be positive, but the R56 will be smaller if $f_1 < 0$.

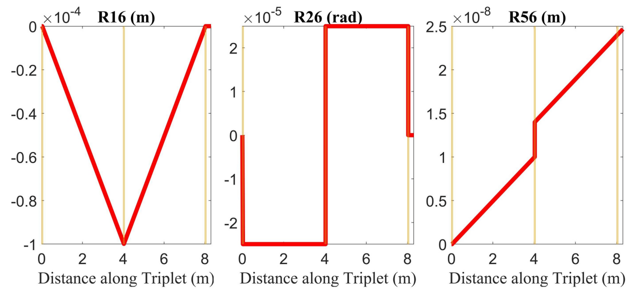

Figure 2: Important beam transport matrix elements through an achromatic offset quadrupole triplet.

Thus, we choose the first quadrupole of the triplet to be a defocusing quadrupole in the plane of the quadrupole offset.

Once we have the beam transport matrix, R, we construct a matrix, Σ_1, describing the initial electron distribution in a single Gaussian microbunch, with standard deviations $\sigma_{x_1}^2 = \langle x_1^2 \rangle$, $\sigma_{x_1'}^2 = \langle x_1'^2 \rangle$, $\sigma_{z_1}^2 = \langle z_1^2 \rangle$ and $\sigma_{\delta_1}^2 = \langle (\frac{\delta\gamma_1}{\gamma})^2 \rangle$. We start at the center of the first quadrupole, where there is zero x-x' correlation, and assume zero correlation in other planes.

$$\Sigma_1 = \begin{bmatrix} \sigma_{y_1}^2 & 0 & 0 & 0 \\ 0 & \sigma_{y_1'}^2 & 0 & 0 \\ 0 & 0 & \sigma_{z_1}^2 & 0 \\ 0 & 0 & 0 & \sigma_{\delta_1}^2 \end{bmatrix}, \ \Sigma = R \Sigma_1 R^T. \tag{5}$$

From the final Σ matrix, we find $\sigma_z = \sqrt{\langle z^2 \rangle}$ and calculate the bunching factor along the new beam trajectory.

Genesis Simulations

To support this analytical matrix model, we performed time-independent simulations of an achromatic offset quadrupole triplet using Genesis [12]. Undulators, quadrupoles and drifts were based on the LCLS-II hard X-ray undulator line (rounded to the nearest period, λ_u), and electron and photon energies were chosen to match CBXFEL, as given in Table 1. Electrons were pre-bunched in 15 vertically polarized undulators, then sent through three horizontally offset quadrupoles to perform a 10 µrad rotation.

Table 2: Genesis Simulation Parameters

B_1'	−64.267 T/m	L_1	4.004 m
B_2'	65.600 T/m	L_{Quad}	5.2 cm
B_3'	−64.267 T/m	L_{Und}	3.3 m
a_w	1.6976	λ_u	2.6 cm
E_{e^-}	10.2 GeV	E_{λ_r}	9.83 keV
σ_{y_1}	1.779×10^{-5} m	$\sigma_{y_1'}$	1.124×10^{-6} rad
σ_{z_1}	3.212×10^{-11} m	σ_{δ_1}	5.198×10^{-4}

Triplet Quadrupole Offsets:

o_1	254 µm	o_2	298 µm	o_3	214 µm

As shown in Fig. 3C, in simulation 78% of the bunching factor was recovered following microbunch rotation. The analytical matrix model predicts 83% recovery. We expect

ISBN: 978-3-95450-213-4 ISSN: 2673-5490 doi:10.18429/JACoW-IPAC2020-WEVIR03

the simulation may differ slightly from the analytical model due to second-order effects. Figure 4C shows the x-z phase space after microbunch rotation. A high bunching factor at an angle in the x-z plane is evident.

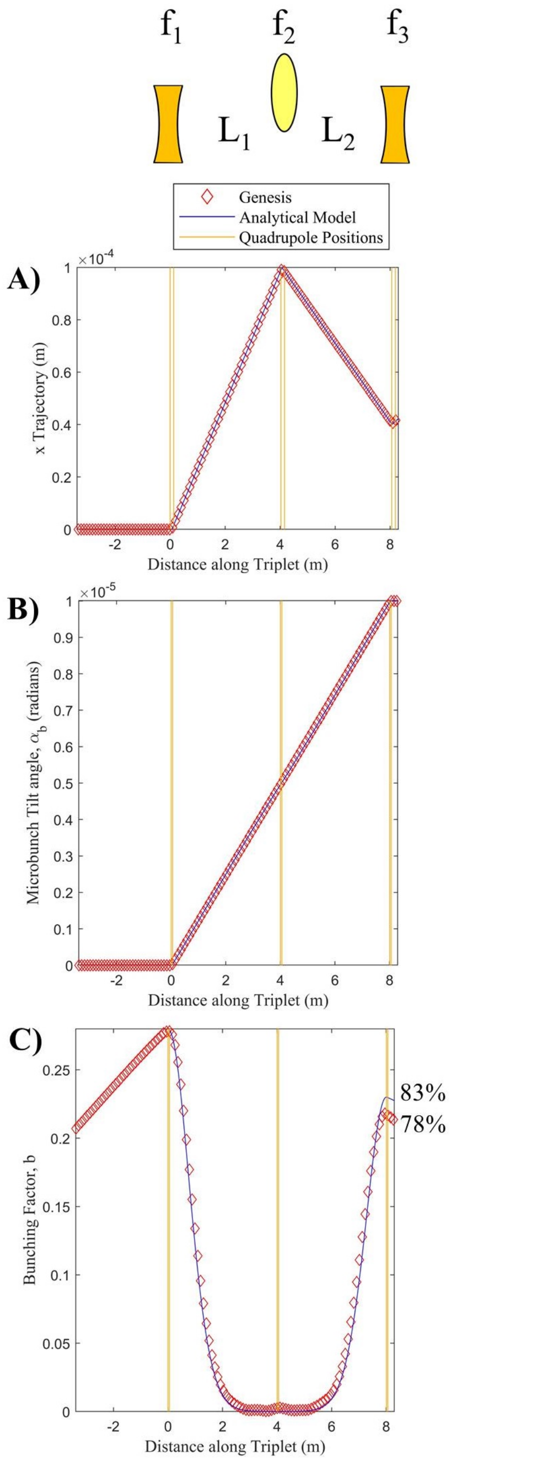

Figure 3: Comparison of analytical matrix model and Genesis simulation through an offset quadrupole triplet: A) electron trajectory, B) tilt angle at which bunching was measured, (determined by the analytical method) C) bunching factor.

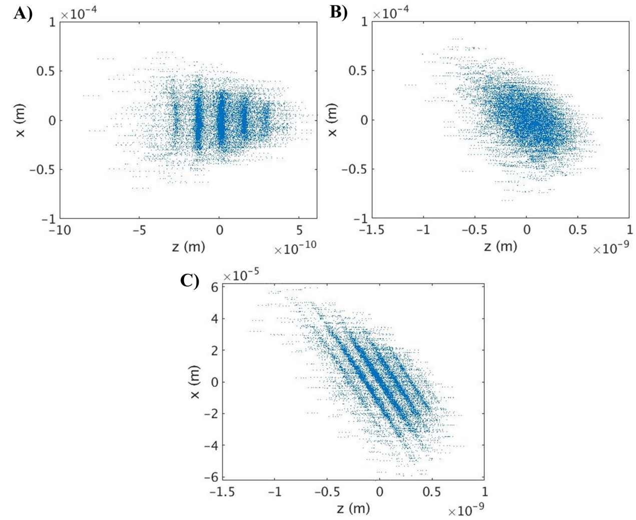

Figure 4: x-z phase space A) directly before the 1st quadrupole, B) in the center of the 2nd quadrupole and C) directly after the 3rd quadrupole. These simulations were done for a single time-independent slice, where Genesis allows electrons to slip into multiple (~ 5) pondermotive buckets, as the undulator equations remain the same. These buckets were retained when converting to z for visual clarity.

FUTURE WORK

We are actively investigating a second-order matrix theory to explain the difference in between the simulated microbunching recovery and the analytical solution. We also need to simulate lasing of these rotated microbunches in re-pointed undulator segments, and perform tolerance testing to understand this system's sensitivity to variations in quadrupole offset and other experimental factors. We will experimentally verify this microbunch rotation once LCLS-II construction is complete. These microbunch rotation studies could be taken beyond this achromatic scheme, which uses existing LCLS-II infrastructure, to make more useful microbunching rotation schemes for CBXFEL and other XFEL applications. Our current lattice uses existing quadrupole magnets in the hard X-ray undulator line, several meters apart. Making this system shorter while keeping R56 low requires short focal length quadrupoles with much stronger gradients (>100 T/m), requiring permanent magnets. We may also investigate the isochronous solution, which also sets R56 to zero, but still requires strong permanent magnets and larger quadrupole offsets.

CONCLUSION

These simulations demonstrate robust angstrom-level microbunch rotation of 10 μrad at electron and photon parameters suitable for CBXFEL, with the potential to rotate to even higher angles. These results support the feasibility of microbunch rotation outcoupling for a cavity-based XFEL, and will be continued to be developed through theoretical, simulation and experimental methods.

ISBN: 978-3-95450-213-4 ISSN: 2673-5490 doi:10.18429/JACoW-IPAC2020-WEVIR03

REFERENCES

[1] J. P. MacArthur, A. A. Lutman, J. Krzywinski, and Z. Huang, "Microbunch Rotation and Coherent Undulator Radiation from a Kicked Electron Beam," *Physical Review X*, vol. 8, no. 4, Nov. 2018. doi:10.1103/PhysRevX.8.041036

[2] K.-J. Kim, Z. Huang, and R. Lindberg, *Synchrotron radiation and free-electron lasers: principles of coherent X-ray generation*, New York, NY, USA: Cambridge University Press, 2017, pp. 118–121.

[3] T. Raubenheimer, "Progress on the LCLS-II and High Energy Upgrade LCLS-II-HE," in *Proc. of Workshop on Future Light Sources (FLS'18)*, Shanghai, March 5-9, 2018. doi:10.18429/JACoW-FLS2018-MOP1WA02

[4] G. Marcus *et al.*, "Cavity-Based Free-Electron Laser Research and Development: A Joint Argonne National Laboratory and SLAC National Laboratory Collaboration," in *Proc. FEL'19*, Hamburg, Germany, Aug. 2019, pp. 282–287. doi:10.18429/JACoW-FEL2019-TUD04

[5] K.-J. Kim *et al.*, "Test of an X-ray Cavity using Double-Bunches from the LCLS Cu-Linac," in *Proc. IPAC'19*, Melbourne, Australia, May 2019, pp. 1887–1890. doi:10.18429/JACoW-IPAC2019-TUPRB096

[6] CBXFEL Physics Requirements Document for the Optical cavity Based X-Ray Free Electron Lasers Research and Development Project. SLAC Internal Publication in Progress, May 2020.

[7] H. P. Freund, P. van der Slot, and Y. Shvyd'ko, "An X-Ray Regenerative Amplifier Free-Electron Laser Using Diamond Pinhole Mirrors," arXiv:1905.06279 [physics.acc-ph] May 2019, Accessed: May 04, 2020. [Online] http://arxiv.org/abs/1905.06279

[8] K. Li, Y. Liu, M. Seaberg, M. Chollet, T. Weiss, and A. Sakdinawat, "Wavefront preserving and high efficiency diamond grating beam splitter for x-ray free electron laser," *Opt. Express*, vol. 28, no. 8, pp. 10939–10950, Apr. 2020. doi:10.1364/OE.380534

[9] Krzywiński *et al.*, "Q-Switching of X-Ray Optical Cavities by Using Boron Doped Buried Layer Under a Surface of a Diamond Crystal," in *Proc. FEL'19*, Hamburg, Germany, Aug. 2019, pp. 122–125. doi:10.18429/JACoW-FEL2019-TUP033

[10] N.G. Gavrilov, G.N. Kulipanov, V.N. Litvinenko, A.S. Sokolov, and N.A. Vinokurov, "On Mutual Coherency of Spontaneous Radiation from Two Undulators Separated by Achromatic Bend," *IEEE Journal of Quantum Electronics*, vol. 27, no. 12, Dec. 1991, pp. 2566–2568. doi:10.1109/3.104134

[11] R. A. Margraf, X. J. Deng, Z. Huang, J. P. MacArthur, and G. Marcus, "Microbunch Rotation for Hard X-Ray Beam Multiplexing," in *Proc. FEL'19*, Hamburg, Germany, Aug. 2019, pp. 665–668. doi:10.18429/JACoW-FEL2019-THP036

[12] Genesis. Version 1.3. S. Reiche. Available: http://genesis.web.psi.ch/index.html

ISBN: 978-3-95450-213-4 ISSN: 2673-5490 doi:10.18429/JACoW-IPAC2020-WEVIR04

ON-AXIS BEAM ACCUMULATION BASED ON A TRIPLE-FREQUENCY RF SYSTEM

Gang Xu, Shichang Jiang*
Key Laboratory of Particle Acceleration Physics and Technology,
Institute of High Energy Physics, Chinese Academy of Sciences,
University of Chinese Academy of Sciences, 100049 Beijing, China

Abstract

Considering the incompatible off-axis injection scheme on the newly constructed light sources, we have proposed a new on-axis accumulation scheme based on the so-called triple-frequency RF system. By means of additional second harmonic cavities, the original static longitudinal acceptance will be lengthened, which will provide the sufficient time to raise a full-strength kicker pulse. Through imposing the specific restriction on the RF parameters, the final bunch length can also be stretched to satisfy the functions of the conventional bunch lengthening system. In this paper, we will move on to explain how to build this complex triple-frequency RF system, and present the relevant simulation works.

INTRODUCTION

One of the intrinsic characteristics of advanced light sources, is their small dynamic aperture, which brings new challenges for the design of corresponding injection scheme [1]. Due to this specific characteristic, conventional off-axis injection schemes might be incompatible. Several new injection schemes are being designed, in which swap-out injection is a mature case and it will be utilized in the latest light sources [2, 3]. Enlightened by few on-axis injection schemes, we also proposed a new on-axis accumulation scheme, which is based on a triple-frequency RF system, consisting of fundamental, second harmonic and third harmonic cavities [4]. Compared to the conventional bunch lengthening system, normally indicating a double-frequency RF system, the extra harmonic cavities will help lengthen the original static longitudinal acceptance. The local extreme point in the potential curve, corresponding to the fixed point in the longitudinal acceptance, is away from the synchrotron phase. As well as the time interval between the circular bunch and the outermost injection point, we expect this value, employing general lattice parameters of the fourth-generation light sources, could be larger if the "golf club" effect is taken into consideration [5]. Based on the current design, the time interval between this two points, can be lengthened to nearly 2 ns, and this value in the single frequency RF system or the double-frequency RF system is less than 1.5 ns. Furthermore if considering the energy loss per turn is related to the energy spread, this time interval is able to be increased about 10% to 15%. So long as the design of the kicker is compatible with the above time limit, there will not be any disturbance to the circular bunch in the whole injection process. Also the injection can be done in multiturn, when the last injected bunch merged to the synchrotron phase, the next kicker pulse can be raised again. This injection scheme also relieve the design for the booster, if a high charge bunch is needed in the storage ring, and all the RF parameters can remain unchanged during the injection. In this paper, we will explain how to build such triple-frequency RF system, and present the relevant simulation results, in allusion to a typical fourth-generation light source.

* jiangsc@ihep.ac.cn

THE CONSTRUCTION OF THE TRIPLE-FREQUENCY RF SYSTEM

Without radiation damping, the single-particle motion while considering the triple-frequency RF system,

$$H(\phi,\delta;t) = \frac{h_f\omega_0\eta}{2}\delta^2 + \frac{\omega_0 e}{2\pi E_0\beta^2}\Big[\sum_{i=1}^{N_f} V_f^i\cos(\phi+\phi_f^i) + \frac{h_f}{h_1}\sum_{j=1}^{N_{h_1}} V_{h_1}^j\cos(\frac{h_1}{h_f}\phi+\phi_{h_1}^j) + \frac{h_f}{h_2}\sum_{k=1}^{N_{h_2}} V_{h_2}^k\cos(\frac{h_2}{h_f}\phi+\phi_{h_2}^k) + \phi U_0\Big], \tag{1}$$

where ϕ and δ are a pair of canonical variables with respect to the time variable t, $\omega_0 = 2\pi c/C$ is the angular revolution frequency of the synchrotron particle, c is the speed of light, C is the circumference of the storage ring. $\eta = \alpha_c - 1/\gamma^2$, $\beta = \sqrt{1-\gamma^2}$, where α_c is the momentum compaction factor of the storage ring, γ is the relativistic factor. Suppose there are N_f fundamental cavities with a harmonic number h_f, N_{h_1} harmonic cavities with a harmonic number h_1, and N_{h_2} harmonic cavities with a harmonic number h_2. V_f^i, $V_{h_1}^j$ and $V_{h_2}^k$ are the voltages of the i-th fundamental cavity, the j-th 2nd harmonic cavity and the k-th 3rd harmonic cavity respectively. ϕ_f^i, $\phi_{h_1}^j$ and $\phi_{h_2}^k$ are the phases of the synchrotron particle relative to the above cavities.

According to the natural mathematical features of the potential curve, and lengthening the bunch longitudinally, we have several restrictions,

$$P(\phi_b) = P_{max}, P'(\phi_b) = 0, P''(\phi_s) = 0. \tag{2}$$

In which function $P(\phi)$ is the beam potential, ϕ_b is the fixed point in the longitudinal acceptance, corresponding to the

ISBN: 978-3-95450-213-4 ISSN: 2673-5490 doi:10.18429/JACoW-IPAC2020-WEVIR04

local extreme point in $P(\phi)$, and ϕ_s is the synchrotron phase. For easier writing, denoting $\phi_1 = \phi_f$, $\phi_2 = \phi_{h_1}$, $\phi_3 = \phi_{h_2}$, $V_1 = V_f, V_2 = V_{h_1}, V_3 = V_{h_2}$ in a triple-frequency RF system. Combining the above Eq. 1 and Eq. 2, finally we have a unified system of nonlinear equations,

$$\begin{cases} -V_1\cos(\phi_1+\phi_s) - 2V_2\cos(2\phi_s+\phi_2) - 3V_3\cos(3\phi_s+\phi_3) = 0, \\ U_0 - V_1\sin(\phi_1+\phi_s) - V_2\sin(2\phi_s+\phi_2) - V_3\sin(3\phi_s+\phi_3) = 0, \\ U_0 - V_1\sin(\phi_b+\phi_1) - V_2\sin(2\phi_b+\phi_2) - V_3\sin(3\phi_b+\phi_3) = 0, \\ U_0(\phi_b-\phi_s) + V_1(\cos(\phi_b+\phi_1) - \cos(\phi_s+\phi_1)) + \\ \frac{V_2}{2}(\cos(2\phi_b+\phi_2) - \cos(2\phi_s+\phi_2)) + \frac{V_3}{3}(\cos(3\phi_b+\phi_3) - \cos(3\phi_s+\phi_3)) = P_{max}. \end{cases} \tag{3}$$

All the RF parameters are able to be solved from Eq. 3, corresponding to three different frequencies respectively. In the Appendix of [1], we have written down their verbose expressions for reference. Considering the optimal bunch lengthening condition, in which the first and second derivatives of the total voltage are nearly zero, the Taylor expansion to it can be simplified while omitting low order terms. Here we introduce a series of auxiliary quantities χ_i, $i = 0, 1, 2, 3, \cdots, n$, where n is the above harmonic number, $\chi_i = V_{n_i}\cos\phi_{n_i}/(V_1\cos\phi_1)$, and $\chi_0 = V_1\cos\phi_1/(V_1\cos\phi_1) = 1$. How to pick up and combine n is based on the RF system, in which $\{0,1\}$ represents a conventional bunch lengthening system, also the double-frequency RF system. Specifically $\{0,1,2\}$ is our proposed triple-frequency RF system. For a dualistic combination $\{0,n\}$, χ_n has a concise form $\chi_n = -1/n$ with a positive integer n. But for the other multivariate cases, χ_n is unable to be expressed so brief. By means of these auxiliary quantities, we can write down a unified V_z up to third order term, $V_z = (-1 - n_1^3\chi_1^3 - n_2^3\chi_2^3 - n_3^3\chi_3^3 - \cdots)V_1\cos\phi_1/6$. Here for a triple-frequency RF system, the first three terms are kept. Thus the Hamiltonian of single-particle motion with the quartic potential $\mathcal{H} = \alpha c\delta^2/2 + \alpha cqz^4/4$,

$$q = \frac{(-1 - n_1^3\chi_1 - n_2^3\chi_2^3)}{6}\frac{eV_1k_1^3}{\alpha cE_0T_0}\cos\phi_1, \tag{4}$$

and k_1 is the wave number, χ_1, χ_2 are defined before.

Due to the additional degree of freedom in the triple-frequency RF system $\{0,\chi_1,\chi_2\}$, there are indeed lots of combinations. Such as the simplest one, the fundamental, second and third harmonic cavities, denoting it as $\{0,1,2\}$. By that analogy if we increase χ_2, there will be $\{0,1,3\}$, $\{0,2,3\}$, a larger χ_2 will make this problem more complicated. Till now we just consider χ_2 up to 5, for each combination, the above steps are forced to repeat to solve all RF parameters. Figure 1 presents the results for the different combinations, in which x-axis is the time interval between ϕ_b and ϕ_s, and y-axis is the cavity voltage in the fundamental cavity.

From the figure we could find that the other combinations of harmonic number are still applicative, while the remaining combinations, which are not presented in the figure, may not be solvable through our methods. Other combinations compared to $\{0,1,2\}$, their cavity voltages are located in different areas, and obviously the numbers of the solutions

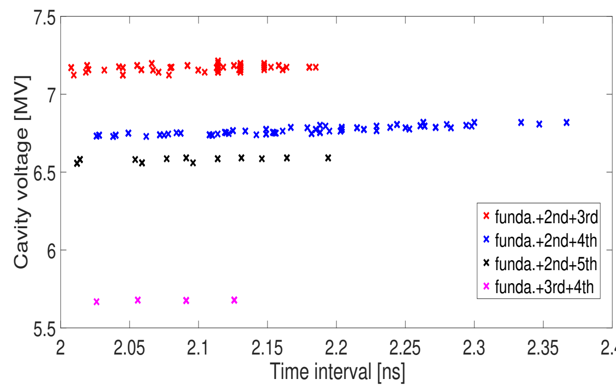

Figure 1: Cavity voltage and time interval between ϕ_b and ϕ_s for the different combinations of harmonic number.

for the first two combinations $\{0,1,2\}$, $\{0,1,3\}$ are much more.

RELEVANT SIMULATION STUDIES

We consider the random noises on the cavity voltages and phases, evaluating the impact to the original injection process. Here we utilize the lattice of High Energy Photon Source (HEPS), the random noises are part of input in the macro-particle simulation, major parameters of HEPS are listed in Table 1 [6].

Figure 2 presents the trajectories of the bunch centroid whether including the random noises in the triple-frequency RF system. Different injection points in the left and right picture, corresponding to dt=0, dp=0 and dt=-2.2 ns, dp=0.03. From the figure the original trajectories are not affected, indicating that no obvious impact to the injection process. In fact, the fundamental cavities are the main power contributor, whether in a double-frequency or a triple-frequency RF system. Energy loss per turn U_0 is larger than 4.3 MeV in HEPS, and a bucket height 3.5% requires more than 7 MV in the fundamental cavities, which may need 5-6 superconducting cavities. For the other harmonic cavites, the designed voltages are only half or less as much, and lesser power exchanges with the beam. Obviously the fundamental cavities are more easily affected and sensitive to the noises.

Figure 3 presents the result whether removing the noises from the fundamental cavities. The right picture only includes the noises on the second and third harmonic cavities, the bunch merges to the synchrotron phase after nearly 10000

ISBN: 978-3-95450-213-4 ISSN: 2673-5490 doi:10.18429/JACoW-IPAC2020-WEVIR04

Table 1: Major parameters of HEPS, noted that energy loss per turn and relevant parameters induced by 14 insertion devices are included, the values are derived from ELEGANT simulation.

Parameter	**Value**	**Unit**
Circumference	1360.4	m
Beam energy	6	GeV
Beam current	200	mA
Natural emittance	26.14	pm
Betatron tunes	114.19/106.18	
Momentum compaction	1.28e-5	
Natural energy spread	1.14e-3	
Energy loss per turn	4.38	MeV
Damping time	7.4/12.4/9.5	ms
Harmonic number	756	
Main RF frequency	166.6	MHz
Main RF cavity voltage	7.16	MV
Second harm. cavity voltage	3.59	MV
Third harm. cavity voltage	0.90	MV
Main RF cavity phase	2.43	rad
Second harm. cavity phase	0.11	rad
Third harm. cavity phase	4.03	rad
Bunch length (no HCs)	2.6	mm
Bunch length with HCs	32.2	mm
Linear synchr. tune (no HCs)	1.2e-3	
Avg. synchr. tune with HCs	7.85e-5	
ID length	84	m
Vacuum chamber radius	3	mm

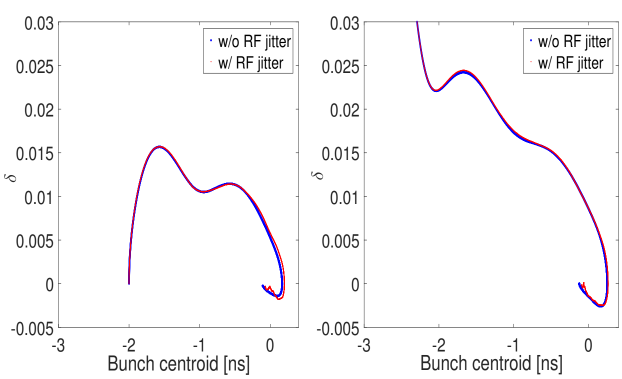

Figure 2: Longitudinal motion of bunch centroid at the presence of noises, injecting at dt=-2 ns, dp=0 (left), and dt=-2.2 ns, dp=0.03 (right), red and blue lines represent the result with and without the noises respectively.

turns and in the next 90000 turns there are only very weak oscillations, less than 0.02 ns from the warm color area. But once adding the noises on the fundamental cavities, in the left picture, the bunch centroid starts irregular oscillations in a larger longitudinal scale, the maximal offset is nearly 0.2 ns.

As for the beam collective instabilities, we investigate the transverse mode-coupling instability (TMCI) using the

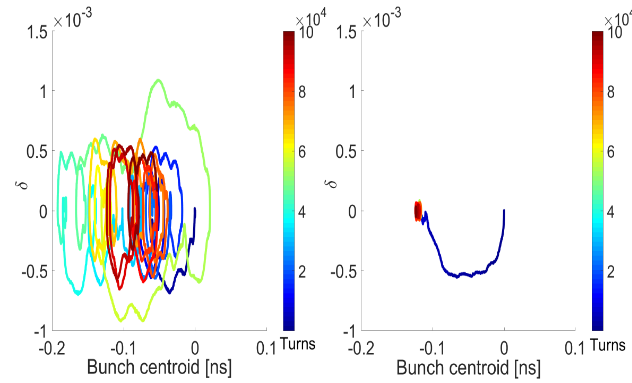

Figure 3: Comparison of the motion of bunch centroid whether removing the noises in the fundamental cavities, in which the picture on the right is after removing.

above triple-frequency RF system. A same numerical method which can refer to [7], numerical analysis results to the TMCI at the presence of the triple-frequency RF system are in Figure 4. Unstable motions will emerge at the

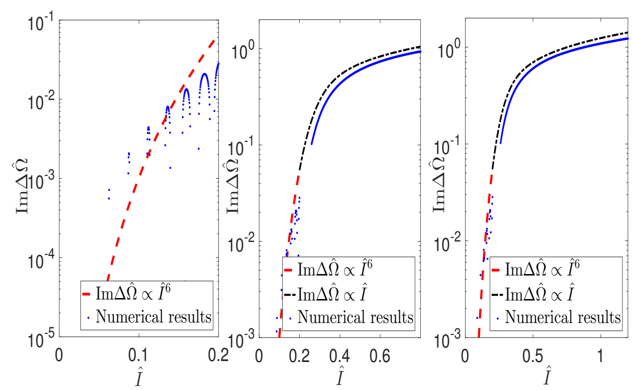

Figure 4: Numerical results and estimated values by scaling law to $\mathrm{Im}\Delta\hat{\Omega}$, representing by blue discrete dots and imaginary lines respectively. Which obeys $\propto \hat{I}^6$ for $\hat{I} < 0.2$ and $\propto \hat{I}$ for greater than 0.2.

convergence of the transverse mode $m = 0$ and $m = 1$, and give the single bunch current threshold I_{th}. The red imaginary line stands for their different asymptotic properties $\mathrm{Im}\Delta\hat{\Omega} \propto \hat{I}^6$ for $\hat{I} < 0.2$, and $\mathrm{Im}\Delta\hat{\Omega} \propto \hat{I}$ for the other side, which is already proposed in M. Venturini's results for the double-frequency RF system. Here we consider this segmented scaling law, and the framework, are still applicative for the triple-frequency RF system.

Simulation results are given by ELEGANT [8] . ILMATRIX gives a single-turn beam transport, the triple-frequency RF system is built through RFCA, and the RW impedance is given in ZTRANVERSE. By means of tuning the single bunch charges, the ever-increasing oscillation of the bunch centroid exactly indicates unstable motion. Thereby the single bunch current threshold, and the growth rates by fitting the growth trajectory of the bunch centroid could be derived. Figure 5 presents the comparison between the estimated values by the scaling law in [7], and the simulation results. The point

ISBN: 978-3-95450-213-4 ISSN: 2673-5490 doi:10.18429/JACoW-IPAC2020-WEVIR04

of intersection with the radiation damping rate, representing by the blue imaginary line, indicates the the single bunch current threshold.

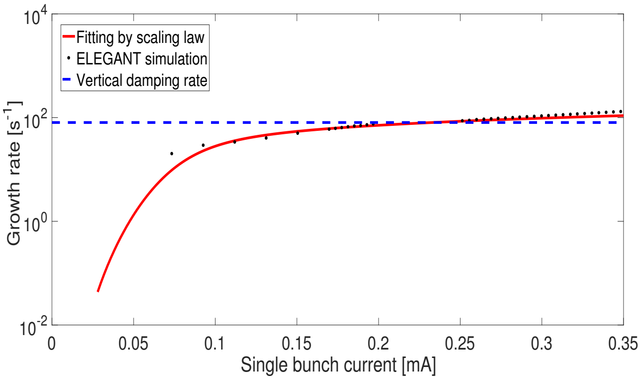

Figure 5: Comparison between ELEGANT simulation and estimated value by fitting scaling law in black dots and red lines, while blue imagnary line indicates vertical damping rate. And the point of intersection nearly 0.23 mA gives single bunch current threshold.

CONCLUSION

The on-axis beam accumulation scheme are given based on a triple-frequency RF system, and we briefly introduce how to build it. In allusion to the noises on the RF system, which may not be influential to the injection. Relevant beam dynamic issues are being studied, the similar analytical method is still applicative compared to the double-frequency RF system. Due to their similar Hamiltonian with the quartic potential in the optimal bunch lengthening condition.

REFERENCES

[1] D. Einfeld *et al.*, "First multi-bend achromat lattice consideratio", *Synchrotron Radiation*, vol. 21, pp. 856-861, 2014. doi:10.1107/S160057751401193X

[2] H. Tarawneh *et al.*, "ALS-II, a Potential Soft X-ray, Diffraction Limited Upgrade of the Advanced Light Source", *Journal of Physics: Conference Series*, vol. 493, p.012020, 2014. doi:10.1088/1742-6596/493/1/012020

[3] M. Borland *et al.*, "Lattice design challenges for fourth-generation storage-ring light sources", *Journal of Synchrotron Radiation*, vol. 21, pp. 912-936, 2014. doi:10.1107/S1600577514015203

[4] S.C. Jiang and G. Xu, "On-axis injection scheme based on a triple-frequency rf system for diffraction-limited storage rings", *Phys. Rev. ST Accel. Beams*, vol. 21, p.110701, 2018. doi:10.1103/PhysRevAccelBeams.21.110701

[5] M. Aiba *et al.*, "Longitudinal injection scheme using short pulse kicker for small aperture electron storage rings", *Phys. Rev. ST Accel. Beams*, vol. 18, p.020701, 2015. doi:10.1103/PhysRevSTAB.18.020701

[6] G. Xu *et al.* "Progress of Lattice Design and Physics Studies on the High Energy Photon Source", in *Proc. 9th Int. Particle Accelerator Conf. (IPAC'18)*, Vancouver, Canada, Apr.-May 2018, pp. 1375-1378. doi:10.18429/JACoW-IPAC2018-TUPMF052

[7] M. Venturini, "Harmonic cavities and the transverse mode-coupling instability driven by a resistive wall", *Phys. Rev. ST Accel. Beams*, vol. 21, p.024402, 2018. doi:10.1103/PhysRevAccelBeams.21.024402

[8] M. Borland, "Elegant: A Flexible SDDS-Compliant Code for Accelerator Simulation", *Tech. Rep. LS-287*, Advanced Photon Source, 2000. doi:10.2172/761286

ISBN: 978-3-95450-213-4 ISSN: 2673-5490 doi:10.18429/JACoW-IPAC2020-WEVIR05

LONGITUDINAL STABILITY WITH LANDAU CAVITIES AT MAX IV

F. J. Cullinan*, Å. Andersson, P. F. Tavares, MAX IV Laboratory, Lund, Sweden

Abstract

The use of Landau cavities was foreseen for both the 1.5 GeV and 3 GeV storage rings at the MAX IV facility from conception. Along with increasing the Touschek lifetime and reducing the emittance degradation due to intrabeam scattering, their purpose is to stabilise the beam in the longitudinal plane. They now play a crucial role in the everyday operation of the two storage rings. This paper outlines the current status and the aspects of longitudinal beam stability that are affected, positively or negatively, by the presence of Landau cavities. Their effectiveness in the two storage rings is also compared.

INTRODUCTION

MAX IV is a synchrotron light source facility in Lund, Sweden. It includes two storage rings: one at 1.5 GeV and another at 3 GeV whose circumference is more than five times larger than the first. A linac injects both rings at full energy and also functions as a light source for the generation of short x-ray pulses. The smaller of the two storage rings has a double-bend achromat lattice while the larger ring, with its multibend-achromat lattice, is a fourth-generation storage ring that is capable of delivering ultrahigh-brightness X-rays because of the low bare-lattice horizontal emittance of 330 pm rad. Both rings operate in top-up during delivery of light to users. Table 1

Table 1: Selected machine parameters of the MAX IV storage rings. The lengths of the lengthened bunches are for 500 mA with flat potential conditions.

Parameter		1.5 GeV Ring	3 GeV Ring
RF frequency	MHz	100	
Landau-cavity harmonic		3	
Design current	mA	500	
Landau-cavity...			
...shunt impedance	MΩ	2.5	
...quality factor		20800	
Main-cavity loaded...			
...shunt impedance	MΩ	0.569	0.310
...quality factor		6760	3690
Natural bunch length	ps	49	40
Lengthened bunch	ps	195	196
Harmonic number		32	176
Momentum compaction		0.000306	0.003055
Bare-lattice energy loss per turn	keV	363.8	114.4
Number of...			
...main cavities		2	5
...Landau cavities		2	3

lists the main parameters of the two storage rings with focus on the RF cavities which are at the same frequency in both rings [1].

Each ring has a double RF system with Landau cavities at the third harmonic of the main RF. The Landau cavities are made of copper, like the main RF cavities, and are passively loaded by the beam itself. In bunch-lengthening mode, the Landau cavities are detuned so that the resonant frequency of their fundamental mode higher than the RF harmonic and to increase or decrease the field level, the detuning is decreased or increased respectively. During operation, autotuning in the low-level RF is used to maintain the cavity voltage at a fixed value [2]. The variation along the bunch of the voltage in the Landau cavities is opposite to that in the main RF cavities so that the total RF voltage is flatter than with a single-RF system. This leads to longer electron bunches which reduces the scattering of electrons within the bunch and this means lower emittance and energy spread and a longer beam lifetime. Furthermore, lengthening the bunches with Landau cavities increases the threshold of certain collective instabilities in both the transverse [3] and longitudinal planes. This paper deals mostly with longitudinal coupled-bunch instabilities in the longitudinal plane, which are the dominant instabilities in both storage rings at MAX IV. These are driven by higher-order modes (HOMs) in the main and Landau cavities, which have no HOM dampers. Landau-cavity bunch lengthening is advantageous in this regard because of two reasons. The first is that the longer bunches have lower form-factors at the frequencies of the higher-order modes and so excite them less strongly. The second is the large spread in the synchrotron tune within the bunches, which means Landau damping of collective instabilities.

The two storage rings at MAX IV present a rare opportunity because the impedances driving the dominant instability in each ring are so similar, differing only in magnitude due to the different cavity numbers. Furthermore, the two rings have been commissioned and ramped in current more or less simultaneously and the observation of longitudinal instabilities during this time differed considerably. A comparison of the current statuses of the two rings in terms of longitudinal stability is listed in Table 2.

LONGITUDINAL STABILITY

This section summarises the different issues in the two storage rings that affect the longitudinal stability and how they are dealt with.

Robinson Mode Coupling

For bunch lengthening, Landau cavities must be tuned slightly higher than the third harmonic of the main RF. At this frequency, they destabilise the Robinson dipole and

* francis.cullinan@maxiv.lu.se

ISBN: 978-3-95450-213-4 ISSN: 2673-5490 doi:10.18429/JACoW-IPAC2020-WEVIR05

Table 2: Comparison of the statuses of the two MAX IV storage rings in terms of longitudinal stability. The delivery current in the 1.5 GeV ring is limited by heating of beamline components while in the 3 GeV ring, it is limited by the available RF power.

Ring		1.5 GeV	3 GeV
Delivery current		400	250
Stable current range	mA	130-500	57–250
Temperature tuning		Minimal	Extensive
Longitudinal feedback		None	Mode-0 phase
Fill pattern		Uniform	Short gap

quadrupole modes (all bunches moving in unison). However, more than enough Robinson damping comes from the main cavities, which are tuned to below the RF generator frequency to match the beam-loaded cavity to the RF transmitter, so that the Robinson dipole and quadrupole modes are stable. However, as the Landau cavities are tuned closer to the third RF harmonic, increasing the field amplitudes and lengthening the bunches, the frequency of the Robinson quadrupole mode decreases while the frequency of the Robinson dipole mode stays roughly constant. This was measured in the two storage rings and compared with theory, as shown in Fig. 1 for the 1.5 GeV ring and Fig. 2 for the

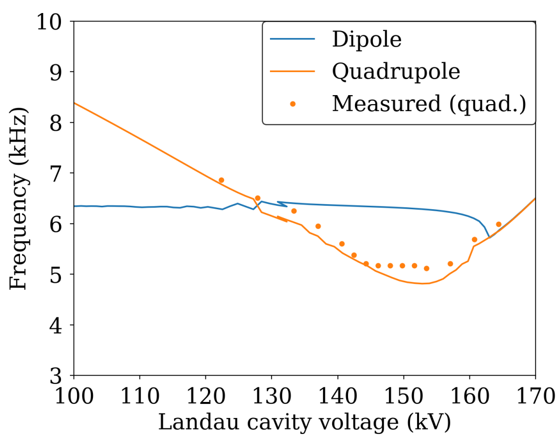

Figure 1: Measured Robinson mode detuning in the 1.5 GeV ring in comparison to the theoretical prediction shown by the solid lines.

3 GeV ring, where the measured energy spread is also shown to show the stability of the beam.

In both rings, it can be seen that at a certain point, which is just before the total RF voltage is fully flattened (zero first derivative at the synchronous phase), the frequencies of the two modes meet. In the 3 GeV ring, a fast-growing coupled Robinson mode instability is observed and so a mode-0 phase feedback [4] was installed for active damping. In the 1.5 GeV ring, on the other hand, no such coupling instability is observed. The most probable reason for this is the excess Robinson damping of the dipole mode in the

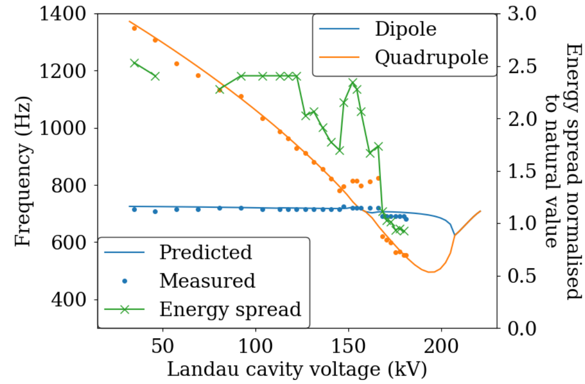

Figure 2: Measured Robinson mode detuning in the 3 GeV ring in comparison to the theoretical prediction shown by the solid lines with the energy spread also shown.

1.5 GeV ring, which is around 100 times faster than in the 3 GeV ring due to the different optimum detuning of the main cavities. This is also thought to be one reason why it was difficult to measure the dipole mode frequency during the experiment in the 1.5 GeV ring. In both rings, the agreement with theory [5] is good, although the horizontal axes for the experimental data had to be rescaled in both cases, most likely due to an error in the calibration of the Landau-cavity fields.

Coupled-bunch Modes

Coupled-bunch modes other than the Robinson mode are typically driven by higher-order modes in the cavities. In the absence of HOM dampers, it is important to try to tune the higher-order modes away from the revolution harmonics. At MAX IV, this has been done using temperature tuning, and again, a large difference was seen between the two rings in terms of the extent to which temperature tuning was necessary, as mentioned in Table 2. One useful tool in the temperature tuning process is transient measurements using the bunch-by-bunch (BBB) feedback system: grow/damp measurements or drive/damp measurements [6]. These are performed above and below the instability threshold respectively and are both ways to directly measure the growth rate of coupled-bunch modes. In the latter case, one coupled-bunch mode is driven by the actuator in the BBB system, which simultaneously damps all other coupled-bunch modes. Then, both the drive and the damping are turned off for a short period (typically ~100 ms) during which time the excited coupled-bunch mode is left to decay at its characteristic rate. In the case of a grow/damp measurement, the spontaneous growth of the least-stable coupled-bunch modes are simply measured above threshold when the longitudinal BBB feedback is switched off for a similarly short period.

Figures 3 and 4 each show the results of drive/damp measurements on a pair of coupled-bunch modes (since the HOM that drives one coupled-bunch mode will damp that mode's complement) in each storage ring. Coupled-bunch mode 167

ISBN: 978-3-95450-213-4 ISSN: 2673-5490 doi:10.18429/JACoW-IPAC2020-WEVIR05

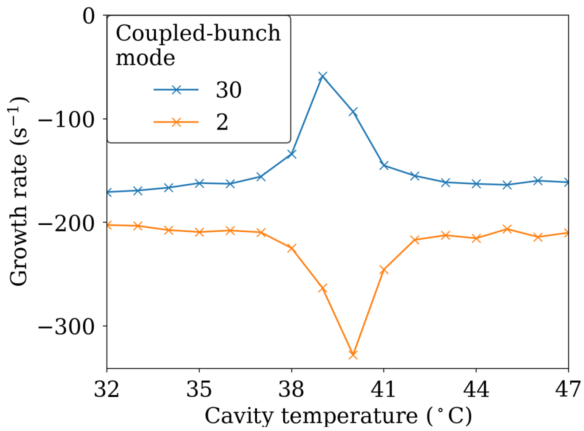

Figure 3: Results of drive/damp measurements of coupled-bunch mode 30 and its complement mode 2 in the 1.5 GeV ring for different temperatures of one of the main cavities.

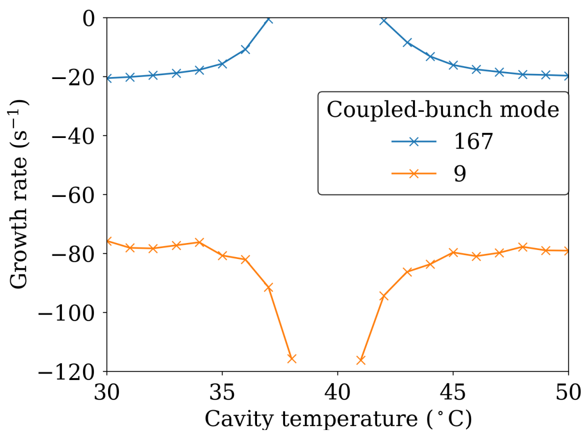

Figure 4: Results of drive/damp measurements of coupled-bunch mode 167 and its complement mode 9 in the 3 GeV ring for different temperatures of one of the main cavities. Data is not shown for coupled-bunch mode 167 at temperatures where it was above threshold and for mode 9, where the BBB feedback was unable to keep the beam stable when on.

in the 3 GeV ring and coupled-bunch mode 30 in the 1.5 GeV ring are both driven by the same HOM which exists in all of the main cavities. Furthermore, these coupled-bunch modes can have very fast growth-rates in both rings when the HOM is tuned close to its nearest revolution harmonic.

As shown in the figures, the drive/damp measurements were performed for different temperatures of a single cavity in each ring. A clear dependence can be seen and the temperatures at which the HOM is resonant, identified. The cavity in question should be run at a temperature that is sufficiently far from this temperature. However, care must also be taken to ensure that the temperature chosen does not bring another mode closer to resonance. Drive/damp measurements are just one way in which the best temperature for a given cavity can be chosen. However, they are limited to modes whose decay differs sufficiently from the radiation damping rate to be measured above the noise and they must be performed at low current, where all coupled-bunch modes are below threshold.

Landau-cavity Tuning

If the harmful HOMs are sufficiently tuned away from the revolution harmonics and there is no risk of a Robinson (mode-coupling) instability, it is possible to stabilise the beam by increasing the fields in the Landau cavities. It is possible to achieve partial stabilisation, where the saturation amplitude of coupled-bunch modes is kept low enough so that the effect on the energy spread is small, or full stabilisation, where the lowest instability threshold is raised to above the stored current. These two situations, though conceptually distinct, can be indistinguishable from the point of view of experimental users.

Experiments have been performed to demonstrate Landau-cavity stabilisation in both rings at MAX IV and here, the results of one such experiment in the 3 GeV ring are presented. The machine was set up with a main RF voltage of 1.045 MV so that full flat potential [7] could be obtained at 149 mA with three passively-driven Landau cavities. Starting from an unstable beam and a uniform machine fill (as opposed to the nonuniform fill used during delivery) at this current, the fields in the Landau cavities were increased gradually, pausing at different steps to measure the energy spread. The results are shown in Fig. 5.

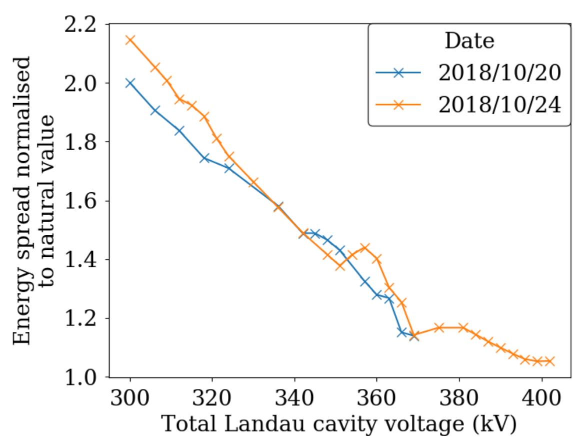

Figure 5: Measured energy spread in uniform fill at 149 mA in the 3 GeV ring as the total Landau-cavity voltage is increased.

As the Landau-cavity field is increased, the coupled-bunch modes that are present begin to saturate at lower amplitudes because of the increased nonlinearity of the RF potential containing the bunches. This continues until the energy spread roughly reaches the level of the natural energy spread. In the 3 GeV ring at lower currents and in the 1.5 GeV ring up to 500 mA, the beam eventually becomes stable with no coupled-bunch modes detected. However, in the 3 GeV ring

ISBN: 978-3-95450-213-4 ISSN: 2673-5490 doi:10.18429/JACoW-IPAC2020-WEVIR05

at this current and above, a slow-oscillating coupled-bunch mode is observed that persists until the Landau cavities are too close to resonance and the growth rate of the Robinson dipole mode exceeds the damping provided by the mode-0 phase feedback. These slow-oscillating coupled bunch modes have very large amplitudes in phase but, because their oscillation period is longer than the radiation damping time, there is no increased energy spread between bunches, which is why there is no increase in energy spread where they appear in Fig. 5. Nevertheless, it has been observed that these slow-oscillating coupled-bunch modes still degrade the quality of light delivered to the beamlines, perhaps indirectly through the phase sensitivity of BPMs disrupting the slow-orbit feedback. For this reason, a nonuniform fill pattern is used in the 3 GeV ring during delivery of light to users. A nonuniform fill improves the stability at high Landau-cavity fields and prevents the appearance of slow-oscillating coupled-bunch modes. The disadvantage of a nonuniform fill is that the bunch-lengthening of the Landau cavities is less effective and this is worse for the beam lifetime and intrabeam scattering. The effect of a nonuniform fill on coupled-bunch instabilities has been well documented in the past [8–11] and the subject continues to be studied at MAX IV, both in terms the static effects of transient beam loading [12] and coupled-bunch modes [13].

DISCUSSION AND CONCLUSION

To explain the difference in behaviour between the two storage rings at MAX IV, it is sufficient to mention the following four points. Firstly, the Robinson damping in the 1.5 GeV ring is faster then in the 3 GeV ring because of the tuning of the main cavities, which as mentioned, is chosen to match the beam-loaded cavity to the RF transmitter. Secondly, the radiation damping is also faster. Thirdly, the 1.5 GeV ring has a lower narrowband impedance because it has fewer cavities and finally, it has a larger revolution frequency. This last point means that it is easier to tune all of the harmful higher-order modes away from the revolution harmonics because they are further apart in frequency.

The comparison is very different when carried out in terms of total charge stored, which is five and a half times larger in the 3 GeV ring for the same beam current. However, it would then make more sense to compare the impedances per unit length in the two rings, of which the lower is in the 3 GeV ring. The comparison of the radiation damping time should then be done in turns instead of absolute time and this is also lower in the 3 GeV ring. The Robinson damping time still corresponds to fewer turns in the 1.5 GeV ring but is a larger factor of the Robinson damping time in the 3 GeV ring. Beyond convention, one good reason for comparing the two rings in terms of beam current up until this point is because it is a parameter for which the design value is the same in both rings.

In any case, Landau cavities play a crucial role in the delivery of light to users in both storage rings at MAX IV. A longitudinally-stable beam has been achieved in the the 1.5 GeV ring for a larger range of currents that includes the design current of 500 mA. With its two storage rings with similar RF systems, the MAX IV laboratory presents a rare opportunity to compare the behaviour of HOM-driven coupled-bunch modes in different-size storage rings and such a comparison has now been carried out.

ACKNOWLEDGEMENTS

The authors would like to thank Robert Bosch for his help with the Robinson mode-coupling measurements, theory and related discussion.

REFERENCES

[1] P. F. Tavares, S. C. Leemann, M. Sjöström, and Å. Andersson, “The MAXIV storage ring project,” *Journal of Synchrotron Radiation*, vol. 21, no. 5, pp. 862–877, Sep. 2014. DOI: 10.1107/S1600577514011503. https://doi.org/10.1107/S1600577514011503

[2] A. Salom *et al.*, “Digital LLRF for MAX IV,” in *8th International Particle Accelerator Conference*, 2017, THPAB135. DOI: 10.18429/JACoW-IPAC2017-THPAB135.

[3] F. J. Cullinan, R. Nagaoka, G. Skripka, and P. F. Tavares, “Transverse coupled-bunch instability thresholds in the presence of a harmonic-cavity-flattened RF potential,” *Phys. Rev. Accel. Beams*, vol. 19, p. 124 401, Dec. 2016. DOI: 10.1103/PhysRevAccelBeams.19.124401. https://link.aps.org/doi/10.1103/PhysRevAccelBeams.19.124401

[4] D. P. McGinnis, “Beam Stabilization and Instrumentation Systems based on Internet of Things Technology,” in *Low-Level Radio Frequency Workshop*, Oct. 2019. arXiv: 1910.07822.

[5] R. A. Bosch, K. J. Kleman, and J. J. Bisognano, “Robinson instabilities with a higher-harmonic cavity,” *Phys. Rev. ST Accel. Beams*, vol. 4, p. 074 401, Jul. 2001. DOI: 10.1103/PhysRevSTAB.4.074401. https://link.aps.org/doi/10.1103/PhysRevSTAB.4.074401

[6] D. Teytelman, “Architectures and algorithms for control and diagnostics of coupled bunch instabilities in circular accelerators,” Other thesis, Jun. 2003.

[7] P. F. Tavares, Å. Andersson, A. Hansson, and J. Breunlin, “Equilibrium bunch density distribution with passive harmonic cavities in a storage ring,” *Phys. Rev. ST Accel. Beams*, vol. 17, p. 064 401, Jun. 2014. DOI: 10.1103/PhysRevSTAB.17.064401. https://link.aps.org/doi/10.1103/PhysRevSTAB.17.064401

[8] G. Bassi, A. Blednykh, and V. Smaluk, “Self-consistent simulations and analysis of the coupled-bunch instability for arbitrary multibunch configurations,” *Phys. Rev. Accel. Beams*, vol. 19, p. 024 401, Feb. 2016. DOI: 10.1103/PhysRevAccelBeams.19.024401. https://link.aps.org/doi/10.1103/PhysRevAccelBeams.19.024401

[9] K. A. Thompson and R. D. Ruth, “Transverse and longitudinal coupled bunch instabilities in trains of closely spaced bunches,” in *Proceedings of the 1989 IEEE Particle Accelerator Conference: Accelerator Science and Technology*, Mar. 1989, 792–794 vol.2. DOI: 10.1109/PAC.1989.73251.

[10] O. Naumann and J. Jacob, “Fractional filling induced Landau damping of longitudinal instabilities at the ESRF,” in *Proceedings of the 1987 Particle Accelerator Conference*, 1987, pp. 1551–1553.

ISBN: 978-3-95450-213-4 ISSN: 2673-5490 doi:10.18429/JACoW-IPAC2020-WEVIR05

[11] K. A. Wang, P. J. Chou, and A. W. Chao, "Study of nonuniform fills to cure the coupled-bunch instability in SRRC," in *Proceedings of the 2001 Particle Accelerator Conference*, 2001, pp. 1981–1983.

[12] T. Olsson, F. J. Cullinan, and Å. Andersson, "Self-consistent calculation of transient beam loading in electron storage rings with passive harmonic cavities," *Phys. Rev. Accel. Beams*, vol. 21, p. 120 701, Dec. 2018. DOI: 10.1103/PhysRevAccelBeams.21.120701. https://link.aps.org/doi/10.1103/PhysRevAccelBeams.21.120701

[13] F. J. Cullinan, Å. Andersson, and P. F. Tavares, "Harmonic-cavity stabilisation of longitudinal coupled-bunch instabilities with a nonuniform fill," Submitted to Phys. Rev. Accel. Beams, 2020.

ISBN: 978-3-95450-213-4 ISSN: 2673-5490 doi:10.18429/JACoW-IPAC2020-WEVIR06

HOLLOW ELECTRON BEAMS IN A PHOTOINJECTOR

A. Halavanau[1], C. Mayes[1], Y. Ding[1], S. Baturin[2], P. Piot[2,3]
[1]SLAC National Accelerator Laboratory, Menlo Park, CA 94025, USA
[2]Northern Illinois University, DeKalb, IL 60115, USA
[3]Argonne National Laboratory, Lemont, IL 60439, USA

Abstract

Photoinjectors have demonstrated the capability of electron beam transverse tailoring, enabled by microlens array (MLA) setups. For instance, electron beams, transversely segmented into periodic beamlet formations, were successfully produced in several experiments at Argonne Wakefield Accelerator (AWA). In this proceeding, we discuss the necessary steps to demonstrate the hollow electron beam generation, with an arbitrary diameter and width with MLAs. We also present beam dynamics simulations and highlight key features of the hollow beam transport in LCLS copper linac.

INTRODUCTION

Hollow electron beams have been well known since 1960s, but due to multiple instabilities pointed out by early researchers [1–12] they have been largely forgotten. Nowadays, the most promising application of the hollow electron beams is proton beam collimation. This novel technique is soon to be implemented at Fermilab Accelerator Science and Technology (FAST) facility and later on at the Large Hadron Collider (LHC) [13–17]. The required hollow electron beams are generated in a special low energy source, mostly incompatible with a conventional accelerator. In this proceeding, we are exploring a different approach. We consider a nominal photoinjector configuration, e.g., the LCLS copper linac photoinjector, and modify the UV laser transverse profile employing spatial shaping techniques [18, 19]. Typically, transverse shaping is performed at some point upstream of the photocathode, which is then imaged onto the photocathode surface with a transport lens system. With the MLA shaping, for instance, one can apply a circular intensity mask at the homogenization point of the MLA, thus controlling parameters of the hollow beam. Other possibilities include the use of digital micromirror devices, axicon lenses, and more exotic Laguerre-Gaussian (LG_{0i}) modes of the laser.

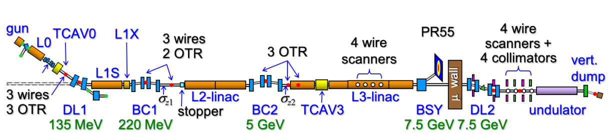

Figure 1: LCLS copper linac hard X-ray beamline.

LCLS PHOTOINJECTOR AND COPPER LINAC SIMULATION

In this section we provide the results of numerical beam dynamics simulations of the entire LCLS copper linac hard X-ray (HXR) beamline, starting at the photocathode, and up to the HXR undulator entrance. LCLS copper linac photoinjector is a 135 MeV machine that comprises of 1.6 cell S-band RF gun with copper cathode and is operating at 120 Hz repetition rate. It is followed by multiple normal conducting travelling wave S-band accelerating structures. For a detailed description of the machine see Ref. [20]. Currently the primary purpose of the LCLS copper linac photoinjector is to produce electron beams for LCLS XFEL operations. The 135 MeV electron beam is then further accelerated in 1 km long linac with the total maximum energy of 14 GeV. We performed our hollow beam numerical study in the LCLS copper linac at a 7.5 GeV beam energy. We note that in the photoinjector the beam is matched into the copper linac via a quadrupole lattice, yielding several betatron oscillations in both vertical and horizontal planes. According to previous studies, such oscillations, in combination with space-charge forces, often lead to a hollow beam break up. An overall layout of the beamline is reported in Fig. 1 and a typical beam envelope evolution in the LCLS photoinjector is presented in Fig. 2. We point out that the nature of instability, destroying the hollow shape, is similar to the one observed in recent coherent electron cooling studies (CeC) at Brookhaven National Laboratory [21]. For our studies we utilized conventional IMPACT-T beam physics code [22]. A detailed description of IMPACT-T 3D space-charge algorithm and it's comparison to other codes is available in Refs. [23–25]. As a guidance for initial simulation, the bunch charge was defined as

$$Q = 9\ \text{pC} \cdot \eta \frac{E_z}{\text{MV/m}} \frac{A}{\text{mm}^2} \tag{1}$$

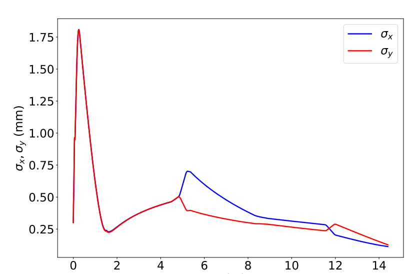

Figure 2: A typical electron beam size evolution in LCLS copper linac photoinjector.

ISBN: 978-3-95450-213-4 ISSN: 2673-5490 doi:10.18429/JACoW-IPAC2020-WEVIR06

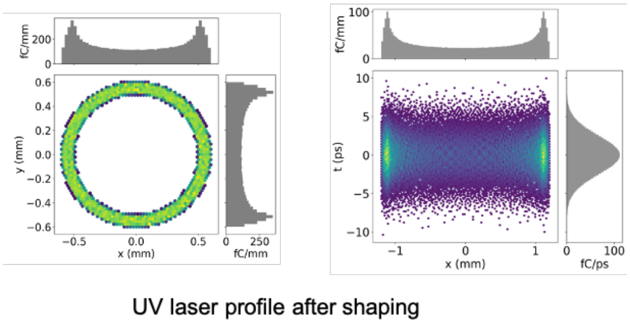

Figure 3: Transverse and longitudinal phase-space of the hollow UV laser beam at LCLS photocathode.

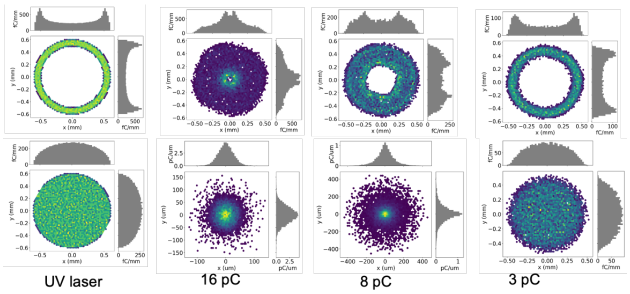

Figure 4: Hollow beam shown in Fig. 3, propagated to the injector exit with the fixed lattice parameters as a function of charge and comparison to a uniform beam of the same charge.

where E_z is the accelerating gradient in the gun, A is the illuminated area on the photocathode, and η is the efficiency parameter [26]. An example of a simulated hollow beam profile is displayed in Fig. 3. The outer radius of the hollow is 0.6 mm, and the thickness is 0.1 mm. We specified the Twiss parameters required for matched beam orbit in the LCLS copper linac and propagated hollow beams of various charges. We established, via numerical simulations, the value of a hollow beam charge, where it becomes free of space-charge instabilities to be about 3 pC. The results are summarized in Fig. 4. Interestingly, the final transverse distribution is almost identical to the one on the cathode.

It is important to point out that throughout the injector, the hollow beam transverse shape changes from round to elliptical and back to round, according to the lattice beta functions; see Figs. 2–5. During this process, the transverse charge density fluctuates along the hollow beam, until it becomes uniform again at the copper linac injection point.

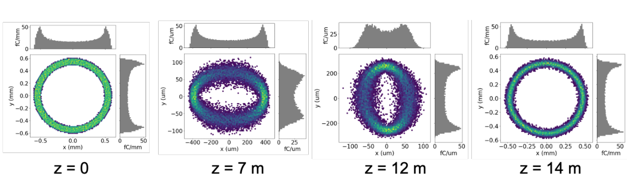

Figure 5: Evolution of the Q = 3 pC charge as a function of distance in the LCLS copper linac injector.

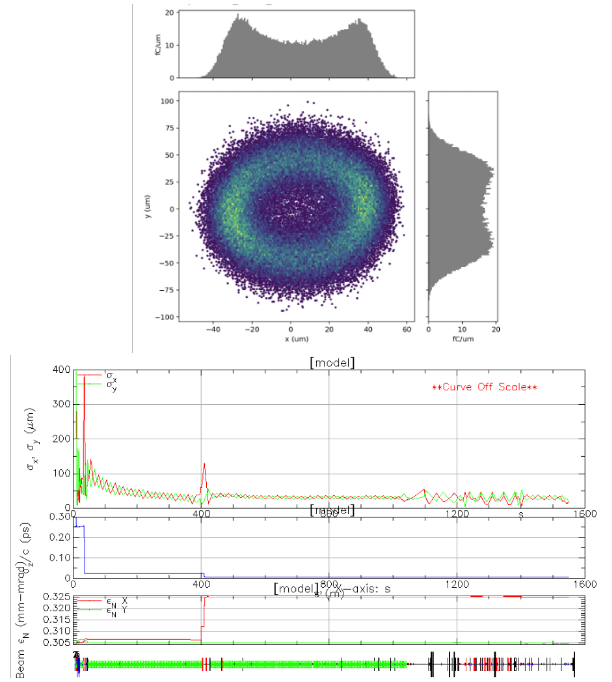

Figure 6: Matched 7.5 GeV hollow beam in the LCLS copper linac propagated up to HXR undulator entrance. The simulation was done in ELEGANT [27] and *Bmad* [28] and yielded almost identical results.

Finally, we sent the injector-made hollow beam into a nominal LCLS copper linac lattice. To gain confidence in the simulation, we used two codes: ELEGANT [27] and *Bmad* [28] with identical lattices, including Coherent Synchrotron Radiation (CSR) and wakefield effects, yeilding almost identical results. The resulting beam envelope and transverse charge density distribution at HXR undulator entrance are presented in Fig. 6. The hollow beam size is effectively demagnified by a factor of 10 compared to the initial laser profile at the cathode. The latter finding is quite remarkable but expected, because the space-charge forces are significantly suppressed at high beam energies.

LUME-IMPACT BEAM DYNAMICS PACKAGE

In order to rapidly prototype and optimize hollow beam simulations for LCLS copper linac photoinjector, we have utilized LUME-IMPACT package [29]. This software includes a collection of helper functions to the conventional PIC code IMPACT-T, that allows easy modification of initial particle distribution, gun and linac phase optimization, and fast beam trajectory matching. In combination with the precision and accuracy of IMPACT-T, we quickly established the range of accelerator parameters, allowing for a hollow beam to be propagated downstream of the injector distortion-free. We have also used initial particle distribution generator DISTGEN package [30] to probe different distributions, and the OPENPMD-BEAMPHYSICS package [31] for handling and plotting simulation results.

ISBN: 978-3-95450-213-4 ISSN: 2673-5490 doi:10.18429/JACoW-IPAC2020-WEVIR06

SUMMARY

We have presented the results of numerical beam dynamics simulation of a hollow electron beam in LCLS copper linac beamline, generated with a transverse UV laser mask. The simulation shows that the beam is only stable at the very low charge values, where the beam becomes emittance-dominated. This however makes hollow electron beams a perfect candidate for beam-based studies. We will report the results of the practical hollow beam applications elsewhere in the near future.

ACKNOWLEDGMENTS

A. Halavanau would like to thank C. Pellegrini and E. Hemsing (SLAC) for many discussions on the historical and practical aspects of hollow electron beam research. Work was supported by the U.S. Department of Energy Contract No. DE-AC02-76SF00515.

REFERENCES

[1] D. Keefe *et al.*, "Experiments on forming, compressing and extracting electron rings for the collective acceleration of ions," *Nuclear Instruments and Methods*, vol. 93 issue 3, pp. 541–556, 1971. doi:10.1016/0029-554X(71)90079-6

[2] D. Keefe, "Particle acceleration by collective effects," in *Proc. Proton Linear Accelerator Conference 1976*, Chalk River, ON, Canada, Sep. 1976, paper F08, pp. 352–357, AECL–5677, S.O. Schriber, (Ed.), Canada. http://jacow.org/l76/papers/f08.pdf

[3] J. D. Lawson, "Electron ring accelerators a cheap path to very high energy protons?", *Nature*, vol. 218, pp. 430–433, May 1968. doi:10.1038/218430a0

[4] C. Pellegrini and A. Sessler, "Lower bounds on ring self-focusing so as to maintain ring integrity during spillout and subsequent acceleration", 1969, Research Org.: Lawrence Berkeley National Lab. (LBNL), Berkeley, CA, USA).

[5] R. Baartman and S. R. Koscielniak, "Stability of hollow beams in longitudinal phase space", *Part. Accel.*, vol. 28, pp. 95–99, 1990. http://cds.cern.ch/record/204038/files/p95.pdf

[6] S. Koscielniak, "Simulation of hollow beams with cancellation of steady state nonlinear space-charge", in *Proc. PAC'91*, San Francisco, CA, USA, vol. 3, pp. 1728–1730, 1991. doi:10.1109/PAC.1991.164759

[7] T. Weiland, "Wake field work at DESY", *IEEE Trans. Nucl. Sci.*, vol. 32, pp. 3471–3475, 1985. doi:10.1109/TNS.1985.4334400

[8] N. Holtkamp, P. Schutt, R. Wanzenberg, T. Weiland, W. Bialowons, M. Bieler, F.J. Decker, and H.C. Lewin, "A strong focussing scheme for hollow beams in the RWT-Collider", in *Proc. EPCA'90*, Nice, France, pp. 673–675, Jun. 1990. http://jacow.org/e90/PDF/EPAC1990_0673.PDF

[9] W. Bialowons *et al.*, "Wake Field Acceleration", In *Proc. LINAC'86*, Stanford, CA, USA, paper TH1–3, pp. 398–404, 1986. http://jacow.org/l86/papers/th1-3.pdf

[10] F.J. Decker *et al.*, "Measurements of the hollow beam at the wake field transformer experiment at DESY", in *Proc. EPCA'90*, Nice, France, pp. 613–615, Jun. 1990. http://jacow.org/e88/PDF/EPAC1988_0613.PDF

[11] W. Bialowons *et al.*, "The wake field transformer experiment at DESY", in *Proc. New Developments in Particle Acceleration Techniques*, CERN-87-11, pp. 298-307, Orsay, France, 1987. https://cds.cern.ch/record/182997/files/CERN-87-11-V-1.pdf

[12] W. Liu and W. Gai, "Wakefield generation by a relativistic ring beam in a coaxial two-channel dielectric loaded structure", *Phys. Rev. ST Accel. Beams*, vol. 12, p. 051301, May 2009. doi:10.1103/PhysRevSTAB.12.051301

[13] V. D. Shiltsev, *Electron Lenses for Super-Colliders*, series: Particle Acceleration and Detection, New York, NY, USA: Springer-Verlag, New York, 2016. doi:10.1007/978-1-4939-3317-4

[14] X. Gu *et al.*, "Electron lenses for head-on beam-beam compensation in RHIC", *Phys. Rev. Accel. Beams*, vol. 20, p. 023501, Feb 2017. doi:10.1103/PhysRevAccelBeams.20.023501

[15] V. Shiltsev, Y. Alexahin, A. Burov, and A. Valishev, "Landau damping of beam instabilities by electron lenses", *Phys. Rev. Lett.*, vol. 119, p. 134802, Sep 2017. doi:10.1103/PhysRevLett.119.134802

[16] G. Stancari, A. Valishev, G. Annala, G. Kuznetsov, V. Shiltsev, D. A. Still, and L. G. Vorobiev, "Collimation with hollow electron beams", *Phys. Rev. Lett.*, vol. 107, p. 084802, Aug 2011. doi:10.1103/PhysRevLett.107.084802

[17] G. Stancari, V. Previtali, A. Valishev, R. Bruce, S. Redaelli, A. Rossi, and B. Salvachua Ferrando, "Conceptual design of hollow electron lenses for beam halo control in the Large Hadron Collider", 2014. arXiv:1405.2033

[18] A. Halavanau, Q. Gao, M. Conde, G. Ha, P. Piot, J.G. Power, and E. Wisniewski, "Tailoring of an Electron-Bunch Current Distribution via Space-to-Time Mapping of a Transversely-Shaped Photoemission-Laser Pulse", *Phys. Rev. Accel. Beams*, vol. 22, p. 114401, 2019. doi:10.1103/PhysRevAccelBeams.22.114401

[19] S. Li *et al.*, Ultraviolet laser transverse profile shaping for improving x-ray free electron laser performance. *Phys. Rev. Accel. Beams*, vol. 20, p. 080704, Aug 2017. doi:10.1103/PhysRevAccelBeams.20.080704

[20] R. Akre *et al.*, "Commissioning the linac coherent light source injector", *Phys. Rev. ST Accel. Beams*, vol. 11, p. 030703, Mar 2008. doi:10.1103/PhysRevSTAB.11.030703

[21] V. Litvinenko *et al.*, "Coherent Electron Cooling Experiment at RHIC: Status and Plans", in *Proc. COOL'19*, Novosibirsk, Russia, Sep. 2019, pp. 35–40, doi:10.18429/JACoW-COOL2019-TUZ01

[22] Ji Qiang, S. Lidia, R.D. Ryne, and C. Limborg-Deprey, "Three-dimensional quasistatic model for high brightness beam dynamics simulation", *Phys. Rev. ST Accel. Beams*, vol. 9, p. 044204, 2006. doi:10.1103/PhysRevSTAB.10.129901
Erratum: *Phys. Rev. ST Accel. Beams*, vol. 10, p. 129901, 2007. doi:10.1103/PhysRevSTAB.9.044204

ISBN: 978-3-95450-213-4 ISSN: 2673-5490 doi:10.18429/JACoW-IPAC2020-WEVIR06

[23] Ji Qiang, R. D. Ryne, S. Habib, and V. Decyk, "An object-oriented parallel particle-in-cell code for beam dynamics simulation in linear accelerators", *J. Comput. Phys.*, vol. 163, pp. 434–451, 2000. doi:10.1006/jcph.2000.6570

[24] Ji Qiang, S. Lidia, R. D. Ryne, and C. Limborg-Deprey, "Three-dimensional quasistatic model for high brightness beam dynamics simulation", *Phys. Rev. ST Accel. Beams*, vol. 9, p. 044204, Apr 2006. doi:10.1103/PhysRevSTAB.10.129901

[25] C. E. Mayes, R. D. Ryne, and D. Sagan, "3D Space Charge in Bmad", in *Proc. IPAC'18*, Vancouver, Canada, Apr.-May 2018, pp. 3428–3430. doi:10.18429/JACoW-IPAC2018-THPAK085

[26] I. V. Bazarov, B. M. Dunham, and C. K. Sinclair, "Maximum achievable beam brightness from photoinjectors", *Phys. Rev. Lett.*, vol. 102, p. 104801, Mar 2009. doi:10.1103/PhysRevLett.102.104801

[27] M. Borland, "elegant: A Flexible SDDS-Compliant Code for Accelerator Simulation", in *Proc. 6th Int. Computational Accelerator Physics Conference (ICAP'00)*, Darmstadt, Germany, September 11-14, 2000. doi:10.2172/761286

[28] D. Sagan, "Bmad: A relativistic charged particle simulation library", *Nucl. Instrum. Meth. A*, vol. 558, pp. 356–359, 2006. doi:10.1016/j.nima.2005.11.001

[29] C. Mayes, "lume-impact package", https://github.com/ChristopherMayes/lume-impact

[30] C. Mayes and C. Gulliford, "distgen package", https://github.com/ColwynGulliford/distgen

[31] C. Mayes, "openPMD-beamphysics package", https://github.com/ChristopherMayes/openPMD-beamphysics

ISBN: 978-3-95450-213-4 ISSN: 2673-5490 doi:10.18429/JACoW-IPAC2020-WEVIR10

ADAPTIVE FEEDBACK AND MACHINE LEARNING FOR PARTICLE ACCELERATORS *

Alexander Scheinker†, Los Alamos National Laboratory, Los Alamos, NM, USA

Abstract

The precise control of charged particle beams, such as an electron beam's longitudinal phase space as well as the maximization of the output power of a free electron laser (FEL), or the minimization of beam loss in accelerators, are challenging tasks. For example, even when all FEL parameter set points are held constant both the beam phase space and the output power have high variance because of the uncertainty and time-variation of thousands of coupled parameters and of the electron distribution coming off of the photo cathode. Similarly, all large accelerators face challenges due to time variation, leading to beam losses and changing behavior even when all accelerator parameters are held fixed. We present recent efforts towards developing machine learning methods along with automatic, model-independent feedback for automatic tuning of charge particle beams in particle accelerators. We present experimental results from the LANSCE linear accelerator at LANL, the EuXFEL, AWAKE at CERN, FACET-II and the LCLS.

INTRODUCTION

Particle accelerators are complex systems with many coupled components including hundreds of radio frequency (RF) accelerating cavities and their RF amplifiers as well as thousands of magnets for steering and focusing charged particle beams and their power sources. Accelerator designs are initially optimized by utilizing analytical beam physics knowledge and simulation studies. Once accelerators are built their performance does not exactly match the theory and models on which their design is based.

The differences between actual and designed systems are due to factors including idealized analytical studies that make simplifying assumptions and misalignment of accelerator components. Beyond not matching their designs, accelerator components and their beams drift unpredictably with time: 1). RF and magnet system amplifiers, power sources, and reference signals drift with temperature and suffer random perturbations from the noise within the electrical grid; 2). The initial 6D (x, y, z, p_x, p_y, p_z) phase space distribution of the beams entering accelerators from ion sources or photo cathodes drift and change unpredictably with time.

Most existing diagnostics are either destructive in nature or only provide beam-averaged measurements. Transverse deflecting cavities (TCAV), which can measure the longitudinal phase space (LPS) of relativistic electron bunches, destroy those bunches in the measurement process [1]. Beam position monitors (BPM) are non-invasive but only provide bunch-averaged position measurements and beam loss monitors provide no beam data beyond specifying a rough estimate of beam loss within a large region of an accelerator.

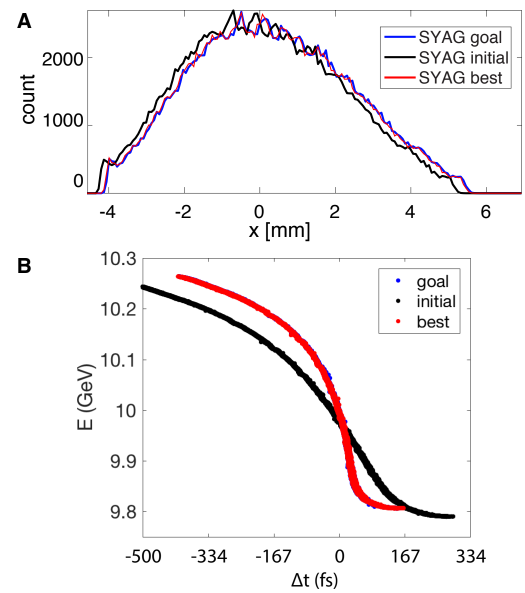

Figure 1: The adaptive model is tuned to match SYAG-based measurements of energy spread spectra (A). Once the modeled (red) and measured (blue) spectra converge the LPS of the measured beam is predicted almost exactly (B).

Because accelerators are uncertain and time-varying systems tuning and optimization require many hours of manual tuning. Tuning is especially challenging at older facilities with limited diagnostics such as the LANSCE linear accelerator at LANL [2], at facilities that must generate extremely short and intense beams such as FACET-II [3], and at facilities which require complex and precisely aligned interactions between multiple beams such as AWAKE [4]. Even the latest and most advanced facilities, especially when making large configuration changes to accommodate various experiment setups such as what must routinely take place at advanced FEL facilities such as the LCLS [5], LCLS-II [6], EuXFEL [7], PALFEL [8], and the SwissFEL [9].

Adaptive feedback and machine learning (ML) approaches are growing in popularity for particle accelerator for magnet tuning [10], non-invasive TCAV LPS diagnostics based on adaptive models at FACET [11], LPS diagnostics based on neural networks (NN) at SLAC [12], FEL light output power maximization at the LCLS and at the EuXFEL [13], surrogate modeling [14], detecting faulty BPMs and for optics corrections at the LHC at CERN by utilizing isolation forest techniques and NNs [15, 16], beam tuning at the SPEAR3 light source via Gaussian processes [17], and

* This research was supported by a LANL Laboratory-Directed Research and Development (LDRD) Director's Initiative project 20200410DI.
† ascheink@lanl.gov

ISBN: 978-3-95450-213-4 ISSN: 2673-5490 doi:10.18429/JACoW-IPAC2020-WEVIR10

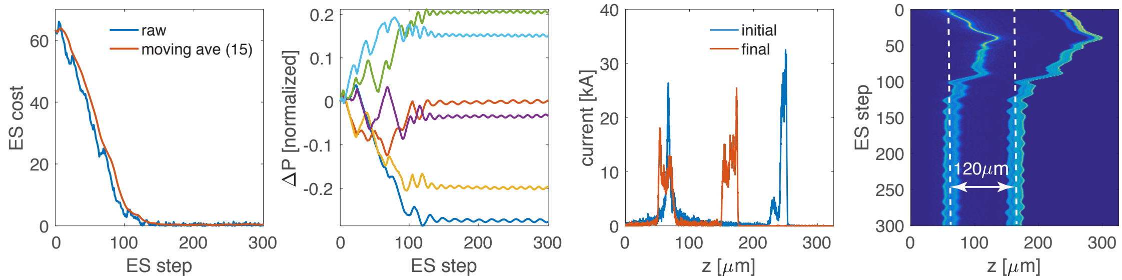

Figure 2: The 3D CNN's output is used as the initial condition for ES tuning.

multiobjective optimization for simultaneous orbit control and emittance minimization at AWAKE [18], .

NON-INVASIVE DIAGNOSTICS

The FACET-II electron bunches are going to be extremely intense with nC charges and few fs bunch lengths. It is challenging to measure the detailed current profiles of intense bunches which damage or destroy intercepting diagnostics and because their few fs bunch lengths are shorter than the resolution of existing TCAV measurements which are limited to ~3fs for highly relativistic bunches. Non-invasive LPS diagnostics for intense, short beams would be useful for most FELs and in particular for particle driven plasma wakefield accelerators (PWA) such as FACET-II in order to enable more precise control of bunch profiles. A first of its kind demonstration of an adaptive non-invasive TCAV LPS diagnostic was developed and tested at FACET to accurately track and predict time varying LPS measurements based only on passive energy spread spectrum measurements [11]. Recently, we have begun developing such adaptive model tuning-based non-invasive diagnostics for the FACET-II beam [19]. Preliminary simulation results are shown in Figure 1 where matching the beam's energy spread spectrum resulted in an exact prediction of the LPS. Once such a diagnostic is up and running, it can enable automated feedback-based control and tuning of the LPS distribution of the FACET-II electron bunch, as shown in Figure 2.

ACCELERATOR TUNING AND CONTROL

Pulse Energy Maximization at LCLS and EuXFEL

At the LCLS and the EuXFEL we have applied an adaptive model-independent feedback control algorithm for automatic maximization of FEL output power [13]. The main strengths of this approach are its ability to handle multiple coupled components simultaneously and tune them based only on noisy measurements of analytically unknown functions.

Beam Loss Minimization at LANSCE

LANSCE simultaneously accelerates intense space charge dominated beams of H^+ and H^- ions and is especially challenging to tune because of very limited diagnostics (few BPMs, mostly beam loss monitors). We applied adaptive feedback to minimize multiple beam loss monitors in various sections of LANSCE simultaneously by tuning 6 parameters

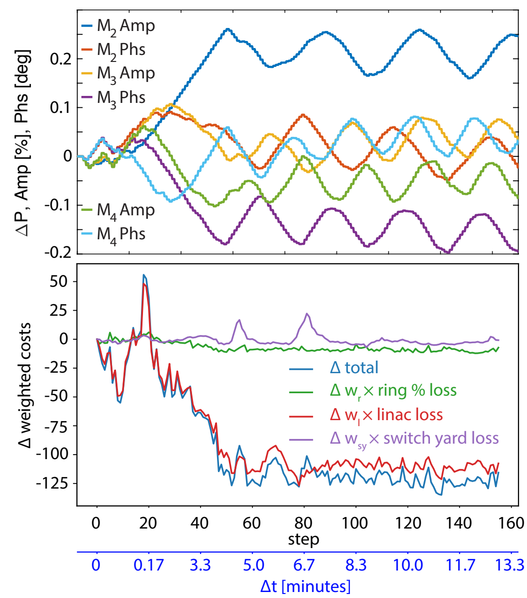

Figure 3: Beam losses and RF module settings.

simultaneously; the amplitude and phase set points of the first three digitally controlled RF modules $M_2 - M_4$. The strength of this algorithm was demonstrated when following a facility wide power glitch the beam came back on with high losses throughout the machine and the adaptive feedback was able to minimize them within ~5 minutes as shown in Figure 3, a task that could have taken up 1 hour of time if an operator had to iteratively tune all 6 knobs one at a time.

Multi-objective Optimization at AWAKE

At the AWAKE PWA facility at CERN the electron beam line provides a tightly focused beam lined up with the 400 GeV proton beam for proton-driven PWA of electrons. Due to coupling, when an effort was made to minimize emittance growth by adjusting two solenoid and three quadrupole magnets directly following the injector, unwanted changes were seen in the beam's trajectory. Therefore we ran two adaptive feedbacks simultaneously, the first slowly adjusted 2 solenoids and 3 quads to minimize emittance growth, while the second adjusted 10 steering magnets at a 3× higher rate to maintain a desired trajectory, resulting in simultaneous emittance minimization and trajectory control via 15 parameter multiobjective optimization, as shown in Figure 4.

ISBN: 978-3-95450-213-4 ISSN: 2673-5490 doi:10.18429/JACoW-IPAC2020-WEVIR10

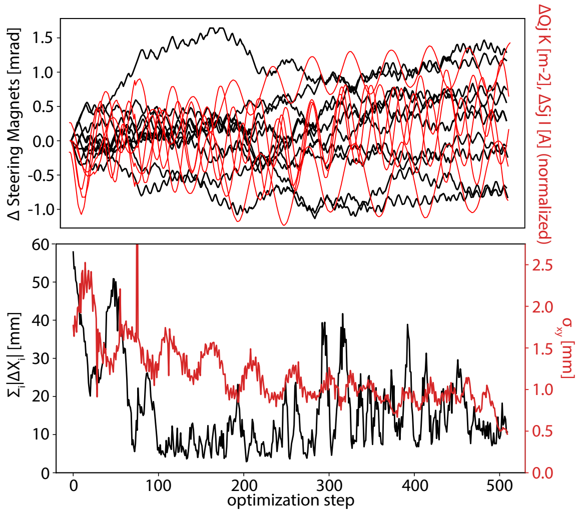

Figure 4: Tuning 15 components at AWAKE.

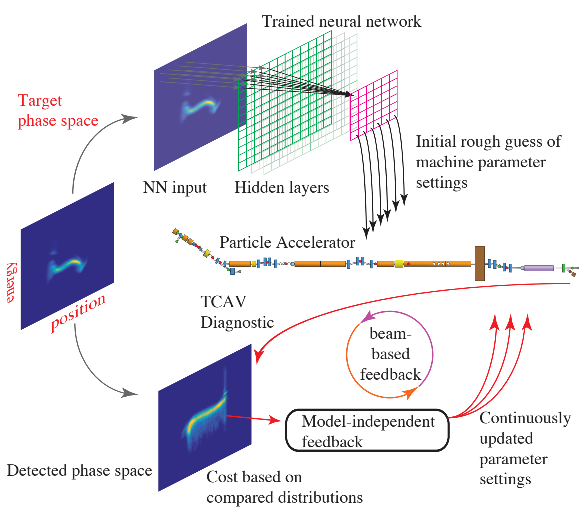

Figure 5: CNN output used as initial guess for ES tuning.

ADAPTIVE MACHINE LEARNING FOR TIME VARYING SYSTEMS

Longitudinal Phase Space Control at the LCLS

One limitation of standard ML-based approaches which use machine or simulation data in order to learn a representation of an accelerator is the fact that their performance drifts as accelerator beams and components change with time. Recently, an adaptive ML approach has been developed for time varying systems, as shown in Figure 5, and has been applied at the LCLS to automatically control the longitudinal phase space of the electron beam [20].

Transfer Learning and Domain Transfer

Additional ways to enable the use of ML for changing systems are transfer learning and domain transfer. A NN can be trained on simulation data and then made more accurate for application to an actual accelerator by utilizing a much smaller set of machine data. This can also update a model for a changing accelerator over time. A recent demonstration of transfer learning and domain transfer trained a convolutional neural network (CNN) to map electron backscatter diffraction (EBSD) measurements to crystal orientations [21]. The CNN was first trained using >200,000 simulations, the last few layers were then retrained using only 1000 experimental measurements. However CNN accuracy was still limited due to noise and significant differences between experimental and simulated measurements. As an additional step domain transfer was applied in the form of training a U-net using 1000 experimental measurements, which pre-filtered experimental data and fed it to the CNN. Transfer learning together with domain transfer created a CNN for mapping EBSD measurements to crystal orientations >1000× faster than existing state of the art EBSD reconstruction methods.

CONCLUSIONS

ML and adaptive feedback control methods are being developed by accelerator facilities around the world and new adaptive machine learning methods are enabling the control and optimization of complex time varying systems.

REFERENCES

[1] C. Behrens *et al.*, “Few-femtosecond time-resolved measurements of X-ray free-electron lasers," *Nature Communications*, vol. 5, p. 3762, 2013. doi:10.1038/s41586-018-0485-4

[2] R. W. Garnett, “LANSCE Accelerator Update and Future Plans," *Journal of Physics: Conference Series*, vol. 1021, no. 1, 2018. doi:10.1088/1742-6596/1021/1/012001

[3] C. Joshi *et al.*, “Plasma wakefield acceleration experiments at FACET II," *Plasma Phys. Controlled Fusion*, vol. 60., p. 034001, 2018. doi:10.1088/1361-6587/aaa2e3

[4] E. Adli *et al.*, “Acceleration of electrons in the plasma wakefield of a proton bunch," *Nature*, vol. 561, pp. 363-367, 2018. doi:10.1038/s41586-018-0485-4

[5] J. Rzepiela *et al.*, “Tuning of the LCLS Linac for user operation," SLAC National Accelerator Lab, Menlo Park, USA, SLAC-PUB-16643, Jul. 2016. https://www.osti.gov/biblio/1261086

[6] T. O. Raubenheimer, “Technical challenges of the LCLS-II CW X-Ray FEL," in *Proceedings of the International Particle Accelerator Conference (IPAC'15)*, Richmond, VA, USA, 2015. doi:10.18429/JACoW-IPAC2015-WEYC1

[7] H. Weise and W. Decking, “Commissioning and first lasing of the European XFEL," in *Proceedings of the Free Electron Laser Conference (FEL'18)*, Santa Fe, NM, USA, 2018. doi:10.18429/JACoW-FEL2017-MOC03

[8] H. S. Kang *et al.*, “FEL performance achieved at PAL-XFEL using a three-chicane bunch compression scheme," *J. Synchrotron Rad*, vol. 26, pp. 1127-1138, 2019. doi:10.1107/S1600577519005861

[9] C. Milne *et al.*, “SwissFEL: the Swiss X-ray free electron laser," *Appl. Sci.*, vol. 7.7, pp. 1-57, 2017. doi:10.3390/app7070720

[10] A. Scheinker, “Model Independent Beam Tuning," in *Proceedings of the 2013 International Particle Accelerator Conference (IPAC'13)*, Shanghai, China, 2013.

ISBN: 978-3-95450-213-4 ISSN: 2673-5490 doi:10.18429/JACoW-IPAC2020-WEVIR10

paper TUPWA068. http://inspirehep.net/record/1337207/files/tupwa068.pdf

[11] A. Scheinker and S. Gessner, "Adaptive method for electron bunch profile prediction," *Phys. Rev. ST Accel. Beams*, vol. 18, p. 102801, 2015. doi:10.1103/PhysRevSTAB.18.102801

[12] C. Emma *et al.*, "Machine learning-based longitudinal phase space prediction of particle accelerators," *Phys. Rev. ST Accel. Beams*, vol. 21, p. 112802, 2018. doi:10.1103/PhysRevAccelBeams.21.112802

[13] A. Scheinker *et al.*, "Model-independent tuning for maximizing free electron laser pulse energy," *Phys. Rev. Accel. Beams*, vol. 22, p. 082802, 2019. doi:10.1103/PhysRevAccelBeams.22.082802

[14] A. Edelen *et al.*, "Machine learning for orders of magnitude speedup in multiobjective optimization of particle accelerator systems," *Phys. Rev. Accel. Beams*, vol. 23, p. 044601, 2020. doi:10.1103/PhysRevAccelBeams.23.044601

[15] E. Fol, J. M. Coello de Portugal, and R. Tomas, "Unsupervised Machine Learning for Detection of Faulty BPMs," in *Proc. of the 2019 International Particle Accelerator Conference (IPAC'19)*, Melbourne, Australia, 2019. doi:10.18429/JACoW-IPAC2019-WEPGW081

[16] E. Fol, J. M. Coello de Portugal, and R. Tomas, "Optics Corrections Using Machine Learning in the LHC," *Proc. of the 2019 International Particle Accelerator Conference (IPAC'19)*, Melbourne, Australia, 2019. doi:10.18429/JACoW-IPAC2019-THPRB077

[17] A. Hanuka *et al.*, "Online tuning and light source control using a physics-informed Gaussian process," arXiv preprint arXiv:1911.01538, 2019. https://arxiv.org/pdf/1911.01538.pdf

[18] A. Scheinker *et al.*, "Online multi-objective particle accelerator optimization of the AWAKE electron beam line for simultaneous emittance and orbit control," *AIP Advances*, vol. 10, p. 055320, 2020. doi:10.1063/5.0003423

[19] A. Scheinker *et al.*, "Adaptive model tuning studies for non-invasive diagnostics and feedback control of plasma wakefield acceleration at FACET-II," *Nucl. Instrum. Methods Phys. Res., Sect. A*, vol. 967, p. 163902, 2020. doi:10.1016/j.nima.2020.163902

[20] A. Scheinker *et al.*, "Demonstration of model-independent control of the longitudinal phase space of electron beams in the Linac-coherent light source with Femtosecond resolution," *Phys. Rev. Lett.*, vol. 121, p. 044801, 2018. doi:10.1103/PhysRevLett.121.044801

[21] Y. F. Shen *et al.*, "Convolutional neural network-based method for real-time orientation indexing of measured electron backscatter diffraction patterns," *Acta Mater.*, vol. 170, pp. 118-131, 2019. doi:10.1016/j.actamat.2019.03.026

ISBN: 978-3-95450-213-4 ISSN: 2673-5490 doi:10.18429/JACoW-IPAC2020-WEVIR11

SAFETY SYSTEM FOR THE RESPECT OF NUCLEAR REQUIREMENTS OF SPIRAL2 FACILITY

P. Anger†, V. Cingal, J.C. Pacary, S. Perret-Gatel, A. Savalle
GANIL Laboratory, Caen, France

Abstract

The SPIRAL2 Facility at GANIL is based on the construction of a superconducting, CW, ion LINAC (up to 5 mA - 40 MeV deuteron beams and up to 1 mA - 14.5 MeV/u heavy ion beams) with two experimental areas called S3 and NFS.

For safety system, SPIRAL2 project system engineering sets up a specific reinforced process, based on V-Model, to validate, at each step, all the requirements (technical, nuclear safety, quality, reliability, interfaces...) from the functional specifications to the final validation.

Since 2016, safety devices have been under construction and in test phase. These tests which are pre-requisites to deliver the first beam demonstrated that both functional and safety requirements are fulfilled. Currently, all of them are in operation for the LINAC and NFS commissioning phases.

This contribution will describe the requirements, the methodology, the quality processes, the technical studies for two system examples, the failure mode and effects analysis, the tests, the status and will propose you a feedback.

INTRODUCTION

GANIL is a nuclear physic laboratory based in France since 1980 and SPIRAL2 is a new facility to extend the capability of GANIL.

Officially approved in May 2005, the SPIRAL2 radioactive ion beam facility (Fig. 1) is based on two phases: A first one including the accelerator, the Neutron-based research area (NFS) and the Super Separator Spectrometer (S3) dedicated to heavy nuclei studies, and a second one including the RIB production process and building, and the low energy RIB experimental hall called DESIR [1, 2].

In 2013, due to budget restrictions, the RIB production part was postponed, and DESIR was planned as a continuation of the first phase.

The first phase SPIRAL2 facility is now built and Desir is under study. The accelerator is installed [3]. The French safety authority agreement is now validated since 2019 according the validation of all safety system and the accelerator is under testing. A first p-beam was accelerated in the LINAC at 33 MeV and injected to experimental hall (NFS) at the end of 2019 [4]. Actually, the accelerator is under commissioning with nominal current at high duty cycle.

† pascal.anger@ganil.fr

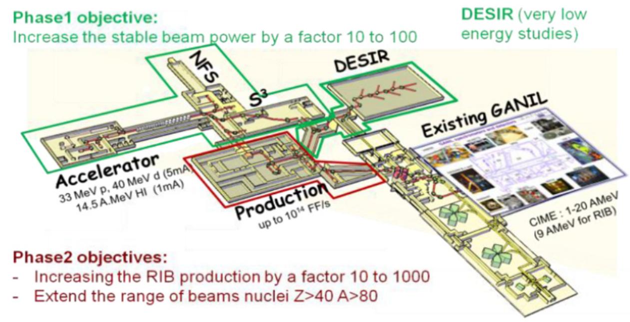

Figure 1: SPIRAL2 project layout, with experimental areas and connexion to the historical GANIL facility.

PROBLEMATIC

The GANIL/SPIRAL2 facility is considered as an “INSTALLATION NUCLEAIRE DE BASE” (INB), administrative denomination for nuclear facilities according to the French law. The GANIL is under the control of the French Nuclear Safety Authority. The classification of the SPIRAL2/GANIL facility in the INB field is due to the characteristics of the beams at the last acceleration state and the use of actinide target.

The goals are to protect workers, public and environment against all identified risks (in normal running, the maximum individual dose is fixed to 1 mSv per year for a worker, and for the most exposed public in the external environment, the impact of the installation is fixed to a maximum value of 10 µSv per year).

Concrete building (14.000 m^3) and an 8 meters underground beam axis, without beam power control is not sufficient for protection against external exposure to ionizing radiation. Active safety systems are then required to control beam losses as well as the operating range.

METHODOLOGY

The objective was to provide all safety system according to the safety requirements (functionalities, independence, dependability, and quality insurance) and according to the beam operation constraints (in particular the safety systems availability).

Since 2010, we have established a system engineering management. It is a very structuring approach for a complex project. The Systems engineering focuses on the needs definition for the customer and for the functional requirements, from the beginning of the cycle (V Model Fig. 2), by documenting the requirements, then with the synthesis of the conception (design), the realization and the validation of the system.

ISBN: 978-3-95450-213-4 ISSN: 2673-5490 doi:10.18429/JACoW-IPAC2020-WEVIR11

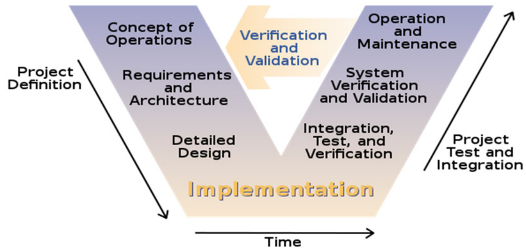

Figure 2: V cycle.

For the safety systems, SPIRAL2 Project uses a specific Quality Management Plan for the Safety (QMPS). This plan is naturally based on the Deming cycle but relies, on the establishment of a particular task force managed to reach the set of the requirements. This task force contributes to validate the conformity (Fig. 3) at each breakpoint or reviews of the V cycle. This checking chain is composed of an independent technical validation, a nuclear safety control, an independent dependability checking, a validation of the integration in the building and the interface conformity with the other processes, a quality and documentation checking. All of those links are required to obtain the safety level for SPIRAL2.

Figure 3: Chain for Safety Quality Management Plan.

Concerning the dependability checking, a Failure Mode and Effects Analysis (FMEA) was realized to eliminate dangerous failures. Criticality is not taken into account. The single failure criterion was selected as dependability criterion. Redundancy, hard-wired systems and dissimilar redundancy are using for the design principle.

FIRST EXAMPLE: SAFETY MACHINE PROTECTION SYSTEM

Controlling the accelerator device activation due to beam losses (beam losses limited to 1 W/m for D+ beams), along with the target and Beam dump activation as well as the operating range is then required with a Safety Enlarged Machine Protection System (EMPS) [5]. This safety EMPS is a part of the entire MPS.

Beam Intensity Monitoring Subsystem

In order to control continuously the intensities and the losses, non-destructive beam intensity measurements are set up along the accelerator. The use of two kinds of non-destructive measurement chains DCCT (Bergoz NPCT-175-C030-HR) and homemade ACCT is justified by the difference of detection principles and by their complementarities (Fig. 4) [6].

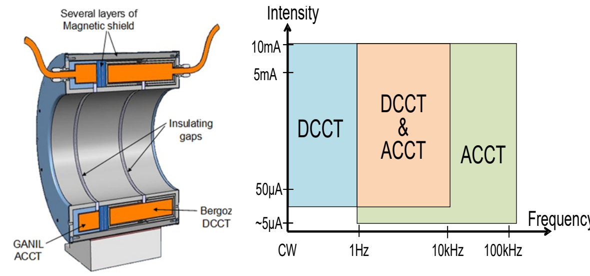

Figure 4: ACCT/DCCT bloc section and operating range.

The DCCTs measure the intensity of continuous and chopped beams with a slow response time. The minimum intensity that can be measured is a few 10 µA due to the offset level. The homemade ACCTs are very efficient, they are faster with rise times about 1 µs and with minimum levels less than 5 µA.

The ACCT or DCCT signal is converted into a pulse frequency entering counters. The threshold values must take into account the qualified uncertainty measurement. A beam cut alarm signal is generated if the counter sets off.

Beam Cuts Treatment Subsystem

This safety-classified subsystem is the core part of the SPIRAL2 MPS; it is a simple and secured one, based on two hard-wired system with a PLC for the operation control (Fig. 5). This system relies in particular on the following beam monitor subsystems:

- ACCT/ DCCT monitors
- Scintillation monitors (BLM) [7]
- Time of Flight monitor
- Beam dump activation control subsystem [8]
- Beam dump Cooling subsystem

It receives alarms from each subsystem. Therefore, it activates the beam cut through commands sent to safe and slow beam stops in the low energy beam line (response time: 1.5 s) in association with a temporary RF stop on the RFQ (response time < 1 ms).

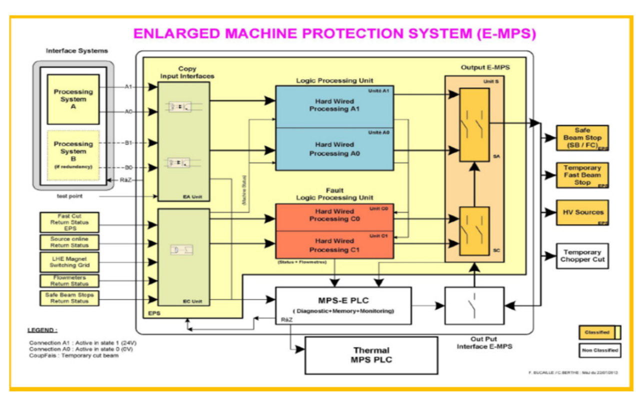

Figure 5: Redundant hard-wired system.

The overall response time was determined by the thermal and activation calculations with safety margin. The expected response times are for the fastest 15 ms (10 ms for the detection, 4 ms for the treatment and 1 ms for the beam cut) to a few seconds for slower ones.

ISBN: 978-3-95450-213-4 ISSN: 2673-5490 doi:10.18429/JACoW-IPAC2020-WEVIR11

SECOND EXAMPLE: LIMITATION OF DISSEMINATION SYSTEM

The need is to minimize the risk of a volatile contamination transfer through the beam lines. This transfer would be caused by a shockwave due to an air inrush in the vacuum chamber [9]. The main characteristics are:

- A contamination velocity considered of 900m/s (this speed was measured at CERN [10]).
- The use of discharge gauges and fast isolation valves with time closing from 10 to 25 ms (Fig. 6).
- An installation of few valve control systems (the closing of these valves depends of the beam path configuration in the high-energy beamlines [11]).
- This System is coupled to a fast Beam cuts treatment and actuator subsystems (RF of RFQ cavity).

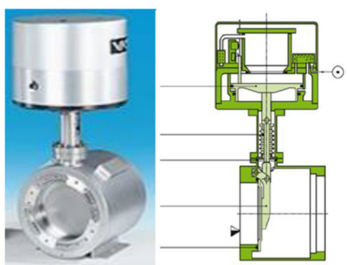

Figure 6: Fast valve of VAT Company.

Taking into account the wave front speed and the fast isolation valve response time, the fast valves are located over 17m (Fig 7) to the target and the sensor for all beam paths and with redundancy (17m / 900m.s^{-1} > valve time closing).

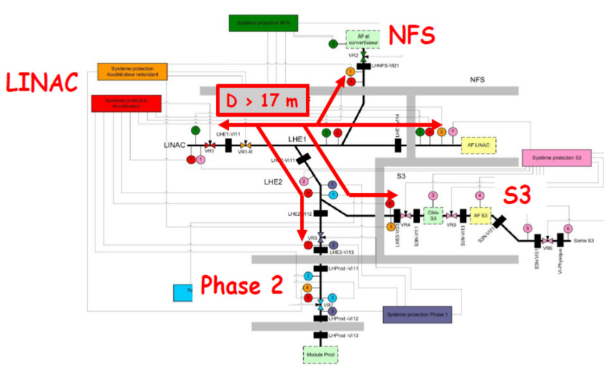

Figure 7: Synoptic of high-energy beam lines.

Concerning the scenario and the timing (Fig. 8):

- In first, if we have a fast vacuum increase, the discharge gauge detected it in 1ms,
- 2 ms later, the valve control box activate the fast valve and the safety command subsystem.
- 1 ms after, the safety command subsystem activates in parallel a temporary fast beam cut with the radiofrequency of the RFQ cavity
- 1 ms later, the 200kW beam are cut-off and the fast isolation valve begin to move
- 1,5 s after a slow beam cut is down (beam stopper in the beam line)

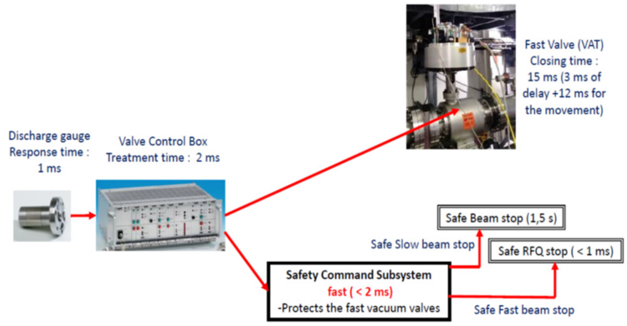

Figure 8: Scenario and timing.

Last September, we realized the overall validation with the beam. So with the excellent subsystem time characteristics, we have a margin of 2,65 ms over an effective time of 0,35 ms to protect the valve from the beam! This safety system was validated with requirement compliance (Fig. 9).

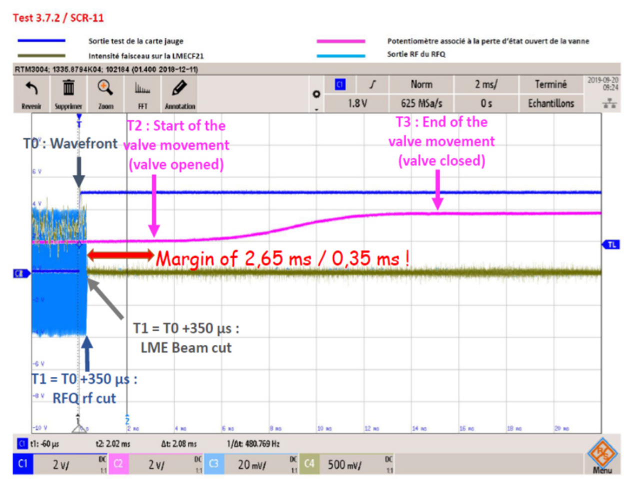

Figure 9: Validation tests in 2019.

TESTS AND SAFETY VALIDATIONS

For each subsystem, the second phase of the V-cycle has been respected [12, 13]. It concerns the followings: unit tests, subsystems tests and global tests, functional tests and tests in a degraded situation according to the FMEA during the design phase (Fig. 10).

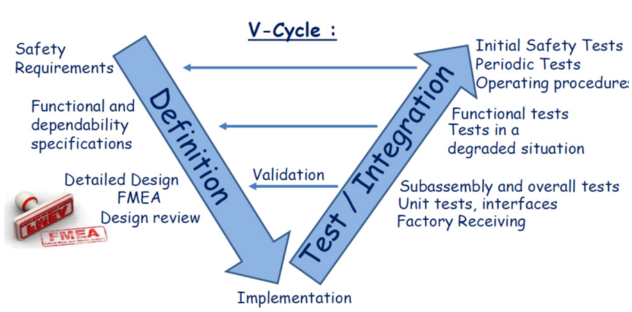

Figure 10: SPIRAL2 Safety V cycle.

Each deviation from the validated design reference requires analysis, processing and validation by the six links of the chain for PMQS. After iteration and complete agreement of the six links, the modifications are carried out

ISBN: 978-3-95450-213-4 ISSN: 2673-5490 doi:10.18429/JACoW-IPAC2020-WEVIR11

with an updating of the different documents (diagrams, technical design files, FMEA ...). A safety-specific quality summary file is completed to prepare the operation phase and to be potentially audited during inspections of the nuclear safety authority.

CONCLUSION

Since 2019, the 22 safety systems for Accelerator and NFS are now installed, tested, validated and in operation in compliance with the Safety requirements and with the quality management.

This status allowed the first Linac beam in 2019 and the first beam test in NFS.

The last French Safety Authority inspection in 2020 revealed no significant deviation: The SPIRAL2 facility is safe!

For the safety systems in order to respect the nuclear requirements of SPIRAL2 facility, our main feedback concerns the followings:

- The required very low beam level for the detection (for example few µA with beam current monitors) integrating the definition of global uncertainties is brilliantly achieved through a specific development for SPIRAL2.
- All safety systems architecture, have progressed to be very reliable and have been hardened by Failure Mode and Effects Analysis (FMEA) through the use of principle like redundancy, dissimilarity, simplification, auto-testing and degraded mode studies
- The performances for every fast system are achieved with margins
- The V-cycle time is long for some system between the start of the design in 2011 and the overall validation in 2019 because time is the main adjustment variable. There has been no change in the safety, the technical performances and the cost requirements.

The goal is reached: Providing complex instrumentation, with multidisciplinary teams, meeting the SPIRAL2 safety and quality requirements, is a technical and human challenge that the SPIRAL2 team has raised.

The new and important work, that has been done on the SPIRAL2 project, to make a high intensity accelerator a safe installation, should allow our accelerators to progress and be safer.

Such as needs = Such as designed = Such as installed and tested = Such as in operation

REFERENCES

[1] SPIRAL2 project. `https://www.ganil-spiral2.eu/le-ganil/presentation/le-projet-spiral-2/la-phase-1-de-spiral2/`

[2] E. Petit, "Progress of the SPIRAL2 Project", in *Proc. 2nd Int. Particle Accelerator Conf. (IPAC'11)*, San Sebastian, Spain, Sep. 2011, paper WEYA01, pp. 1912-1916.

[3] P. Anger *et al.*, "Spiral2 Project: Integration of the Accelerator Processes, Construction of the Buildings and Process Connections", in *Proc. 13th Int. Conf. on Heavy Ion Accelerator Technology (HIAT'15)*, Yokohama, Japan, Sep. 2015, paper TUA2C01, pp. 153-155.

[4] P. Dolegieviez et al "Status of the SPIRAL2 Project", presented at the *11th Int. Particle Accelerator Conf. (IPAC'20)*, Caen, France, May 2020, paper TUVIR12, this conference.

[5] M. H. Moscatello, C. Berthe, C. Jamet, and G. Normand, "Machine Protection System for the SPIRAL2 Facility", in *Proc. 3rd Int. Particle Accelerator Conf. (IPAC'12)*, New Orleans, LA, USA, May 2012, paper WEPPD044, pp. 2612-2614.

[6] S. Leloir, T. Andre, B. Ducoudret, C. Jamet, G. Ledu, and C. Potier de Courcy, "Measurement and Control of the Beam Intensity for the SPIRAL2 Accelerator", in *Proc. 2nd Int. Beam Instrumentation Conf. (IBIC'13)*, Oxford, UK, Sep. 2013, paper WEPF33, pp. 900-902.

[7] F. Negoita "BLM for SPIRAL2: status of the project", in *Proc. LIA COSMA Workshop*, Bucharest, Romania, Jan. 2017.

[8] C. Haquin, P. Anger, J. C. Deroy, G. Normand, F. Pillon, and A. Savalle, "Development of a Safety Classified System with LabVIEW and EPICS", *in Proc. 16th Int. Conf. on Accelerator and Large Experimental Control Systems (ICALEPCS'17)*, Barcelona, Spain, Oct. 2017, pp. 1221-1223. doi:10.18429/JACoW-ICALEPCS2017-THCPA04

[9] M. Faye, M. Ady and R. Levallois, "Measurement of atmospheric air inrush speed into a high vacuum vessel", presented at the *2nd European conference of Non-equilibrium Gas Flows (NEGF15)*, Eindhoven, Netherlands, Dec. 2015.

[10] G. Vandoni, M. Ady, M. A. Hermann, R. Kersevan, and D. T. Ziemianski, "Leak Propagation Dynamics for the HIE-ISOLDE Superconducting Linac", *in Proc. 5th Int. Particle Accelerator Conf. (IPAC'14)*, Dresden, Germany, Jun. 2014, pp. 2351-2353. doi:10.18429/JACoW-IPAC2014-WEPME039

[11] R. Levallois "systèmes de vide de SPIRAL2 et contraintes particulières", presented at *the rencontre nationale du Réseau des Technologies du Vide du CNRS*, France, Dec. 2014.

[12] Q. Tura, C. Berthe, O. Danna, M. Faye, A. Savalle, and J. Suadeau, "Safety Control of the Spiral2 Radioactive Gas Storage System", *in Proc. 16th Int. Conf. on Accelerator and Large Experimental Control Systems (ICALEPCS'17)*, Barcelona, Spain, Oct. 2017, paper THPHA107, pp. 1629-1633, doi:10.18429/JACoW-ICALEPCS2017-THPHA107

[13] J. C. Pacary "Rénovation du système de sûreté des accès et du Tableau de Contrôle des Rayonnements au GANIL", presented at the *Journées Accélérateurs de la Société Française de Physique,* Roscoff, France, Oct. 2011.

ISBN: 978-3-95450-213-4 ISSN: 2673-5490 doi:10.18429/JACoW-IPAC2020-WEVIR12

MACHINE LEARNING TECHNIQUES FOR OPTICS MEASUREMENTS AND CORRECTIONS

E. Fol*, G. Franchetti† *, R. Tomás, CERN, 1211 Geneva 23, Switzerland
also at *Johann-Wolfgang Goethe University, 60438 Frankfurt am Main, Germany
† GSI Helmholtzzentrum für Schwerionenforschung, 64291, Darmstadt, Germany

Abstract

Recently, various efforts have presented Machine Learning (ML) as a powerful tool for solving accelerator problems. In the LHC a decision tree-based algorithm has been applied to detect erroneous beam position monitors demonstrating successful results in operation. Supervised regression models trained on simulations of LHC optics with quadrupole errors promise to significantly speed-up optics corrections by finding local errors in the interaction regions. The implementation details, results and future plans for these studies will be discussed following a brief introduction to ML concepts and its suitability to different problems in the domain of accelerator physics.

INTRODUCTION

Accelerator physics problems build a wide range of complex numerical and analytical tasks, e.g. modeling of different aspects of beam behavior, machine performance optimization, measurements data acquisition, and analysis. The growing complexity of modern and future accelerators provides the motivation to explore alternative techniques, which can complement traditional methods or even surpass their performance and offer opportunities to build more efficient and powerful tools. Machine Learning (ML) techniques have been introduced into numerous scientific and industrial areas demonstrating human-surpassing performance in pattern recognition, forecasting, and optimization tasks. These ML concepts can find analogies in the domain of accelerator physics as it will be shown in the following.

Considering the particular case of optics measurements and corrections, traditional techniques meet their limitation, e.g. dealing with erroneous signal artefacts that cannot be related to known patterns in the measurements data. Unsupervised ML techniques cover these limitations by learning the thresholds for anomalies detection directly from the given data as it will be shown on the example of identification of beam position monitors (BPM) faults. Another example is the optics perturbations caused by magnetic gradient field errors, which have to be corrected in order to control the beam optics. Supervised ML models built on simulations of the optics perturbed with thousands of realisations of quadrupolar magnet errors can predict the actual magnetic errors present in the machine, providing additional information for the computation of correction settings. Due to hardware and electronics issues, the signal measured at the BPMs suffers from noise that produces uncertainties in the optics functions reconstructed from the harmonic analysis of BPM turn-by-turn readings. For this problem a special kind of Neural Networks named Autoencoder has been applied as a denoising technique improving the precision of phase measurements, thus potentially leading to more precise computed corrections based on the measured optics. The following section presents a short overview on latest achievements of applying ML to different types of particle accelerators.

MACHINE LEARNING CONCEPTS IN ACCELERATOR PHYSICS

The concept of ML is known since the middle of the last century. The definition of ML is referred to computer programs and algorithms that automatically improve with experience by learning from examples with respect to some class of task and performance measures without being explicitly programmed [1]. Based on this definition we can determine a domain of accelerator tasks that can be potentially solved using ML techniques. Such tasks can be concerned by building models where analytical solutions do not exist, but the models can be “learned” from given examples instead of building them from sets of explicit rules. When building ML solutions, we should define a performance measure, e.g. accelerator performance parameter such as beam size or pulse energy. It is also important to differentiate a specific “class of task”, such that ML tools are designed for particular accelerator components which can be easily tested and controlled. Currently existing ML-based methods for accelerators can be divided into virtual diagnostics, control and optimization, anomaly detection and predictive modeling. A more detailed overview for beam diagnostics can be found in [2, 3], recent advances for the field of ML for accelerators control are described in [4–7].

Most of the ML efforts in accelerator physics are being developed for automatic machine optimization, since ML methods demonstrate notable advantages compared to numerical techniques in solving control tasks for non-linear, time-varying systems with large parameter spaces. Two techniques have found an especially wide application in this domain - Bayesian optimization [8] and Reinforcement Learning [9, 10]. Control tasks can be approached in both model-based and model-independent ways, e.g. using adaptive learning techniques to implement feedback algorithms for optimizing and tuning complex noisy systems [11–13]. Predictive modeling techniques also include Gaussian Processes, which can be used to build models relating a set of parameters (e.g. quadrupole settings) to an optimization

* elena.fol@cern.ch

ISBN: 978-3-95450-213-4 ISSN: 2673-5490 doi:10.18429/JACoW-IPAC2020-WEVIR12

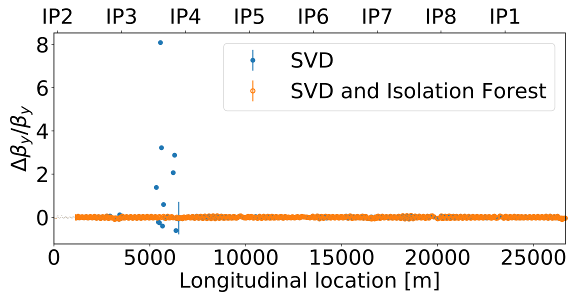

Figure 1: Comparison between β-beating measured from SVD-cleaned data and additional cleaning with IF. The data is obtained during ion commissioning in 2018.

function (e.g. pulse energy) offering the advantage to be able not only to give predictions, but also estimate uncertainty bounds [14]. ML concepts provide techniques to build virtual diagnostics tools that can assist in case a direct measurement would have negative impact on operation or in the locations where no physical instrumentation can be placed. The diagnostics of various beam properties using surrogate models has been applied at various facilities [15–19].

ML-based tools are being developed to tune and control machine and beam behaviour [20–23]. Recently, a fully-automated collimators alignment based on beam loss spikes classification using supervised learning has become a standard tool in the LHC operation. This approach significantly reduced time and human effort needed for the the setup of the collimators system [24]. Further ML-techniques for beam dynamics studies at the LHC are presented in [25] demonstrating applications for optimisation of beam lifetime and losses, detection of collective beam instabilities and beam heating effects, as well as outlier detection in dynamic aperture simulations. Anomaly detection techniques are suitable for the detection of unusual events that do not conform to expected patterns. It can be performed using classification on labeled data (supervised learning), unsupervised learning techniques including clustering or semi-supervised learning methods such as autoencoder. One of the examples of anomaly detection at the LHC, the detection of faulty BPMs is presented in detail in the next section.

UNSUPERVISED DETECTION OF FAULTY BEAM POSITION MONITORS

In presence of faulty BPM signal, the optics functions computed from harmonic analysis of BPM readings [26, 27] are contaminated by outliers, which have to be manually removed followed by repeated optics analysis. Most of the noise and faulty signals can be removed using predefined thresholds, as well as through applying advanced signal-improvement techniques based on SVD [28]. However few nonphysical values are usually observed in the optics computed from the data cleaned with these techniques. In order to reduce the manual effort and save operational time, an anomaly detection technique called Isolation Forest (IF) [29] has been incorporated into optics measurements software infrastructure. IF is a decision-tree-based algorithm, which requires only the expected contamination rate (fraction of outliers in the data) as input parameter. This method recently became a standard part of optics measurements at LHC and has been successfully used during beam commissioning and machine developments under different optics configurations in 2018. Operational results, statistics on simulations, and comparison to clustering techniques can be found in [3, 30]. Application of IF algorithm significantly improved the reliability of the obtained optics functions and reduced the human efforts in cleaning of measurement data. We were able to identify faulty BPMs independently of the settings of previously-available cleaning tools. Determining the optimal values of the SVD settings has been shown to be crucial for the performance of the SVD-based cleaning technique [31]. However, when applying the SVD-based method with optimal settings obtained from extensive simulations studies, we could not match the results achieved using IF algorithm.

Reconstructing the optics from the harmonic-analysis data excluding the bad BPMs identified by IF prevents the appearance of outliers in the computed optical functions. Figure 1 shows an example of improving the optics computation using IF-cleaned data. It has been shown that IF is capable to identify the BPMs failing in most of the measurements, whose fault reasons could not be observed previously in the properties of the signal. Generally, we demonstrated the ability of IF technique to complement efficiently the traditional cleaning tools by removing the remaining faulty BPMs.

SUPERVISED REGRESSION MODELS FOR OPTICS CORRECTIONS

Currently, LHC optics corrections are performed in two steps, i.e. local corrections based on Segment-by-Segment technique [32] and global corrections using Response Matrix approach. Local corrections are applied around Interaction Points (IPs) where the quadrupoles are individually powered, while global corrections are performed by trimming also the circuits - quadrupoles powered in series [33,34]. These methods allow achieving unprecedentedly low β-beating [26], however the currently applied methods do not offer the possibility to estimate the entire set of actual individual magnet errors around the ring. Supervised regression models trained on a large number of LHC simulations demonstrate the potential to predict the individual quadrupole errors from the measured optics perturbations caused by these errors.

Building a Supervised Model

The general idea of applying supervised learning to optics corrections is to build regression models that use the difference between measured and design optics as input features and produce the magnet errors as output. The first preliminary approach is presented in [35] and is based on the optics perturbations introduced by quadrupoles powered in series excluding the errors in the triplet magnets around the IPs. Here we present a more realistic approach, where

ISBN: 978-3-95450-213-4 ISSN: 2673-5490 doi:10.18429/JACoW-IPAC2020-WEVIR12

the simulated optics perturbations are introduced by single quadrupole errors around the entire ring including the IP triplets. In order to build the training set, we randomly assign errors to all quadrupoles available in the LHC according to the expected error distribution [36] and apply these errors using the settings for 2018 optics with $\beta^* = 40$ cm. We use simulated phase advance, β^*, and normalized dispersion deviations from the ideal optics as model input (3346 features in total). The output variables are the quadrupole errors used to introduce the simulated deviations from the design optics (1256 target variables). Gaussian noise generated as a random distribution with the factor $10^{-3} \times 2\pi$ and scaled by $\sqrt{\beta}$, β-function value at the BPM location, are added to the simulated phase advance measurements used as input features. The normalized dispersion is given Gaussian noise of $4 \times 10^{-3}\ \sqrt{\mathrm{m}}$ estimated from the measurements in 2018. As it was shown in [37], applying complex models such as Orthogonal matching pursuit or convolutional neural network does not result in significantly better corrections, so we use a least-squares linear regression with weights regularization [38, 39] as baseline model for the following studies.

Table 1: The effect of noise on the predictive power of a regression model. Regression models are trained on 60 000 samples, using only the noisy phase advances as input features, simulated for 2016 optics with $\beta^* = 40$ cm. Mean absolute error (MAE) of prediction is given in the units of absolute quadrupole errors [$10^{-5}\mathrm{m}^{-2}$]. R^2 defines the coefficient of determination.

Noise [2π]	Total MAE	Triplets MAE	R^2
5×10^{-4}	1.71	1.44	0.67
1×10^{-3}	2.19	1.48	0.43
2×10^{-3}	2.5	1.52	0.25
4×10^{-3}	2.69	1.57	0.13
6×10^{-3}	2.75	1.59	0.09
8×10^{-3}	2.79	1.61	0.07
1×10^{-2}	2.82	1.61	0.05

Evaluating Regression Models

To be noted that, due to degeneracy, there are infinite possible error distributions that reproduce the same behaviour and hence, a solution to determine a unique set of quadrupole errors from the optics perturbations does not exist. However, we can validate the regression models from the ML point of view since the simulated errors used as true output values in training data are available. The typical figures of merit for regression tasks are the mean absolute error (MAE) to compare the difference between true target values and the output of the model and the coefficient of explained variance (R^2 score). In order to conclude on the learning performance, the dataset is separated into training (80%) and test (20%) sets. A big increase in the number of training samples does not necessarily result in a large increase of predictive power of the model. Considering the amount of time and storage

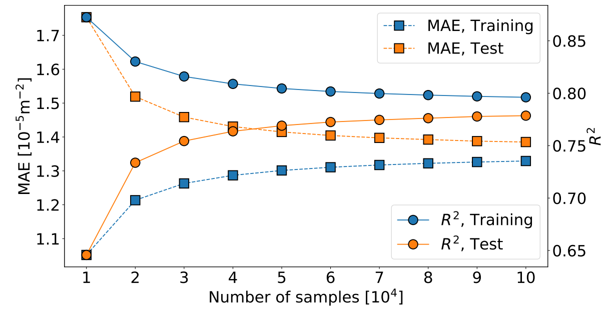

Figure 2: Model cross validation based on the loss (MAE) and R^2 coefficient depending on the number of available samples. The loss is constantly decreasing with the growing number of samples, while R^2 is increasing. This trend indicates a reasonable learning behaviour, however using datasets larger than ca. 70 000 samples does not improve the scores significantly.

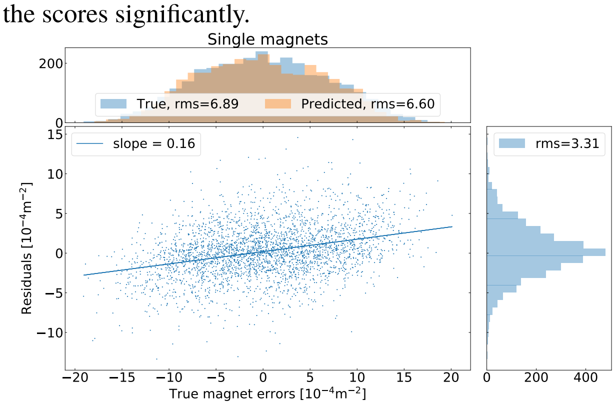

Figure 3: Results of triplet error prediction using LR model trained on 3304 input features, 100 000 samples demonstrating the relative error prediction in single quadrupoles in the triplets. The computed slope is the correlation between true values and residuals, indicating the generalization error of the model.

needed to handle the training simulation data, especially for the future online application, we need to determine the optimal training set size. The change of the model scores with respect to the number of samples (*learning curve*) also indicates the ability of the model to learn from the given data and indicates the dataset size required to achieve the optimal model performance as shown in Figure 2. In the next section we present the results from the regression model using 75 000 samples in total for training and test.

Results

The final evaluation of the model is performed on 100 independently-generated simulations. We define the correlation between the size of the simulated magnet errors and the size of residuals (difference between true and predicted values) as generalization error and compare the rms values of simulated and predicted error distributions. Figure 3 demonstrates the results of the errors prediction of the triplets quadrupoles located close to IPs and producing the largest optics perturbations.

ISBN: 978-3-95450-213-4 ISSN: 2673-5490 doi:10.18429/JACoW-IPAC2020-WEVIR12

The previously described results are obtained from simulations. We also investigate the ability of regression models to compute magnet errors to correct the β-beating in the virgin machine, using LHC data from 2016 commissioning, measured for $\beta^* = 40$ cm before any corrections. Since normalized dispersion and β^* are not available in this measurement set, we need to train the model using only the phase advance deviations from ideal optics as input features. In this case, the model achieves significantly smaller training and test scores than regression model trained on larger amount of features ($R^2 = 0.45$ compared to 0.78), demonstrating the importance of normalized dispersion and β^* for the magnet errors reconstruction. Since the actual magnet errors generating the measured optics perturbations in the uncorrected machine are unknown, we cannot evaluate the model prediction as in the case of simulations. Instead, we reconstruct the β-beating from the predicted quadrupole errors and compare it to the measurement. The difference is then the expected remaining optics errors after applying the predicted strengths as corrections. According to the residual β-beating obtained by comparing the measured and the reconstructed optics using the predicted magnetic errors, the absolute β-beating in Beam 1 can be potentially reduced from rms values of 12% and 54% to 2% and 7% in horizontal and vertical planes, respectively. For Beam 2, the rms β-beating decreases from 49% to 9% in the horizontal and from 12% to 3% in the vertical plane. The obtained regression-based corrections can be potentially improved by training a more powerful model including the sextupoles misalignments and non-linear effects. In case non-linearities are added, a Neural Network (NN) regression model will be potentially needed in order to resolve non-linear correlations using the hidden layers. The application of NN can be also advantageous for the training procedure. After training a NN-model for a specific optics setting, we can avoid fully re-training a new model for a different optics. Instead, only the last layer will have to be re-trained on additional data for the new optics. This can reduce the amount of training data and time needed to create predictive regression models.

We also investigated the effect of the noise on predictive power of the model. The comparison of prediction errors between models trained on the input data given different noise factors is shown in Table 1. Loss values indicate that the accuracy of the triplet errors prediction is less concerned by the noise than the rest of the magnets. The study shows how important is to keep the measurements noise level as low as possible. Next section focuses specifically on this problem and its possible ML-based solution.

RECONSTRUCTION AND DENOISING OF PHASE MEASUREMENTS

As shown in Table 1, reducing the noise in the phase-advance measurement used as input for quadrupole errors prediction models can potentially improve the accuracy of the prediction. Moreover, the presence of the noise enforces acquisition of several turn-by-turn measurements for each beam in order to obtain statistically significant error bars in the optics functions caused by the uncertainties due to the noise in BPM signal. A possible ML-based solution to reduce the noise in the phase measurements is the application of autoencoder [40]. We trained an autoencoder network on a set of noisy phase measurements simulated as described in the previous section as well as the originally simulated phase measurements. During the training, the autoencoder aims to minimize the difference between true output, i.e simulated phase advances without noise, and the output produced by the network from the noisy input data. To perform the denoising and produce the original phase as output, the model needs to extract features that capture relevant information in the data. Applying an autoecoder trained on 10 000 simulated phase advance measurement sets demonstrates the reduction of the simulated phase noise by a factor of 2.

Another potential application of autoencoder is the reconstruction of missing BPM signal. We trained an autoencoder using simulated phase advance measurements set where 10% data points have been replaced by 0 indicating a missing value, e.g. if a BPM has been identified as faulty and removed in previous analysis stages. As training output we provide the original set of phase advances without missing values, such that autoencoder output can be compared to this original output. The training target is to minimize the difference between original phase advances and autoencoder output. The MAE computed for 100 validation samples is $0.93 \times 10^{-3} [2\pi]$. This method can be applied in order to reconstruct the missing values to provide the input to quadrupole errors prediction regression models trained on simulations.

SUMMARY

Although ML techniques have found their first applications in accelerator physics just a few years ago, they already have been proven as powerful tools for various control, optimization and automation tasks. We presented several applications developed for optics measurements and corrections at the LHC. Operational results of the application of decision tree based technique for faulty BPMs detection show its effectiveness and advantages compared to the cleaning using the traditional techniques only.

The application of regression models allows to gain knowledge about quadrupole errors in the LHC obtaining the entire set of errors around the ring in one step as demonstrated by simulating the LHC optics. It was possible since the the trained model was able to relate the optics deviations from ideal model to magnets errors that caused these perturbations. This has been shown on simulations of 2018 optics as well as on LHC measurements from 2016 commissioning. The quality of phase measurements which is the fundamental part of optics and corrections computation can be potentially improved by applying autoencoder network in order to perform denoising of the measured data and reconstruct the missing BPM signal.

ISBN: 978-3-95450-213-4 ISSN: 2673-5490 doi:10.18429/JACoW-IPAC2020-WEVIR12

REFERENCES

[1] T. Mitchell, "Machine Learning", 1st ed., McGraw-Hill, Inc., New York, USA (1997).

[2] E. Fol, J. M. Coello de Portugal, R. Tomás, "Application of Machine Learning to Beam Diagnostics", presented at the IBIC'18, Shanghai, China, Sep. 2018, paper TUOA02.

[3] E. Fol, R. Tomas, G. Franchetti, and J. M. Coello de Portugal, "Application of Machine Learning to Beam Diagnostics", presented at the FEL'19, Hamburg, Germany, Aug. 2019, paper WEB03.

[4] A. Scheinker *et al.*, "Advanced Control Methods for Particle Accelerators", arXiv:2001.05461v1, 2019.

[5] A. L. Edelen *et al.*, "Neural Networks for Modeling and Control of Particle Accelerators", in *IEEE Transactions on Nuclear Science*, vol. 63, no. 2, pp. 878-897, April 2016. doi:10.1109/TNS.2016.2543203

[6] A. L. Edelen *et al.*, "Opportunities in Machine Learning for Particle Accelerators", arXiv:1811.03172, 2018.

[7] S. Biedron, "Adding Data Science and More Intelligence to Our Accelerator Toolbox", in *Proc. IPAC'19*, Melbourne, Australia, May 2019, pp. 1191–1197. doi:10.18429/JACoW-IPAC2019-TUZPLM1

[8] J. Mockus, *Bayesian Approach to Global Optimization*, Dordrecht, Netherlands: Kluwer Academic Publishers, 1989.

[9] R. S. Sutton, A. G. Barto, *Reinforcement Learning: An Introduction*, MA, USA: MIT Press, 2018.

[10] T. P. Lillicrap *et al.*,"Continuous control with deep reinforcement learning", arXiv:1509.02971 (2015).

[11] A. Scheinker *et al.*, "Demonstration of Model-Independent Control of the Longitudinal Phase Space of Electron Beams in the Linac-Coherent Light Source with Femtosecond Resolution", *Phys. Rev. Lett.*, vol. 121, no. 4, p. 004801, Jul 2018. doi:10.1103/PhysRevLett.121.044801

[12] A. Scheinker, M. Krstic, "Model-free stabilization by extremum seeking", USA: Springer, 2017. doi:10.1007/978-3-319-50790-3

[13] A. Scheinker *et al.*, "Model-independent tuning for maximizing free electron laser pulse energy", *Phys. Rev. Accel. Beams*, vol. 8, p. 082802, Aug. 2019. doi:10.1103/PhysRevAccelBeams.22.082802

[14] J. Duris *et al.*, "Bayesian optimization of a free-electron laser.", *Phys. Rev. Lett.*, vol. 124, no. 12, p. 124801, Mar 2020. doi:10.1103/PhysRevLett.121.044801

[15] C. Emma *et al.*,"Machine learning-based longitudinal phase space prediction of particle accelerators",*Phys. Rev. Accel. Beams*, vol. 21, p. 112802, Nov. 2018. doi:10.1103/PhysRevAccelBeams.21.112802

[16] X. Y. Xu, Y. B. Leng, and Y. M. Zhou, "Machine Learning Application in Bunch Longitudinal Phase Measurement", in *Proc. IPAC'19*, Melbourne, Australia, May 2019, pp. 2625–2628. doi:10.18429/JACoW-IPAC2019-WEPGW064

[17] B. Gao *et al.*, "Deep Learning Applied for Multi-Slit Imaging Based Beam Size Monitor" in *Proc. IPAC'19*, Melbourne, Australia, May 2019, pp. 2587–2590. doi:10.18429/JACoW-IPAC2019-WEPGW049

[18] A. L. Edelen, S. Biedron, S. V. Milton, and J. P. Edelen, "First Steps Toward Incorporating Image Based Diagnostics into Particle Accelerator Control Systems Using Convolutional Neural Networks", in *Proc. NAPAC'16*, Chicago, IL, USA, Oct. 2016, pp. 390–393. doi:10.18429/JACoW-NAPAC2016-TUPOA51

[19] D. Vilsmeier, M. Sapinski and R. Singh, "Space-charge distortion of transverse profiles measured by electron-based ionization profile monitors and correction methods", *Phys. Rev. Accel. Beams*, vol. 22, p. 052801, May. 2019. doi:10.1103/PhysRevAccelBeams.22.052801

[20] G. Ha *et al.*, "Precision control of the electron longitudinal bunch shape using an emittance-exchange beam line", *Phys. Rev. Lett.*, vol. 118, no. 10, p. 104801, Mar 2017. doi:10.1103/PhysRevLett.118.104801

[21] M. Buchanan,"Depths of learning", *Nature Phys.*, vol. 14, p. 328, Apr. 2018. doi:10.1038/s41567-018-0098-8

[22] Y. B. Kong *et al.*,"Predictive ion source control using artificial neural network for RFT-30 cyclotron", *Nucl. Instrum. Meth. A*, vol. 806, pp. 56-60, Jan 2012. doi:10.1016/j.nima.2015.09.095.

[23] A. L. Edelen *et al.*,"Machine Learning to Enable Orders of Magnitude Speedup in Mult-Objective Optimization of Particle Accelerator Systems", *Phys. Rev. Accel. Beams*, vol. 23, p. 044601, Apr. 2020. 10.1103/PhysRevAccelBeams.23.044601

[24] G. Azzopardi *et al.*, "Operational results on the fully automatic LHC collimator alignment", *Phys. Rev. Accel. Beams*, vol. 22, p. 093001, Apr. 2020. 10.1103/PhysRevAccelBeams.22.093001

[25] P. Arpaia, *et al.*, "Machine learning and beam dynamics activities at the CERN Large Hadron Collider", submitted for publication.

[26] T. Persson *et al.*, "LHC optics commissioning: A journey towards 1% optics control", *Phys. Rev. Accel. Beams*,vol. 20, p. 061002, Jun. 2017. 10.1103/PhysRevAccelBeams.20.061002.

[27] R. Tomás *et al.*, "Review of linear optics measurement and correction for charged particle accelerators",*Phys. Rev. Accel. Beams*,vol. 20, p. 054801, May. 2017. 10.1103/PhysRevAccelBeams.20.054801

[28] R. Calaga, R. Tomás, "Statistical analysis of RHIC beam position monitors performance", *Phys. Rev. ST Accel. Beams*,vol. 7, p. 042801, Apr. 2004. 10.1103/PhysRevSTAB.7.042801

[29] F. Liu, K. M. Ting, Z. Zhou, "Isolation Forest", in *Proceedings of the 2008 Eighth IEEE International Conference on Data Mining*, USA, 2008, pp. 413-422. doi:10.1109/ICDM.2008.17.

[30] E. Fol, J. M. Coello de Portugal, and R. Tomás, "Unsupervised Machine Learning for Detection of Faulty Beam Position Monitors", in *Proc. IPAC'19*, Melbourne, Australia, May 2019, pp. 2668–2671. doi:10.18429/JACoW-IPAC2019-WEPGW081

[31] E. Fol, R. Tomás, "Isolation forest algorithm for faulty Beam Position Monitors detection", to be published.

ISBN: 978-3-95450-213-4 ISSN: 2673-5490 doi:10.18429/JACoW-IPAC2020-WEVIR12

[32] A. Langner *et al.*, “Developments of the Segment-by-Segment Technique for Optics Corrections in the LHC”, in *Proc. IPAC’15*, Richmond, VA, USA, May 2015, pp. 419–422. doi:10.18429/JACoW-IPAC2015-MOPJE054

[33] M. Aiba *et al.*, “First β-beating measurement and optics analysis for the CERN Large Hadron Collider”, *Phys. Rev. Accel. Beams*, vol. 12, p. 081002, Aug. 2008. 10.1103/PhysRevSTAB.12.081002

[34] J. W. Dilly *et al.*, “An Updated Global Optics Correction Scheme”, CERN, Geneva, Switzerland, Rep. CERN-ACC-NOTE-2018-0056.

[35] E. Fol, F. S. Carlier, J. M. Coello de Portugal, A. Garcia-Tabares, and R. Tomas, “Machine Learning Methods for Optics Measurements and Corrections at LHC”, in *Proc. IPAC’18*, Vancouver, Canada, Apr.-May 2018, pp. 1967–1970. doi:10.18429/JACoW-IPAC2018-WEPAF062

[36] P. Hagen *et al.*, “WISE: a Simulation of the LHC Optics Including Magnet Geometrical Data”, in *Proc. EPAC’08*, Genoa, Italy, Jun. 2008, paper TUPP091, pp. 1744–1746.

[37] E. Fol, J. M. Coello de Portugal, G. Franchetti, and R. Tomás, “Optics Corrections Using Machine Learning in the LHC”, in *Proc. IPAC’19*, Melbourne, Australia, May 2019, pp. 3990–3993. doi:10.18429/JACoW-IPAC2019-THPRB077

[38] T. L. Lai, H. Robbins, “Strong consistency of least-squares estimates in regression models”, *Journal of Multivariate Analysis*, vol. 23, no. 1, pp. 77–92, 1987. doi:10.1016/0047-259X(87)90179-5

[39] R. M. Rifkin, R. A. Lippert, “Notes on Regularized Least Squares”, Tech. MIT, Massachusetts, USA, Rep. MIT-CSAIL-TR-2007-025, CBCL-268, 2007.

[40] P. Vincent, H. Larochelle,“Stacked Denoising Autoencoders: Learning Useful Representations in a Deep Network with a Local Denoising Criterio”, *Journal of Machine Learning Research*, vol. 11, pp. 3371–3408, Dec. 2010.doi:10.5555/1756006.1953039

ISBN: 978-3-95450-213-4 ISSN: 2673-5490 doi:10.18429/JACoW-IPAC2020-WEVIR16

A NOVEL NONDESTRUCTIVE DIAGNOSTIC METHOD FOR MeV ULTRAFAST ELECTRON DIFFRACTION

X. Yang†, J. Li, M. Fedurin, V. Smaluk, L. Yu, L. Wu, Y. Zhu, T. Shaftan,
Brookhaven National Laboratory, Upton, NY 11973, USA
W. Wan, ShanghaiTech University, Shanghai, China

Abstract

A real-time non-destructive technique to monitor Bragg-diffracted electron beam energy, energy-spread, and spatial-pointing jitter by analysis of the mega-electron-volt ultrafast electron diffraction pattern, is experimentally verified. The shot-to-shot fluctuation of the diffraction pattern is decomposed into two basic modes, i.e., the distance between the Bragg peaks as well as its variation (radial mode) and the overall lateral shift of the whole pattern (drift mode). Since these two modes are completely decoupled, the Bragg-diffraction method can simultaneously measure the shot-to-shot energy fluctuation with $2 \cdot 10^{-4}$ precision and spatial-pointing jitter in the wide range from 10^{-4} to 10^{-1}. The key advantage of this method is the possibility to extract the electron beam energy spread concurrently with the ongoing experiment. This enables the online optimization of the electron beam, especially for future high-charge single-shot ultrafast electron diffraction (UED) and ultrafast electron microscopy (UEM) experiments. Furthermore, the real-time energy measurement enables filtering out off-energy shots, improving the resolution of time-resolved UED. As a result, this method can be applied to the entire UED user community, beyond the traditional electron beam diagnostics used by accelerator physicists.

INTRODUCTION

In recent years, there has been a growing interest in developing single-shot mega-electron-volt (MeV) ultra-fast electron diffraction (UED) systems [1-12]. Comparing to the commonly used electron diffraction in the 100 keV energy range, the main advantages of relativistic electron diffraction are reduced space charge effects and the higher penetration depth. The UED can also resolve much finer structural details compared to X-rays due to the hundreds-fold shorter wavelength of electrons in the required sub-picosecond timescale. However, single-shot imaging with high spatial resolution and small beam size on the sample is a significant challenge and it requires much brighter electron sources. For instance, the RF gun needs to be three orders of magnitude brighter than the present state-of-the-art guns to outrun beam-induced damage of the sample in biomolecular single-particle imaging, achieving "diffraction-before-destruction" [13]. On the other hand, the multi-shot operation requires significantly reduced beam brightness, but with much lower tolerances to the shot-to-shot energy and spatial-pointing fluctuation. To meet these requirements, we need a real-time non-destructive monitor of the electron beam energy and spatial-pointing jitter to characterize the shot-to-shot energy fluctuation and energy spread of the electron beam.

Here we report our proof-of-principle experiment of characterizing the shot-to-shot energy jitter, spatial-pointing jitter, and energy spread of the electron beam for UED and UEM using a novel Bragg-diffraction method (BDM). The experiment was carried out on the existing high-charge high-brightness low-energy electron source developed at Brookhaven National Laboratory (BNL) with the capability of generating 3.3 MeV electron bunches with 10 pC charge (0.62·108 electrons) and 0.1 to 1 ps bunch length [10,11]. We were able to measure simultaneously the shot-to-shot energy fluctuation and spatial-pointing jitter of the electron beam in real-time via eigen-decomposing the variation of the diffraction pattern to two decoupled modes (radial and transverse) and obtain the dispersion of the beamline optics at the detector. Beyond tracking changes of the intensity, position, and width of diffraction patterns [14], we applied the dispersion and Bragg-diffraction (BD) peak width to extract the beam energy spread. The measured beam energy spread agrees reasonably well with Impact-T simulations [15] and with the direct beam-size measurement without crystal diffraction. The non-destructive measurement of the electron beam parameters and beamline optics opens a possibility of online minimization of the shot-to-shot energy jitter, spatial-pointing jitter, and energy spread, which is impossible with the conventional dipole-based diagnostic tools. We have experimentally demonstrated the BDM can provide a nearly complete set of beam-based diagnostic information for online optimization of the RF system stability and minimization of the dispersion at the detector. This is crucial for the future development of single-shot UED and UEM facilities with high-charge electron beam.

EXPERIMENTAL RESULTS

The schematic layout of the UED setup is shown in Figure 1a. The peaks of a BD image shown in Fig. 1b are formed by the summation of the intensity distribution of all diffracted electrons. The diffraction pattern of a single electron is determined by the constructive interference governed by Bragg's law $2d \sin\theta = n\lambda$, where θ is the incident angle, d is the crystal interplanar distance, λ is the de Broglie wavelength, n is the order of Bragg reflections. For the data analysis, we choose two BD peaks (i and j in Fig. 1b) with the largest separation, highest peak intensities, the same reflection order (ni,j = n) and crystal interplanar distance (di,j = d). Before, we compared the result

† xiyang@bnl.gov

ISBN: 978-3-95450-213-4 ISSN: 2673-5490 doi:10.18429/JACoW-IPAC2020-WEVIR16

from one BD-peak pair (i and j) to the result from two pairs (i and j, k and l) and found them similar. The separation between this highest-intensity peak pair (Dij) is determined by the interplane distance d, the distance between the sample and the detector LS2D and the electron beam energy E:

$$D_{ij}(E,d) = L_{S2D} \cdot \{\tan[2\theta_i(E,d)] - \tan[2\theta_j(E,d)]\} = L_{S2D} \cdot 2 \cdot \tan\left[2\sin^{-1}\left(\frac{n\cdot\lambda(E)}{2d}\right)\right] \approx L_{S2D} \cdot \frac{2n\cdot\lambda(E)}{d} \quad (1)$$

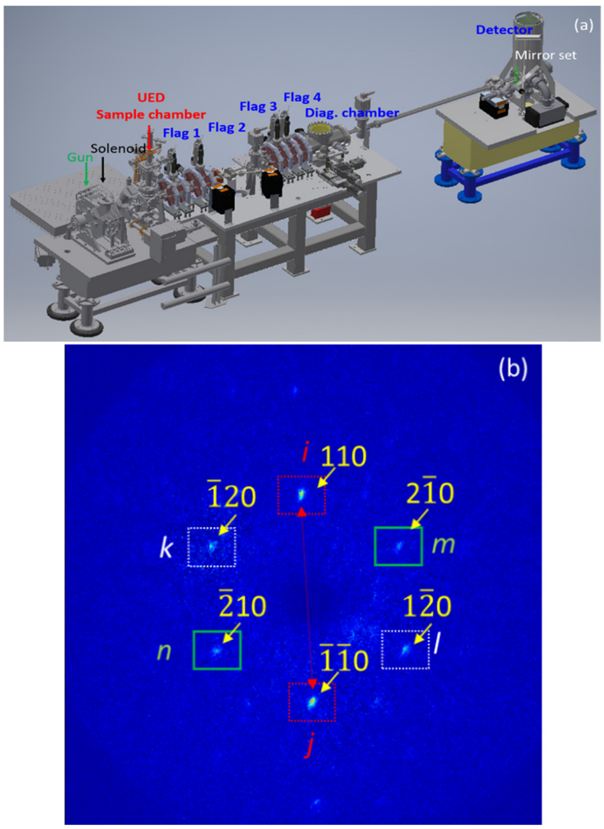

Figure 1: (a) Schematic layout of the UED beamline with marked positions of the UED sample chamber, the YAG screens, and the detector. All the quadrupoles were turned off. (b) Single-shot Bragg diffraction image on the detector. Miller indexes of the Bragg peaks used in data analysis are labelled by yellow colour.

This separation between two BD peaks i and j can be used to measure the electron beam energy and shot-to-shot energy jitter: $\frac{\Delta D_{ij}}{D_{ij}} = \frac{\Delta\lambda}{\lambda} = -\frac{\Delta E}{E}$. The center position of a BD peak can be fitted with precision about 0.05 pixel, which determines the ultimate precision of the energy and energy jitter measurement as 10-4. There is no need for the detailed information of the crystal interplanar distance and the sample-to-detector distance unless one wants to calibrate the absolute beam energy.

There are two basic components associated with the shot-to-shot fluctuation of the BD image. We call the expansion and contraction of the BD image in the radial direction with respect to the image center as the radial mode, and the transverse motion of the whole BD image as the transverse mode. The shot-to-shot energy jitter contributes to the radial mode only, as shown in Figure 2.

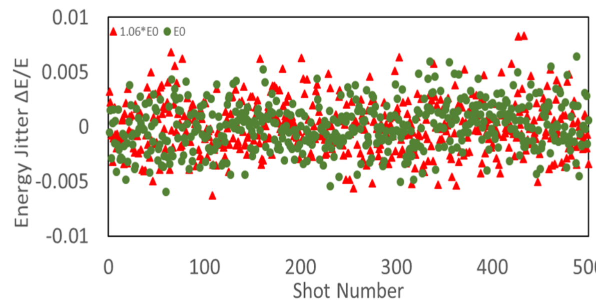

Figure 2: The shot-to-shot energy fluctuation ΔE/E measured at two different beam energies: 0.216% rms at E0 (green) and 0.239% rms at 1.06E0. They are similar.

The transverse mode includes both the spatial-pointing jitter and the dispersive jitter resulted from the combinatory effect of the non-zero dispersion at the detector and the shot-to-shot beam energy fluctuation. The horizontal η_x and vertical η_y dispersion at the detector is caused by the steering from the Earth's magnetic field [10, 11], orbit correctors and the beam off-center at the solenoid. When the beam energy fluctuates shot-to-shot, the non-zero dispersion at the detector results in the transverse motion ΔR of the BD image:

$$R\left(\eta_x, \eta_y, \frac{\Delta E}{E}\right) = \sqrt{\Delta x^2 + \Delta y^2} = \sqrt{\left(\eta_x \cdot \frac{\Delta E}{E}\right)^2 + \left(\eta_y \cdot \frac{\Delta E}{E}\right)^2} = \sqrt{\eta_x{}^2 + \eta_y{}^2} \cdot \frac{\Delta E}{E} \quad (2)$$

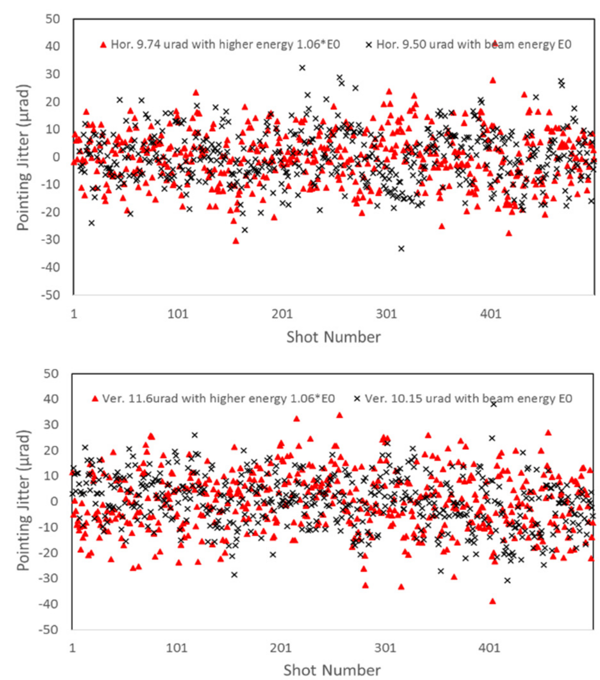

Figure 3: The shot-to-shot pointing jitter measured at two different beam energies: E0 (black) and 1.06E0 (red), the energy jitter is comparably small. The results are similar, about 10 µrad spatial-pointing jitter in both horizontal (top) and vertical (bottom) direction.

If the shot-to-shot energy jitter is small (<0.3% without a slow drift or periodic oscillation), the transverse mode is mainly determined by the spatial-pointing jitter of the UED system (e.g. shot-to-shot laser pointing jitter at the

ISBN: 978-3-95450-213-4 ISSN: 2673-5490 doi:10.18429/JACoW-IPAC2020-WEVIR16

cathode), as shown in Figure 3. However, the spatial-pointing jitter still can be extrapolated from the uncorrelated part of the shot-to-shot 'pointing jitter *vs* energy jitter' dependency, even if the shot-to-shot energy jitter is large. Both cases give similar results, about 10 µrad in both horizontal and vertical directions.

The correlation between the transverse motion of the BD image and the energy jitter can be applied to measure the dispersion. Several sets of data with a large (about 2% peak-to-peak) shot-to-shot energy jitters being were collected and analysed. The overall error of the dispersion measurement is about 6% estimated as $\sqrt{e_1^2 + e_2^2}$. Here the error $e_1 = 0.02$ is caused by the use of different data analysis methods, and $e_2 = 0.06$ is the statistical error. By fitting the pointing jitter vs energy jitter (Fig. 4), we obtain the dispersion $\eta_y \approx 0.0098$ from the equation $\Delta y = \eta_y \cdot \frac{\Delta E}{E}$. Similarly, we obtain $\eta_x \approx 0.004$ with a 10% error.

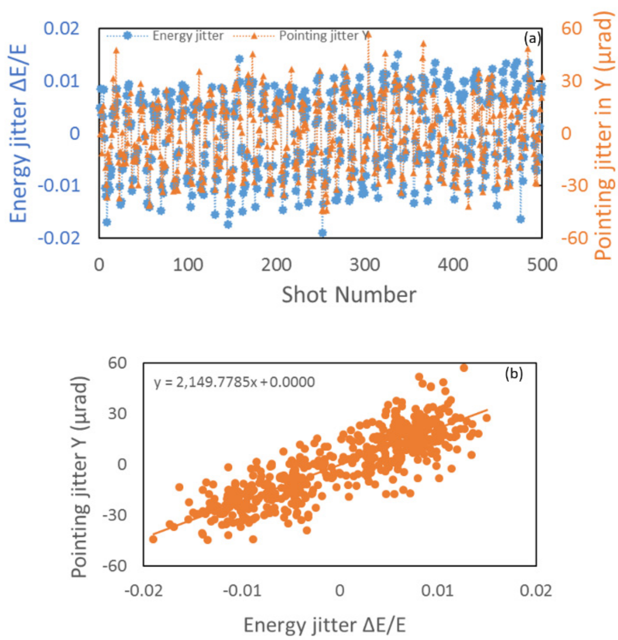

Figure 4: Top: energy jitter (blue, left y-axis) and pointing jitter in y (orange, right y-axis) vs shot number. Bottom: correlation of the pointing jitter and energy jitter.

Different widths σ_x and σ_y of BD peaks are caused by the different dispersions η_x and η_y and the non-zero beam energy spread $\delta E/E$. With the reasonable assumption $\varepsilon_x \approx \varepsilon_y$ and $\beta_x \approx \beta_y$ based on the previous experimental result [10], we can obtain the beam energy spread $\frac{\delta E}{E} = \sqrt{\frac{\sigma_y^2 - \sigma_x^2}{\eta_y^2 - \eta_x^2}}$ using the dispersion measured by the BDM. We compared the energy spread obtained from the measured BD peak widths to the direct beam size measurement without crystal diffraction. The results are consistent and agree reasonably well with Impact-T simulations, as shown in Figure 5. The horizontal error bars come mainly from the laser power fluctuation.

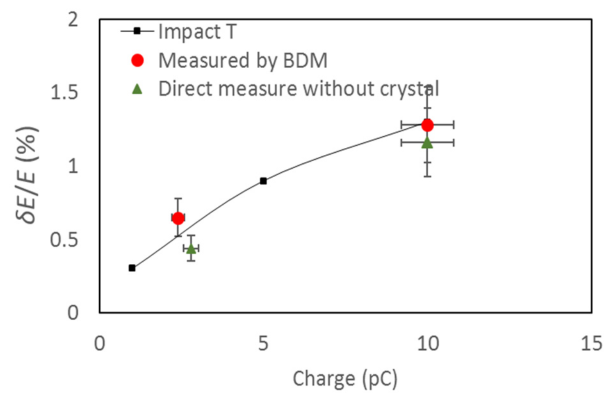

Figure 5: The beam energy spread measured via the BDM (red circles) and direct beam size measurement (green triangles) compared with Impact-T simulations (black squares).

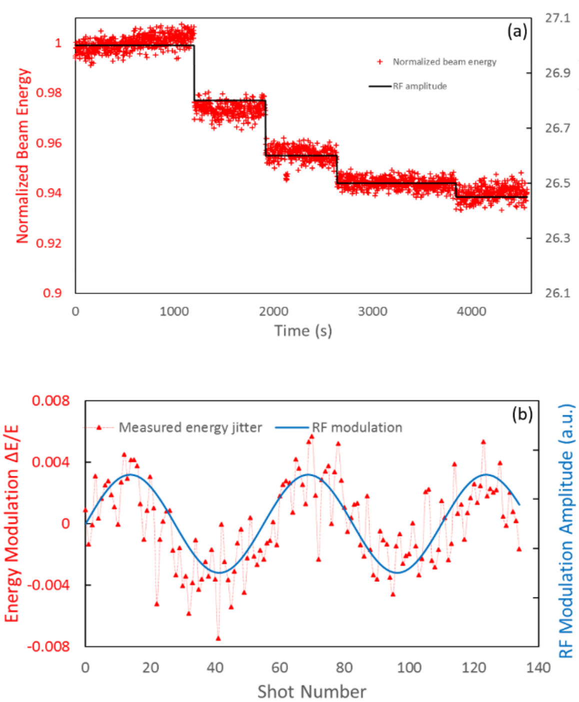

Figure 6: Top: normalized electron beam energy (red, left y-axis) and RF high voltage amplitude (black, right y-axis). Bottom: normalized electron beam energy (red, left y-axis) and LLRF modulator amplitude (blue, right y-axis).

Thus, the BDM can be used to measure the shot-to-shot energy fluctuations, the dispersion, the spatial-pointing jitter, and the beam energy spread. Furthermore, the BDM can be applied to calibrate the electron beam energy in real-time with different RF settings. We measured the beam energy while the RF high-voltage amplitude was varied, the results are shown as Fig. 6a. We also modulated the low-level RF (LLRF) input of the high-voltage amplifier with a sine wave and measured the beam energy variation by the BD method, the result is shown in Fig. 6b. The reason why we chose to vary the beam energy via modulating the amplitude of the LLRF drive signal is that this modulation varies only the RF amplitude not the phase seen by the beam. This feature allows the measurement to be

ISBN: 978-3-95450-213-4 ISSN: 2673-5490 doi:10.18429/JACoW-IPAC2020-WEVIR16

automated because there is no need for the phase correction during the measurement.

CONCLUSION

It is important to monitor the stability of the electron beam non-destructively during the UED experiments. The novel BDM provides an in-situ measurement of the electron beam parameters and beamline optics. Compared to the conventional destructive method based on the beam deflection by a dipole magnet, the unique combination of non-destructiveness and capability of simultaneous measuring the electron beam energy, position and width enables the online optimization of the beam parameters. This is especially important for the future high-charge single-shot UED and UEM development. The dispersion can be measured precisely with a large shot-to-shot energy oscillation. However, if the energy fluctuation is small, we can deliberately introduce an RF modulation with the desired amplitude. The BDM can also be a powerful tool for the RF system diagnostics and troubleshooting. As a further development, we plan to install a quadrupole quadruplet downstream of the mirror reflecting the diffraction pattern to the detector. This mirror has a hole in the center allowing the core of the non-interacted electron beam to pass through and reach the dump. The standard quadrupole scan can provide missing information of the beam emittance to make the online non-destructive diagnostic package complete [16].

REFERENCES

[1] L. Yu, Y. Zhu, T. Shaftan, L. Doom, BNL LDRD # 16-010, 63 (2016). https://www.bnl.gov/ldrd/files/pdf/2016_LDRD_Activities.pdf

[2] P. Zhu, et al., "Femtosecond time-resolved MeV electron diffraction", *New J. of Physics* **17**, 063004 (2015). doi:10.1088/1367-2630/17/6/063004

[3] A. He, F. Willeke, and L. H. Yu, "Ultrashort x-ray pulse generation by electron beam slicing in storage rings", *Phys. Rev. ST Accel. Beams* **17**, 040701 (2014). doi:10.1103/PhysRevSTAB.17.040701

[4] A. He et al., "Design of low energy bunch compressors with space charge effects", Phys. Rev. ST Accel. Beams 18, 014201, (2015). doi:10.1103/PhysRevSTAB.18.014201

[5] J. Yang, et al., "Diffractive imaging of a rotational wavepacket in nitrogen molecules with femtosecond megaelectronvolt electron pulses", *Nat. Commun.* **05**, 11232 (2016). doi:10.1038/ncomms11232

[6] S. P. Weathersby, et al., "Mega-electron-volt ultrafast electron diffraction at SLAC National Accelerator Laboratory", *Rev. Sci. Instrum.* **86**, 073702 (2015). doi:10.1063/1.4926994

[7] F. Fu, et al., "High quality single shot ultrafast MeV electron diffraction from a photocathode radio-frequency gun", *Rev. Sci. Instrum.* **85**, 083701 (2014). doi:10.1063/1.4892135

[8] P. Musumeci, et al., "High quality single shot diffraction patterns using ultrashort megaelectron volt electron beams from a radio frequency photoinjector", *Rev. Sci. Instrum.* **81**, 013306 (2010). doi:10.1063/1.3292683

[9] R. Li, et al., "Experimental demonstration of high quality MeV ultrafast electron diffraction", *Rev. Sci. Instrum.* **80**, 083303 (2009). doi.org/10.1063/1.3194047

[10] Yang, X., Yu, L., Smaluk, V. et al. "A compact tunable quadrupole lens for brighter and sharper ultra-fast electron diffraction imaging", *Sci Rep* **9**, 5115 (2019). doi:10.1038/s41598-019-39208-z

[11] X. Yang et al., "Tuning Quadrupoles for Brighter and Sharper Ultra-fast Electron Diffraction Imaging", in *Proc. 10th Int. Particle Accelerator Conf. (IPAC'19)*, Melbourne, Australia, May 2019, pp. 3571-3573. DOI: 10.18429/JACoW-IPAC2019-THPMP053

[12] W. Wan, F. Chen, and Y. Zhu, "Design of compact ultrafast microscopes for single- and multi-shot imaging with MeV electrons", *Ultramicroscopy* **194**, 143-153 (2018). doi:10.1016/j.ultramic.2018.08.005

[13] J. C. H. Spence, "Outrunning damage: Electrons vs X-rays—timescales and mechanisms", *Struct. Dyn.* 4 (2017) 044027. doi:10.1063/1.4984606

[14] Weathersby et al., "Mega-electron-volt ultrafast electron diffraction at SLAC National Accelerator Laboratory", *Rev. Sci. Instrum.* **86,** 073702 (2015). doi:10.1063/1.4926994

[15] J. Qiang, S. Lidia, R. D. Ryne, C. Limborg-Deprey, "Three-dimensional quasistatic model for high brightness beam dynamics simulation", *Phys. Rev. Special Topics - Accel. Beams* 9, 044204, (2006). doi:10.1103/PhysRevSTAB.9.044204

[16] M. Minty, Diagnostics. CERN Accelerator School, 2004.

ISBN: 978-3-95450-213-4 ISSN: 2673-5490 doi:10.18429/JACoW-IPAC2020-THVIR12

FLASH RADIATION THERAPY: ACCELERATOR ASPECTS

Patriarca†, L. De Marzi, S. Meyroneinc, V. Favaudon, Institut Curie, Orsay, France

Abstract

One of the new paradigms in radiation therapy (RT) is the FLASH dose delivery irradiation technique. The FLASH methodology consists in delivering millisecond pulses of radiation (total beam-on time < 100-500 ms) delivered at a high mean dose-rate (> 40-100 Gy/s) and pulse amplitude (≥ 106 Gy/s), over 2000 times faster than in conventional RT. New accelerator ideas are under development or are being tested to deliver this type of beam. In this paper we will report the accelerator technology used for the pre-clinical studies and the necessary developments to deliver this novel dose RT technique.

INTRODUCTION

Radiation therapy (RT) is one of the most effective cancer treatment and control, and is used in the treatment of 50 to 60% of cancers. Over 95% of the cancer treatment using RT techniques are realised with linear accelerators delivering MV photons or electron of less than 25 MeV. These machines are combined with multi-leaf collimators to adapt the beam to the tumour shape and imaging devices for positioning the patient. One of the main limitations of RT is that the dose delivered to the tumour is constrained by the dose that can be tolerated by the surrounding normal tissues. Recently, a strategy to overcome this limitation, based on the optimisation of the dose delivery method by using non-conventional temporal microstructures of the beam was proposed [1]. The so-called FLASH-RT has emerged. In the following, a short review of the main pre-clinical radiobiology studies is presented with a special focus on the accelerators used to deliver a FLASH irradiation. Subsequently the up-to-date machine designs for clinical applications are discussed.

THE FLASH EFFECT

The "FLASH effect” was proposed by Favaudon et al. at Institut Curie (France) [1] as the result of very high dose-rate irradiation (pulse amplitude ≥ 10^6 Gy/s, or mean dose rate > 40 Gy/s), short beam-on duration (≤ 500 ms) and large doses per fraction (≥ 10 Gy) on in-vivo samples [2]. The lung fibrogenesis in C57BL/6J mice receiving 15–17 Gy in bilateral thorax irradiation with 4.5 MeV pulsed electron beams was investigated. Animals were exposed to single doses in short pulses so that the total irradiation time was less than 500 ms. Mice were also exposed to “conventional” (CONV) dose-rate irradiations (≤ 0.03 Gy/s). No complications were developed on the healthy tissues after a FLASH irradiation (up to 23 Gy), while the CONV treatment generates lung fibrosis in the totality of the irradiated animals. In contrast, FLASH was as efficient as CONV when irradiating tumours (Fig. 1).

These results were also reproduced and thoroughly extended by several teams in the last five years. In particular, the group headed by Dr. Vozenin in Lausanne (Switzerland) reported excellent results on mice, cats, pigs (summarised in a review article [3]), and a promising outcome in the treatment of a first human patient has also been reported [4]. Very recently, the biological mechanisms that underlie the FLASH effect in lung have also been identified [5].

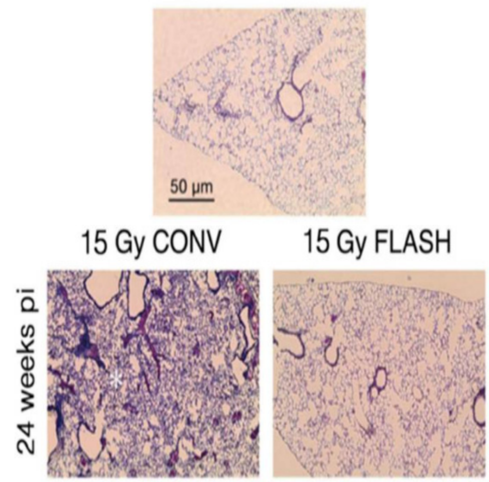

Figure 1: FLASH irradiation spares lung at doses known to induce fibrosis in mice following conventional dose-rate irradiation (CONV) (modified from [1]).

ACCELERATORS USED IN THE PRE-CLINICAL FLASH STUDIES

In the next section, an overview of the machines used to study the FLASH effect is presented.

Prototypes Low-Energy Electron LINACs

Kinetron, the “reference” accelerator used by Dr. Fauvaudon at Institut Curie is a S-band linear electron accelerator designed by a French company (CGR-MeV) in 1987 to investigate free radical reactions in macromolecules at the submicrosecond time-scale and the electron transfer kinetics [6] (Fig. 2). It is a compact electron linac with nominal energy of 4.5 MeV, and a set of parameter easily adjustable as the pulse repetition frequency (0.1 – 200 Hz), the pulse length (0.05 – 2 µs) and with a mean dose rate up to 7000 Gy/s. The Kinetron is powered by a magnetron and is fitted with a thermionic triode electron gun. Precise adjustment of the grid potential of the triode allows the total control of the emitted current and pulse width in the FLASH operating mode. A more complete description of the machine parameters can be found in [6, 7].

Oriatron eRT6, the general design of the machine by PMB-Alcen was derived by the Kinetron. The 6 MeV

† annalisa.patriarca@curie.fr

ISBN: 978-3-95450-213-4 ISSN: 2673-5490 doi:10.18429/JACoW-IPAC2020-THVIR12

experimental linac was recently installed at the Lausanne University Hospital (Switzerland) also for preclinical studies. The specificity of the eRT6 accelerator design is the possibility to work at high-dose rates using a much higher beam current (maximum peak current ~ 300 mA and mean value of 30 µA) than conventional electron clinical machines (peak current ~ 1mA and mean value of 0.1 µA). More details can be found in [8].

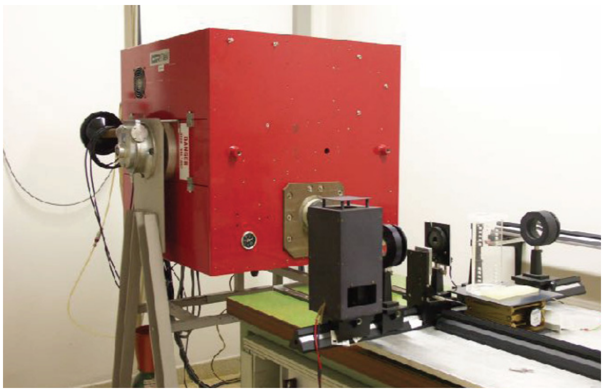

Figure 2: Kinetron accelerator.

Modified Clinical Electron LINACs

The following linacs [9, 10] have been successfully employed to deliver electron beams with dose rate exceeding 200 Gy/s. The bremsstrahlung target was removed and the irradiation position of the samples was chosen to be an intermediate position inside the treatment head allowing a good compromise between dose rate, field size and flatness. However, the field sizes obtained are only suitable for small-animal experiments.

Schüler et al. [9] succeeded in delivering FLASH dose-rates (~ 200 Gy/s) using a modified Varian Clinac 21EX at 9 and 20 MeV. A 13-fold increase in dose rate was observed for the 9 MeV beam at 400 nA and a 40-fold for the 20 MeV beam at 110 nA.

Lempart et al. [10] also proposed some methods to achieve an increased dose rate (up to 300 Gy/s) on an 8 MeV Elekta Precise linac in particular by removing the scattering foils from the beam path.

Photons Sources: Synchrotron Light Sources

To date, FLASH effect using photons beams has been demonstrated using ultrahigh dose rate x-ray beams generated at a synchrotron light source (the European Synchrotron Research Facilities - ESRF, France) [11]. A quasi-continuous 100 keV x-rays beam was delivered with an in-slice dose rate of 12,000 Gy/s (200 mA peak current, mean dose rate 37 Gy/s). Despite a major interest as a research tool, synchrotron beams are now limited as they can only cover small field sizes, and in addition kV x-rays are usually not well suited for the treatment of deep-seated tumours.

Protons Sources: Cyclotrons

Several research groups are investigating the feasibility of FLASH-RT with proton beams. In particular, the capabilities of proton accelerators to achieve high instantaneous pulsed dose rate and high mean dose rate as required for the FLASH effect [12, 13, 14] are investigated. A group from Institut Curie (France) published an example of irradiation setup that can be found in Fig. 3 [12]. Very recently, Diffenderfer el al. [15] has demonstrated a significant FLASH effect while irradiating mice intestine (loss of proliferating cells in intestinal crypts) with a 230 MeV scattered proton beam at high dose-rate (around 90 Gy/s) with an isochronous cyclotron. This promising result is however mitigated by the maximum field size that can be used to ensure such a dose rate, limited to a few cm diameter targets.

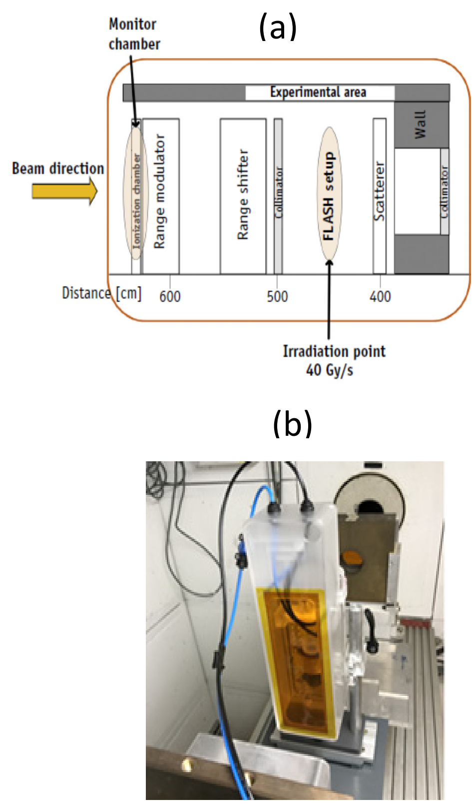

Figure 3: (a) Beamline used for the proof of concept of FLASH proton irradiation at Institut Curie and (b) setup for small animal experiments.

ACCELERATORS FOR CLINICAL FLASH IRRADIATIONS

In the attempt to bring FLASH-RT towards clinical operations, the accelerator "magic bullet" is still to be defined. Among the challenges to be solved, from the accelerator point of view one should answer the question: how to produce beam intensities capable of delivering tens of Gy in less than 500 ms, and preferably not more than 100 ms? There is an evident need to increase by hundreds-fold the beam output of the machine, which ideally has to fit existing clinical vaults, should be easy to operate and

ISBN: 978-3-95450-213-4 ISSN: 2673-5490 doi:10.18429/JACoW-IPAC2020-THVIR12

maintain, cost-affordable, and which can be coupled with imaging devices for the patient positioning (all the more so since the irradiation will be very short and hypofractionated). To date, the only proposed solution is a MV photon source – the PHASER (Pluridirectional High-energy Agile Scanning Electronic Radiotherapy) [16] (Fig. 4). The favorable depth-dose characteristics and reduced entrance doses of MV photons remain interesting for future 3D volume optimization. But according to the authors the use of Very High Energy Electrons (VHEE) is also a possible alternative as VHEE may be advantageous in terms of depth-dose profile, reduced lateral scattering (low penumbrae) and enabling pencil beam scanning, favoring better dose conformity and integral dose intermediate between photons and protons.

PHASER

To answer the question: how to produce hundreds-fold beam output (with respect to conventional accelerators)? Maxim et al. [16] proposed the use of a new accelerator science to invent an innovative RF power distribution: DRAGON Distributed RF-coupling Architecture with Genetically Optimized cell desigN. The idea is to distribute the RF power independently to each cell without coupling between the cells: in this way the system achieves higher efficiency (80% vs 20% for standard clinical linacs), higher shunt impedance (2.5-4-fold: 200 MΩ/m at X-band) and a higher repetition rate.

In order to fit the existing treatment vaults, the authors propose the use of compact RF phased-Array Power Distribution of waveguides (RAPiD) : 16 (at least) power input combine the power of modular small klystrons (klystrinos) in order to feed the 16 output port, that are coupled with 16 stationary beamlines capable to deliver intensity modulated beams without any mechanical device/motions by using a dedicated electron beam scanning system (Scanning Pencil-beam High-speed INtensity-modulated X-ray source (SPHINX). Thanks to a stationary bremsstrahlung target and a fixed collimator it is possible to perform intensity modulated treatment without collimators. To perform positioning for the treatment a solution is also provided.

To conclude, the various solutions proposed by the SLAC/Stanford team show that R&D on accelerator and RF power designs can make RT more affordable, allows a better exploitation of the potential of FLASH irradiations, a reduction in costs, and space requirements can be ensured by multiplexing the RF sources (the peak power from each source can be reduced). High clinical efficiency can be obtained by combining multiple linacs with CT scanners for motion management.

The authors also proposed a system to deliver VHEE FLASH RT. Technically they suggest the production of a spatially patterned electron source by projecting an optical image into a photocathode. The electron "image" is then accelerated intact through a high-gradient DRAGON linac, steered and augmented to the treatment volume, producing an intensity-modulated treatment field.

This solution is motivated by the much lower beam current needed when treating directly with VHEE (no bremsstrahlung target), and by the potential advantages of using VHEE in RT, like a flatter depth-dose profile than photons or a less sensitivity to heterogeneities [17]. In addition, thanks to recent high-gradient linac technology developments, (CLIC >100 MV/m, W-band >200MV/m) VHEE (100–250 MeV) could be a cost-effective option in RT. In this regard, several groups have realized dosimetry studies at multiple facilities with VHEE at high dose rates [18, 19, 20, 21].

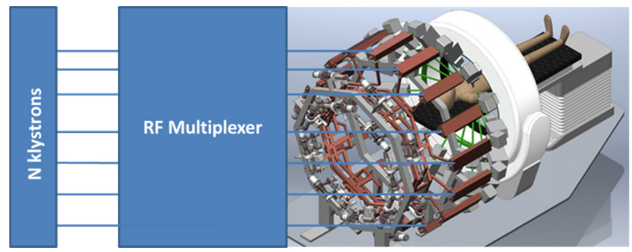

Figure 4: PHASER design (modified from [14]).

CONCLUSION

FLASH-RT pre-clinical studies, with different particle sources and types, has demonstrated an increased therapeutic index enabling higher doses well tolerated by normal tissues, and represents a promising irradiation technique aiming at reducing RT potential side effects. Multidisciplinary teams are working together to provide further studies that enable to understand the impact of the total dose per fraction, temporal patterning and fractionation scheme, total exposure rate, protocols for the beam calibration and absolute dosimetry [22], radiation quality impact on the tissue response, as well as the fundamental biological mechanisms. The accelerator community could play an important role in the development of alternative solutions to provide FLASH irradiators, in order to develop future clinical trials, and help to find some strategies to irradiate large volumes in less than a few hundreds of ms with important doses.

ACKNOWLEDGEMENTS

The authors would like to thank Dr. Faus-Golfe for fruitful discussions.

REFERENCES

[1] V. Favaudon *et al.*, "Ultrahigh dose-rate FLASH irradiation increases the differential response between normal and tumour tissue in mice", *Sci.Transl Med* 2014;6:245-293. DOI: 10.1126/scitranslmed.3008973

[2] A. Mazal *et al.*, "FLASH and minibeams in radiation therapy: the effect of microstructures on time and space and their potential application to protontherapy.", *Br J Radiol* 2020; 93: 20190807. DOI: 10.1259/bjr.20190807

[3] M. C. Vozenin *et al.*, "Biological Benefits of Ultra-high Dose Rate FLASH Radiotherapy: Sleeping Beauty Awoken", *Clin Oncol (R Coll Radiol)* 2019;31(7):407-415. DOI: 10.1016/j.clon.2019.04.001

[4] J. Bourhis, W. J. Sozzi, P. G. Jorge *et al.,* "Treatment of a first patient with FLASH-radiotherapy", *Radiother Oncol*. 2019;139:18-22. DOI: 10.1016/j.radonc.2019.06.019

[5] C. Fouillade, S. Curras-Alonso, L. Giuranno *et al.*, "FLASH irradiation spares lung progenitor cells and limits the incidence of radio-induced senescence", *Clin Cancer Res.* 2020;26:1497-1506. DOI: 10.1158/1078-0432.CCR-19-1440

[6] V. Favaudon *et al.*, "Time-resolved dosimetry of pulsed electron beams in very high dose-rate, FLASH irradiation for radiotherapy preclinical studies", *Nucl. Instrum. Methods*, Volume 944, 2019, 162537, ISSN 0168-9002, https://doi.org/10.1016/j.nima.2019.162537.

[7] P. Lansonneur *et al.*, "Simulation and experimental validation of a prototype electron beam linear accelerator for preclinical studies." *Phys Med.* 2019;60:50-57. DOI: 10.1016/j.ejmp.2019.03.016

[8] M. Jaccard, M.T. Durán, K. Petersson, *et al.*, "High dose-per-pulse electron beam dosimetry: Commissioning of the Oriatron eRT6 prototype linear accelerator for preclinical use", *Med Phys*. 2018; 45(2):863-874. DOI: 10.1002/mp.12713

[9] E. Schüler, S. Trovati, G. King, *et al.*, "Experimental Platform for Ultra-high Dose Rate FLASH Irradiation of Small Animals Using a Clinical Linear Accelerator", *Int J Radiat Oncol Biol Phys*. 2017;97(1):195-203. DOI: 10.1016/j.ijrobp.2016.09.018

[10] M. Lempart, B. Blad, G. Adrian, et al., "Modifying a clinical linear accelerator for delivery of ultra-high dose rate irradiation.", *Radiother Oncol.* 2019;139:40-45. DOI: 10.1016/j.radonc.2019.01.031

[11] P. Montay-Gruel, A. Bouchet, M. Jaccard et al., "X-rays can trigger the FLASH effect: Ultra-high dose-rate synchrotron light source prevents normal brain injury after whole brain irradiation in mice" *Radiother Oncol.* 2018;129(3):582-588. DOI: 10.1016/j.radonc.2018.08.016

[12] A. Patriarca, C. Fouillade, M. Auger et al., "Experimental set-up for FLASH proton irradiation of small animals using a clinical system", *Int J Radiat Oncol Biol Phys* 102 (3) (2018) 619–626. DOI: 10.1016/j.ijrobp.2018.06.403

[13] S. Van de Water, S. Safai, J. M. Schippers, D. C. Weber and A. J. Lomax, "Towards FLASH proton therapy: the impact of treatment planning and machine characteristics on achievable dose rates", *Acta Oncologica* 58 (2019) 1463–1469. DOI: 10.1080/0284186X.2019.1627416

[14] P. Van Marlen, M. Dahele, M. Folkerts *et al.*, "Bringing FLASH to the clinic: Treatment planning considerations for ultrahigh dose-rate proton beams", *Int J Radiat Oncol Biol Phys*. 2019;106:621-629. https://doi.org/10.1016/j.ijrobp.2019.11.011

[15] E. S. Diffenderfer, I. I. Verginadis, M. N. Kim *et al.*, "Design, Implementation, and in Vivo Validation of a Novel Proton FLASH Radiation Therapy System", *Int J Radiat Oncol Biol Phys*. 2020; 106(2):440-448. DOI: 10.1016/j.ijrobp.2019.10.049

[16] P. G. Maxim, S. G. Tantawi and B. W. Jr Loo, "PHASER: A platform for clinical translation of FLASH cancer radiotherapy", *Radiother Oncol*. 2019; 139:28-33. DOI: 10.1016/j.radonc.2019.05.005

[17] C. DesRosiers, V. Moskvin, A.F. Bielajew, L, Papiez, "150-250 meV electron beams in radiation therapy", *Phys Med Biol*. 2000; 45(7):1781-1805. DOI: 10.1088/0031-9155/45/7/306

[18] A. Lagzda, R. M. Jones, D. Angal-Kalinin, J. K. Jones, and K. Kirkby, "Relative Insensitivity to Inhomogeneities on Very High Energy Electron Dose Distributions", in Proc. *8th Int. Particle Accelerator Conf. (IPAC'17)*, Copenhagen, Denmark, May 2017, pp. 4791–4794. DOI: 10.18429/JACoW-IPAC2017-THPVA139

[19] M. Bazalova-Carter, M. Liu, B. Palma *et al.*, "Comparison of film measurements and Monte Carlo simulations of dose delivered with very high-energy electron beams in a polystyrene phantom", *Med Phys.* 2015;42(4):1606-1613. DOI: 10.1118/1.4914371

[20] A. Subiel, V. Moskvin, G. H. Welsh *et al.*, "Dosimetry of very high energy electrons (VHEE) for radiotherapy applications: using radiochromic film measurements and Monte Carlo simulations", *Phys Med Biol.* 2014;59(19):5811-5829. DOI:10.1088/0031-9155/59/19/5811

[21] L. Karsch, E. Beyreuther, T. Burris-Mog *et al.*, "Dose rate dependence for different dosimeters and detectors: TLD, OSL, EBT films, and diamond detectors", *Med Phys.* 2012; 39(5):2447-2455. DOI: 10.1118/1.3700400

[22] Metrology for advanced radiotherapy using particle beams with ultra-high pulse dose rates. http://uhdpulse-empir.eu

CERN-MEDICIS: A UNIQUE FACILITY FOR THE PRODUCTION OF NON-CONVENTIONAL RADIONUCLIDES FOR THE MEDICAL RESEARCH

C. Duchemin[1,2], J. P. Ramos[1,2,*] , T. Stora[1,†], E. Aubert[1], N. Audouin[3], E. Barbero[1], V. Barozier[1], A. P. Bernardes[1], P. Bertreix[1], A. Boscher[1], D. Burnel[1], R. Catherall[1], M. Cirilli[1], E. Chevallay[1], T. E. Cocolios[2], J. Comte[1], B. Crepieux[1], M. Deschamps[1], K. Dockx[2], A. Dorsival[1], V. N. Fedosseev[1], P. Fernier[1], R. Formento-Cavaier[1,3], V. M. Gadelshin[1,4,5], S. Gilardoni[1], J. L. Grenard[1], F. Haddad[3,6], R. Heinke[2], B. Juif[1], M. Khan[7], U. Köster[8], L. Lambert[1], G. Lilli[1], G. Lunghi[1], B. A. Marsh[1], Y. Martinez Palenzuela[2], R. Martins[1], S. Marzari[1], N. Menaa[1], N. Michel[3,6], F. Pozzi[1], F. Riccardi[1], J. Riegert[1], N. Riggaz[1], S. Rothe[1], S. Stegemann[2], Z. Talip[9], J. Thiboud[1], N. P. van der Meulen[9], J. Vollaire[1], N. T. Vuong[1], K. Wendt[4], S. Wilkins[1],
on behalf of the CERN-MEDICIS collaboration
[1]CERN, Geneva, Switzerland
[2]KU Leuven, Institute for nuclear and radiation physics, Leuven, Belgium
[3]GIP ARRONAX, Nantes, France
[4]Johannes Gutenberg University, Mainz, Germany
[5]Ural Federal University, Yekaterinburg, Russia
[6]SUBATECH, Institut Mines Telecom Atlantique, CNRS/IN2P3, Université de Nantes, France
[7]Pakistan Institute of Nuclear Science and Technology, Islamabad, Pakistan
[8]Institut Laue Langevin, Grenoble, France
[9]Paul Scherrer Insitute, Villigen, Switzerland

Abstract

CERN-MEDICIS (MEDical Isotopes Collected from ISolde) is a facility at CERN (Switzerland) dedicated to the production of non-conventional radionuclides for research and development in imaging, diagnostics and radiation therapy done at partner institutes. It exploits, in a controlled radiation area suited for the handling of unsealed radioactive sources, a target irradiation station positioned between the High Resolution Separator (HRS) ISOLDE target station and its beam dump, a target remote handling system and a dedicated isotope separator beam line. It irradiates targets with the 1.4 GeV Proton Synchroton Booster (PSB), and also receives activated target materials from external institutes, notably during CERN's Long Shut-Downs. The irradiated target is heated to high temperatures (up to 2300°C) to allow for the release of the isotopes of interest out of the target which are subsequently ionized. The ions are accelerated and the beam is steered through an offline mass separator. The radionuclide batches are, this way, extracted through mass separation and implanted into a thin metallic collection foil up to an energy of 60 keV. After collection, the isotope source is prepared to be dispatched to biomedical research centers (Figure 1).

Since its commissioning in December 2017, the CERN-MEDICIS facility has provided non-conventional medical radionuclides such as Tb-149, Tb-152, Tb-155, Tm-165, Er-169 and Yb-175 with high specific activity, some for the first time, to research institutes and hospitals, being part of the MEDICIS collaboration, for R&D in imaging or treatment [1].

* Current affiliation: SCK CEN, Mol, Belgium
† Corresponding author: thierry.stora@cern.ch

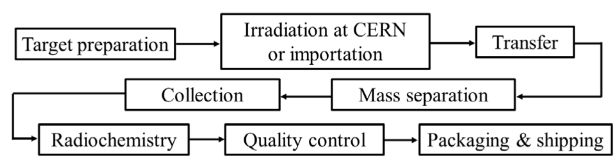

Figure 1: CERN-MEDICIS' steps from target preparation to radioisotopes shipping.

THE CERN-MEDICIS COLLABORATION

The research program at CERN-MEDICIS is driven by a collaboration agreement between CERN and several partners which includes research institutes, hospitals and universities [1]. The installation has been built as an extension of the ISOLDE facility [2] for research purposes on medical isotopes in view of providing the collaborating institutes with radioisotopes of high specific activity for their research programs [3]. The CERN-MEDICIS scientific program is shaped from the biomedical projects submitted by the members to the Collaboration Board which evaluates the needs of the community and the technical feasibility. The first collection of radionuclides took place in December 2017 at the end of the commissioning period. Since then, the collaboration board approved already 25 proposals. The list of radionuclides of interest once defined is thus re-evaluated at each board, mostly for applications in theranostics, combining diagnosis and therapy. Among them we can find scandium isotopes such as Sc-44 and Sc-47 [4-6]. Sc-44 is of interest for Positron Emission Tomography (PET) and Sc-47 for use in both, therapy and Single Photon Emission Computed Tomography (SPECT). As for Sc-47, Cu-67 is a radionuclide of interest for theranostic

ISBN: 978-3-95450-213-4 ISSN: 2673-5490 doi:10.18429/JACoW-IPAC2020-THVIR13

applications [7]. CERN-MEDICIS has already demonstrated the possibility of producing three out of the four terbium isotopes of high interest for nuclear medicine [8], which include the alpha emitter Tb-149 [9], the positron emitter Tb-152 [10], the gamma and Auger emitter Tb-155 [11]. Completing this so-called "swiss army knife" of nuclear medicine [12], is Tb-161 which is available from nuclear reactors. CERN-MEDICIS is also focusing on the collection of Sm-153, Tm-167, Er-169, Yb-175 and the alpha emitter Ac-225 [1]. These radionuclides are produced either by using the PSB beam [13], or using target materials irradiated at external partner institutes, such as the high flux reactor at Institut Laue Langevin (ILL) in Grenoble (France) [14] and at the high power cyclotron at ARRONAX (Accélerateur pour la Recherche en Radiochimie et en Oncologie à Nantes Atlantique) in Nantes (France) [15].

IRRADIATION AT ISOLDE WITH THE CERN PROTON BEAM

Before each irradiation a dedicated target unit is built, which is compatible with both ISOLDE and MEDICIS facilities. It is composed of a water-cooled aluminium vacuum vessel which encloses a tubular tantalum oven inside of which a target material is placed. As can be seen in Figure 2, the MEDICIS target is larger (50 mm diameter) than the ISOLDE one (20 mm diameter). The oven is connected to an ion source via a transfer line [16]. The target is brought from the CERN-MEDICIS laboratory to the ISOLDE target area via an automatic rail conveyor system (RCS). The MEDICIS target is installed for irradiation between the HRS target station onto which the proton beam is directed for the online mass separation performed at ISOLDE, and the beam dump. The MEDICIS target is irradiated by the fraction of the primary proton beam which did not interact with the ISOLDE target and by the secondary particles generated from the ISOLDE target's irradiation. FLUKA simulations [17, 18] have been performed in order to assess the number of primary protons and their energy spectrum that reach the MEDICIS target with ISOLDE targets made of different materials. The geometry [19] includes the full representation of the ISOLDE and MEDICIS targets (see Figure 2) with the beam dump located downstream of the MEDICIS target. Analytically, the number of hadrons $N(x)$ that reach the end of an ISOLDE target (x=19.6 cm) without being subject to any inelastic interaction can be expressed as [20]:

$$N(x) = N_0\,.\exp(-x/\lambda) \qquad (1)$$

with N_0 the initial number of primaries entering the volume, x the length of the target in cm and λ the inelastic interaction length at beam energy in cm, which is characteristic for each target material.

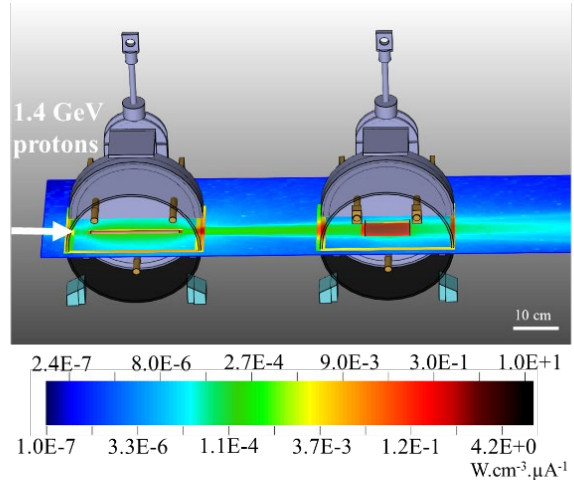

Figure 2: Visualisation of the ISOLDE (left) and MEDICIS target (right) irradiated by the 1.4 GeV proton beam. The deposited energy is represented in $W.cm^{-3}.\mu A^{-1}$.

The first column in Table 1 gives a summary of the ISOLDE target materials with their apparent density in the second column. Column 3 gives the fraction F of hadrons $N(x)/N_0$ using equation (1), while column 4 provides F obtained by FLUKA simulations (star density, a star being defined as a hadronic inelastic interaction occurring at an energy higher than 50 MeV). It should be noted that ISOLDE uses UC_2-2C targets with an apparent density of 3.5 $g.cm^{-3}$ [3] for about 60% of its physics program. Consequently, the MEDICIS target can exploit about 2/3 of the PSB's primary protons (see Table 1).

Table 1: Fraction F of primary protons leaving the ISOLDE target unit without inelastic interaction.

ISOLDE target material	Density ($g.cm^{-3}$)	F – equation (1)	F – Monte Carlo
UC_2-2C [3]	3.5	64%	69%
Ta [3]	2.0‡	80%	83%
UC_2-2C (nano) [21]	1.4	85%	86%
Ti [3]	0.8	88%	89%
CaO [22]	0.4	93%	93%
None§	-	97%	97%

Figure 3 shows the proton fluences in lethargy representation, expressed in $cm^{-2}.primary^{-1}$, at the entrance and at the exit of an ISOLDE UC_2-2C target, and at the entrance of the MEDICIS target. This figure illustrates that for 60% of ISOLDE's beam time, the protons impinging on the MEDICIS target have an energy spectrum ranging between 1.3 and 1.4 GeV.

Once the target has been irradiated, it is transported back to MEDICIS with the same rail conveyor system (RCS). From this point onward, a KUKA® robot handles the target (see Figure 4) and is used to connect it to the target station to start the isotope collection [23]. It should be noted that, when no MEDICIS target is placed downstream of the

‡ Ta target densities can vary between 0.8 and 4 g/cm^3

§ The beam is passing through the target vessel only

ISBN: 978-3-95450-213-4 ISSN: 2673-5490 doi:10.18429/JACoW-IPAC2020-THVIR13

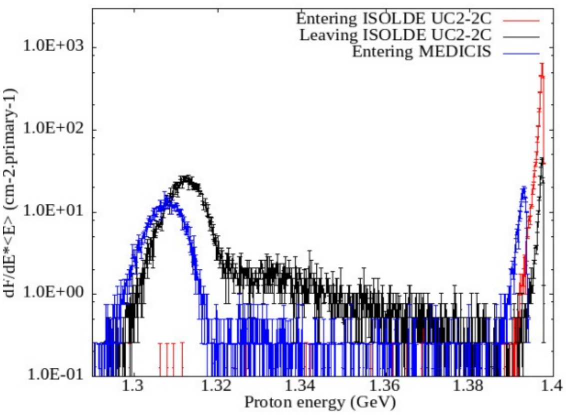

Figure 3: Lethargy representation of the proton fluence spectra at the entrance and the exit of an ISOLDE UC_2-2C target and at the entrance of a MEDICIS target.

Figure 4: KUKA® robot manipulating a MEDICIS target placed on the rail conveyor system (RCS).

ISOLDE target, the beam is directly stopped in the beam dump. The MEDICIS target takes advantage of these unused protons without impacting the physics program at ISOLDE and acts as a parasitic facility.

Due to an efficient remote handling system, the MEDICIS facility can collect and provide its partner institutes with short-lived medical radionuclides of only a few hours half-lives. After the irradiation it takes on average: (i) 12 min for the RCS to bring the target back from the irradiation point, (ii) 15 min to measure the target's dose rate and install it with the KUKA® robot on the MEDICIS frontend, and finally, (iii) 3 hours to condition the target unit for extraction (vacuum, high voltage and heating). Thus, the MEDICIS facility can start extracting radioisotopes after about 3.5 hours after irradiation of the target. Additionally, in synergy with ISOLDE, targets can also be parasitically irradiated at the MEDICIS irradiation point to produce long-lived radioisotopes and used afterwards on the ISOLDE frontends, thus extending the program with so-called winter physics into CERN's shutdown period, as demonstrated in the recent study of RaF molecules [24].

USE OF EXTERNAL SOURCES

At the end of 2018 CERN started its Long Shutdown 2 (LS2) for a duration of 2.5 years, during which the CERN accelerators are closed for maintenance. As a consequence, no proton beams are accelerated for the diverse experimental program until 2021 and, in particular, no targets can be irradiated. CERN-MEDICIS is one of the very few facilities at CERN still operating during LS2, performing offline mass separation of radionuclides from materials irradiated by external partner institutes such as ARRONAX and ILL.

Feasibility tests with $^{168}Er_2O_3$ targets irradiated at ILL for the separation of Er-169 [25] were performed in 2018, during which a first high specific activity batch of 18 MBq was collected. ARRONAX possesses a high-power cyclotron capable of delivering proton, deuteron and alpha particle beams. To provide CERN-MEDICIS with externally irradiated sources, thin Gd foils are irradiated by 30 MeV protons offering the maximum production cross-section for the generation of Tb-155 through Gd-nat(p,xn) reactions [26]. However, other radioisotopes such as Tb-154 and Tb-156 are co-produced. These radionuclides can only be purified by mass separation in order to supply the research institutes with pure and high specific activity collections of Tb-155. Before being shipped to CERN-MEDICIS the irradiated Gd foils are dissolved and the solution is evaporated on a dedicated sample holder, developed to be rapidly and securely transferred into the target tantalum oven, from which the isotopes are evaporated in order to be ionized and mass separated. In 2019 irradiated target materials were also received from the high flux reactor of the Institut Laue Langevin (ILL) in Grenoble. Prior to the irradiation quartz vials were filled with enriched target materials such as Er-168, Yb-174 and Pt-194. The vials were sealed and irradiated at the ILL high-flux nuclear reactor for the production of radioisotopes via neutron activation. The stable isotopes of the same chemical element present in the enriched material and co-produced impurities, justify the need to perform mass separation to collect the radionuclide of medical interest with the highest purity and specific activity. The decontamination, opening and transfer into the tantalum oven was performed at CERN-MEDICIS, with a dedicated automatic transfer system developed in 2019 to reduce the dose received by the operator and avoid any risk of contamination.

OPERATION IN 2018 AND 2019

Prior to a collection the target unit is coupled to the MEDICIS target station. The target is heated to very high temperatures, typically above 2000 °C, to allow for the diffusion and effusion of the radionuclides of interest out of the target to an ion source for subsequent ionization. The ions are then accelerated and sent through a mass separator. The MEDICIS target station includes a coupling flange held at a potential usually ranging from 30 kV to 60 kV and a grounded extraction electrode, placed after an acceleration gap ranging from 50 to 100 mm from the ion source exit. An Einzel lens is used to shape the ion beam downstream of the extraction electrode. More information regarding the MEDICIS beam line can be found in Ref. [23]. In addition, the MELISSA (MEDICIS Laser Ion Source for Separator Assembly) laser laboratory [27, 28], in service since April 2019, helps to increase the separation efficiency

ISBN: 978-3-95450-213-4 ISSN: 2673-5490 doi:10.18429/JACoW-IPAC2020-THVIR13

and the selectivity. The radioisotopes are extracted in the form of Radioactive Ion Beams (RIB) and implanted into one-sided zinc-coated gold foils (0.5 mm thick). Once the implantation is completed the samples are retrieved from the collection chamber using a shielded trolley. This trolley can be directly connected to a shielded fume hood, under which the samples are retrieved and conditioned to be measured by γ-spectrometry, for subsequent transport to the partner institutes or for further radiochemistry manipulation.

Operation with CERN Proton Beam in 2018

In 2018, the first year of operation after the facility's commissioning, the targets consisted mostly of 20 mm diameter tantalum rolls as used at ISOLDE, while the nominal 50 mm targets were under development. In total the MEDICIS program exploited 1.8E19 of the delivered protons, which represents 33% of the protons sent to the HRS target station. An additional 6.0E18 protons were sent to MEDICIS by deflecting the proton beam below the ISOLDE target while the latter was setting up for physics runs. This so-called direct irradiation mode increased the production rate considerably in the 20 mm diameter MEDICIS targets. Five radionuclides of medical interest were collected in 2018: Er-169 as feasibility tests, Tb-149, Tb-152, Tb-155 and Tm-165 as a generator of the Er-165 Auger emitter, with activities from 1 to 137 MBq and separation efficiency ε up to 1.6% (see Table 2). Four radioisotope batches were shipped: two were delivered to the University Hospital in Lausanne (CHUV, CH) and two others to the National Physical Laboratory (NPL, UK) [11]. MEDICIS has successfully collected and shipped Tb-149 within less than 7 hours after the end of irradiation. That year the facility provided 235 MBq (End of Collection) suitable for medical applications out of a total of 1.7 GBq, including tests and isobaric molecular activities. The facility was operated with a total of 12 target units, including prototypes, some being reused up to four times, thereby reducing operational costs and generated radioactive waste. Including machine development runs, the total radioisotope collection time amounted to about 220 hours.

Operation with External Sources in 2019

In 2019 during LS2, ILL and ARRONAX provided CERN-MEDICIS with external sources. Three radionuclides of medical interest were collected after mass separation: Tb-155, Er-169 and Yb-175 (see Table 2). Four research institutes received activity, including NPL (UK), KU Leuven/SCK CEN (BE), Hopitaux Universitaires de Genève (HUG) and the Paul Scherrer Institute (PSI) in Switzerland. The latter could perform first preclinical tests with high specific activity Yb-175. Fifteen collections were performed for a total of 870 MBq and with separation efficiency of up to 6%, exploiting the Resonance Ionization Laser Ion Source (RILIS) laser ionization from MELISSA. It should be noted that using external irradiated material and in contrast to the mode of operation that involves irradiation with PS Booster protons, there is no activation of the target unit itself. Operation in 2019 was achieved with eight new target units, some of them re-used up to three times.

The selection of the target and the ion source, both critical elements for the optimisation of isotope separation, is under constant development. It is based on the combined expertise available from the ISOLDE facility and the ISOL community, as well as the specific experience gained from the batch mode offline separation performed at MEDICIS. To this end, radiochemistry is also included in the radioisotope delivery chain and will soon be available at CERN-MEDICIS.

Table 2: Overview of the collected radioisotopes (ε: separation efficiencies)

Radio-nuclide	Target	Ion Source	Collec-tion (MBq)	ε (%)
Tb-149	^{nat}Ta	W/Re	8	-
Tb-152	^{nat}Ta	Re	1	-
Tb-155	^{nat}Gd/^{nat}Ta	W/Re/ MELISSA	71	1.2
Tm-165	^{nat}Ta	Re	137	1.6
Er-169	$^{168}Er_2O_3$	W/Re/ MELISSA	369	0.5
Yb-175	$^{174}Yb_2O_3$	W/Re/ MELISSA	519	6.0

CONCLUSION AND OUTLOOK

After a successful first commissioning phase in 2017, CERN-MEDICIS has shown its capability of delivering radionuclides with high specific activity to partner institutes of the MEDICIS collaboration. Radioisotopes of medical interest were collected using both, production with the proton beam delivered by the CERN PS Booster and using external sources. The latter mode of operation allows CERN-MEDICIS to be one of the few facilities operating during CERN's Long Shutdown 2. After a period of maintenance and upgrades at the end of 2019, the facility resumed operation in March 2020. CERN-MEDICIS will restart its program throughout LS2 to deliver mass-separated medical radionuclides using external irradiated material. Besides ARRONAX with gadolinium target irradiation for the collection of Tb-155, PSI will provide its first external sources to CERN-MEDICIS this summer to proceed with the mass-separation of the Auger emitter Tm-167. Sm-153 will be mass separated from enriched Sm-152 irradiated at the SCK CEN BR2 reactor. The Pakistan Atomic Research Reactor, which has recently joined the collaboration, will also provide external irradiated materials notably from neutron activation of enriched Pt-194 for the production of Pt-195m. In addition, studies will be performed for assessing the feasibility of separating Ac-227 from Ac-225, an alpha emitter of high interest for targeted alpha therapy. Extracting radionuclides with long half-lives from targets previously operated at ISOLDE before LS2 will finally be explored further. This already allowed ISOLDE to extend its physics program in 2018, and will continue providing parasitically-irradiated targets for offline studies at ISOLDE.

ISBN: 978-3-95450-213-4 ISSN: 2673-5490 doi:10.18429/JACoW-IPAC2020-THVIR13

Based on the experience and lessons learnt during its 1st year, MEDICIS will resume operation with protons in 2021 and continue providing its partner institutes with high specific activity radionuclides, some of them for the first time.

ACKNOWLEDGEMENTS

The authors would like to thank all colleagues involved in the development and operation of the facility, notably from EN-CV, EN-SMM, EN-STI, EN-HE, EN-DHO, HSE-RP, BE-BI, BE-OP, TE-EPC, TE-VSC CERN's groups and the collaborating institutes. We wish to thank all the members of the CERN-MEDICIS collaboration for their commitment, support and advice. Funding is also acknowledged through the CERN & Society Foundation, the Flanders Research Foundation (FWO), the CERN Knowledge Transfer fund and the European Commission (MEDICIS-Promed, H2020 contract #642889). N. Audouin, F. Haddad and N. Michel acknowledge the support from the ANR Grants: ANR-11-EQPX-0004, ANR-11-LABX-18-01 and ANR-16-IDEX-0007.

REFERENCES

[1] CERN-MEDICIS website and list of approved projects: `https://medicis.cern`

[2] R. Catherall *et al.*, "The ISOLDE facility", *Journal of Physics G: Nuclear and Particle Physics*, vol. 44, no. 9, p. 094002, 2017.

[3] R. M. Dos Santos Augusto, L. Buehler, Z. Lawson , S. Marzari, M. Stachura, T. Stora and the CERN-MEDICIS collaboration, "CERN-MEDICIS (MEDical Isotopes Collected from ISolde): a new facility", *Applied Sciences,* vol. 4, no. 2, pp. 265-281, 2014.

[4] S. Huclier-Markai *et al.*, "Promising scandium radionuclides for nuclear medicine: a review on the production and chemistry up to in vivo proofs of concept", *Cancer Biother Radiopharm.,* vol. 33, no. 8, pp. 316–29, 2018.

[5] C. Müller *et al.*, "Promising prospects for ^{44}Sc-/^{47}Sc-based theragnostics: application of ^{47}Sc for radionuclide tumor therapy in mice", *J. Nucl. Med.*, vol. 55, no. 10, pp. 1658–64, 2014.

[6] C. Muller *et al.*, "Scandium and terbium radionuclides for radiotheranostics: current state of development towards clinical application", *Brit. J. Radiol.*, vol. 91, p. 20180074, 2018.

[7] C. Biggin, M. Harris, A. Hedt and C. Jeffer, "Radiological properties of Next Generation Theranostics (Cu-64/Cu-67)", *J. Nucl. Med.*, vol. 58, no. supp. 1, p 1014, 2017.

[8] R. Formento-Cavaier *et al.*, "Terbium radionuclides for theranostics applications: a focus on MEDICIS-Promed", *Physics Procedia*, vol. 90, pp. 157-163, 2017.

[9] C. Müller *et al.*, "Alpha-PET with terbium-149: evidence and perspectives for radiotheragnostics", *EJNMMI Radiopharm. Chem.,* vol. 1, p. 5, 2016.

[10] C. Müller *et al.*, "Preclinical investigations and first-in-human application of ^{152}Tb-PSMA-617 for PET/CT imaging of prostate cancer", *EJNMMI Research*, vol. 9, article no. 68, 2019.

[11] B. Webster *et al.*, "Chemical Purification of Terbium-155 from Pseudo-Isobaric Impurities in a Mass Separated Source Produced at CERN", *Scientific Reports,* vol. 9, p. 10884, 2019.

[12] C Müller *et al.*, "A Unique Matched Quadruplet of Terbium Radioisotopes for PET and SPECT and for α- and β−-Radionuclide Therapy: An In Vivo Proof-of-Concept Study with a New Receptor-Targeted Folate Derivative", *J. Nucl. Med.* vol. 53, no. 12, pp. 1951-1959, 2012.

[13] K. Hanke, "Past and Present Operation of the CERN PS Booster", *International Journal of Modern Physics A,* vol. 28, no. 13, article id. 1330019, 2013.

[14] U. Köster *et al.*, "Radioisotope production at the high-flux reactor of Institut Laue Langevin", *Radiotherapy and Oncology,* vol. 102, supp. 1, pp. S169-S170, 2012.

[15] F. Haddad *et al.*, "ARRONAX, a high energy and high intensity cyclotron for nuclear medicine", *Eur. J. Med. Mol. Imaging,* vol. 35 pp.1377-1387, 2008.

[16] U. Köster, "ISOLDE target and ion source chemistry", *Radiochimica Acta,* vol. 89, p. 749, 2001.

[17] G. Battistoni, "Overview of the FLUKA code", *Annals of Nuclear Energy*, vol. 82, pp. 10-18, 2015.

[18] T. T. Bohlen *et al.*, "The FLUKA Code: Developments and Challenges for High Energy and Medical Applications", *Nuclear Data Sheets,* vol. 120, pp. 211-214, 2014, version: 2011-3.0, released 16 Dec. 2019, `https://fluka.cern/`

[19] C. Theis *et al.*, "Interactive three-dimensional visualization and creation of geometries for Monte Carlo calculations", *Nucl. Instrum. Methods A*, vol. 562, pp.827-829, 2006.

[20] J. Donald Cossairt, "Radiation Physics for Personnel and Environmental Protection", Fermilab, Batavia, IL, USA, Rep. TM-1834, p. 93, 2007.

[21] J. P. Ramos, "Thick solid targets for the production and online release of radioisotopes: The importance of the material characteristics - A review", *Nucl. Instrum. Methods B* vol. 463, pp. 201-210, 2020.

[22] J. P. Ramos *et al.*, "Intense $^{31-35}$Ar beams produced with a nanostructured CaO target at ISOLDE", *Nucl. Instrum. Methods B*, vol. 320, pp. 83–88, 2014.

[23] Y. Martinez Palenzuela *et al.*, "The CERN-MEDICIS isotope separator beam line", submitted for publication.

[24] R. Garcia Ruiz, R. Berger, J. Billowes *et al.,* "Spectroscopy of short-lived radioactive molecules", *Nature* vol. 581, pp. 396–400, 2020.

[25] R. Formento-Cavaier *et al.*, "Very high specific activity erbium ^{169}Er production for potential receptor-targeted therapy". *Nucl. Instrum. Methods B* vol. 463, pp. 468-471, 2020.

[26] C. Vermeulen *et al.*, "Cross sections of proton-induced reactions on ^{nat}Gd with special emphasis on the production possibilities of 152Tb and 155Tb", *Nucl. Instrum. Methods B* vol. 275, pp. 24-32, 2012.

[27] V. M. Gadelshin *et al.*, "MELISSA: Laser Ion Source setup at CERN-MEDICIS facility", *Nucl. Instrum. Methods* vol. 463, pp. 460-463, 2020.

[28] V. M. Gadelshin, S. Wilkins and the MEDICIS collaboration, "First laser ions at the CERN-MEDICIS facility", *Hyperfine Interactions*, vol. 241, no. 1, article no. 55, 2020.

ISBN: 978-3-95450-213-4 ISSN: 2673-5490 doi:10.18429/JACoW-IPAC2020-THVIR14

DEVELOPMENT OF A HYBRID ELECTRON ACCELERATOR SYSTEM FOR THE TREATMENT OF MARINE DIESEL EXHAUST GASES*

T. Torims†, G. Pikurs, K. Kravalis, A. Ruse, Riga Technical University, Riga, Latvia
A. G. Chmielewski, A. Pawelec, Z. Zimek
Institute of Nuclear Chemistry and Technology, Warsaw, Poland
G. Mattausc, Fraunhofer Institute for Organic Electronics,
Electron Beam and Plasma Technology FEP, Dresden, Germany
M. Vretenar, CERN, Geneva, Switzerland

Abstract

The paper outlines the overall results of the ARIES Proof-of-Concept (PoC) project,[1] which seeks to tackle the shipping industry's most pressing problem, its large-scale emissions of nitrogen oxides (NO_x), sulphur oxides (SO_x) and particulate matter (PM), by developing a hybrid exhaust gas-cleaning technology that combines an EB accelerator with improved wet-scrubbing technology. It is unique – in a single technological system – and addresses all three types of emissions simultaneously. It promises to be cheaper and more efficient than existing solutions. There are two main stages involved: 1) SO_2 and NO_x oxidation during the irradiation of wet gases by the EB from the accelerator and 2) the absorption of pollution products into an aqueous solution. For the very first time, test trials in a real maritime environment were conducted and attracted the interest of the maritime industry, policy makers and the accelerator community. The PoC has clearly confirmed the potential of this technology and forms a solid basis for the full-scale application of the hybrid system on sea-going ships. The results of this project are of the highest relevance to the accelerator community, as well as the maritime industry and policy makers.

MOTIVATION AND CONTEXT

Heavy fuel oil (HFO) is the main energy source used by the maritime industry. Almost all medium and low-speed marine diesel engines run on HFO with a high sulphur content, leading to the formation of three main pollutants: NO_x, SO_x and PM. These emissions have been gradually restricted worldwide. When entering Emission Control Areas (ECA) or ports, ships switch to 0.1% sulphur content fuel, marine gasoil (MGO). Since 2020, maritime transport has had to comply with the worldwide 0.5% emission sulphur cap, under MARPOL Annex VI Regulation 14.

In the North America ECA, not only SO_x, but also NO_x and PM have been regulated and the North/Baltic Sea Sulphur ECA will be in place from 2021. A similar policy initiative is currently undertaken in the Mediterranean Sea [1]. These are so-called Tier III requirements, limiting NO_x emissions to between 3.4 and 2 g/kWh. It is expected that further requirements for significant PM reductions will be imposed [2]. The maritime community faces a serious challenge to fulfil these limitations [3].

Existing Technologies and Prior Attempts

Cutting SO_x. To comply with sulphur emission limitations [4], the shipping industry currently has two workable options [5]: a) to opt for universal usage of expensive MGO, or b) to install exhaust gas cleaning systems (scrubbers [6]), which reduce SO_x and PM emissions from ship engines, generators and boilers, allowing ships to continue using HFO.

However, there may be pertinent operational issues involved in running marine engines designed for HFO continuously on MGO and the price difference between the two could considerably increase shipping costs. Today scrubbers are the preferred solution to comply with SOx limitations, hence there is a growing incentive for ship owners to invest in scrubbers. However, implementation costs are very high: 1M to 5M EUR for the equipment [7] alone. Therefore, in the absence of a more cost-effective technological solution, it will be very challenging in the near future to equip the global fleet of about 60,000 vessels.

Dealing with NOx. NO_x production is not directly related to the type of fuel, but to the combustion process itself. Switching to MGO therefore doesn't solve this issue. In order to achieve NO_x emission compliance, some form of additional technology has to be installed on-board. Usually this is a costly and complicated, selective catalytic reduction (SCR) system. Naturally, marine scrubbing and denitration systems are expected to be compatible, although this is not the case. As such, ships are being equipped with two separate purifying systems: one for SO_x and another for NO_x.

PM trapping. The most common methods for removing PM from exhaust fumes are the Continuously Regenerating Trap, Diesel Particulate Filter and Diesel Oxidation Catalyst. However, they can only be used for emissions from low-sulphur fuels. Also the nanoparticles, the most harmful form of PM (e.g. PM_{10} and $PM_{2.5}$) are not sufficiently prevented from entering the ambient air.

Prior attempts. The ship-emission challenge is not new *per se*; there have been various efforts to find feasible alternatives, such as the Humid Air Motor, Exhaust Gas Recirculation, Plasma-Catalysis, Nano-Membrane Filters, etc. Several of these projects [8-12] were EU financed and presented to the stakeholders. Yet to this day, they cannot

* This project has received frunding from the European Unions's Horizon 2020 Research and Innovation programme under grant agreement No 730871
† toms.torims@rtu.lv

ISBN: 978-3-95450-213-4 ISSN: 2673-5490 doi:10.18429/JACoW-IPAC2020-THVIR14

be cost-effectively installed on ships. These alternative methods typically target SO_X, and neglect NO_x, PM, volatile organic compounds (VOC) and hazardous polycyclic aromatic hydrocarbons (PAH). To date, only a few studies have been conducted on the simultaneous removal of NO_x and SO_2 in a single process [13-16]. They mostly rely on the use of electrolysis and electromagnetic techniques, but have not resulted in uptake by the maritime industry.

Novel Hybrid Accelerator Technology

The proposed technology is fundamentally different and could help to address the global challenge of air pollution and emission cuts. It is based on pollutant removal by combining two correlated technological stages (see Fig. 1), electron beam irradiation (EB) of flue gas with subsequent wet-chemical scrubbing [17, 18]:

EB irradiation: electrons are accelerated by a high voltage in a vacuum, before being injected through thin foil windows into the exhaust gases in the atmospheric pressure processing chamber. The energetic electrons collide with exhaust gas molecules and produce reactive free radicals, atoms, ions and secondary electrons that decompose the pollutant molecules in the irradiated exhaust gases. These excited species and radicals react with NO and SO_2 to form their higher oxidation compounds: NO mainly forms NO_2, then by increasing the applied dose becomes NO_3 and SO_2 forms SO_3. Due to the high water-vapour concentration in the exhaust gas, HNO_3 and H_2SO_4 are formed and are easily soluble in the scrubbing liquid. Additionally, PM and organic pollutants like VOC and PAH are effectively eliminated by EB-formed plasma [19, 20].

Wet scrubber: subsequently the pollution products from the exhaust gases are absorbed into an aqueous solution - in a closed-loop wet scrubber. The seawater is used as the scrubbing solution, with the limited addition of liquid oxidant (e.g. $NaClO_2$) to scrub soluble products from the oxidation reactions [21]. Wash water after cleaning is recirculated. If the SO_2 inlet concentration is high, the removal efficiency of NO increases noticeably, especially at a higher irradiation dose range. The effect of the presence of SO_2 in enhancing NO_x removal efficiency can be explained by the chain of reactions - HO_2 radicals, which are produced during reactions with SO_2, react with NO and oxidize them into NO_2. This in turn is later converted to HNO_3. Therefore, when the NO inlet concentration is high, as in the case of HFO, this synergistic effect is more advantageous at high SO_2 concentrations.

From Science to Society:Transfer of Technology

Relevance to the Accelerator Community initiatives. This endeavour was possible due to a genuine commitment among the Accelerator Community to develop societal accelerator applications. EB environmental applications have been addressed in the "Applications of Particle Accelerators in Europe" [22]. Equally the role of particle accelerators to meet the needs of society at large is emphasised in "Accelerators for America's" [23]. This idea has been elaborated further in the ARIES project under "Industrial and Societal Applications" [24].

Matching Maritime Policy and Industry needs. The maritime industry is looking for suitable, economically effective and fast solutions for *green shipping*. Despite various policy actions [25-28], so far they have met with limited success. Therefore, considering that *inter alia* the European shipping industry welcomes the European Green Deal [29], this hybrid technology is offering a tangible solution for the maritime industry and its stakeholders' needs.

Economic feasibility. In order to make this hybrid technology attractive to the maritime industry and prove its feasibility to policy makers, unbiased cost effectiveness analysis is needed. It is not enough to show operationally that this technology works; its clear business case must be established. This is a decisive factor, along with safety considerations, for the acceptance and further uptake of the technology. This innovative technology could be proliferated only if it is less costly than the combined cost of existing marine SO_x and NO_x abatement solutions and fulfils all the relevant maritime safety requirements.

PROOF OF CONCEPT

The magnitude of this societal challenge goes far beyond the capacity of any individual research institution or company and requires a wide collaborative effort. Therefore, a multidisciplinary *Collaboration* was summoned: partners with world-class expertise in accelerator and maritime technologies, shipping and economic analysis have teamed up to offer an alternative for *green shipping*.

The **Virtue** of this project is its connection of two distinct communities: maritime and accelerator specialists. This is not merely a scientific or technological undertaking, bringing particle accelerators onboard ships. It is also an opportunity for the accelerator community to understand the compliance requirements of the shipping industry and marine engineering, as well as for the maritime community to build trust with the established research institutions and scientific community.

Commitment. Through its multidisciplinary and multisectoral composition, the actual collaboration demonstrates the potential of the hybrid system's application onboard ships. Importantly, the partners have greatly contributed their own resources—this clearly demonstrates aspiration—especially from the maritime community. The total budget of the PoC project was 0.5M EUR, of which about 90% were direct contributions from partners and only 10% was EC contribution. This resulted in a great collaborative

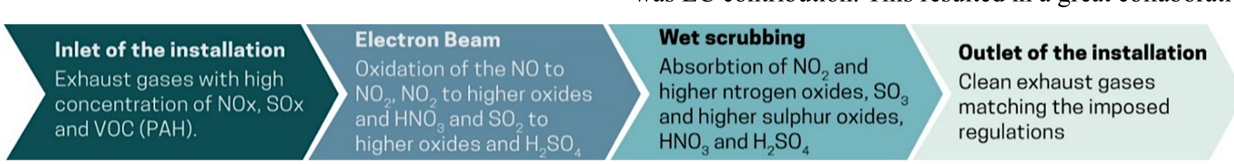

Figure 1: Principle of the hybrid electron accelerator technology for the treatment of marine diesel exhaust gases.

ISBN: 978-3-95450-213-4 ISSN: 2673-5490 doi:10.18429/JACoW-IPAC2020-THVIR14

spirit within this partnership, building multilateral trust and commitment to continue development of the hybrid technology until its full implementation onboard ships.

Engaging stakeholders. To ensure that contact with reality was maintained, from the outset this project was exposed to the rigorous scrutiny of stakeholders. Naturally, development of the hybrid off-gas cleaning system has pushed back existing technological and acceptance boundaries. Therefore, the partners are engaging with the EC, IMO, IACS, EGCSA, TIARA consortium and others. The Italian Coast Guard and ABS are also directly participating in an advisory capacity.

Objectives. The collaboration is aiming to expand particle accelerator technologies into the maritime domain by developing the said technology. This requires demonstration and validation, to provide the maritime industry with a much-needed innovative, cost-effective solution that would substantially improve the environmental performance of fleets, by significantly reducing ship emissions. In order to achieve this *green shipping* goal, the PoC project was tasked with the following pivotal objectives:

1. To conceptually prove the electron-beam accelerator application for the effective treatment of marine diesel exhaust gases.
2. To prove its technical feasibility within the real ship environment—advance the technology to TRL3.
3. To demonstrate that the technology in question is capable of removing sufficient levels of SO_x and NO_x.
4. To provide a sound financial evaluation of the cost-effectiveness of this technology.
5. To engage with and inform all relevant stakeholders during the project.

CONCEPT AND EXPERIMENTAL SET-UP

Methodology. The demonstration was performed using a mobile platform of the linear type of accelerator, directly connected to the ship exhaust duct. Crucial flue gas parameters were measured: flue gas velocity, flue gas temperature and flue gas composition (see Fig. 2).

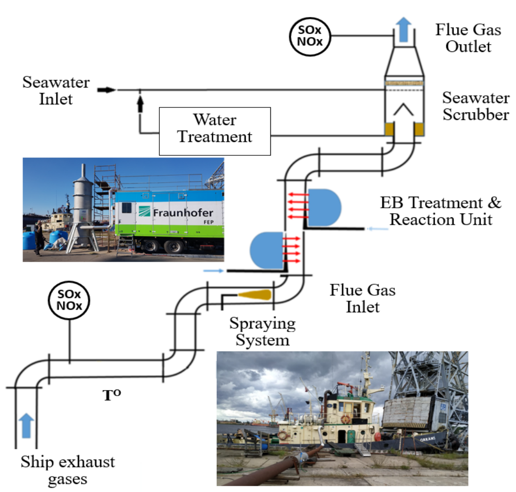

Figure 2: Hybrid electron accelerator system.

Of all the generally accepted methods for considering the mass exchange process, in this case the most appropriate is to quantify the mass exchange process, including absorption efficiency (see Eq. (1)). This value offers a simple and transparent way to assess the impact of the main process parameters on the effectiveness of gas treatment. It has been assumed that the absorption efficiency is a function of the following variables:

$$\eta = f(Ue, L/G, H, Co, Cr). \tag{1}$$

where η - absorption efficiency [%], *Ue* - gas velocity calculated on the empty column cross-section [m/s], *L/G* - spraying density of the absorption solution, litres of solution per cubic meter of gas [L/m^3], *H* - column packing height [m], *Co* - initial concentration of NO_x (calculated as NO_2) in the gas, [mg/m^3] or [vol%], and *Cr* - concentration of the absorption solution, [kg/m^3] or [mass%].

Pilot installation. A fully operational tugboat "Orkāns" berthed at the pier of Riga Ship Yard was used as the source of flue gas. This ship is equipped with double two-stroke 450 kW Diesel engines. The outlet of the exhaust gas duct was flexibly connected to the accelerator complex by a 320 mm diameter pipeline of almost 20 m in length.

A mobile accelerator unit WESENITZ-II was provided by Fraunhofer FEP and used as an EB irradiation device. The facility is usually operated for seed dressing, but was modified for flue gas treatment. The irradiation chamber was of rectangular cross section (120 x 1560 mm²) and 1180 mm in height. The exhaust gas flowed vertically from bottom to top and was irradiated from both sides by means of two 125 kV EB accelerators. The maximal current for one accelerator was 100 mA. A single 10 µm Ti foil facilitated the electron exit into the irradiation chamber. It was cooled and protected against condensates and PM by an intense tangential air flow curtain. In order to protect the accelerator unit against potentially excessive gas temperatures, a spray cooler was installed in the connecting pipeline between the ship and the accelerator. In the course of experiments however, it was proven that the air curtain alone sufficiently protects the thin electron window foil.

A counter-current gas-liquid flow packed closed-loop scrubber was selected as the absorber for the purposes of this project. The device of 1.2 m diameter and 5.5 m height was filled with *Bialecki* rings. The filling height was 2.6 m. The circulating water was stored in two tanks filled with 3 m^3 of seawater. The Baltic Sea water from the tanks was filtered and pumped to a system of nozzles located at the top of the scrubber and sprayed into the top of the scrubber, then flowed to the bottom of the device and back to the tank by gravity. The gas from the irradiation unit was directed to the lower part of the scrubber and released into the atmosphere by a stack located at the top of the device. In order to maintain the water's ability to absorb acidic gases, its pH was kept above 7.5 by the addition of sodium hydroxide. To enhance the oxidation potential and improve NO_x removal efficiency, an oxidant ($NaClO_2$) was also added to the water. The tested oxidant concentration was in the range of 0 – 3.3 mg/L (see Fig. 3).

ISBN: 978-3-95450-213-4 ISSN: 2673-5490 doi:10.18429/JACoW-IPAC2020-THVIR14

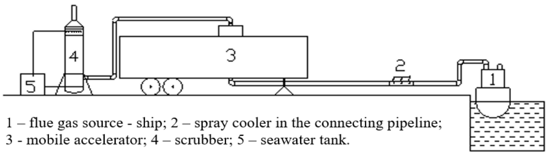

Figure 3. General scheme of pilot installation.

Measurements. All of the flue gas generated by the ship's engine was treated in the system. The experiments were conducted for three engine loads (0% - idling run, 50% and 100%). The flue gas sampling points were located upstream of the accelerator, at the exit of the scrubber and at the gas outlet stack. In this way, the gas composition was measured at the inlet of the installation, after irradiation and after treatment at the outlet of the system. Moreover, five temperature measurement points were installed: downstream from the engine, upstream of the spray cooler, at the irradiation unit gas inlet, the scrubber inlet and the scrubber gas outlet, along with a gas velocity measurement point, before irradiation.

Economic feasibility. A comprehensive economic and financial analysis was carried out by an independent assessor Biopolinex - from the point of view of the end user and the manufacturer of the accelerator system. The investment profitability was assessed on the basis of discounted cash flows, Net Present Value (NPV), Internal Rate of Return (IRR) and repayment period. The breakeven point was calculated. The result was validated by a sensitivity analysis of the volatility of the key financial parameters.

RESULTS AND CONCLUSIONS

Engineering. The most important achievement of the PoC was the technical integration of the diesel engine, with the upstream accelerator process chamber, where Ti foil was protected by an air curtain and a wet scrubber downstream. The flow of flue gases was induced by diesel engine over pressure, which induced proper gas flow against pressure drop for all the process installation components. The accelerator complex and protection windows with titanium foils were not damaged by the high temperature off-gas flow. Earlier lab experiments were successfully validated, and the analytical methods were tested. This successful operation of a ship-port based installation verified the assumptions that are fundamental to continuing the project for the full on-board system development.

Collaboration of Riga Technical University, Institute of Nuclear Chemistry and Technology, CERN, Fraunhofer Institute for Organic Electronics, Electron Beam and Plasma Technology FEP, Remontowa Marine Design, Riga Ship Yard and Biopolinex by its commitment and dedicated efforts of the core team enabled us to achieve all the objectives set for the PoC. Notably, it demonstrated that for the very first time, the two underlying technologies for the envisaged system (accelerators and scrubbers) can be combined in a real maritime environment – reaching TRL 3 – instrumental for the green shipping policy.

Conclusions

The **economic analysis** confirmed the profitability of the hybrid technology vis-à-vis the HFO option with the conventional scrubber off-gases abatement costs. This is true for both *optimistic* and *optimal* financial risk associated scenarios, indicating the high market potential of the maritime application of the hybrid technology.

Abatement of NO_x and SO_x. Although, the environmental and operational restrictions of the port only allowed for the usage of desulfurized (eventually SO_x free) marine fuel, even with a non-homogeneous and moderate irradiation dose, a significant reduction of up to 45.8% of NO_x was recorded (see selected results in Table 1 and overall in Figs. 4 and 5). This was matched by the measurement profiles of the other exhaust gases family parameters and matched with the analytical and prior lab trials. A very good correspondence was observed, which enabled us to affirmatively predict the significant reduction of SO_x in a full-scale (Fig. 6), on-board system operating with HFO.

Table 1: Removal Efficiencies of the NO and NO_x

Parameter	**Unit**	**Values**		
En. load	%	0	50	100
Ox.conc.	mg/l	0	1	3,3
Gas flow r.	Nm^3/h	3316	4751	4915
Gas t. inlet	°C	51	136	124
Dose	kGy	4,1	5,7	5,5
Inlet conc.	NO ppm	95	252	298
	NO_x ppm	110	271	317
Rem. rate	NO %	81,8	57,4	65,2
	NO_x %	38,8	38,0	45,8

The NO_x removal was examined for different engine loads and different concentrations of oxidant.

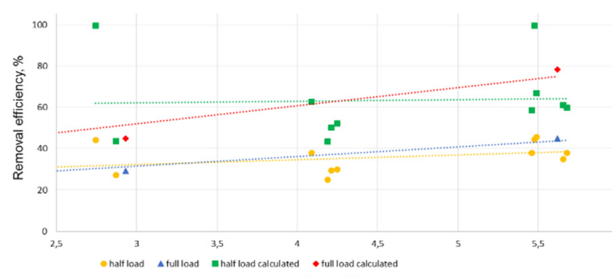

Figure 4. Dose dependence of NO_x removal efficiency for 50% and100 % engine load.

The increase of oxidant concentration in the process water in the scrubber has a strong positive impact on NO_x removal efficiency (Fig. 5).

ISBN: 978-3-95450-213-4 ISSN: 2673-5490 doi:10.18429/JACoW-IPAC2020-THVIR14

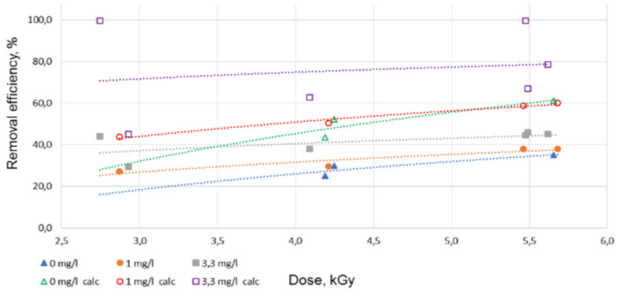

Figure 5. Dose dependence of NO_x removal efficiency for different concentrations of oxidant.

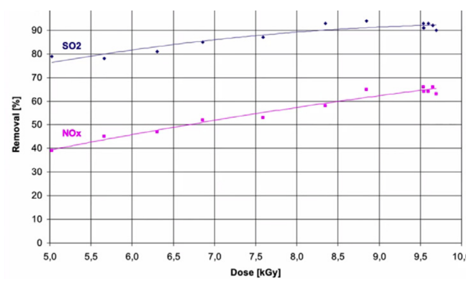

Figure 6. Dose dependence of SO_2 and NO_x matched with previous laboratory tests.

Way forward. Based on the promising results of the PoC project and with the great support of the stakeholders, maritime and accelerator partners, the initial Collaboration has been considerably enlarged. The partners are keen to pursue further developments of the hybrid technology and *inter alia* have prepared the *Hybrid Exhaust-gas-cleaning Retrofit Technology for International Shipping* – HERTIS project [30] proposal. This is an unprecedented, multi-disciplinary undertaking, linking together the maritime and particle accelerator communities under the umbrella of scientific research: it is a joint endeavour of 12 partners from 8 European countries. Enhancing Collaboration with the following: University of Tartu; the major shipping industry players include Grimaldi Group, the American Bureau of Shipping and Ecospray; the economical feasibility and business case are to be impartially evaluated by business experts KPMG; the environmental impact assessment expertise and objectiveness was conducted by Western Norway Research Institute.

REFERENCES

[1] European Parliament, `https://www.europarl.europa.eu/doceo/document/E-9-2019-004160-ASW_EN.html`

[2] European Commission, `https://ec.europa.eu/clima/policies/transport_en`

[3] OECD, `https://www.itf-oecd.org/sites/default/files/docs/sulphur-emissions-shipping.pdf`

[4] IMO MARPOL Annex VI, Resolution MEPC.259(68), Directives 2012/33/EU, 1999/32/EC, 2016/802/EU and EU Regulation 2015/757, US EPA Vessel General Permit

[5] European Maritime Safety Agency, `http://www.emsa.europa.eu/main/air-pollution/emission-abatement-methods.html`

[6] CERN, `https://aries.web.cern.ch/aries-proof-concept-fund`

[7] Reuters, `https://www.reuters.com/article/uk-shipping-fuels-scrubbers/sulphur-scrubbers-no-silver-bullet-for-shipping-industry-wartsila-idUKKBN1HR1V6`

[8] European Commission, INEA, "Back from Black -Study and deployment of the affordable scrubber retro fitting technology for SME ship owners", "`https://ec.europa.eu/inea/en/connecting-europe-facility/cef-transport/2014-eu-tm-0379-m&%20cordis.europa.eu/project/rcn/100218/reporting/en`

[9] European Commission, TRIMIS, "JOULES project - Joint Operation for Ultra Low Emission Shipping". `https://trimis.ec.europa.eu/project/joint-operation-ultra-low-emission-shipping`

[10] European Commission, CORDIS, "HERCULES-2 project - Fuel flexible, near -zero emissions, adaptive performance marine engine". `https://cordis.europa.eu/project/id/634135`

[11] European Commission, CORDIS, "BLUESHIP project - Electrospun functionalized nano-materials for ultra-compact de-NOX SCR system in naval shipping", `https://cordis.europa.eu/project/id/605102`

[12] European Commission, CORDIS, "DEECON project - Innovative After-Treatment System for Marine Diesel Engine Emission Control", `https://cordis.europa.eu/project/id/284745`

[13] I. Boscarato *et al.*, "Green shipping: Marine engine pollution abatement using a combined catalyst/seawater scrubber system. 1. Effect of catalyst", *Journal of Catalysis*, vol. 328, pp. 248-257, 2015. `doi.org/10.1016/j.jcat.2014.12.013`

[14] Y. Shaolong *et al.*, "Removal of NO_x and SO_2 from simulated ship emissions using wet scrubbing based on seawater electrolysis technology", *Chemical Engineering Journal*, vol. 331, pp. 8-15, 2018. `doi.org/10.1016/j.cej.2017.08.083`

[15] T-W. Chien and H. Chu, "Removal of SO_2 and NO from flue gas by wet scrubbing using an aqueous $NaClO_2$ solution", *Journal of Hazardous Materials*, vol. 80, issues 1-3, pp. 43-57, 2000. `doi.org/10.1016/S0304-3894(00)00274-0`

[16] D-S. Jin *et al.*, "Simultaneous removal of SO_2 and NO by wet scrubbing using aqueous chlorine dioxide solution", *Journal of Hazardous Materials*, vol. 135, issues 1-3, pp. 412-417, 2006. `doi.org/10.1016/j.jhazmat.2005.12.001`

[17] A.G. Chmielewski *et al.*, "A method of reducing high concentrations of nitrogen oxides in the exhaust gases from diesel engines using electron beam radiation and wet scrubbing", European Patent application EP3398673 (A1), July 11, 2017.

[18] J. Licki *et al.*, "Electron beam treatment of simulated marine diesel exhaust", *Nukleonika*, vol. 60, issue 3, pp. 689-695, 2015. `doi:10.1515/nuka-2015-0098`

ISBN: 978-3-95450-213-4 ISSN: 2673-5490 doi:10.18429/JACoW-IPAC2020-THVIR14

[19] A.G. Chmielewski *et al.*, “A hybrid plasma-chemical system for high-NOx flue gas treatment”, *Radiation Physics and Chemistry*, vol. 144, pp. 1-17, 2018. doi.org/10.1016/j.radphyschem.2017.11.005.

[20] M. Siwek and A.G. Chmielewski, “Process engineering aspects of diesel engine off gases treatment”, Report, B series nr 2, Institute of Nuclear Chemistry and Technology, Warsaw, Poland, 2018. http://www.ichtj.waw.pl/ichtj/publ/b_report/PDF-B-raport/siwek2018B_02.pdf

[21] E. Zwolinska, *et al.*, “Removal of high concentrations of NOx and SO_2 from diesel off-gases using a hybrid electron beam”, *Energy Reports*, vol. 6, pp. 952-964, 2020. doi: 10.1016/j.egyr.2020.04.008

[22] EuCARD-2, http://cds.cern.ch/record/2716155/files/CERN-ACC-2020-0008.pdf

[23] U.S. Department of Energy, “Accelerators for Energy and the Environment”, in *Accelerators for America's Future*, 2010, pp. 10-23, http://www.acceleratorsamerica.org/files/Report.pdf

[24] ARIES - Accelerator Research and Innovation for European Science and Society - Integrating Activity project of Horizon 2020, https://aries.web.cern.ch/wp3

[25] European Maritime Safety Agency, http://www.emsa.europa.eu/main/sustainable-toolbox/relevant-eu-projects.html

[26] International Maritime Organisation, http://www.imo.org/en/OurWork/Environment/PollutionPrevention/AirPollution/Pages/IMO-Publications.aspx

[27] European Commission, Climate Action, https://ec.europa.eu/clima/policies/transport/shipping_en

[28] European Commission, INEA, https://ec.europa.eu/inea/horizon-2020

[29] European Community Shipowners’ Associations, https://www.ecsa.eu/news/european-shipping-industry-welcomes-european-green-deal

[30] HERTIS project proposal, https://www.rtu.lv/writable/public_files/RTU_hertis_flyer.pdf

ISBN: 978-3-95450-213-4 ISSN: 2673-5490 doi:10.18429/JACoW-IPAC2020-THVIR15

ACCELERATORS FOR APPLICATIONS IN ENERGY AND NUCLEAR WASTE TRANSMUTATION

A. Fabich†, D. Vandeplassche, U. Dorda, H. Aït Abderrahim, SCK CEN, Mol, Belgium

Abstract

SCK CEN is at the forefront of Heavy Liquid Metal (HLM) nuclear technology worldwide with the development of the MYRRHA accelerator driven system (ADS) [1]. An Accelerator Driven System (ADS) is a concept using high power proton accelerators in energy production and nuclear waste transmutation. Amongst typical beam performance requirements, the operational reliability of the accelerator is exceptionally demanding. The advantages and challenges of different driver options, like cyclotrons and linacs, are evaluated and worldwide design studies are summarized. The MYRRHA design is based on a 600 MeV superconducting proton linac. The first stage towards its realization was recently approved to be constructed by SCK CEN in Belgium. The 100 MeV linac will serve as technology demonstrator for MYRRHA as well as driver for two independent target stations, one for radio-isotope research and production of radio-isotopes for medical purposes, the other one for fusion materials research. MYRRHA in its final implementation is envisaged as an international large research infrastructure open for scientific and industrial user-communities.

MOTIVATION FOR ADS

While alternative, renewable energy sources combined with increased efficiencies are being developed, there remains the clear need for complementary large-scale base-load power stations and a strategy for handling the already accumulated nuclear waste. Conventional reactors feature the following two main issues:

- Operation of a critical system: The neutrons emitted during the fission of one atom hit other atoms and trigger their fission. In order to keep the system running, a multiplication factor of K = 1 must be used. This factor is defined by the fission material and reactor configuration. The only control is given by the insertion of additional absorbing elements that limit the exponential increase of activity.
- Radiotoxic waste with >10.000 years half life time. The minor actinides (Np, Am, Cm) are the main concern due to their high radiotoxicity, heat emission and long half-life.

The concept of an ADS [2] is to load the reactor with subcritical mass of fissile material ($k_{eff} < 1$). Left alone, this implies that the chain reaction would naturally shut down exponentially with time (in the order of 10^{-5} to 10^{-6} sec). In order to keep the chain reaction going and hence the power level constant in the reactor, additional neutrons are provided from a spallation target inside the reactor that is driven by a high-power proton particle accelerator. In case of issues, the accelerator is turned off and the chain reaction automatically slows down. This also removes the need for highly enriched fission material.

These kinds of reactor will be loaded with the Plutonium and Minor Actinides "waste" resulting from the reprocessed spent fuel of the nuclear power plants. With help of the subcritical reactor, transmutation can be efficiently achieved. In contrast to conventional reactors, an ADS can safely transmute a large amount of these minor actinides. As shown in Fig. 1, an ADS allows to reduce the time needed to store the nuclear waste to a level that is compatible with the lifetime of human-made buildings.

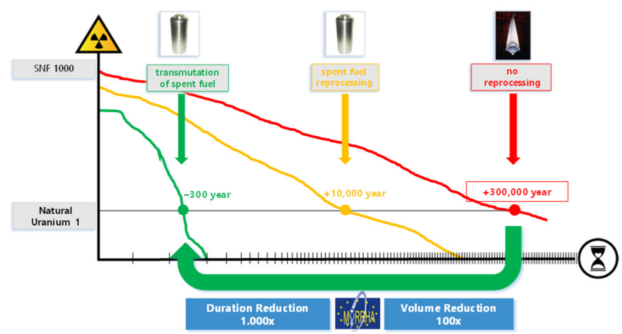

Figure 1: While reprocessing of waste and reuse of Pu in conventional reactors allows to reduce the burden of nuclear waste radiotoxicity by a factor 30, an ADS can reduce the life time by a factor 1000.

REQUIREMENTS ON THE ACCELERATOR

While the exact requirements on the particle accelerator will depend on the design details of the reactor, the following beam requirements can be stated:

- Particle type: protons, readily available and accelerated for neutron production
- Energy: >500 MeV to be in the region of usable neutron production cross-section.
- Beam power: multiple MW, achieving a usable neutron density.
- Reliability: MTBF > multiple weeks. Any beam trips must be resolved within a few seconds as otherwise this would impose severe thermal stress on the reactor materials and components. Furthermore, any longer beam trip requires a time-consuming reactor restart lasting a few days.
- The beam emittances are only important to safely accelerate and transport the beam through the accelerator.

From this list the following additional design choices can be derived:

† Adrian.fabich@sckcen.be

ISBN: 978-3-95450-213-4 ISSN: 2673-5490 doi:10.18429/JACoW-IPAC2020-THVIR15

- CW operation allows to reduce the space charge and the stress on the spallation target. Furthermore, it allows certain technological choices, in view of reliability, e.g. solid-state amplifiers.
- Need for a fault tolerance scheme: Within a few seconds, a failure is detected, a new configuration is deployed and a fast recommissioning to full power beam operation is performed.

While some groups study also more exotic configurations like an FFAG, the two main options are cyclotrons or superconducting linacs.

DIFFERENT APPROACHES – PAST AND PRESENT

When the first ideas of an ADS were developed, the only available accelerator type that could be envisaged to fulfil the requirements were normal conducting cyclotrons. Based on the successful operation of the 600 MeV, MW-class normal-conducting cyclotron at PSI (with a 72 MeV injector cyclotron), various concepts were proposed e.g. [3]. Since then many ideas have been followed studying e.g. stacked cyclotrons [4] mainly focusing on R&D aspects of super conducting cyclotrons making them more reliable, more compact or make the need for an injector cyclotron obsolete.

Since the advent of superconducting RF-technology, the option of linacs was also studied. The first example is the MYRRHA project that has been studied since 1999 [5, 6] and is explained in more detail in the following section. This approach was then also chosen by the Chinese ADS-project C-ADS [7] which was launched in 2011 and operates a test-injector since 2014. The target of the current extension phase is 500 MeV at 5 mA, with the final configuration aiming for 1 GeV at 15 mA. The reliability target is to have less than 25.000 beam trips/year with 1 s < t < 10 s. The second example, the MYRRHA project is detailed in the following chapters.

MYRRHA AND ITS FIRST IMPLEMENTATION PHASE (MINERVA)

Overview

The concept of an ADS has been studied at SCK CEN in Mol (Belgium) since a long time [5] which lead to the inception of the MYRRHA project in 1998 [8]. MYRRHA (Multi-purpose hYbrid Research Reactor for High-tech Applications) aims to demonstrate the ADS concept at pre-industrial scale, demonstrate transmutation and being a multipurpose and flexible irradiation facility. The project follows a staged implementation plan:

- Phase 1, also referred to as MINERVA: SC linac to 100 MeV, 4 mA CW
- Phase 2: extending linac to 600 MeV
- Phase 3: sub-critical reactor connected to the linac

The funding for the initial 100 MeV stage was approved by the Belgian government in 2018 and implementation has started at SCK CEN, the Belgium nuclear research center, which currently operates three nuclear reactors for research, education and industry, e.g. production of radiopharmaceuticals.

The MINERVA ground breaking is planned for summer 2022, and first accelerator operation in 2026. The project is setup to only have a relatively small core team at SCK CEN leveraging many international collaborations and aims to outsource significant parts to our industrial partners.

The 2nd and 3rd phases of MYRRHA are envisaged to be implemented until 2035, within an international consortium.

Accelerator Configuration

While in the final configuration the accelerator will feature two injectors and accelerate a 4 mA CW beam to 600 MeV, the first implementation stage, will be limited to 100 MeV with a single injector (see Fig. 2).

The injector consists of an ECR ion source, a LEBT with space charge compensation and two solenoids, a 4-rod RFQ (IAP Frankfurt) [9] and a normal conducting 176.1 MHz CH-cavity section including several rebunching cavities accelerating to 17 MeV (Fig. 3).

After the injector switchyard, the protons will be accelerated in superconducting single 352.2 MHz spoke cavities to 100 MeV. The design of the Single Spoke cavity has been developed by IPNO and first prototypes have been successfully tested [9]. There are 30 cryo-modules each housing 2 cavities. Each cavity is powered by a dedicated solid-state amplifier.

In the later extension stage, it is envisaged to switch at 100 MeV to switch to medium beta cavities, where it is not yet finally decided which type, spoke at 352.2 MHz or elliptical at 704.4 MHz, they are going to be. At around 200 MeV it is then foreseen to switch to 704.4 MHz elliptical cavities with a matched beta of 0.7.

As the RF-cavities in the injector must be individually matched to the beam energy, no serial redundancy is possible and thus two injectors are envisaged for MYRRHA. On the other hand, serial redundancy with approx. 30% overhead is applied in the single spoke section. Local compensation schemes have already been established, where the loss of one RF-cavity is compensated by the next neighbours. In the future, a global compensation scheme will be studied to distribute the compensation over the whole machine. While this will increase the requirements on the control system to reconfigure many elements, it will allow to use the cavities more effectively. More detailed studies e.g. on the orbit correction as part of the fast recommissioning are under investigation.

Operational Injector Test Stand

Since March 2019 an injector test stand is available and accelerating protons (Fig. 4). It is used to test critical components like the RFQ or the CH cavities along with the solid-state amplifiers as well as e.g. the space charge compensation in the LEBT.

ISBN: 978-3-95450-213-4 ISSN: 2673-5490 doi:10.18429/JACoW-IPAC2020-THVIR15

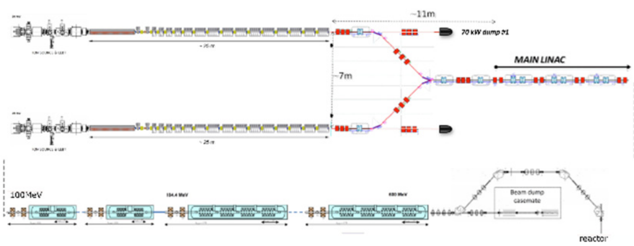

Figure 2: The final MYRRHA accelerator layout. In the first implementation phase, called MINERVA, only a single injector and up to 100 MeV (the single spoke section) will be constructed.

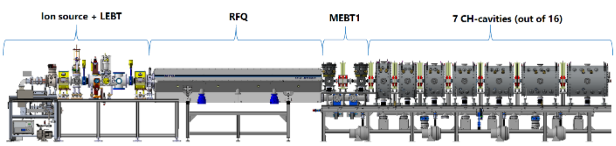

Figure 3: Sketch of the injector test stand as foreseen to be installed. The elements up (including) the RFQ are already available.

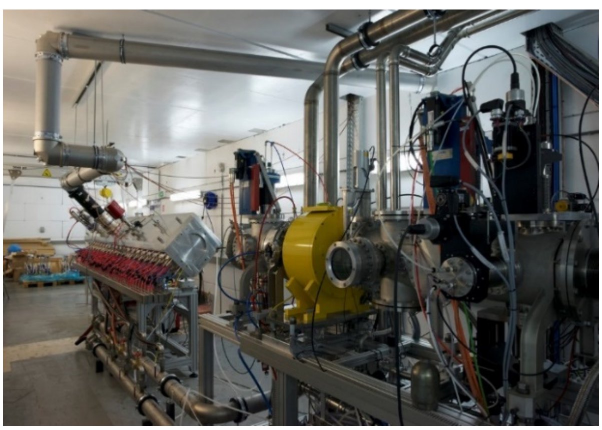

Figure 4: Photo of the injector test stand just before the connection of the RFQ to the LEBT.

Proton Target Facility

While MINERVA will at the start be used to develop and prove to meet the stringent reliability requirements, it will in parallel be able to deliver beam to a Proton Target Facility (PTF). It is envisaged to be able to kick up to 0.5 ms beam pulses with up 250 Hz to the PTF facility, allowing up to 0.2 mA on fissile material targets or up to 0.5 mA on non-fissile material targets [10].

The generated high-purity Radioactive Ion Beams (RIB) will be used for physics experiments and as well as radioisotopes collection for medical research and use purpose [10].

The layout of this Isotope Separation OnLine (ISOL) system is strongly inspired by the proton target irradiation facility ARIEL at TRIUMF. The chosen modular facility providing required shielding whilst allowing ISOL components maintenance and target replacement. The envisaged conceptual target configuration is shown in Fig. 5.

ACKNOWLEGEMENTS

The authors would like to acknowledge the work of their SCK CEN colleagues as well as many international collaboration partners and the Belgian Federal Government for the continuous support and funds for the MYRRHA project.

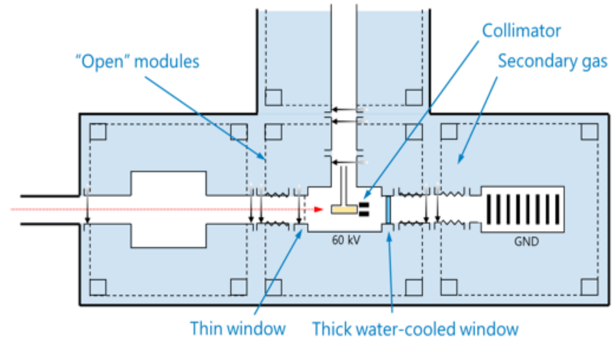

Figure 5: Envisaged ISOL target concept where up to 0.5 mA beam current is available in parallel to the other user stations.

REFERENCES

[1] H. Aït Abderrahim and P. D'hondt, "MYRRHA: A European Experimental ADS for R&D Applications, Status ad Mid-2005 and Prospective towards Implementation, *Journal of Nuclear Science and Technology*, Vol. 44, No. 3, pp.491-498, 2007. doi:10.1080/18811248.2007.9711313

[2] C. Rubbia *et al.*, "An energy amplifier for cleaner and inexhaustible nuclear energy production driven by a particle beam accelerator", 1993, CERN/AT/93-47.

[3] C. Rubbia *et al.*, "Conceptual design of a fast neutron operated high power energy amplifier", 1995, CERN/AT/95-44.

[4] P. McIntyre *et al.*, "Superconducting Sector Magnets for a Flux-Coupled Isochronous Cyclotron Stack." *IEEE Trans. on Appl. Superconductivity*, vol. 13, No. 2, Jun. 2003. doi:10.1109/TASC.2003.812669

[5] H. Aït Abderrahim and Y. Jongen, "ADONIS: the proton-driven neutron source for radioisotope production", 1999, *in IAEA-TECDOC-1065.*

[6] H. Saugnac *et al.*, "The MYRRHA Spoke Cryomodule Design", in *Proc. LINAC'14*, Geneva, Switzerland, Aug.-Sep. 2014, paper TUPP082, pp. 613-615.

[7] Shuhui Liu *et al.*, "Commissioning of China ADS demo Linac and baseline design of CiADS project", *2020 J. Phys.: Conf. Ser.*, vol. 1401, p. 012009. doi:10.1088/1742-6596/1401/1/012009

[8] MYRRHA, https://myrrha.be/

[9] S. Lamprecht *et al.*, "Conditioning of the Frontline Cavities of the MYRRHA Injector", in *Proc. 10th Int. Particle Accelerator Conf. (IPAC'19)*, Melbourne, Australia, May 2019, pp. 895-897. doi:10.18429/JACoW-IPAC2019-MOPTS023

[10] L. Popescu *et al.*, "High-power target development for the next-generation ISOL facilities", *Nucl. Instr. Meth. Phys. Res. B*, vol. 463, pp. 262-268, 2020. doi.org/10.1016/j.nimb.2019.05.023

ISBN: 978-3-95450-213-4   ISSN: 2673-5490

List of Authors

Bold papercodes indicate primary authors; ~~crossed out~~ papercodes indicate 'no submission'

11th Int. Particle Acc. Conf. IPAC2020, Caen, France JACoW Publishing
ISBN: 978-3-95450-213-4 ISSN: 2673-5490

ISBN: 978-3-95450-213-4 ISSN: 2673-5490

ISBN: 978-3-95450-213-4 ISSN: 2673-5490

ISBN: 978-3-95450-213-4 ISSN: 2673-5490